Ministry of Science and Higher Education of the Russian Federation
ITMO University

ISSN 2220-8054

NANOSYSTEMS:

PHYSICS, CHEMISTRY, MATHEMATICS

2023, volume 14(2)

Наносистемы: физика, химия, математика

2023, том 14, № 2

N A N O
Ф&Х&М

NANOSYSTEMS:

PHYSICS, CHEMISTRY, MATHEMATICS

Address: ITMO University, Kronverkskiy pr., 49, St. Petersburg 197101, Russia.
Phone: +7(812)607-02-54, **Journal site:** http://nanojournal.ifmo.ru/,
E-mail: nanojournal.ifmo@gmail.com

AIM AND SCOPE

The scope of the journal includes all areas of nano-sciences. Papers devoted to basic problems of physics, chemistry, material science and mathematics inspired by nanosystems investigations are welcomed. Both theoretical and experimental works concerning the properties and behavior of nanosystems, problems of its creation and application, mathematical methods of nanosystem studies are considered.

The journal publishes scientific reviews (up to 30 journal pages), research papers (up to 15 pages) and letters (up to 5 pages). All manuscripts are peer-reviewed. Authors are informed about the referee opinion and the Editorial decision.

CONTENT

MATHEMATICS

PHYSICS

CHEMISTRY AND MATERIAL SCIENCE

ERRATUM

NANOSYSTEMS:
PHYSICS, CHEMISTRY, MATHEMATICS

Original article

Rasulov T.H., Bahronov B.I. *Nanosystems: Phys. Chem. Math.*, 2023, **14** (2), 151–157.
http://nanojournal.ifmo.ru
DOI 10.17586/2220-8054-2023-14-2-151-157

Existence of the eigenvalues of a tensor sum of the Friedrichs models with rank 2 perturbation

Tulkin H. Rasulov[a,b], Bekzod I. Bahronov[c]

Bukhara State University, Bukhara, Uzbekistan

[a]rth@mail.ru, [b]t.h.rasulov@buxdu.uz, [c]b.bahronov@mail.ru

Corresponding author: Tulkin H. Rasulov, rth@mail.ru

ABSTRACT In the paper we consider a tensor sum $H_{\mu,\lambda}$, $\mu, \lambda > 0$ of two Friedrichs models $h_{\mu,\lambda}$ with rank two perturbation. The Hamiltonian $H_{\mu,\lambda}$ is associated with a system of three quantum particles on one-dimensional lattice. We investigate the number and location of the eigenvalues of $H_{\mu,\lambda}$. The existence of eigenvalues located respectively inside, in the gap, and below the bottom of the essential spectrum of $H_{\mu,\lambda}$ is proved.

KEYWORDS tensor sum, Hamiltonian, lattice, quantum particles, non-local interaction, Friedrichs model, eigenvalue, perturbation.

ACKNOWLEDGEMENTS The authors thank the anonymous referee for reading the manuscript carefully and for making valuable suggestions.

FOR CITATION Rasulov T.H., Bahronov B.I. Existence of the eigenvalues of a tensor sum of the Friedrichs models with rank 2 perturbation. *Nanosystems: Phys. Chem. Math.*, 2023, **14** (2), 151–157.

1. Introduction

The problem of the existence of bound states of quantum particles (from the mathematical point of view the existence of the eigenvalues of the corresponding Hamiltonian) is very important in modern mathematical physics. Its usefulness is demonstrated by the particle storage problem. As an example of such an application the storage of hydrogen in nanolayered structures can be given. These systems can be used to produce an effective and safe fuel containers. It is well known that a particle can be stored in disturbed (curved, deformed, etc.) nanolayers. Experiments show that after intercalation into a nanolayered structure, hydrogen ions are concentrated near defects of the structure. In terms of mathematics, this means that the discrete spectrum of the corresponding Hamiltonian is not empty, and the eigenfunctions are localized near the structure defects. The problem of quantum particles storage in a nanolayered structures is considered in [1] and the system of a few electrons in 2D quantum waveguides coupled through a window is studied. The bound states induced by the disturbance are investigated. In [2] a number of numerical results for the bound state energies of one and two-particle systems in two adjacent 3D layers, connected through a window is presented and the relation between the shape of the window and the energy levels, as well as the number of eigenfunction's nodal domains are investigated. For mathematical models of quantum wave guides, it was shown in [3] that in some situations two interacting particles can be trapped more easily than a single particle. In this paper, we consider the existence of an eigenvalue for the Hamiltonian of a three-particle system on a lattice (three-particle discrete Schrödinger operator), the case where the discrete spectrum of the considered Hamiltonian is not empty. Here, the role of the two-particle discrete Schrödinger operator is played by the Friedrichs model.

Spectral properties of the operators known as the Friedrichs model [4] are important in the problems of analysis, mathematical physics, and probability theory. The latter operators act in the Hilbert space $L_2(\mathcal{M}, d\mu)$, where $(\mathcal{M}, d\mu)$ is a manifold with measure, according to the rule

$$(Af)(p) = u(p)f(p) - \alpha \int\limits_{\mathcal{M}} D(p,q)f(q)d\mu(q), \quad f \in L_2(\mathcal{M}, d\mu), \tag{1.1}$$

where the function $u(\cdot)$ is a function on the manifold $\mathcal{M} \subset \mathbb{R}^{\mathrm{d}}$, the function $D(\cdot,\cdot)$ is a function of two variables on the manifold $\mathcal{M}^2$, and α is a coupling constant. In [4] it was established that in the case where $\mathcal{M} = [-1;1] \subset \mathbb{R}$, $u(q) = q$ and $\alpha > 0$ is small, the operator A up to finitely many eigenvalues has an absolutely continuous spectrum and that this operator in its absolutely continuous subspace is unitarily equivalent to the operator A_0 of the form

$$(A_0 f)(p) = u(p)f(p), \quad f \in L_2(\mathcal{M}, d\mu). \tag{1.2}$$

Later, a more general model (in which $\mathcal{M}$ is an arbitrary interval in $\mathbb{R}$, the function f takes values in a Hilbert space $\mathcal{H}$, and the kernel D is replaced with a bounded operator in $\mathcal{H}$) was suggested in [5], and the results in [4] were transferred to it. This generalization essentially extended the range of application of the theory. It was shown in [6], developing the results of [5], and already entirely completely in [7] that the requirement that the parameter α be small can be dropped

under certain restrictions on the kernel D (namely, under the assumption that it is compact and that it belongs to the Hölder class with an exponent $\mu > 1/2$). In this case, the spectrum of A_0 consists of an absolutely continuous part filling an interval $\mathcal{M} \subset \mathbb{R}$ and possibly finitely many eigenvalues with finite multiplicity. The existence of wave operators related to A_0 was also proved in [5] and [7] (also see [8] and [9] for the Friedrichs model).

In the present paper, we consider a tensor sum $H_{\mu,\lambda}$, $\mu, \lambda > 0$ of two Friedrichs models $h_{\mu,\lambda}$ with rank two perturbation. The Hamiltonian $H_{\mu,\lambda}$ is associated with a system of three quantum particles on one-dimensional lattice. We investigate the number and location of the eigenvalues of $H_{\mu,\lambda}$. The existence of eigenvalues located respectively inside, in the gap, and below the bottom of the essential spectrum of $H_{\mu,\lambda}$ is proved.

2. Friedrichs model

We denote by $\mathbb{T}$ the one-dimensional torus. The operations addition and multiplication by real numbers elements of $\mathbb{T} \subset \mathbb{R}$ should be regarded as operations on $\mathbb{R}$ modulo $2\pi\mathbb{Z}$. For example, if $x = 3\pi/5$, $y = 2\pi/3 \in \mathbb{T}$, then $x + y = -11\pi/15$, $10x = 0 \in \mathbb{T}$.

Let $L_2(\mathbb{T})$ be the Hilbert space of square integrable (complex) functions defined on $\mathbb{T}$.

We consider the bounded and self-adjoint Friedrichs model $h_{\mu,\lambda}$ acting on the Hilbert space $L_2(\mathbb{T})$ as

$$h_{\mu,\lambda} := h_{0,0} - \mu k_1 + \lambda k_2,$$

where $h_{0,0}$ is the multiplication operator by the function $u(\cdot)$:

$$(h_{0,0}g)(x) = u(x)g(x),$$

and k_α, $\alpha = 1, 2$ are non-local interaction (integral) operators:

$$(k_\alpha g)(x) = v_\alpha(x) \int\limits_{\mathbb{T}} v_\alpha(t)g(t)dt, \quad \alpha = 1, 2.$$

Here $g \in L_2(\mathbb{T})$; $\mu, \lambda > 0$ are positive reals, $u(\cdot)$ and $v_\alpha(\cdot)$, $\alpha = 1, 2$ are real-valued continuous functions on $\mathbb{T}$.

It is remarkable that the choice of operators k_1 and k_2 with different signs allows to study the eigenvalues of $h_{\mu,\lambda}$ located to the left and to the right of its essential spectrum (see Theorem 2.4).

Throughout this paper, we assume the following additional assumptions.

Assumption 2.1. *The function $u(\cdot)$ is a twice continuously differentiable function on $\mathbb{T}$, has minima at the points $x_1, \cdots, x_n \in \mathbb{T}$ and has maxima at the points $y_1, \cdots, y_m \in \mathbb{T}$.*

Assumption 2.2. *We suppose that*

$$\mathrm{mes}(\mathrm{supp}\{v_1(\cdot)\} \cap \mathrm{supp}\{v_2(\cdot)\}) = 0, \tag{2.1}$$

where $\mathrm{mes}(\cdot)$ is the Lebesgue measure on $\mathbb{R}$ and $\mathrm{supp}\{v_\alpha(\cdot)\})$ is the support of the function $v_\alpha(\cdot)$.

The following example shows that the class of functions $u(\cdot)$ and $v_\alpha(\cdot)$, $\alpha = 1, 2$ satisfying above mentioned Assumptions 2.1 and 2.2 is nonempty. To prove this fact, we introduce the functions of the form:

$$\begin{aligned} u(x) &= 1 - \cos(3x); \\ v_1(x) &= \begin{cases} \sin x, & x \in [0; \pi]; \\ 0, & \text{othervice}; \end{cases} \\ v_2(x) &= \sin x - v_1(x), \quad x \in \mathbb{T}. \end{aligned} \tag{2.2}$$

Then, it is easy to check that points $x_1 = 0$, $x_2 = 2\pi/3$, $x_3 = -2\pi/3$ and $y_1 = \pi$, $y_2 = \pi/3$, $y_3 = -\pi/3$ are the extremal points for the function $u(\cdot)$. Validness of the condition (2.1) follows from the constructions of $v_\alpha(\cdot)$, $\alpha = 1, 2$.

The spectrum, the essential spectrum and the discrete spectrum of a bounded self-adjoint operator will be denoted by $\sigma(\cdot)$, $\sigma_{\mathrm{ess}}(\cdot)$ and $\sigma_{\mathrm{disc}}(\cdot)$, respectively.

By the definition, the perturbation $-\mu k_1 + \lambda k_2$ of the operator $h_{0,0}$ is a self-adjoint operator of rank two. Therefore, in accordance with the Weyl theorem [10] about the invariance of the essential spectrum under the finite rank perturbations, the essential spectrum of the operator $h_{\mu,\lambda}$ coincides with the spectrum of $h_{0,0}$:

$$\sigma_{\mathrm{ess}}(h_{\mu,\lambda}) = \sigma(h_{0,0}) = [m; M],$$

where the numbers m and M are defined by

$$m := \min_{x\in\mathbb{T}} u(x), \quad M := \max_{x\in\mathbb{T}} u(x).$$

In order to study the spectral properties of the operator $h_{\mu,\lambda}$, we introduce the following bounded self-adjoint operators (Friedrichs model with rank one perturbation) $h_\mu^{(1)}$, $h_\lambda^{(2)}$ acting on $L_2(\mathbb{T})$ in accordance with the rule

$$h_\mu^{(1)} := h_{0,0} - \mu k_1, \quad h_\lambda^{(2)} := h_{0,0} + \lambda k_2. \tag{2.3}$$

Let $\mathbb{C}$ be the field of complex numbers. We define the analytic functions $\Delta_\mu^{(1)}(\cdot)$ and $\Delta_\lambda^{(2)}(\cdot)$ (the Fredholm determinant associated with the operator $h_\mu^{(1)}$ and $h_\lambda^{(2)}$, respectively) in $\mathbb{C}\setminus[m;M]$ by

$$\Delta_\mu^{(1)}(z) := 1-\mu I_1(z), \quad \Delta_\lambda^{(2)}(z) := 1+\lambda I_2(z),$$

$$I_i(z) := \int\limits_{\mathbb{T}} \frac{v_i^2(t)dt}{u(t)-z}, \quad i=1,2.$$

Then the Birman-Schwinger principle and the Fredholm theorem imply that [11, 12] the operator $h_\mu^{(1)}$ ($h_\lambda^{(2)}$) has an eigenvalue $z\in\mathbb{C}\setminus[m;M]$ if and only if $\Delta_\mu^{(1)}(z)=0$ ($\Delta_\lambda^{(2)}(z)=0$). From here, it follows that for the discrete spectrum of $h_\mu^{(1)}$ and $h_\lambda^{(2)}$ the equalities

$$\sigma_{\rm disc}(h_\mu^{(1)}) = \{z\in\mathbb{C}\setminus[m;M]:\ \Delta_\mu^{(1)}(z)=0\}; \tag{2.4}$$

$$\sigma_{\rm disc}(h_\lambda^{(2)}) = \{z\in\mathbb{C}\setminus[m;M]:\ \Delta_\lambda^{(2)}(z)=0\} \tag{2.5}$$

hold.

The following lemma establishes a relation between eigenvalues of $h_{\mu,\lambda}$ and $h_\mu^{(1)}$, $h_\lambda^{(2)}$.

Lemma 2.3. *Let Assumption* 2.2 *be fulfilled. The number $z\in\mathbb{C}\setminus[m;M]$ is an eigenvalue of $h_{\mu,\lambda}$ if and only if z is an eigenvalue one of the operators $h_\mu^{(1)}$ and $h_\lambda^{(2)}$.*

Proof. Let the number $z\in\mathbb{C}\setminus[m;M]$ be an eigenvalue of $h_{\mu,\lambda}$ and $g\in L_2(\mathbb{T})$ be the corresponding eigenfunction. Then g satisfies the equation

$$(u(x)-z)g(x)-\mu v_1(x)\int\limits_{\mathbb{T}} v_1(t)g(t)dt+\lambda v_2(x)\int\limits_{\mathbb{T}} v_2(t)g(t)dt=0. \tag{2.6}$$

It is easy to see that for any $z\in\mathbb{C}\setminus[m;M]$ the relation $u(x)-z\neq 0$ holds for all $x\in\mathbb{T}$. Then equation (2.6) implies

$$g(x)=\frac{\mu v_1(x)d_1-\lambda v_2(x)d_2}{u(x)-z}, \tag{2.7}$$

where

$$d_\alpha := \int\limits_{\mathbb{T}} v_\alpha(t)g(t)dt, \quad \alpha=1,2. \tag{2.8}$$

Substituting the expression (2.7) for g into (2.8) and using Assumption 2.2, that is, the condition (2.1), we conclude that equation (2.6) has a nonzero solution if and only if the system of equations

$$\Delta_\mu^{(1)}(z)d_1=0,$$
$$\Delta_\lambda^{(2)}(z)d_2=0$$

has a nonzero solution, i.e., if the condition $\Delta_\mu^{(1)}(z)\Delta_\lambda^{(2)}(z)=0$ holds. If we set $v_1(x)\equiv 0$ ($v_2(x)\equiv 0$), then by the definitions of $h_{\mu,\lambda}$ and $h_\mu^{(1)}$ ($h_\lambda^{(2)}$), we obtain that $h_{\mu,\lambda}=h_\mu^{(1)}$ ($h_{\mu,\lambda}=h_\lambda^{(2)}$). The last two facts complete the proof. □

By Lemma 2.3, if the Assumption 2.2 is valid, then the discrete spectrum of $h_{\mu,\lambda}$ and $h_\mu^{(1)}$, $h_\lambda^{(2)}$ are related by the equality

$$\sigma_{\rm disc}(h_{\mu,\lambda})=\sigma_{\rm disc}(h_\mu^{(1)})\cup\sigma_{\rm disc}(h_\lambda^{(2)}).$$

We note that the operators $h_\mu^{(1)}$ and $h_\lambda^{(2)}$ have a structure simpler than that of $h_{\mu,\lambda}$, and therefore, the latter equality plays an important role in further investigating the spectrum of $h_{\mu,\lambda}$.

In what follows, C_1, C_2 and C_3 denote various positive constants, the values of which are not specified.

Theorem 2.4. *Let Assumptions* 2.1 *and* 2.2 *be fulfilled. If $v_1(x_\alpha)\neq 0$ for some $\alpha\in\{1,2,...,n\}$ and $v_2(y_\beta)\neq 0$ for some $\beta\in\{1,2,...,m\}$, then for all values of $\mu,\lambda>0$ the operator $h_{\mu,\lambda}$ has two simple eigenvalues $E_\mu^{(1)}\in(-\infty;m)$ and $E_\lambda^{(2)}\in(M;\infty)$.*

Proof. By Assumption 2.1, the function $u(\cdot)$ is a twice continuously differentiable function on $\mathbb{T}$, has minima at the points $x_1,\cdots,x_n\in\mathbb{T}$. Therefore, there exist numbers $C_1,C_2>0$ and $\delta>0$ such that

$$C_1|x-x_j|^2\le u(x)-m\le C_2|x-x_j|^2, \quad x\in U_\delta(x_j), \quad j=\overline{1,n}. \tag{2.9}$$

If $v_1(x_\alpha)\neq 0$ for some $\alpha\in\{1,2,...,n\}$, then there exist numbers $C_1>0$ and $\delta>0$ such that

$$v_1(x)\ge C_1, \quad x\in U_\delta(x_\alpha). \tag{2.10}$$

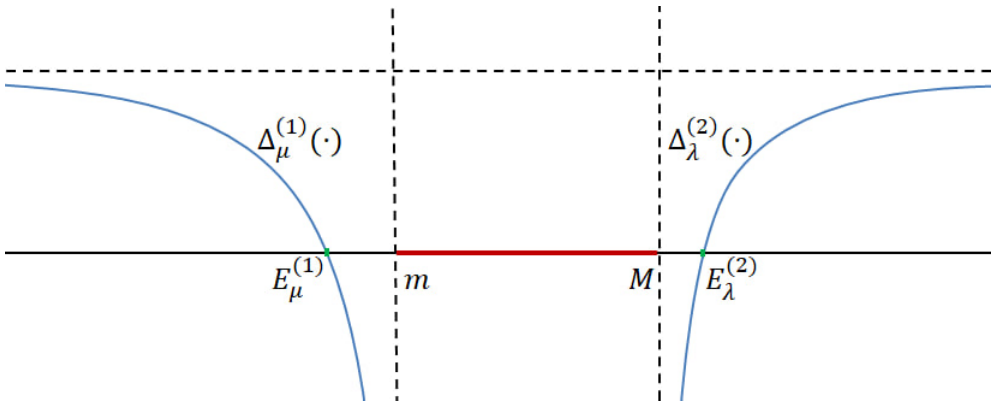

FIG. 1. Spectrum of $h_{\mu,\lambda}$

Using estimates (2.9) and (2.10), we have

$$\int\limits_{\mathbb{T}} \frac{v_1^2(t)dt}{u(t)-m} \geq \int\limits_{U_\delta(x_\alpha)} \frac{v_1^2(t)dt}{u(t)-m} \geq C_1 \int\limits_{U_\delta(x_\alpha)} \frac{dt}{|t-x_\alpha|^2} = \infty.$$

From here, we obtain that $\Delta_\mu^{(1)}(m) = -\infty$. One can see that $\Delta_\mu^{(1)}(z) \to 1$ as $z \to -\infty$. Since the function $\Delta_\mu^{(1)}(\cdot)$ is decreasing on $(-\infty; m]$ for the case $v_1(x_\alpha) \neq 0$ we obtain that the operator $h_\mu^{(1)}$ has unique eigenvalue $E_\mu^{(1)}$ smaller than m. By Lemma 2.3, the number $E_\mu^{(1)}$ is an eigenvalue of $h_{\mu,\lambda}$. It is clear that $\Delta_\lambda^{(2)}(z) > 1$ for all $z < m$. Therefore, the operator $h_\lambda^{(2)}$ has no eigenvalues smaller than m. Consequently, the number $E_\mu^{(1)}$ is the unique eigenvalue of $h_{\mu,\lambda}$.

We note that $u(\cdot)$ is a twice continuously differentiable function on $\mathbb{T}$, has maxima at the points $y_1, \cdots, y_n \in \mathbb{T}$. Therefore, there exist $C_1, C_2 > 0$ and $\delta > 0$ such that

$$C_1|x-y_j|^2 \leq M - u(x) \leq C_2|x-y_j|^2, \quad y \in U_\delta(y_j), \quad j = \overline{1,n}. \tag{2.11}$$

If $v_2(y_\beta) \neq 0$ for some $\beta \in \{1, 2, ..., n\}$ then there exist $C_1 > 0$ and $\delta > 0$ such that

$$v_2(y) \geq C_1, \quad y \in U_\delta(y_\beta). \tag{2.12}$$

Using estimates (2.11) and (2.12), we have

$$\int\limits_{\mathbb{T}} \frac{v_2^2(t)dt}{u(t)-M} \leq -\int\limits_{U_\delta(y_\beta)} \frac{v_2^2(t)dt}{M-u(t)} \leq -C_1 \int\limits_{U_\delta(y_\beta)} \frac{dt}{|t-y_\beta|^2} = -\infty.$$

The latter assertion yields that $\Delta_\lambda^{(2)}(M) = -\infty$. It is easy to check that $\Delta_\lambda^{(2)}(z) \to 1$ as $z \to \infty$. Since the function $\Delta_\lambda^{(2)}(\cdot)$ is decreasing on $[M; \infty)$ from the fact $v_2(y_\beta) \neq 0$ we obtain that the operator $h_\lambda^{(2)}$ has an eigenvalue $E_\lambda^{(2)}$ bigger than M. By Lemma 2.3, the number $E_\lambda^{(2)}$ is an eigenvalue of $h_{\mu,\lambda}$. By the construction of $\Delta_\mu^{(1)}(\cdot)$, we have $\Delta_\mu^{(1)}(z) > 1$ as $z > M$. So, the operator $h_\mu^{(1)}$ has no eigenvalues bigger than M. Therefore, the number $E_\lambda^{(2)}$ is the unique eigenvalue of $h_{\mu,\lambda}$. □

3. Three-particle model operator

In this section, at first, we provide an overview of the model Schrödinger operator.

We consider the discrete Schrödinger operator $\widehat{A} := \widehat{A}_0 - \widehat{K}$ acting in the space $l_2(\mathbb{Z}^2)$. The kinetic energy $\widehat{A}_0$ is given by a convolution with a function of the general form:

$$(\widehat{A}_0\widehat{\psi})(s_1,s_2) = \sum_{n_1,n_2\in\mathbb{Z}} u_0(s_1-n_1, s_2-n_2)\widehat{\psi}(n_1,n_2),$$

and the potential energy $\widehat{K}$ is defined as follows

$$(\widehat{K}\widehat{\psi})(s_1,s_2) = (u_1(s_1)+u_2(s_2))\widehat{\psi}(s_1,s_2).$$

We assume that the functions $u_0(\cdot,\cdot)$ and $u_\alpha(\cdot)$, $\alpha = 1, 2$ satisfy the conditions

$$|u_0(s_1,s_2)| \leq C_0 \exp(-a(|s_1|+|s_2|)), \quad a > 0;$$
$$|u_\alpha(s_1)| \leq C_\alpha \exp(-b_\alpha|s_1|), \quad b_\alpha > 0, \quad \alpha = 1,2,$$

where C_α, $\alpha = 0, 1, 2$ are positive constants.

The operator $\widehat{A}$ is a particular case of the lattice model Hamiltonian studied in [13, 14].

It is remarkable that in [15] the diffraction approach applications to the quantum scattering problems of three three-dimensional charged quantum particles are considered for the construction of the Schrödinger operator eigenfunction asymptotics in different domains of configuration space.

Let $L_2(\mathbb{T}^n)$ be the Hilbert space of square integrable (complex) functions defined on $\mathbb{T}^n$, $n = 1, 2$ and $\mathcal{F} : l_2(\mathbb{Z}^2) \to L_2(\mathbb{T}^2)$ be the standard Fourier transformation:

$$(\mathcal{F}\widehat{\psi})(x,y) = \frac{1}{2\pi} \sum_{n_1,n_2\in\mathbb{Z}} \widehat{\psi}(n_1,n_2) \exp(i[(x,n_1)+(y,n_2)]).$$

Then (see [14]), the operator

$$A := \mathcal{F}\widehat{A}\mathcal{F}^{-1} : L_2(\mathbb{T}^2) \to L_2(\mathbb{T}^2)$$

can be represented as $A := A_0 - K_1 - K_2$, where the operators A_0 and K_α, $\alpha = 1, 2$ are defined by

$$(A_0 f)(x,y) = k_0(x,y)f(x,y), \quad f \in L_2(\mathbb{T}^2);$$

$$(K_1 f)(x,y) = \int_{\mathbb{T}} k_1(x-s)f(s,y)ds, \quad (K_2 f)(x,y) = \int_{\mathbb{T}} k_2(y-s)f(x,s)ds, \quad f \in L_2(\mathbb{T}^2).$$

Here $k_0(\cdot,\cdot)$ and $k_\alpha(\cdot)$ are the Fourier transforms of the functions $u_0(\cdot,\cdot)$ and $u_\alpha(\cdot)$, $\alpha = 1, 2$, respectively. Usually, the operator A is called the momentum representation of the discrete operator $\widehat{A}$.

Let $L_2^{\rm s}(\mathbb{T}^2)$ be the Hilbert space of square integrable symmetric (complex) functions defined on $\mathbb{T}^2$.

Let us consider the Hamiltonian of the form

$$H_{\mu,\lambda} : L_2^{\rm s}(\mathbb{T}^2) \to L_2^{\rm s}(\mathbb{T}^2), \quad H_{\mu,\lambda} := H_{0,0} - \mu(V_{11}+V_{12}) + \lambda(V_{21}+V_{22}), \tag{3.1}$$

where $H_{0,0}$ is the multiplication operator by the function $u(x) + u(y)$:

$$(H_{0,0}f)(x,y) = (u(x)+u(y))f(x,y),$$

and $V_{\alpha\beta}$, $\alpha, \beta = 1, 2$ are non-local interaction operators:

$$(V_{\alpha 1}f)(x,y) = v_\alpha(x)\int_{\mathbb{T}} v_\alpha(t)f(t,y)dt, \quad (V_{\alpha 2}f)(x,y) = v_\alpha(y)\int_{\mathbb{T}} v_\alpha(t)f(x,t)dt, \quad \alpha = 1, 2.$$

Here $f \in L_2^{\rm s}(\mathbb{T}^2)$. By the definition, the operators V_{ij}, $i, j = 1, 2$ are partial integral operators with degenerate kernel of rank 1.

It is clear that the operator $H_{\mu\,\lambda}$ is bounded and self-adjoint in $L_2^{\rm s}(\mathbb{T}^2)$.

We note that the operator $H_{\mu,\lambda}$ is related with the Schrödinger operators of a system of three particles on a three-dimensional lattice and such type operators were studied in [11, 16–18]. In [16, 17], the sufficient conditions for the finiteness and infiniteness of the discrete spectrum are found. In [11], the Efimov effect for model discrete Schrödinger operator was demonstrated when the parameter function $w(\cdot,\cdot)$ has a special form. In [18], the essential spectrum and the number of eigenvalues of the typical model were studied for the function $w(\cdot,\cdot)$ of the form $w(p,q) = u(p)u(q)$.

Main result of the note is the following lemma.

Lemma 3.1. *Let Assumption* 2.1 *and* 2.2 *be fulfilled.* (i) *For any $\mu, \lambda > 0$, the numbers $2E_\mu^{(1)}$ and $2E_\lambda^{(2)}$ are simple eigenvalues of $H_{\mu,\lambda}$. Moreover,*

$$\sigma_{\rm ess}(H_{\mu,\lambda}) = [E_\mu^{(1)}+m\,; E_\mu^{(1)}+M] \cup [2m\,; 2M] \cup [E_\lambda^{(2)}+m\,; E_\lambda^{(2)}+M];$$

$$\sigma_{\rm pp}(H_{\mu,\lambda}) = \{2E_\mu^{(1)}\,; E_\mu^{(1)}+E_\lambda^{(2)}\,; 2E_\lambda^{(2)}\}.$$

(ii) *For any fixed $a < m$ and $b > M$, there are two numbers $\mu_0 = \mu_0(a) > 0$ and $\lambda_0 = \lambda_0(b) > 0$, respectively, such that the numbers $2a$, $a+b$ and $2b$ are eigenvalues of H_{μ_0,λ_0}.*

(iii) *For any $c \in [2m; 2M]$, there exist two numbers $\mu_1 > 0$ and $\lambda_1 > 0$ such that the number c is an eigenvalue of H_{μ_1,λ_1}.*

Proof. From the definitions of $H_{\mu,\lambda}$ and $h_{\mu,\lambda}$, we obtain the representation

$$H_{\mu,\lambda} = h_{\mu,\lambda} \otimes I + I \otimes h_{\mu,\lambda},$$

where I is the identity operator on $L_2(\mathbb{T})$.

Therefore, by theorem on the spectrum of the tensor sum of two operators, the equality

$$\sigma(H_{\mu,\lambda}) = \sigma(h_{\mu,\lambda}) + \sigma(h_{\mu,\lambda}) \tag{3.2}$$

holds.

(i) By Theorem 2.4, for any $\mu, \lambda > 0$, the operator $h_{\mu,\lambda}$ has two eigenvalues $E_\mu^{(1)} \in (-\infty; m)$ and $E_\lambda^{(2)} \in (M; \infty)$. Hence,

$$\sigma(h_{\mu,\lambda}) = \{E_\mu^{(1)}\} \cup [m; M] \cup \{E_\lambda^{(2)}\}.$$

Then by (3.2), the numbers $2E_\mu^{(1)}$ and $2E_\lambda^{(2)}$ are simple eigenvalues of $H_{\mu,\lambda}$. In addition,

$$\sigma_{\rm ess}(H_{\mu,\lambda}) = [E_\mu^{(1)} + m; E_\mu^{(1)} + M] \cup [2m; 2M] \cup [E_\lambda^{(2)} + m; E_\lambda^{(2)} + M];$$

$$\sigma_{\rm pp}(H_{\mu,\lambda}) = \{2E_\mu^{(1)}; E_\mu^{(1)} + E_\lambda^{(2)}; 2E_\lambda^{(2)}\}.$$

Moreover, $\sigma_{\rm disc}(H_{\mu,\lambda}) = \sigma_{\rm pp}(H_{\mu,\lambda})$ if and only if $E_\mu^{(1)} + E_\lambda^{(2)} \in (E_\mu^{(1)} + M; 2m) \cup (2M; E_\lambda^{(2)} + m)$.

(ii) Let for any $a < m$, $b > M$, $\mu_0 = \mu_0(a) = (I_1(a))^{-1}$, $\lambda_0 = \lambda_0(b) = (-I_2(b))^{-1}$ the equalities $\Delta_{\mu_0}^{(1)}(a) = 0$ and $\Delta_{\lambda_0}^{(2)}(a) = 0$ hold. By Lemma 2.3, the numbers a and b are eigenvalues of the operator h_{μ_0,λ_0}. From equality (3.2) we conclude that the numbers $2a$, $a + b$, $2b$ are eigenvalues of H_{μ_0,λ_0}.

(iii) Let $c \in [2m; 2M]$ be arbitrary. Then for any $b > 2M - m$, we have $c - b < m$. Denote $\mu_1 = (I_1(c - b))^{-1}$ and $\lambda_1 = (-I_2(b))^{-1}$. It is clear that $\Delta_{\mu_1}^{(1)}(c - b) = 0$ and $\Delta_{\lambda_1}^{(2)}(b) = 0$. By Lemma 2.3, the numbers $c - b$ and b are eigenvalues of $h_{\mu_1,\lambda}$ $(\lambda > 0)$ and h_{μ,λ_1} $(\mu > 0)$. From here, we obtain that the numbers $c - b$ and b are eigenvalues of h_{μ_1,λ_1}. From equality (3.2), we obtain that the number c is the eigenvalue of H_{μ_1,λ_1}.

So, in this paper, it was shown that there are two eigenvalues lying, correspondingly, to the left and to the right of the essential spectrum for the Friedrichs model $h_{\mu,\lambda}$. The existence of the threshold eigenvalues and virtual levels (threshold energy resonances) for a generalized Friedrichs model have been studied in [19–21]. We recall also that the symmetric operators of the form $S := A \otimes I + I \otimes T$, where A is symmetric and $T = T^*$ is (in general) unbounded, is considered in [22] and a boundary triplet Π_S for S^* preserving the tensor structure is constructed. This paper presents also an application of the result to 1D Schrödinger operators. Such operators naturally arise in problems of simulation of quantum particle having point contact to reservoirs.

References

[1] Popov I.Y., Melikhov I.F. Multi-particle bound states in window-coupled 2D quantum waveguides. *Chinese J. of Physics - Taipei*, 2015, **53**(3), P. 0802/1–12.

[2] Bagmutov A.S., Popov I.Y. Window-coupled nanolayers: window shape influence on one-particle and two-particle eigenstates. *Nanosystems: Physics, Chemistry, Mathematics*, 2020, **11**(6), P. 636–641.

[3] Linde Y. Geometrically induced two-particle binding in a waveguide. *J. Phys. A: Math. Gen.*, 2006, **39**(18), P. 5105–5114.

[4] Friedrichs K.O. Uber die Spectralzerlegung einee Integral operators. *Math. Ann.*, 1938, **115**, P. 249–272.

[5] Friedrichs K.O. On the perturbation of continuous spectra. *Comm. Pure Appl. Math.*, 1948, **1**, P. 361–406.

[6] Faddeev L.D. The construction of the resolvent of the Schrödinger operator for a three-particle system, and the scattering problem. *Sov. Phys. Dokl.*, 1963, **7**, P. 600–602.

[7] Faddeev L.D. On a model of Friedrichs in the theory of perturbations of the continuous spectrum. *Am. Math. Soc., Transl.*, II. Ser., 1967, **6**(2), P. 177–203.

[8] Yafaev D.R. Mathematical Scattering Theory [in Russian], St. Petersburg State Univ., St. Petersburg, 1994; English transl. (Transl. Math. Monogr., Vol. 105), Amer. Math. Soc., Providence, R. I., 1992.

[9] Faddeev L.D., Merkuriev S.P. Quantum Scattering Theory for Several Particle Systems. *Math. Phys. Appl. Math.*, Vol. 11, Kluwer, Dordrecht, 1993.

[10] Reed M., Simon B. *Methods of Modern Mathematical Physics*. IV: Analysis of Operators. Academic Press, New York, 1979.

[11] Rasulov T.Kh. Asymptotics of the discrete spectrum of a model operator associated with the system of three particles on a lattice. *Theoret. and Math. Phys.*, 2010, **163**(1), P. 429–437.

[12] Albeverio S., Lakaev S.N., Muminov Z.I. The threshold effects for a family of Friedrichs models under rank one perturbations. *J. Math. Anal. Appl.*, 2007, **330**, P. 1152–1168.

[13] Mogilner A.I. Hamiltonians in solid state physics as multiparticle discrete Schrödinger operators: problems and results. *Advances in Sov. Math.*, 1991, **5**, P. 139–194.

[14] Zhukov Yu.V. The Iorio-O'Caroll theorem for an N-particle lattice Hamiltonian. *Theor. Math. Phys.*, 1996, **107**(1), P. 478–486.

[15] Budylin A.M., Koptelov Ya.Yu., Levin S.B. On asymptotic structure of three-body scattering states for the scattering problem of charged quantum particles. *Advances in Quantum Chemistry*, 2021, **84**, P. 347–424.

[16] Albeverio S., Lakae S.N.v, Djumanova R.Kh. The essential and discrete spectrum of a model operator associated to a system of three identical quantum particles. *Rep. Math. Phys.*, 2009, **63**(3), P. 359–380.

[17] Albeverio S., Lakaev S.N., Muminov Z.I. On the number of eigenvalues of a model operator associated to a system of three-particles on lattices. *Russ. J. Math. Phys.*, 2007, **14**(4), P. 377–387.

[18] Eshkabilov Yu.Kh., Kuchkarov R.R. Essential and discrete spectra of the three-particle Schrödinger operator on a lattice. *Theor. Math. Phys.*, 2012, **170**(3), P. 341–353.

[19] Rasulov T.H., Dilmurodov E.B. Eigenvalues and virtual levels of a family of 2×2 operator matrices. *Methods of Functional Analysis and Topology*, 2019, **25**(1), P. 273–281.

[20] Rasulov T.H., Dilmurodov E.B. Analysis of the spectrum of a 2×2 operator matrices. Discrete spectrum asymptotics. *Nanosystems: Physics, chemistry, mathematics*, 2020, **11**(2), P. 138–144.

[21] Rasulov T.H., Dilmurodov E.B. Infinite number of eigenvalues of 2×2 operator matrices: Asymptotic discrete spectrum. *Theoret. and Math. Phys.*, 2020, **205**(3), P. 1564–1584.

[22] Boitsev A.A., Brasche J.F., Malamud M.M., Neidhardt H., Popov I.Yu. Boundary Triplets, Tensor Products and Point Contacts to Reservoirs. *Ann. Henri Poincare*, 2018, **19**, P. 2783–2837.

Submitted 16 January 2023; revised 18 March 2023; accepted 19 March 2023

Information about the authors:

Tulkin H. Rasulov – Bukhara State University, Bukhara, Uzbekistan; ORCID 0000-0002-2868-4390; rth@mail.ru, t.h.rasulov@buxdu.uz

Bekzod I. Bahronov – Bukhara State University, Bukhara, Uzbekistan; ORCID 0000-0001-8924-0825; b.bahronov@mail.ru

Conflict of interest: the authors declare no conflict of interest.

NANOSYSTEMS:
PHYSICS, CHEMISTRY, MATHEMATICS

Akhmadjanov T., Rakhimov E.Yu. *Nanosystems: Phys. Chem. Math.*, 2023, **14** (2), 158–163.
http://nanojournal.ifmo.ru
DOI 10.17586/2220-8054-2023-14-2-158-163

Original article

Corrugated non-stationary optical fiber

Turgunali Akhmadjanov[1,a], Ergashali Yu. Rakhimov[2,b]

[1]National University of Uzbekistan, Tashkent, Uzbekistan

[2]National Scientific Research Institute of Renewable Energy Sources, Tashkent, Uzbekistan

[a]t.akhmadjanov@nuu.uz, [b]eyurakhimov@gmail.com

Corresponding author: Turgunali Akhmadjanov, t.akhmadjanov@nuu.uz

ABSTRACT Using numerical methods, we study the fractal properties of the optical paths difference for rays propagating in a model of a homogeneous optical fiber with periodically curved (corrugated) wall and other wall periodically oscillating according to the sine law. Also the angle of entry of the rays into the optical fiber and their coordinates in the exit plane is investigated.

KEYWORDS numerical analysis, dynamics, optical fiber, corrugation, phase image, optical path difference, fractal property

FOR CITATION Akhmadjanov T., Rakhimov E.Yu. Corrugated non-stationary optical fiber. *Nanosystems: Phys. Chem. Math.*, 2023, **14** (2), 158–163.

1. Introduction

One of the main factors limiting the range of wave propagation (for example, low-frequency sound in the ocean [1] or optical rays in an optical fiber [2]) is the medium inhomogeneity in the direction of wave propagation. As a result of the influence of such inhomogeneity on the propagation time of modes in an optical fiber, the intermode dispersion and chaos appear which affect on the possibility of using the optical fiber in telecommunications and many other areas. This requires a reduction of the dispersion effect, i.e., the propagation time of the mode. At present, there are various ways of compensation the dispersion in optical fibers [3–5].

Interesting theoretical and experimental results concerning to the propagation of electromagnetic waves in inhomogeneous or corrugated optical fibers were obtained [6–10]. The problems of such type are intensively studied last decade [11–15]. In some cases, the inhomogeneity can be described as periodic perturbation along the optical fiber axis (analogously to internal waves in the ocean [1]). In this case, a group of waves, the length of which is in resonance with the inhomogeneity of the medium, can be caught in the effective optical fiber channel [16]. This effect is similar to nonlinear resonance in classical mechanics [17].

Numerical methods were used in the simplest model of homogeneously filled optical fiber, one wall of which is periodically curved (corrugated) and absolutely reflective. Fine characteristics of the optical fiber dynamics, in particular, the fractal properties of the propagation time and spatial frequency, were determined [18]. In the model of a cosine bent optical fiber, a phase map and a histogram of optical fibers were obtained and the level of chaos in them was studied [19]. The dynamics of particles in this system, the change of their energy in time were studied, and their phase images were determined using the reflection obtained during the space spreading of the stationary and non-stationary billiard plane of the stadium [20–22].

In this work, using numerical methods, we studied the fractal properties of the difference in the optical paths of rays propagating in the model of uniformly filled optical fiber one wall of which is periodically curved (corrugated) and the second wall oscillates periodically according to the sinusoidal law. The walls assumed to be absolutely reflective. The dependence of the coordinates on the optical fiber exit plane of the angle of entry of rays into the optical fiber is studied.

2. Numerical experiment

Let us consider the simplest model of an absolutely reflecting, homogeneously filled optical fiber with one wall periodically curved (corrugated) (Fig. 1). Here a is the non-corrugated channel width, L is the spatial period of the corrugated wall, and z is the longitudinal coordinate. The curve describing the difference between the wall and the non-corrugated level in one period is determined by the function $f(\xi)$, where $\xi = \{z/L\}$ is the fractional part of the normalized longitudinal coordinate z/L. Naturally, one the following inequality holds: $0 < \xi < 1$. Let the non-corrugated upper wall periodically oscillate according to the following law: $y_0 = a_0 \sin(\omega t)$. Correspondingly, the optical fiber width equals to $a + y_0$. Here a_0 is the vibration amplitude for the wall, and ω is the oscillation frequency.

Let the light source be located on the upper wall of the optical fiber at the point $z_0 = 0$ along the longitudinal coordinate. The optical fiber path consists of straight segments that return sequentially from the walls of the optical fiber. Let's denote by z_n the nth ray return from the oscillating upper wall, and denote the angle between the ray path and the z

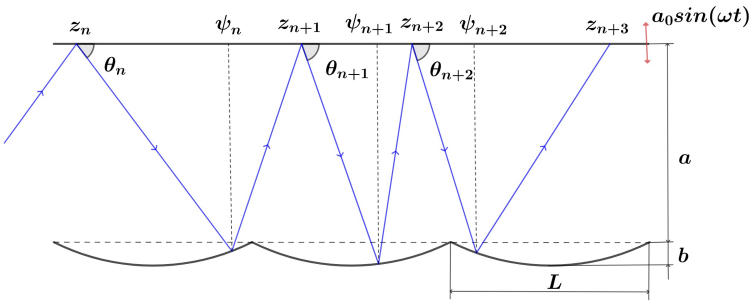

FIG. 1. The model of the optical fiber channel

axis by θ_n. The relationship between the values $(z_n,\ \theta_n)$ and $(z_{n+1},\ \theta_{n+1})$ for single return from the corrugated wall is expressed by the following system of equations obtained from simple geometry:

$$\begin{cases} \psi_n = z_n + (a + y_0 + f(\psi_n)) \cot \theta_n, \\ \theta_{n+1} = \theta_n - 2 \arctan\left(f'(\psi_n)\right), \\ z_{n+1} = z_n + (a + y_0 + f(\psi_n)) \cot \theta_{n+1}. \end{cases} \tag{1}$$

In this expression, ψ_n is the longitudinal coordinate of the point of collision of the nth time collision of the ray coming from the vibrating upper wall with the lower corrugated wall. The phase frequency of the optical fiber is:

$$\Omega = \frac{2\pi}{L}. \tag{2}$$

The system of equations (1) is written with hidden function $f(\xi)$. To write it explicitly, one needs an explicit representation of the function $f(\xi)$. We use the following profile at one period: $f(\xi) = 4b\xi(1-\xi)$. The maximum deviation of the wall from the non-corrugated level is b.

Solving the system (1), one obtains the results presented in Fig. 2(a,b). This figure shows the results of a numerical calculation of the relationship between the optical path difference $\Delta S(\theta_0, z) = S_0(\theta_0, z) - z$ at distance z and the initial exit angle θ_0 from the light source at distance $z_0 = 0$. In this work, when the difference in the optical paths of the rays entering an optical fiber of length z at close angles to each other is equal to the difference $\Delta S_n(\theta_{0n}, z) - \Delta S_{n-1}(\theta_{0n-1}, z) = 10^{-12}$ in the optical paths of the rays leaving the optical fiber The difference in the optical paths of the rays $\Delta\theta_0$ entering at these two angles was considered mutually equal. The difference of the input angle from each other is the sample time. N is the number of resonant input angles (i.e., the pitch width). It is possible to exit back for some optical fibers. Their number was set to Nr, and thus their optical path difference was taken to be zero. It should be noted that the rays can return to the corrugated wall one or more times in one cycle [16].

It can be seen from Fig. 2 that the difference between the optical paths of the rays entering the optical fiber is the same in a certain range of entry angles. But it is not generally. In Fig. 2(a), the optical path differences are not close to each other in the above interval, i.e., $N = 0.01 \approx 0.6^\circ$ From Fig. 2(b), it can be seen that the optical fiber entry angles $N = 0.46 \approx 23^\circ$ are close to each other in the main resonant part.

In general, the dependence of the number of resonant rays on the parameters of the oscillating wall can be seen in the dynamic map (Fig. 3). It is not difficult to see from Fig. 3 that large values of N correspond to the interval $0.75 < \omega/\Omega < 0.85$. If the value $\omega/\Omega = 0.8$ of the ratio a_0/a increases, the value of N will also increase, and accordingly, the value of Nr will also change (Fig. 4).

It can be seen from Fig. 5 that the resonance capture of the rays does not change after the value of the optical fiber length $z > 300L$, and the stair width is maintained.

Next, we will consider the dependence of the step on the width of the stairs (Fig. 6). The purpose is to determine whether the width of the stairs will decrease or increase if the measurement step is reduced.

If the measurement step is reduced while the non-corrugated wall is not vibrating, the length of the "stair" is divided into smaller "stairs" corresponding to the small step [16, 18]. But if the wall is moving, the width of the stairs is kept unchanged. We determine the width of the stairs as follows:

$$N(\Delta\theta_0) = \left(\frac{1}{\Delta\theta_0}\right)^D. \tag{3}$$

Here $N(\Delta\theta_0)$ is the number of angles with equal optical path difference, $\Delta\theta_0$ is the measurement step, D is the fractal dimension. It can be seen from Fig. 6 that the value of D is equal to one, which means that the step width does not depend on the measurement step.

If we determine the dependence of the rays entering the optical fiber with the initial angle θ_0 on the coordinate of the exit from the optical fiber, since the length of the optical fiber is chosen the same, the x coordinate of the optical fiber

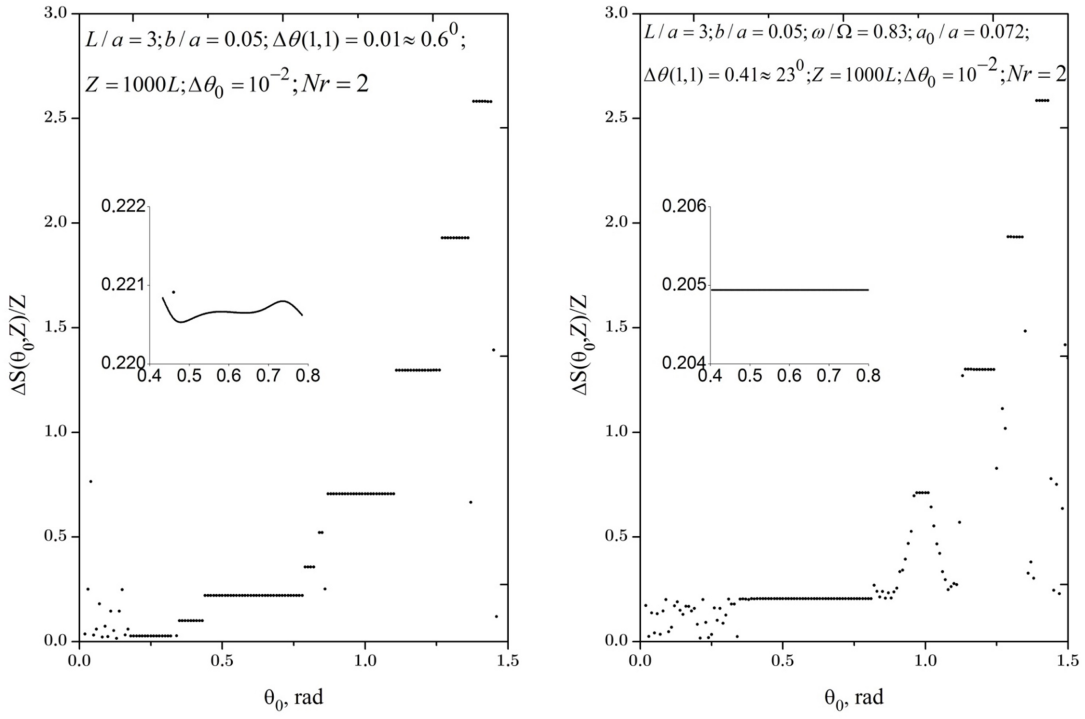

(a) (b)

FIG. 2. The dependence of the difference in the optical paths of the rays on the angle of entry: a) the upper wall does not oscillate and oscillates in b) position. In that $L/a = 3$, $b/a = 0.05$, $\omega/\Omega = 0.83$, $a_0/a = 0.072$, $z = 1000L$, $\Delta\theta_0 = 10^{-2}$ the split image was magnified 100 times and $\Delta\theta_0 = 10^{-3}$ counted step by step.

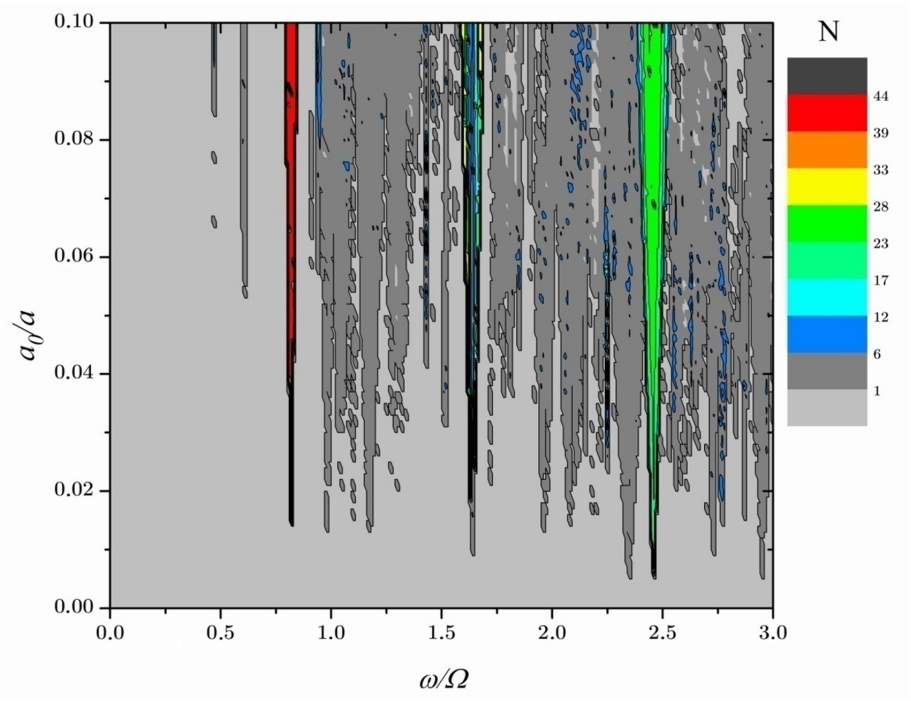

FIG. 3. Map of the dependence of the width of the main resonance $\Delta\theta(1,1)$ on the frequency and amplitude of the oscillating wall. Here, N is the number of initial resonance angles θ_0. Here $L/a = 3$, $b/a = 0.05$, $Z = 500L$, $\Delta\theta_0 = 10^{-2}$

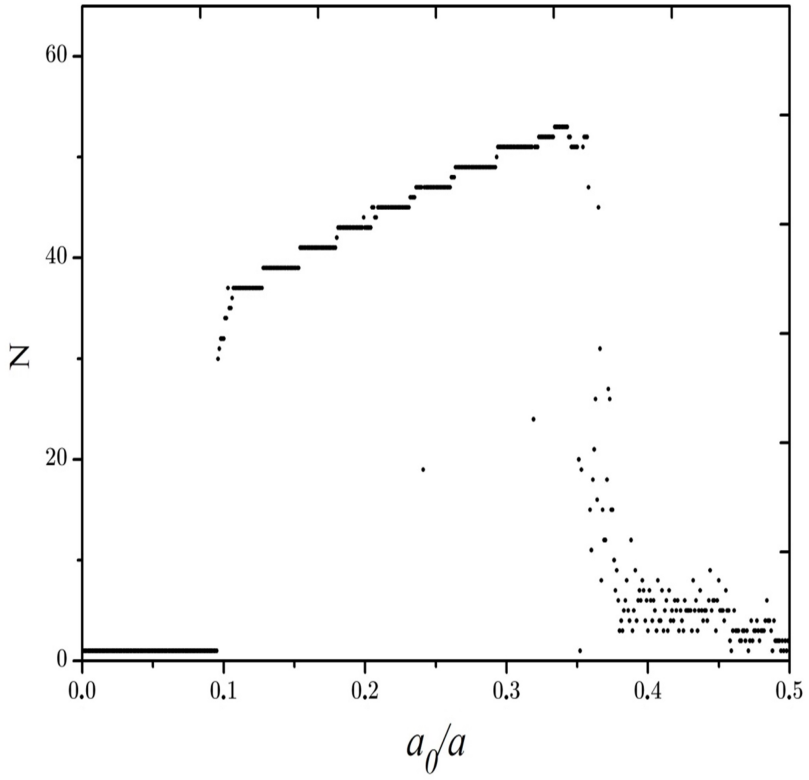

FIG. 4. Dependence of the value of N on the value of the ratio a_0/a. $L/a = 3$; $b/a = 0.03$, $\omega/\Omega = 0.8$, $z = 1000L$, $\Delta\theta_0 = 10^{-2}$

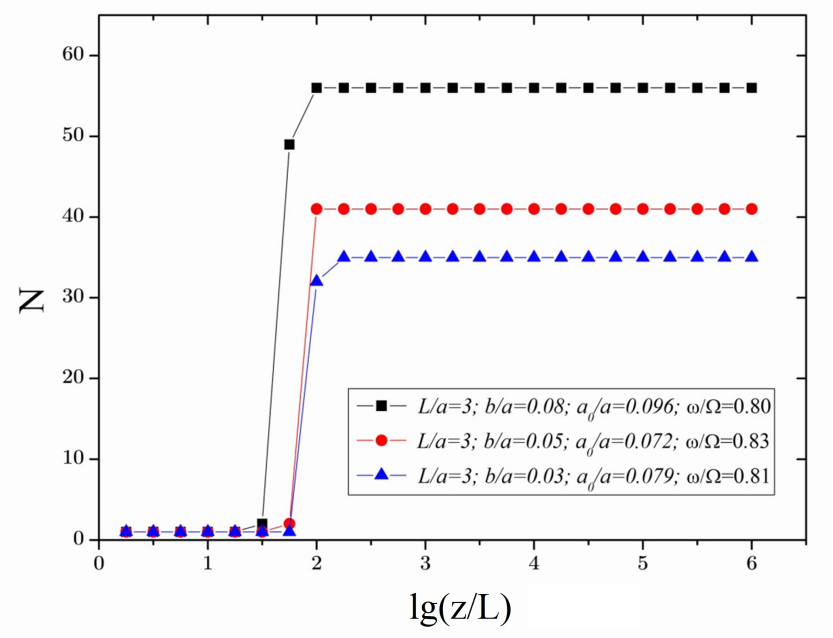

FIG. 5. Dependence of the width of the stairs on the length of the optical fiber

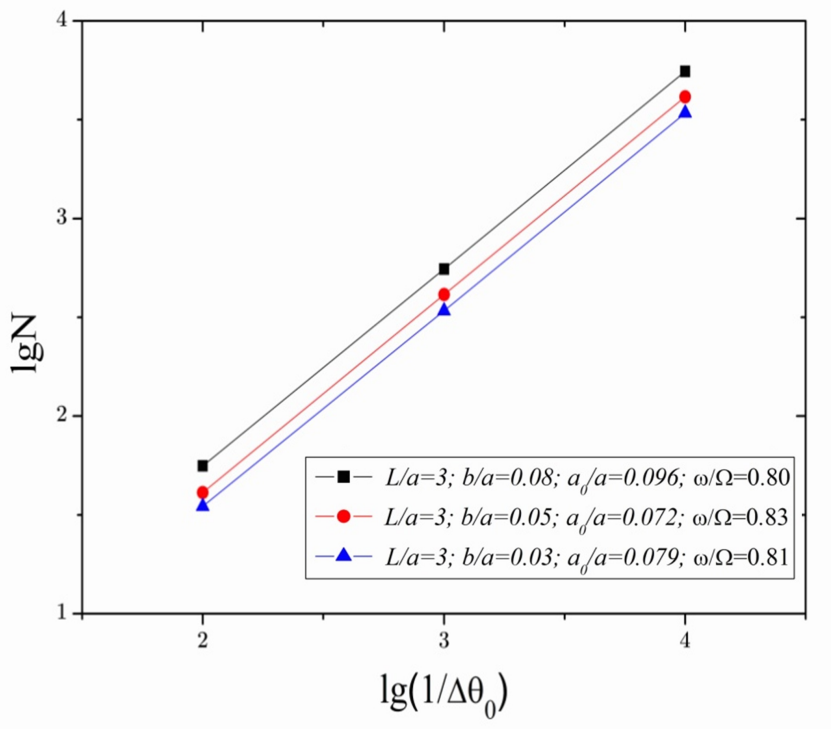

FIG. 6. Dependence of the width of the stairs on the measurement step. One has $D = 1$ in all three cases

at the exit is unchanged, and it is equal to the length of the optical fiber z. Therefore, we only observe the relationship between the Y coordinate and the angle of entry (Fig. 7).

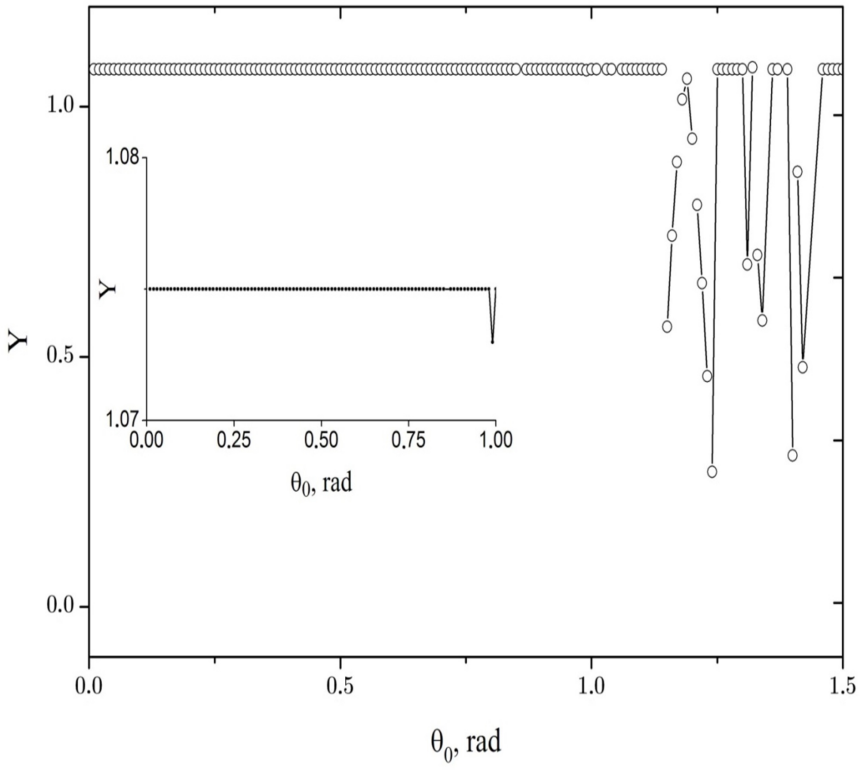

FIG. 7. Dependence of Y on θ_0. $b/a = 0.05$, $L/a = 3$, $\omega/\Omega = 0.8$, $a_0/a = 0.1$, $z = 1000L$, $\Delta\theta_0 = 10^{-2}$

In this case, it can be seen from Fig. 7 that the optical paths of the rays that resonate in the optical fiber are equal and exit from the optical fiber at the same coordinate.

3. Conclusion

When rays are scattered in an optical fiber with one wall corrugated and one wall oscillating under the influence of external periodic noise, the optical paths of the rays entering the optical fiber are equalized in a certain interval, that is, there is no time dispersion in the propagation of signals. It was found that these resulting optical channels strongly depend on external noise parameters. The width of the optical channels remains unchanged at the values of the optical fiber length $z > 300L$. Reducing the entrance angle does not affect the channel size. Also, it was found that the rays falling on the resonance come out of the optical fiber at the same coordinate.

References

[1] Medwin H., Clay C.S. *Fundamentals of Acoustic Oceanography*. Academic Press, San Diego, 1998, 739 p.

[2] Unger H.G. *Planar Optical Waveguides and Fibres*. Oxford University Press, 1978, 770 p.

[3] Singh M. Different dispersion compensation techniques in fiber optic communication system: A survey. *Int. J. of Advanced Research in Electronics and Communication Engineering (IJARECE)*, 2015, **4** (8), P. 2236–2240.

[4] Sharma R., Gupta A.K., Kaur S., Singh N. Performance Analysis of DCF Compensation Techniques. *2021 2nd Int. Conf. on Computational Methods in Science & Technology (ICCMST)*, Mohali, India, 17–18 December 2021, P. 158–161.

[5] Ghosh A.K., Patel N. Changes in the characteristics of chaotic optical signals owing to propagation in optical fibers. *Optics and Photonics for Information Processing XIII*, 6 September 2019, 111360S.

[6] Marcuse D. Coupled Mode Theory of Round Optical Fibers. *Bell System Technical J.*, 2013, **52** (6), P. 817–842.

[7] García-Martin A., Torres J.A., Sáenz J.J., Nieto-Vesperinas M. Transition from diffusive to localized regimes in surface corrugated optical waveguides. *Appl. Phys. Lett.*, 1997, **71**, 1912.

[8] Chaikina E.I., Stepanov S., Navarrete A.G., Méndez E.R., Leskova T.A. Formation of angular power profile via ballistic light transport in multimode optical fibers with corrugated surfaces. *Phys. Rev. B*, 2005, **71**, 085419.

[9] Doppler J., et al. Reflection resonances in surface-disordered waveguides: strong higher-order effects of the disorder. *New J. Phys.*, 2014, **16**, 053026.

[10] Akhmadjanov T., Rakhimov E., Otajanov D. Particle dynamics in corrugated rectangular billiard. *Nanosystems: Phys., Chem., Math.*, 2015, **6** (2), P. 262–267.

[11] Dietz O., Kewes G., Neitzke O., Benson O. Coupled-mode approach to square-gradient Bragg-reflection resonances in corrugated dielectric waveguides. *Phys. Rev. A*, 2015, **92**, 043834.

[12] Lipton R., Polizzi A., Thakur L. Novel metamaterial surface from perfectly conducting subwavelength corrugations. *SIAM J. Appl. Math.*, 2017, **77** (4), P. 1269–1291.

[13] Kovacs, B., Kraft F.A., Szabo Z., et al. Near cut-off wavelength operation of resonant waveguide grating biosensors. *Sci. Rep.*, 2021, **11**, 13091.

[14] Higuita M.A.U., Bruhier H., Hochedel M., Kampfe Th., Vocanson F., et al. Resonant waveguide grating fabrication on planar and cylindrical substrates using a photosensitive TiO_2 sol-gel approach. *Optical Materials Express*, 2021, **11** (1), P. 12–22.

[15] Lobanov I.S., Trifanov A.I., Trifanova E.S., Popov I.Y., Fedorov E.G., Pravdin K.V., Moskalenko M.A. Photon generation in resonator with time dependent boundary conditions. *Nanosystems: Physics, Chemistry, Mathematics*, 2021, **12** (1), P. 73–80.

[16] Abdullaev S.S., Zaslavskii G.M. Nonlinear dynamics of rays in inhomogeneous media. *Soviet J. of Experimental and Theoretical Physics*, 1981, **53** (2), 265.

[17] Zaslavsky G.M. *Stochasticity of dynamical systems*. Nauka, Moscow, 1984.

[18] Abdullaev S.S., Zaslavskiĭ G.M. Classical nonlinear dynamics and chaos of rays in problems of wave propagation in inhomogeneous media. *Sov. Phys. Usp.*, 1991, **34**, 645.

[19] Leonel E.D., da Costa D.R., Dettmann C.P. Scaling invariance for the escape of particles from a periodically corrugated waveguide. *Physics Letters A*, 2012, **376**, P. 421–425.

[20] Ryabov A.B., Loskutov A. Time-dependent focusing billiards and macroscopic realization of Maxwell's Demon. *J. Phys. A: Math. Theor.*, 2010, **43**, 125104.

[21] Loskutov A.Yu. Dynamical chaos: systems of classical mechanics. *Phys. Usp.*, 2007, **50**, 939.

[22] Matrasulov D.U., Yusupov J.R., Sabirov K.K., Sobirov Z.A. Time-dependent quantum graph. *Nanosystems: Physics, Chemistry, Mathematics*, 2015, **6** (2), P. 173–181.

Submitted 24 October 2022; revised 16 March 2023; accepted 17 March 2023

Information about the authors:

Turgunali Akhmadjanov – National University of Uzbekistan, Faculty of Physics, Department of Photonics, University, str.4, 100174, Tashkent, Uzbekistan; ORCID 0000-0002-6484-1226; t.akhmadjanov@nuu.uz

Ergashali Yu. Rakhimov – National Scientific Research Institute of Renewable Energy Sources, Chingiz Aitmatov str. 2B, 100014, Tashkent, Uzbekistan; ORCID 0000-0001-7128-4598; eyurakhimov@gmail.com

Conflict of interest: the authors declare no conflict of interest.

NANOSYSTEMS:
PHYSICS, CHEMISTRY, MATHEMATICS

Rakhmanov S.Z., et al. *Nanosystems: Phys. Chem. Math.*, 2023, **14** (2), 164–171.
http://nanojournal.ifmo.ru
DOI 10.17586/2220-8054-2023-14-2-164-171

Original article

Optical high harmonic generation in a quantum graph

Saparboy Z. Rakhmanov[1,a], Ikhvoliddin B. Tursunov[2,b], Khikmatjon Sh. Matyokubov[3,c], Davron U. Matrasulov[4,d]

[1]Chirchik State Pedagogical University, Chirchik, Uzbekistan

[2] National Universty of Uzbekistan, Vuzgorodok, Tashkent, Uzbekistan

[3] Urgench State University, Urgench, Uzbekistan

[4] Turin Polytechnic University in Tashkent, Tashkent, Uzbekistan

[a]saparboy92@gmail.com, [b]ixvoliddin.tursunov.1998.04.07@gmail.com, [c]hikmat0188@mail.ru, [d]dmatrasulov@gmail.com

Corresponding author: Saparboy Z. Rakhmanov, saparboy92@gmail.com

ABSTRACT High ordered harmonic generation in a quantum graph is studied by considering quantum star graph interacting with external monochromatic optical field. Using the numerically obtained solutions of the time-dependent Schrödinger equation on quantum graph, main characteristics of high harmonic generation are computed. In particular, time-dependence of the average dipole moment and high harmonic generation spectra, determined as the generated field intensity as a function of harmonic order are analyzed. Extension of the proposed model to the case of other graph topologies and application to the problem of tunable high harmonic generation are discussed.

KEYWORDS quantum graphs, optical high harmonic generation, average dipole moment, harmonic generation spectra, quantum graph in electromagnetic field.

ACKNOWLEDGEMENTS This work is supported by the grant of the Ministry of Innovative Development of the Republic of Uzbekistan, World Bank Project “Modernizing Uzbekistan National Innovation System” (Ref. Nr. REP-05032022/235).

FOR CITATION Rakhmanov S.Z., Tursunov I.B., Matyokubov Kh.Sh., Matrasulov D.U. Optical high harmonic generation in a quantum graph. *Nanosystems: Phys. Chem. Math.*, 2023, **14** (2), 164–171.

1. Introduction

Study of the nonlinear optical phenomena occurring in quantum regime is of importance for many practically important tasks appearing in the intersection such topics as quantum optics, atom optics, and optoelectronics. From the viewpoint of fundamental research, the importance of such studies is related to attosecond physics and the physics of ultrafast phenomena, while the practical importance is caused by the relevance to high-power laser generation, optical materials design and optoelectronic device fabrication. An interesting aspect of this topic is optical harmonic generation in quantum regime, which attracted much attention recently [1, 2] in the context of atomic physics and some confined low-dimensional quantum systems, such as quantum wells and dots. One of the main tasks in this field is achieving slowly-decaying (as a function of harmonic order) harmonic generation intensity. Solving of such problem is complicated due to the typical features of the harmonic emission spectra of an atom in a strong optical field, which are known as “the plateau” and “the cutoff”. These latter are a wide frequency region with harmonics of comparable intensities, and an abrupt intensity decrease at the end of the plateau. Physical mechanisms of such effects have been explained within the so-called “three-step” model. Existence of such effect makes difficult generating of very high order harmonics and ultrashort pulses, as their intensity becomes very small at high harmonic orders. Therefore, revealing of the high harmonic generation (HHG) regime, where the intensity would slowly decay as a function of harmonic order is of importance for different practical tasks. Study of HHG in low-dimensional quantum systems can be one of the ways providing achieving of such a goal. In this paper, we address the problem of optical high harmonic generation in branched quantum wires. These latter are modeled in terms of the quantum graphs, which are determined as a set of wires connected to each other according to a rule, called topology of the graph [3–5]. Generation of the topical harmonics is assumed as to be caused by the interaction of branched quantum wires with an external monochromatic optical field. Using the eigenfunctions of the quantum graph, we compute numerically the average dipole moment as a function of generated frequencies. Also, as the main characteristics of the high harmonic generation process, we compute the spectrum of the high harmonic generation which is determined as the intensity of the field generated by the interaction of the branched quantum wire with the external optical field. Earlier, quantum graphs have attracted much attention in different contexts for modeling particle and quasiparticle dynamics in branched structures (see Refs. [3–16]).

2. Schrödinger equation on graphs

Here we briefly recall basic quantum graphs theory following Refs. [4, 10]. Graphs are the systems consisting of vertices which are connected by edges. The edges are connected according to a rule which is called the topology of the graph. Topology of the graph is described in terms of the adjacency matrix [4,5]:

$$C_{ij} = C_{ji} = \begin{cases} 1, & \text{if } i \text{ and } j \text{ are connected;} \\ 0, & \text{otherwise;} \end{cases} \qquad i, j = 1, 2, ..., N.$$

Earlier, quantum graphs were extensively studied in the context of quantum chaos theory [4–6]. Strict mathematical formulation of the boundary conditions was given by Kostrykin and Schrader [3]. Inverse problems on quantum graphs have been studied in Refs. [7–9]. An experimental implementation of quantum graphs on (optical) microwave waveguide networks is discussed in the Ref. [8]. Despite the fact that different issues of quantum graphs and their applications have been discussed in the literature, the problem of driven graphs is still remaining as less-studied topic.

Quantum particle dynamics on a graph is described by one-dimensional multi-component Schrödinger equation [4,5] (in the units $\hbar = 2m = 1$):

$$-\frac{d^2\phi_b(x)}{dx^2} = k^2\phi_b(x), \quad b = (i, j), \tag{1}$$

where b denotes a bond connecting i-th and j-th vertices, and for each bond b, the component ϕ_b of the total wave function ϕ is a solution of Eq. (1). In Eq. (1) components are related through the boundary conditions, providing continuity and current conservation [4]:

$$\begin{cases} \bullet \text{ Continuity,} \\ \phi_{i,j}|_{x=0} = \varphi_i, \;\; \phi_{i,j}|_{x=L_{i,j}} = \varphi_j \;\; \text{for all} \;\; i < j \;\; \text{and} \;\; C_{i,j} \neq 0. \\ \bullet \text{ Current conservation,} \\ -\sum\limits_{j<i} C_{i,j} \dfrac{d\phi_{j,i}(x)}{dx}\Big|_{x=L_{i,j}} + \sum\limits_{j>i} C_{i,j} \dfrac{d\phi_{i,j}(x)}{dx}\Big|_{x=0} = \lambda_i\varphi_i. \end{cases} \tag{2}$$

Here, the parameters λ_i are free parameters which determine the type of boundary conditions. The Dirichlet boundary conditions correspond to the case when all the $\lambda_i = \infty$. Solution of Eq. (1) obeying the above boundary conditions can be written as

$$\phi_{i,j} = \frac{C_{i,j}}{\sin kL_{i,j}}(\varphi_i \sin k(L_{i,j} - x) + \varphi_j \sin kx),$$

where the quantities φ_i are the solutions of the algebraic system following from the continuity conditions:

$$\sum_{j\neq i} \frac{kC_{i,j}}{\sin kL_{i,j}}(-\varphi_i \cos kL_{i,j} + \varphi_j) = \lambda_i\varphi_i.$$

The eigenvalues of Eq. (1) can be found from the spectral equation

$$\det\left(h_{i,j}(k)\right) = 0 \tag{3}$$

where

$$h_{i,j}(k) = \begin{cases} -\sum\limits_{m\neq i} C_{i,m} \cot kL_{i,m} - \dfrac{\lambda_i}{k}, & i = j \\ C_{i,j} \sin^{-1} kL_{i,j}, & i \neq j \end{cases}$$

Here we focus on the simplest graph topology, star graph. In this case, since the graph has only single non-boundary vertex, unlike the notations in Eqs. (1) and (2), indices are assigned to the bonds (not to the vertices), i.e. L_j means j-th bond. Thus, in special case of star graph, the boundary conditions can be written as [10]

$$\begin{cases} \phi_1|_{y=0} = \phi_2|_{y=0} = ... = \phi_N|_{y=0}, \\ \phi_1|_{y=L_1} = \phi_2|_{y=L_2} = ... = \phi_N|_{y=L_N} = 0, \\ \sum\limits_{j=1}^{N} \dfrac{\partial}{\partial y}\phi_j|_{y=0} = 0. \end{cases} \tag{4}$$

The eigenvalues of star graph can be found from the following spectral equation [10]

$$\sum_{j=1}^{N} \tan^{-1}(k_n L_j) = 0. \tag{5}$$

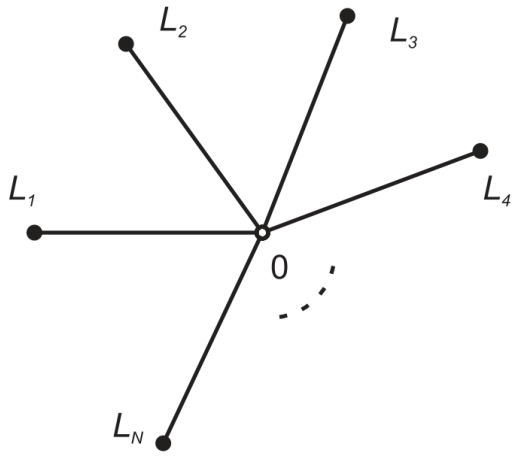

FIG. 1. Sketch of a metric star graph. L_j is the length of the j th bond with j=1, 2,. ..,N

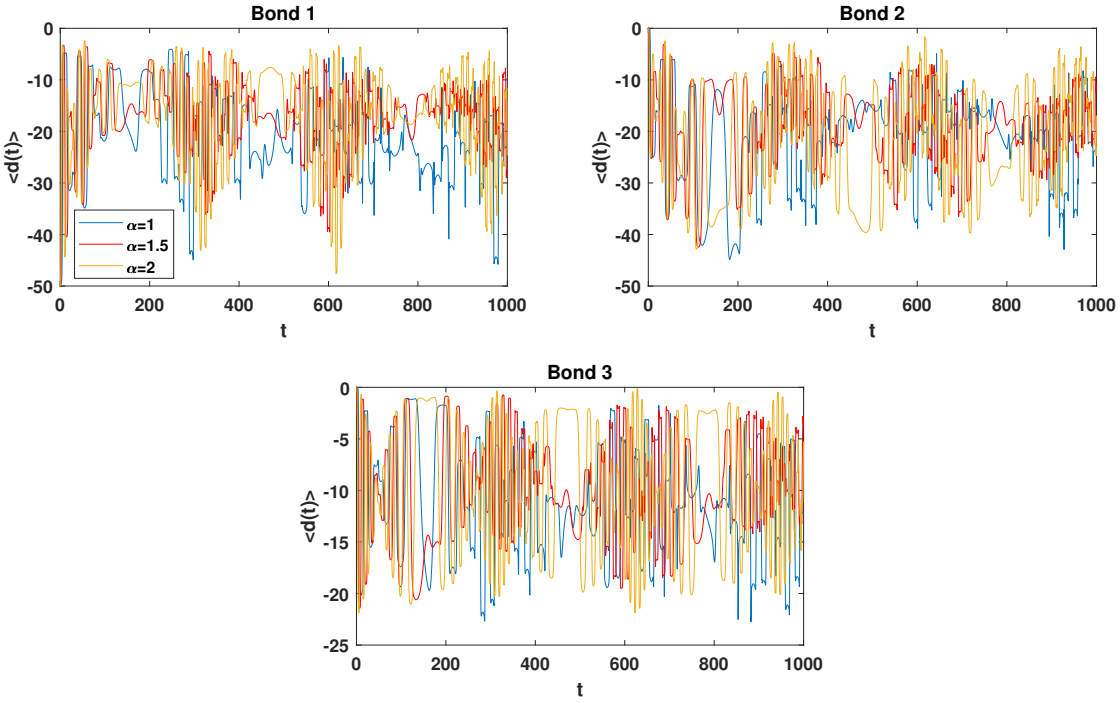

FIG. 2. Average dipole moment as a function of time on star graph at different values of α parameter for external field's amplitude, $\epsilon = 0.1$ and frequency, $\omega_0 = 0.01$

Corresponding eigenfunctions are given as [10]

$$\phi_{j,n} = \frac{B_n}{\sin(k_n L_j)} \sin(k_n(L_j - y)), \tag{6}$$

where

$$B_n = \sqrt{\frac{2}{\sum_j \frac{L_j + \sin(2k_n L_j)}{\sin^2(k_n L_j)}}}.$$

The functions $\phi_{j,n}$ are orthonormal, i.e., fulfill the following condition:

$$\sum_{j=1}^{N} \int_0^{L_j} \phi^*_{j,m}(x)\phi_{j,n}(x)dx = \delta_{mn}. \tag{7}$$

In the next section, we use these eigenfunctions for computing the high harmonic generation spectrum.

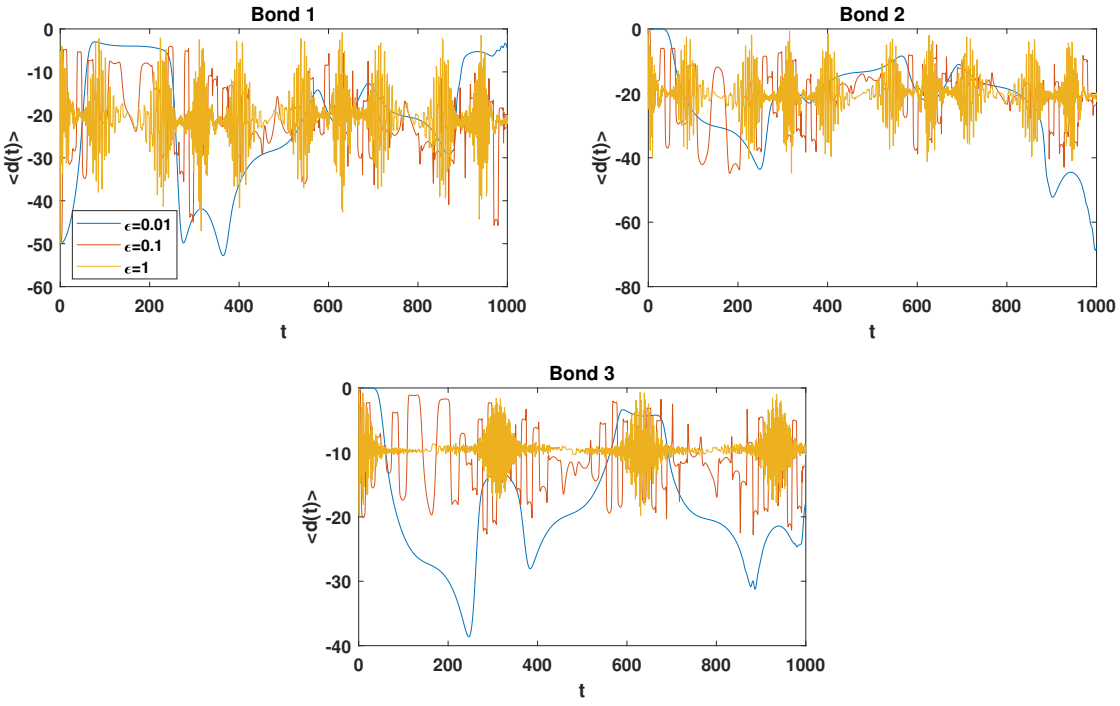

FIG. 3. Average dipole moment as a function of time on star graph at different values of amplitude of the external field for field's frequency, $\omega_0 = 0.01$, for length of each bond, $L_1 = 200.31$, $L_2 = 205.53$ and $L_3 = 210.18$

3. Driven star graph by external potential

Consider a quantum star graph (Y-junction) interacting with an external linearly polarized monochromatic electromagnetic field. Such system can be described by the following time-dependent (multi-component) Schrödinger equation:

$$i\frac{\partial \Psi_j(x,t)}{\partial t} = \left[-\frac{d^2}{dx^2} + \epsilon x \cos\omega_0 t\right]\Psi_j(x,t), \qquad j = 1,2,3, \tag{8}$$

where ϵ and ω_0 are the amplitude and the frequency of the optical field, respectively.

The solution of Eq. (8) can be written in terms of the complete set of solutions of Eq. (1)

$$\Psi_j(x,t) = \sum_n C_n(t)\phi_{j,n}(x), \tag{9}$$

where $\phi_{j,n}(x)$ are given by Eq. (6).

Substituting (9) into Eq. (8) and using the condition given by Eq. (7), we get a system of first order ordinary differential equations which has the form

$$i\dot{C}_n(t) = \varepsilon_n C_n(t) + \sum_m C_m(t)V_{nm}, \tag{10}$$

where

$$V_{nm} = \sum_j \int_0^{l_j} \phi^*_{j,n}\hat{V}(t)\phi_{j,m}dx = \epsilon\cos\omega_0 t \sum_j \int_0^{l_j} x\phi^*_{j,n}\phi_{j,m}dx$$

and ε_n are the eigenvalues of the unperturbed system.

Using numerically found solutions of Eq. (8), one can compute physically observable characteristics of the system "quantum star graph + external optical field".

In numerical calculations, we choose the Gaussian wave packet given on the first bond of the graph as the initial state:

$$\Psi_1(x,0) = \Phi(x) = \frac{1}{\sqrt{2\pi}\sigma}e^{-\frac{(x-\mu)^2}{2\sigma}}, \tag{11}$$

with σ being the width of the packet. For other bonds, the initial wave function is assumed to be zero, i.e. $\Psi_2(x,0) = \Psi_3(x,0) = 0$.

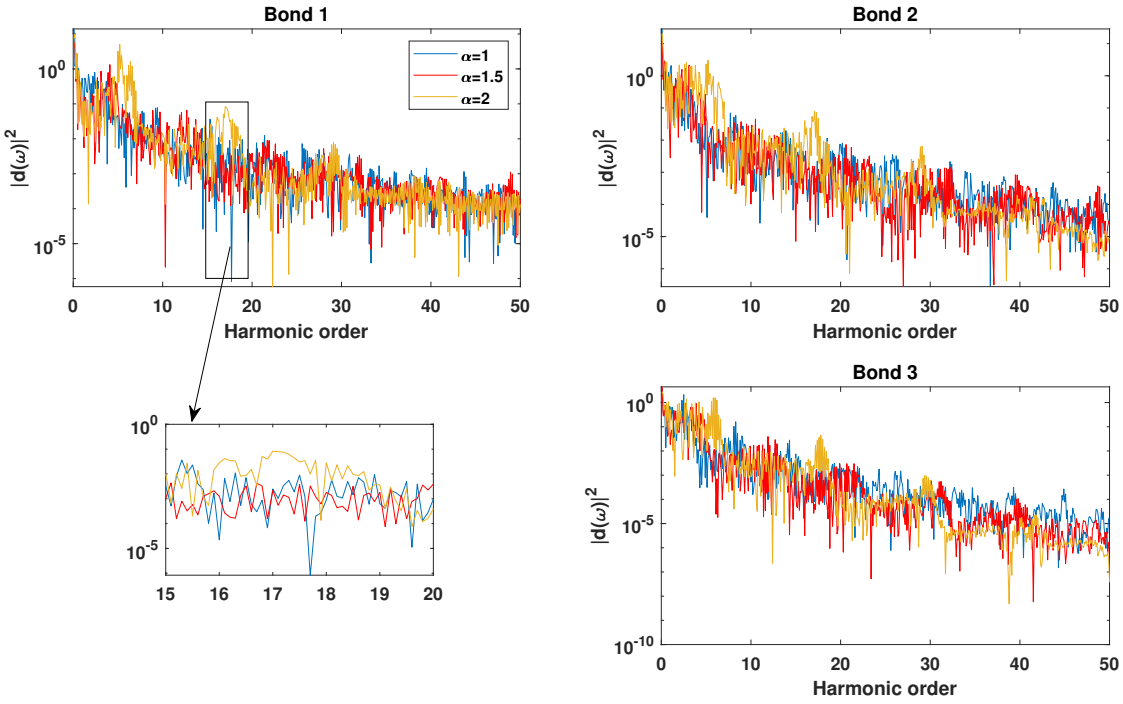

FIG. 4. Spectrum of harmonic generation on star graph at different values of α parameter for external field's amplitude, $\epsilon = 0.1$, and frequency, $\omega_0 = 0.01$, for duration of interaction, $T = 1000$

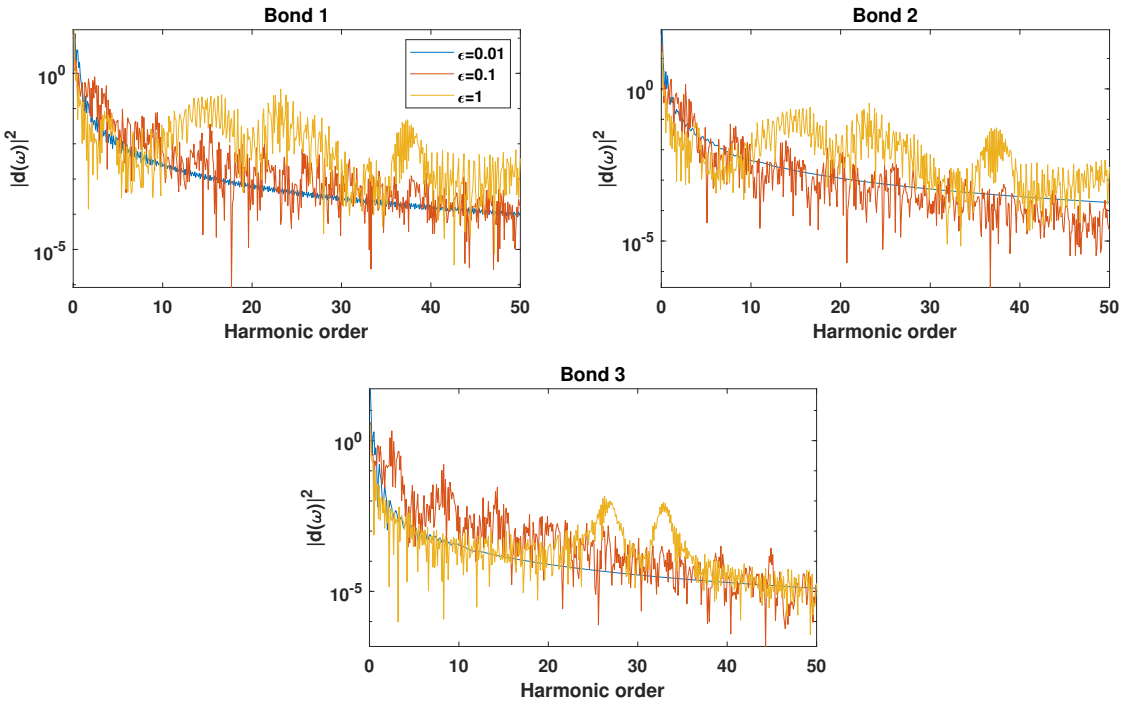

FIG. 5. Spectrum of harmonic generation on star graph at different values of amplitude of external field for field's frequency, $\omega_0 = 0.01$, for length of each bond, $L_1 = 200.31$, $L_2 = 205.53$ and $L_3 = 210.18$, for duration of interaction, $T = 1000$

For such initial conditions, the expansion coefficients at $t = 0$ can be written as

$$C_n(0) = \int_0^{l_1} \Phi(x)\phi_{1n}^*(x)dx.$$

4. High harmonic generation in star graph

Consider high harmonic generation caused by the interaction of the quantum star graph with the external monochromatic optical field. One of the main characteristics of such process is the average (expectation) value of the dipole moment which is determined as [1]

$$\langle d_j(t)\rangle = -\langle \Psi_j(x,t)|x|\Psi_j(x,t)\rangle, \qquad j = 1,2,3.$$

To compute $\langle d_j(t)\rangle$, one can use the solution of Eq. (8). In terms of the expansion coefficients in Eq. (9), one can write the average dipole moment as

$$\langle d_j(t)\rangle = -\sum_{m,n} C_m^*(t)C_n(t)\tilde{V}_{jmn},$$

where $\tilde{V}_{jmn} = \int\limits_0^{L_j} x\phi_{j,n}^*\phi_{j,m}dx$.

In the following, all the plots are produced by choosing the initial state as Gaussian wave packet determined in Eq. (11) and coming from the first bond. Furthermore, we choose the bond lengths as $L_j = \alpha l_j$. The width and the initial position of the packet are fixed as $\sigma = 10$, $\mu = 50$, respectively. Fig. 2 presents the plots of the average dipole moment for star graph with the bond lengths, $l_1 = 200.31$, $l_2 = 205.53$ and $l_3 = 210.18$, as a function of time at different values of α. The amplitude and the frequency of the electromagnetic field are taken as $\epsilon = 0.1$ and $\omega_0 = 0.01$, respectively. As it can be seen from this plot, $\langle d_j(t)\rangle$ is quasi periodic in time and the period decreases as the parameter α increases.

In Fig. 3, plots show time-dependence of the average dipole moment of each bond at different values of amplitude of the external field strength, $\epsilon = 0.01$ (blue line), $\epsilon = 0.1$ (red line) and $\epsilon = 1$ (yellow line). One can see the strong dependence on the amplitude of the electromagnetic field. Period of the quasi periodic average dipole moment decreases as the amplitude of the electromagnetic field grows.

Another important characteristics of the high harmonic generation in quantum regime is its spectrum which is determined in terms of its intensity on each bond (as a function of frequency generated) and given as

$$I_j(\omega) = |d_j(\omega)|^2 = \left| \frac{1}{T}\int\limits_0^T e^{-i\omega t}\langle d_j(t)\rangle dt \right|^2, \tag{12}$$

where T is the total duration of interaction of the quantum graph with the external optical field. The total harmonic generation intensity is defined as the sum of those on each bond. The main practically relevant feature of the high harmonic generation intensity is the appearance of "the plateaus" at certain values of the generated frequency. In other words, the high harmonic generation spectrum, which is determined as the ratio of the external field frequency and the frquency of generated one, $N = \omega/\omega_0$, consists of a plateau where the harmonic intensity is nearly constant over many orders and a sharp cutoff. As higher the number of plateaus, as attractive the harmonic generation from the viewpoint of attosecond physics and high power laser generation [17,18]. Fig. 4 presents the plot of $I(N)$ on each bond of the quantum star graph for different values of α choosing the field parameters as $\epsilon = 0.1$, $\omega_0 = 0.01$ and $T = 1000$. In Fig. 4, one can see the decreasing of the spectrum as harmonic order increases. Moreover, for large values of the length of bonds, the intensity of high order harmonics increases. Existence of "quasi-plateau" can be seen from the inset. Fig. 5 shows plots of the spectrum of the harmonic generation at different values of the external field strength and field's frequency, $\omega_0 = 0.01$ for bond length chosen as $L_1 = 200.31$, $L_2 = 205.53$ and $L_3 = 210.18$ for duration of interaction, $T = 1000$. The plot shows that the HHG intensity is strongly depends on the field strength. For higher values of ϵ, one can observe increasing of the intensity. The above study can be directly extended to any branching topology of a quantum graph (e.g., tree, hexagon, loop, H-graph, etc). Of course, complicated branching topologies should provide wider opportunity for the HHG-process.

5. Conclusion

In this paper, we studied high harmonic generation in quantum star graph caused by its interaction with the external monochromatic optical field. The average dipole moment as a function of time is analyzed as one of the characteristics of HHG. The harmonic generation spectrum described in terms of the generation intensity as a function of the harmonic order given by the ratio of the generated harmonics to that of the external field, is computed at different values of the external field strength, as well as for different bond lengths. Appearance of narrow plateau was shown by analyzing the plots of the HHG spectra. The model considered in this study can be implemented, e.g., in different quantum wire networks fabricated on the basis of superconductors, semiconductors or other low-dimensional quantum materials. Some versions of such quantum wire networks have been studied earlier in Refs. [19–22]. Extension of the above model to the case of other branching topologies and external (e.g., bi-, or poly-chromatic, or nonlinearly polarized) fields can provide an effective tool for tunable high harmonic generation in low-dimensional structures. In addition, the model can be considered as a version of the quantum graph based laser concept. Such concepts have been earlier discussed in [23–43].

References

[1] Boyd R.W. *Nonlinear Optics*, 2007, 3rd ed, Academic Press.

[2] Tong X., Chu Sh. Theoretical study of multiple high-order harmonic generation by intense ultrashort pulsed laser fields: A new generalized pseudospectral time-dependent method. *Chem. Phys. B*, 1997, **217**(2-3), P. 119–130.

[3] Kostrykin R., Schrader R. Kirchhoff's rule for quantum wires. *J. Phys. A: Math. Gen*, 1999, **32**, P. 595–630.

[4] Kottos T., Smilansky U. Periodic Orbit Theory and Spectral Statistics for Quantum Graphs. *Ann. Phys.*, 1999, **274**, P. 76–124.

[5] Gnutzmann S. and Smilansky U. Quantum graphs: Applications to quantum chaos and universal spectral statistics. *Adv. Phys.*, 2006, **55**, P. 527–625.

[6] Gnutzmann S., Keating J.P., Piotet F. Eigenfunction statistics on quantum graphs. *Ann. Phys.*, 2010, **325**, P. 2595–2640.

[7] Boman J., Kurasov P. Symmetries of quantum graphs and the inverse scattering problem. *Adv. Appl. Math.*, 2005, **35**, P. 58–70.

[8] Hul O., Bauch S., Pakoński P., Savytskyy N., Życzkowski K. and Sirko L. Experimental simulation of quantum graphs by microwave networks. *Phys. Rev. E.*, 2004, **69**, P. 056205/1-7.

[9] Cheon T., Exner P., Turek O. Approximation of a general singular vertex coupling in quantum graphs. *Ann.Phys.*, 2010, **325**, P. 548–578.

[10] Keating J.P. Fluctuation statistics for quantum star graphs. Quantum graphs and their applications. *Contemp. Math.*, 2006, **415**., P. 191–200.

[11] Matrasulov D.U., Yusupov J.R., Sabirov K.K., Sobirov Z.A. Time-dependent Quantum Graph. *Nanosystems: Physics, Chemistry, Mathematics*, 2015, **6**(2), P. 173–181.

[12] Yusupov J.R., Sabirov K.K., Ehrhardt M., Matrasulov D.U. Transparent quantum graphs. *Phys. Lett. A.*, 2019, **383**, P. 2382–2388.

[13] Matrasulov D.U., Sabirov K.K. and Yusupov J.R. PT-symmetric quantum graphs. *J. Phys. A.*, 2019, **52**, P. 155302/1-11.

[14] Nikiforov D.S., Blinova I.V. and Popov I.Y. Schrödinger and Dirac dynamics on time-dependent quantum graph. *Indian J. Phys.*, 2019, **93**(7), P. 913–920.

[15] Yusupov J.R., Sabirov K.K., Asadov Q.U., Ehrhardt M. and Matrasulov D.U. Dirac particles in transparent quantum graphs: Tunable transport of relativistic quasiparticles in branched structures. *Phys. Rev. E.*, 2020, **101**, P. 062208/1-8.

[16] Yusupov J.R., Sabirov K.K. and Matrasulov D.U. Dirac particles on periodic quantum graphs. *Phys. Rev. E.*, 2021, **104**, P. 014219/1-7.

[17] Strelkov V.V., Platonenko V.T., Sterzhantov A.F. and Ryabikin M.Yu. Attosecond electromagnetic pulses: generation, measurement, and application. Generation of high-order harmonics of an intense laser field for attosecond pulse production. *Phys. Uspekhi*, 2016, **59**(5), P. 425–445.

[18] Winterfeldt C., Spielmann C., Gerber G. Optimal control of high-harmonic generation. *Rev. Mod. Phys.*, 2008, **80**(2), P. 117–140.

[19] Kohmoto M. Quantum wire networks with quantized Hall effect. *J. Phys. Soc. Jpn.*, 1999, **62**, P. 4001–4008.

[20] Aharony A., Entin-Wohlman O. Discrete versus Continuous Wires on Quantum Networks. *J. Phys. Chem. B*, 2009, **113**, P. 3676–3680.

[21] Medina J., Green D., Chamon C. Networks of quantum wire junctions: A system with quantized integer Hall resistance without vanishing longitudinal resistivity *Phys. Rev. A., B*, 2013, **87**, P. 045128.

[22] Caudrelier V., Mintchev M., Ragoucy E. Quantum wire network with magnetic flux. *Phys. Lett. A.*, 2013, **377**, P. 1788–1793.

[23] Lepri S., Trono C., Giacomelli G. Complex Active Optical Networks as a New Laser Concept. *Phys.Rev.Lett.*, 2017, **118**, P. 123901.

[24] Rotter S. Network lasers. *Nature Photonics*, 2019, **13**, P. 140–145.

[25] Brabec T., Krausz F. Intense few-cycle laser fields: Frontiers of nonlinear optics. *Rev. Mod. Phys.*, 2000, **72**(2), P. 545–591.

[26] Yousef I., et.al. Relativistic high-power laser matter interactions. *Phys. Rep.*, 2006, **427**(2-3), P. 41–155.

[27] Winterfeldt C., Spielmann C., and Gerber G. Colloquium: Optimal control of high-harmonic generation. *Rev. Mod. Phys.*, 2008, **80**(1), P. 117–140.

[28] Krausz F., Ivanov M. Attosecond physics. *Rev. Mod. Phys.*, 2009, **81**, P. 163–234.

[29] Nisoli M., Sansone G. New frontiers in attosecond science Author links open overlay panel. *Prog. Quant. Electr.*, 2009, **33**, P. 17–59.

[30] Kohler M.C., Pfeifer T., Hatsagortsyan K.Z.,Keitel C.H. Frontiers of Atomic High-Harmonic Generation. *Advances In Atomic, Molecular, and Optical Physics*, 2012, **61**, P. 159–208.

[31] Ahn D., Chuang S.L. Optical gain in a strained-layer quantum-well laser. *IEEE J. Quantum Electron*, 1988, **24**, P. 2400–2406.

[32] Rosencher E., Bois Ph. Model system for optical nonlinearities: Asymmetric quantum wells. *Phys. Rev. B.*, 1991, **44**, P. 11315–11327.

[33] Milanovic V., Ikonic Z., Indjin D. Optimization of resonant intersubband nonlinear optical susceptibility in semiconductor quantum wells: The coordinate transform approach. *Phys. Rev. B.*, 1996, **53**, P. 10887–10893.

[34] Xie W., J.Lumin. The nonlinear optical rectification of a confined exciton in a quantum dot. **131**. P. 943–946.

[35] Li B., Guo K-X., Zhang C.-J., Zheng Y.-B. The second-harmonic generation in parabolic quantum dots in the presence of electric and magnetic fields. *Phys. Lett. A*, 2007, **367**, P. 493–497.

[36] Liu J-T., Su F-H., Wang H. Model of the optical Stark effect in semiconductor quantum wells: Evidence for asymmetric dressed exciton bands. *Phys. Rev. B.*, 2009, **80**, P. 113302/1-4.

[37] Shao Sh., Guo K-X., Zhang Z-H., Li N., Peng Ch. Studies on the second-harmonic generations in cubical quantum dots with applied electric field. *Physica B: Physics of Condensed Matter*, 2011, **406**, P. 393–396.

[38] Karimi M.J., Keshavarz A., Second harmonic generation in asymmetric double semi-parabolic quantum wells: Effects of electric and magnetic fields, hydrostatic pressure and temperature. *Physica E*, 2012, **44**, P. 1900–1904.

[39] Zhai W. A study of electric-field-induced second-harmonic generation in asymmetrical Gaussian potential quantum wells. *Physica B*, 2014, **454**, P. 50–55.

[40] Bondarenko V., Zauzny M. Intrinsic optical intersubband bistability in quantum well structures: Role of multiple reflections. *Phys. Rev. B.*, 2015, **91**, P. 035303/1-20.

[41] Kotova L.V., Platonov A.V., Kats V.N. Optical activity of quantum wells. *Phys. Rev. B.*, 2016, **94**, P. 165309/1-5.

[42] Mohammadi S.A., Khordad R., Rezaei G. Optical properties of a semispherical quantum dot placed at the center of a cubic quantum box: Optical rectification, second and third-harmonic generations. *Physica E*, 2016, **76**, P. 203–208.

[43] Rakhmanov S., Matrasulov D., Matveev V.I. Quantum dynamics of a hydrogen-like atom in a time-dependent box: Cooling, compressing and diffusive ionization in non-adiabatic regime. *Eur. Phys. J. D.*, 2018, **72** P. 177/1-8.

Submitted 14 February 2023; revised 28 March 2023; accepted 29 March 2023

Information about the authors:

S. Z. Rakhmanov – Chirchik State Pedagogical University, 104 Amir Temur Str., 111700, Chirchik, Uzbekistan; ORCID 0000-0001-8569-1709; saparboy92@gmail.com

I. B. Tursunov – National Universty of Uzbekistan, Vuzgorodok, 100174, Tashkent, Uzbekistan; ixvoliddin.tursunov.1998.04.07@gmail.com

Kh. Sh. Matyokubov – Urgench State University, 14 H. Olimjon Str., 220100 Urgench, Uzbekistan; ORCID 0000-0002-6642-5488; hikmat0188@mail.ru

D. U. Matrasulov – Turin Polytechnic University in Tashkent, 17 Niyazov Str., 100095, Tashkent, Uzbekistan; ORCID 0000-0001-8957-0058; dmatrasulov@gmail.com

Conflict of interest: the authors declare no conflict of interest.

NANOSYSTEMS:
PHYSICS, CHEMISTRY, MATHEMATICS

Dweik J., Koabaz M. *Nanosystems: Phys. Chem. Math.*, 2023, **14** (2), 172–177.
http://nanojournal.ifmo.ru
DOI 10.17586/2220-8054-2023-14-2-172-177

Original article

Study of ion partitioning in nanoporous materials by analytical approach and molecular modeling

Jalal Dweik[a], Mahmoud Koabaz[b]

Jinan University, Tripoli, Lebanon

[a]Jalal.douwayk@jinan.edu.lb, [b]mahmoud.koabaz@jinan.edu.lb

Corresponding author: Jalal Dweik, Jalal.douwayk@jinan.edu.lb

ABSTRACT Physical and chemical processes that occur in nano-confined aqueous solutions, particularly the role of "solute-interface" and "solute-solute" interactions within nanopores, are the source of filtration selectivity and require further investigation. The goal is to clarify the validity of different approximations based on the macroscopic mean field approach by comparing them with computational techniques such as Monte Carlo (GCMC) and classical molecular dynamics (MD). These techniques are used to study the distribution of ions at the water/nanopore interface. At the molecular scale, the results show that the distribution of ions depends on their size, polarizability and the structure of water when it is explicitly added to the model, which cannot be reproduced by the primitive model using the GCMC and the mean field approach based on the Poisson–Boltzmann equation.

KEYWORDS nanoporous materials, molecular dynamics, ions distribution, water structure

FOR CITATION Dweik J., Koabaz M. Study of ion partitioning in nanoporous materials by analytical approach and molecular modeling. *Nanosystems: Phys. Chem. Math.*, 2023, **14** (2), 172–177.

1. Introduction

Nanoporous materials have become critical components in various fields including, nanotechnology, geology, chemistry and biology [1–6]. Conventional applications of nanoporous materials include: gas and liquid separation, catalysis, energy storage, sensing, biomedical applications and environmental remediation. Understanding of ion transport provides a design guide for synthetic nanoporous membranes used in applications such as nano-filtration. The physical mechanism of ion partitioning has been studied through various approaches described below.

1.1. Donnan approach

The concept of this theory [7, 8] assumes, firstly, that the ion activities inside and outside the pore are equal to their concentrations and, secondly, the electroneutrality inside and outside the pore. The model also takes into account the presence of charged groups on the internal walls, which results is an excess of counter-ions in close proximity of the surface and a partial exclusion of co-ions in this area. When the surface charge is weak or absent, the concentration of solutes inside the pore is identical to the concentration of the bulk, and the distribution of ions becomes uniform.

1.2. Mean field approach

The theory of Poisson–Boltzmann (PB) equation explains the electrostatic interactions occurring within the pore by regarding the solvent as a continual medium and the ions in the solution as point charges. However, this leads to a lack of specificity in ion identification. The Donnan method is consistent with the mean field approach based on the PB equation for surfaces that have weak or no charge [9].

1.3. Grand canonical Monte Carlo (GCMC) simulation technique

A study by Vlachy and coworkers [10] examined the concentration profiles using a grand canonical Monte Carlo (GCMC) simulation technique. The GCMC approach, which used the primitive model [11], explicitly describes ions but treats the solvent as a continuous medium. The study investigated the exclusion of solutes from uncharged cylindrical pores using three approaches: Donnan, PBE, and GCMC using the primitive model. The concentration profiles for a pore radius of 1 nm showed that the anion was excluded near the pore surface using the GCMC approach, while both the Donnan and PB models showed a homogeneous distribution of solutes. However, due to thermal fluctuations and strong ion-ion correlations, the mean field and Donnan approaches were unable to accurately describe the exclusion of electrolytes from uncharged pores.

1.4. Classical molecular dynamics

The current understanding of ionic transport across nanopores based on macroscopic (Donnan) and mesoscopic (Primitive model using GCMC and PB) fluid physics is only partial. This paper presents a molecular simulation study [12–17] of the ions behavior at the water/nanopore interface, focusing on the effect of a neutral atomic surface from hydrophobic to hydrophilic case. The behavior of ions at the interface is characterized by determining the density distribution and the coefficient of partition.

2. Methods

2.1. Numerical method and analytical approach

We first study the ion transport for a single salt in a cylindrical nanochannel at the macroscopic mean field level, by using both a numerical method and an analytical approach. We employ a space-charge (SC) model [18] based on the nonlinear Poisson–Boltzmann (PB) equation for the electrostatic potential $\tilde{\psi}(\tilde{r})$, as well as the extended Nernst–Planck ion flux and the Stokes equations, all as a function of two dimensionless parameters: the ratio of the pore radius r_p, to the Debye length based on the feed concentration, r_p/λ_c, and the ratio of the pore radius to the Debye length based on the membrane charge density, r_p/λ_m. The Poisson–Boltzmann equation which determines the electric potential inside the pore has the following form:

$$\frac{2}{\tilde{r}}\frac{\partial}{\partial\tilde{r}}\left(r\frac{\partial\tilde{\psi}}{\partial\tilde{r}}\right)\approx\left(\frac{r_p}{\lambda_c}\right)^2\left(e^{+\tilde{\psi}}-e^{-\tau\tilde{\psi}}\right), \tag{1}$$

where

$$\tilde{\psi}=-\frac{z_1F\psi(x,\tilde{r})}{RT}\geq 0,\quad \tilde{r}=\frac{r}{r_p},\quad \tau=\frac{|z_2|}{|z_1|}. \tag{2}$$

Here F is the Faraday constant, z_i is the ion valence, and λ_c is the Debye length associated with the concentration C given by:

$$\lambda_c=\left(\frac{RT\varepsilon}{2\nu_1z_1^2F^2C}\right)^{1/2}\propto C^{-1/2}. \tag{3}$$

The boundary conditions at the surface and the condition at the center and of the pore can be presented in dimensionless form:

$$\left.\frac{\partial\tilde{\psi}}{\partial\tilde{r}}\right|_{\tilde{r}=1}=4\sigma^*,\qquad \left.\frac{\partial\tilde{\psi}}{\partial\tilde{r}}\right|_{\tilde{r}=0}=0, \tag{4}$$

where

$$\sigma^*=\frac{1}{4}\left(\frac{r_p}{\lambda_m}\right)^2, \tag{5}$$

λ_m is the Debye length associated with the membrane charge density:

$$\lambda_m=\left(\frac{2\varepsilon RT}{|z_1|F^2|X_m|}\right)^{1/2}\propto|X_m|^{-1/2}, \tag{6}$$

where X_m is defined as follows

$$X_m=\frac{2\sigma_w}{Fr_p}. \tag{7}$$

The "radial equilibrium" approximation which gives one the concentration $c_i(r)$ (the Boltzmann distribution):

$$c_i(r,x)\approx k_i(x,r)\nu_iC(x), \tag{8}$$

where

$$k_i(x,r)=\exp\left[-\frac{z_iF\psi(x,r)}{RT}\right], \tag{9}$$

with $C(x)$ being the electrolyte concentration equivalent to the concentration of a bulk solution in equilibrium with the pore at position x and ν_i (the stoichiometric coefficient) represents the number of ions coming from the dissociated electrolytes. Here we take the case where there are two ionic species $I=1$ and 2. So, the condition of electroneutrality is described by $\nu_1z_1+\nu_2z_2=0$ or $\nu_1|z_1|=\nu_2|z_2|$:

$$(\mathrm{Counter-ion})_{z_1}^{\nu_1}(\mathrm{Co-ion})_{z_2}^{\nu_2}\ \longrightarrow\ \nu_1(\mathrm{Counter-ion})^{z_1}+\nu_2(\mathrm{Co-ion})^{z_2}.$$

The index ($i=1$) represents the counter ions and the index ($i=2$) represents the co-ions.

2.2. Classical molecular dynamic (MD)

In order to study the validity of both the mean field (macroscopic) theory and mesoscopic Primitive Model (implicit water, explicit ions), we performed classical Molecular Dynamics (MD) simulations that are especially suitable for investigating phenomena occurring at the nanoscale. We used the *Amber9* MD package [19] to perform NVT simulations of water (Pol3) at 300 K containing NaI at 1 M in a $30 \times 30 \times 190$ Å^3 simulation box (in the x-, y-, z-directions, respectively) with periodic boundary conditions in all three directions (Fig. 1). The Verlet leap frog algorithm was used to integrate the equations of motion with a time step of 1 fs. The simulations were performed at a constant temperature of 300 K using the weak coupling method thermostat [20] with a relaxation time step of 3 ps for the thermostat. Each simulation consisted of an equilibration stage of 5 ns followed by a data collection stage of 2 ns and the OH bond vibrations were frozen using the Shake algorithm [21]. The polarisable ions are described as charged soft sphere using the parameters in Table 1. The model walls consisted of neutral Lennard–Jones spheres starting at $z = 70$ Å and $z = 120$ Å (Table 2). The particle distribution in the nanopores and the ionic partition coefficients have been calculated from the simulation results, with $K_{PB} = C_P/C_B$, where C_P and C_B are respectively the average concentration of ions inside the pore and within the water layer (reservoirs).

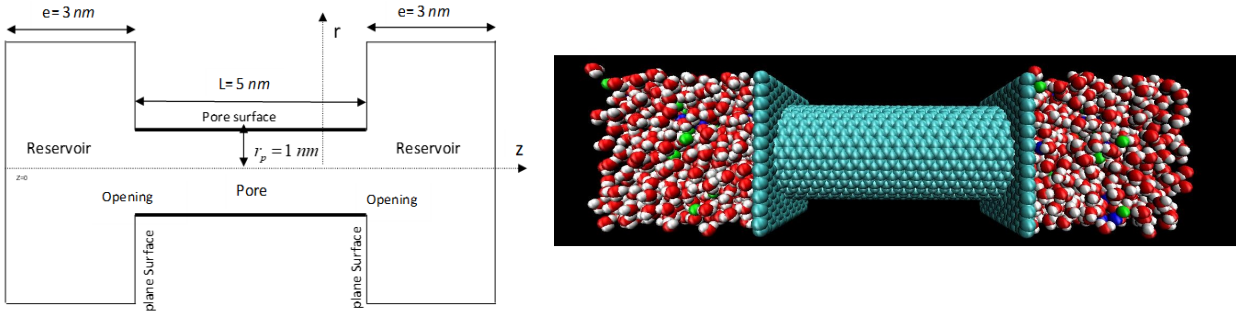

(a) (b)

FIG. 1. The left side of the figure shows a schematic representation of the model system (a), while the right side shows a visual representation of 1 M NaI in POL3 water simulated system (b)

TABLE 1. Potential parameters for polarizable ions and polarizable rigid water POL3

Element	σ (Å)	ε (kcal/mol)	Charge	α_i (Å^3)
H	0.000	0.000	+0.365	0.17
O	3.210	0.156	−0.730	0.52
Na	2.341	0.1	+1	0.24
I	5.160	0.1	−1	6.90

TABLE 2. Potential parameters for surface atoms (SA), describe the characteristics of the surface atoms

Element	Surface nature	σ (Å)	(kcal/mol)	Charge
SA1	hydrophobic	2.343	0.03	0
SA2	hydrophilic	2.343	1.86	0

3. Results

3.1. Analytical approach

Figure 2 shows that the behavior of the *salt-nanopore* system depends critically on the location in the r_p/λ_m vs. r_p/λ_c plane: Zones (1) and (2) demarcate the validity of the (weak potential) Debye–Huckel (DH) approximation; zones (1), (2), (3), and (5) demarcate the validity of the Extended Homogeneous (EH) approximation for which the radial variations of the potential and ionic concentrations are weak [for $r_p/\lambda_m < 2$ the *Donnan* (homogeneous) theory is

valid]; zones (5) and (6) demarcate the validity of the Good Co-ion Exclusion (GCE) approximation [22, 23] for which the salt exclusion is high because the concentration of co-ions is negligible; Zone (4) is an intermediate zone. For sufficiently high values of membrane charge, or r_p/λ_m, and/or sufficiently low values of external salt concentration, r_p/λ_c, the mean field approach breaks down due to thermal fluctuations and strong *ion-ion* correlations. The mean field approach thus becomes inaccurate in parts of zones (4) and (6), as has already been shown using the grand canonical Monte Carlo simulation technique [24] applied to the Primitive Model: for fixed external salt concentration (bulk) and small values of X_m, the simulated value for the exclusion parameter $\Gamma = 1 - \langle c_{\text{co-ion}} \rangle / c_{\text{co-ion}}$ is coherent with mean-field non-linear PB approach ($\langle c_{\text{co-ion}} \rangle / c_{\text{co-ion}}$ is the ratio of the average co-ion concentration in the pore to that in the external salt). Finally, the concentration of ions inside the nanopore approaches to the concentration in the bulk (outside the nanopore) when the surface charge of the nanopore become negligible. In this case the PB calculation and GCMC results is coherent with the experimental data [4].

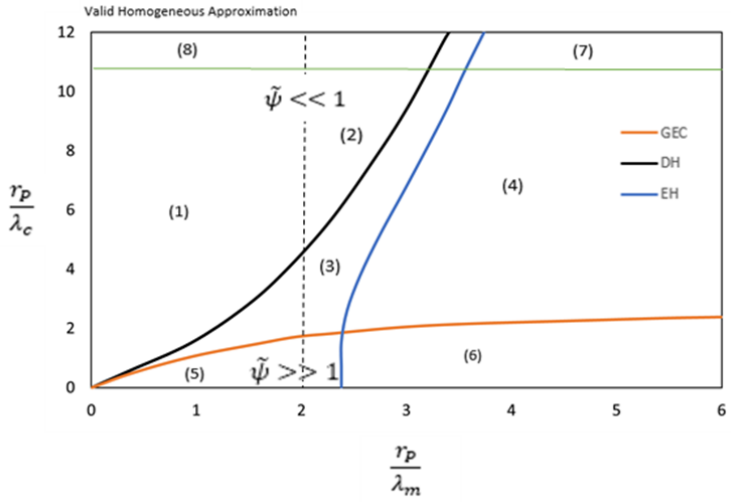

FIG. 2. Schematic Representation of the validity domain of the analytical approximations. Representation of different zones: (1) and (2): Validity of the Homogeneous and Debye–Huckel (DH), zone: (1), (2) and (3): Validity of EH zone of order 1, (5) and (6): Validity of the Homogeneous zone and inhomogeneous GEC (4): Intermediate zone (7): Validity of the plane approximation (8): Validity of the plane Debye–Huckel approximation. The blue curve delimits the area of EH. The dotted line delimits the H area

3.2. Molecular modeling

Based on molecular dynamics computing, we determine the radial distribution of water molecules and ions within the pore. Fig. 3 shows the concentration profile of ions (Na^+ and I^-) and Oxygen from water molecules (O) along the radial direction r of the nanopore in the two cases: hydrophobic and hydrophilic nanopore surface. The nature of the pore surface can influence the structure of water molecules within a pores. In hydrophilic pores, the water molecules are attracted to the nanopore surface, and, as a result, water molecules tend to form structured layers close to the nanopore surface, while it is less structured in hydrophobic pore. To further characterize the dynamics of water molecules, their self-diffusion coefficients were calculated from the derivative of the mean square displacement (MSD) along z-axis with respect to time:

$$D = \frac{1}{2t} < (z(t) - z(0))^2 . \tag{10}$$

The results show that the diffusion coefficient in hydrophobic nanopore surface (1.3×10^{-5} cm^2/s) is four times larger than the coefficient observed for the hydrophilic pore (0.32×10^{-5} cm^2/s). In this situation, the classical idea of image charge, which suggests that ions are repelled from the surface, does not hold true. Instead, when considering larger ions such as iodide, the volume fraction that these ions occupy becomes significant and results in higher free energy costs. As a result, these ions tend to move towards the hydrophobic interface. The way large polarizable I^- anions are distributed at the water/hydrophobic nanopore interface is similar to how they are distributed at the water/vapor interface [25], where they are found at the interface. Fig. 3(a) shows that the I^- anion peak is located below the water molecule peak at $r = 6$ Å, while in Fig. 3(b), it is at $r = 3$ Å, indicating that there is a higher concentration of I^- anions towards the hydrophilic center of the pore. In this zone, the number of the water molecules is low, whereas the Na^+ cations are located at the center of the pore, where they are hydrated by water molecules as a result of their small size and low polarizability. As mentioned above, the size effect is a critical factor that impacts how ions are adsorbed and distributed at the interface between water and nanopores. The reason for this size effect is due to the energy required to solvate ions, as their presence

can interfere with hydrogen bonding. On one hand, small solutes (such as Na^+) can be easily solvated by water molecules without disrupting the hydrogen bonding network, which means that there is no exclusion of these ions. On the other hand, large solutes (such as I^-) cannot be solvated without significantly hindering the process. The partition coefficient of I^- anions to measure the effect of the pore's surface properties (hydrophobic/hydrophilic) on the concentration of these ions inside the pore is calculated. The partition coefficient for the hydrophilic surface ($K_{PB} = 0.60$) is larger than for the hydrophobic surface ($K_{PB} = 0.52$). This result is consistent with the radial distribution obtained inside the pore (Fig. 3), which shows more I^- anions inside the pore for the hydrophilic surface compared to the hydrophobic surface.

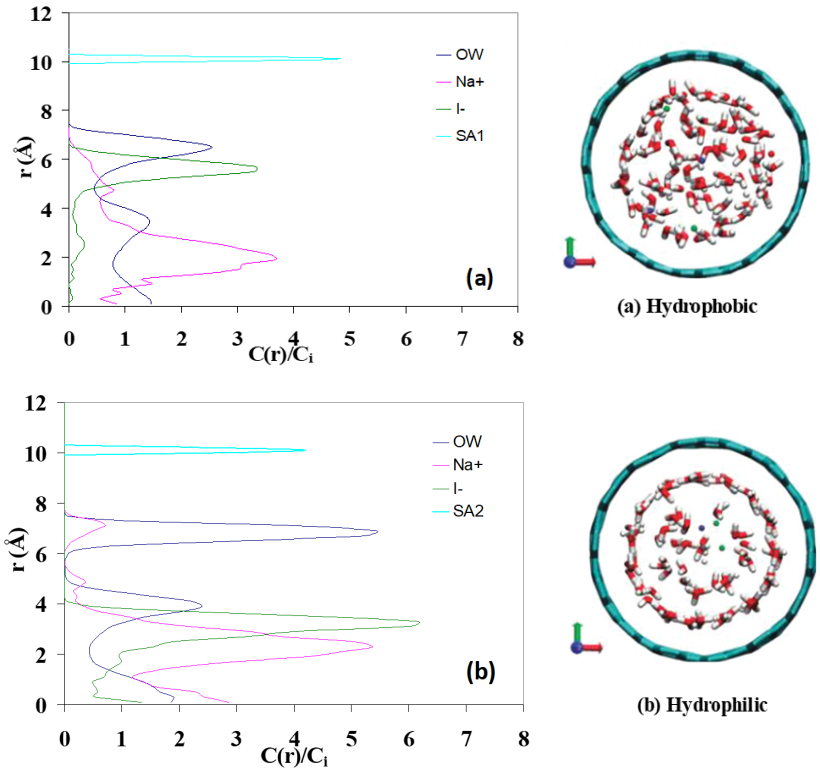

FIG. 3. The left side shows the ratio of concentration profile, $C(r)/Ci$, (Ci – concentration in the bulk phase) for polarizable sodium/iodide (NaI) ions and water molecules (a) hydrophobic pore and (b) hydrophilic pore in radial direction. The right side of Fig. 3 shows a snapshot in the direction opposite to the z-axis in the interval (50 Å$< z <$ 70 Å). The color convention used is: oxygen (O) in red; hydrogen (H) in white; sodium (Na) in blue; iodide (I) in green; and wall atom in light blue.

4. Conclusion

This paper provides a description of a MD simulation study focusing on the behavior of water and ions in nanoporous media. The primitive model and macroscopic mean field based on PB equation, which treat the solvent as a dielectric continuum, are unable to explain the results presented in the paper. The simulations highlight the importance of the atomic surface in the phase behavior of electrolyte solutions in contact with the nanopore surface. Our results indicate that due to the surface influences the distribution of water at the interface is well structured. Water structures play a significant role in the distribution of ions in the system. In this study, the behavior of NaI aqueous electrolyte's cations and anions was examined in nanopore. Different behaviors were observed among the cations and anions, as some were found within the pore center and others were adsorbed at the pore interface. In hydrophobic nanopores, small Na^+ cations tended to be in the pore center, while large polarizable I^- anions tended to accumulate at the interface. On the other hand, in hydrophilic nanopores, the anions tended to concentrate in the center of the pore. The water structure and distribution of ions in the system were affected by surface effects. The distribution of ions in the system was mainly dependent on their size and polarizability, particularly, to the large I^- anion and the small Na^+ cation. The advantages of the current simulation and interpretation technique can easily be extended to a large class of synthetic nano-materials in the presence of various ionic solutions. More extensive MD simulations are being conducted to better understand the behavior of the nanoporous system under investigation and to determine the validity domains of macro- and mesoscopic approaches.

References

[1] Dresner L., Kraus K.A. Ion exclusion and salt filtering with porous ion-exchange materials. *J. Phys. Chem.*, 1963, **67**, P. 990–998.

[2] Jacazio G., Probstein R.F., Sonin A.A., Yung D. Electrokinetic salt rejection in hyperfiltration through porous materials: Theory and experiments. *J. Phys. Chem.*, 1972, **76**, P. 4015–4023.

[3] Siwy Z., Fulinski A. Origin of Noise in Membrane Channel Currents. *Phys. Rev. Lett.*, 2002, **89**, P. 158101–158104.

[4] Crozier P.S., Rowley R.L. Molecular dynamics simulation of continuous current flow through a model biological membrane channel. *Phys. Rev. Lett.*, 2001, **86**, P. 2467–2470.

[5] Roux B., Karplus M. Molecular dynamics simulations of the gramicidin channel. *Annu. Rev. Biophys. Biomol. Struct.*, 1994, **23**, P. 731–761.

[6] Jardat M., Hribar-Lee B., Vlachy V. Self-diffusion of ions in charged nanoporous media. *Soft Matter.*, 2012, **8**, P. 954–964.

[7] Donnan F.G. The theory of membrane equilibrium and membrane potential in the presence of a non-dialyzable electrolyte. A contribution to physical-chemical physiology. *Z. Für Elektrochem. Und Angew. Phys. Chem.*, 1911, **17**, P. 572–581.

[8] Palmeri J., Blanc P., Larbot A., David P. Theory of pressure-driven transport of neutral solutes and ions in porous ceramic nanofiltration membranes. *J. Membrane Sci.*, 1999, **160** (2), P. 141–170.

[9] Chang C.W., Chu C.W., Su Y.S., Yeh L.H. Space charge enhanced ion transport in heterogeneous polyelectrolyte/alumina nanochannel membranes for high-performance osmotic energy conversion. *J. Mater. Chem. A*, 2022, **10**, P. 2867–2875.

[10] Jamnik B., Vlachy V.J. Ion Partitioning between Charged Micropores and Bulk Electrolyte Solution. Mixtures of Mono- and Divalent Counterions and Monovalent Co-Ions. *Am. Chem. Soc.*, 1995, **117** (30), P. 8010–8016.

[11] Dubois M., Zemb T., Belloni L., Deville A., Levitz P., Setton R. Osmotic pressure and salt exclusion in electrostatically swollen lamellar phases. *J. Chem. Phys.*, 1992, **96**, P. 2278–2286.

[12] Hartnig C., Witschel C., Spohr E., Bunsenges Ber. Molecular dynamics study of electrolyte-filled pores. *Phys. Chem.*, 1998, **102**, P. 1689–1692.

[13] Boiteux C., Kraszewski S., Ramseyer C., Girardet C. Ion conductance vs. pore gating and selectivity in KcsA channel: modeling achievements and perspectives. *J. of Molecular Modeling*, 2007, **13**, P. 699–713.

[14] Allen T.W., Kuyucak S., Chung S.H. Molecular dynamics study of the KcsA potassium channel. *Biophys. Chem.*, 2000, **86**, P. 1–14.

[15] Compoint M., Carloni P., Ramseyer C., Girardet C. Molecular dynamics study of the KcsA channel at 2.0-angstrom resolution: stability and concerted motions within the pore. *Biochimica Biophysica Acta – Biomembranes*, 2004, **1661**, P. 26–39.

[16] Corry B., Allen T.W., Kuyucak S., Chung S.H. A model of calcium channels. *Biochim. Biophys. Acta*, 2000, **1509**, P. 1–6.

[17] Berendsen H.J.C., Postma J.P.M., Van Gunsteren W.F., Dinola A., Haak J.R. Molecular dynamics with coupling to an external bath. *J. Chem. Phys.*, 1984, **81** (8), P. 3684–3690.

[18] Caldwell J.W., Kollman P.A. Structure and Properties of Neat Liquids Using Nonadditive Molecular Dynamics: Water, Methanol, and N-Methylacetamide. *J. Phys. Chem.*, 1995, **99** (16), P. 6208–6219.

[19] Gupta A., Rajan A.G., Carter E.A., Stone H.A. Ionic Layering and Overcharging in Electrical Double Layers in a Poisson-Boltzmann Model. *Phys. Rev. Lett.*, 2020, **125**, 1103.

[20] Caldwell J.W., Kollman P.A. Structure and Properties of Neat Liquids Using Nonadditive Molecular Dynamics: Water, Methanol, and N-Methylacetamide. *J. Phys. Chem.*, 1995, **99** (16), P. 6208–6219.

[21] Hijnen H.J.M., Van Daalen J., Smit J.A.M.J. The application of the space-charge model to the permeability properties of charged microporous membranes. *Colloid Interface Sci.*, 1985, **107**, P. 525–539.

[22] Palmeri J., Blanc P., Larbot A., David P. Theory of pressure-driven transport of neutral solutes and ions in porous ceramic nanofiltration membranes. *J. Membrane Sci.*, 1999, **160**, P. 141–170.

[23] Case D.A., et al. *AMBER9*. University of California, San Francisco, 2006.

[24] Jungwirth P., Tobias D.J. Specific ion effects at the air/water interface. *Chem. Rev.*, 2002, **106**, P. 1259–1281.

[25] Chandler D. Interfaces and the driving force of hydrophobic assembly. *Review Nature*, 2005, **437**, P. 640–647.

Submitted 23 February 2023; revised 18 March 2023; accepted 24 March 2023

Information about the authors:

Jalal Dweik – Professor in Mathematics and Physics, Jinan University, Zaytoun Abi-Samra, P.O. Box: 808, Tripoli, Lebanon; ORCID 0009-004-2988-0918; Jalal.douwayk@jinan.edu.lb

Mahmoud Koabaz – Assistant Professor in Mathematics and Physics, Jinan University, Zaytoun Abi-Samra, P.O. Box: 808, Tripoli, Lebanon; ORCID 0000-0003-0370-1120; mahmoud.koabaz@jinan.edu.lb

Conflict of interest: the authors declare no conflict of interest.

NANOSYSTEMS:
PHYSICS, CHEMISTRY, MATHEMATICS

Original article

Tupyakov D., Ivankov N., et al. *Nanosystems: Phys. Chem. Math.*, 2023, **14** (2), 178–185.
http://nanojournal.ifmo.ru
DOI 10.17586/2220-8054-2023-14-2-178-185

Theoretical study of the EDFA optical amplifier implementation scheme improving the performance of a quantum key distribution system integrated with an WDM optical transport network

Daniil Tupyakov, Nikita Ivankov, Irina Vorontsova, Fedor Kiselev, Vladimir Egorov

ITMO University, St. Petersburg, Russia

Corresponding author: Daniil Tupyakov, dvtupiakov@itmo.ru

ABSTRACT A version of an erbium doped fiber amplifier (EDFA) application scheme designed to increase the efficiency of the simultaneous quantum key distribution session and transmission of information by classical channels in a single optical fiber is explored. A theoretical study of the possibility to use EDFA in the explored way was conducted by numerical simulation methods. The mathematical model is based on the EDFA dynamics equations and the equations that determine the secure key generation rate in case of the subcarrier-wave quantum key distribution. A method for determining the optimal parameters of the scheme under study is described and the evaluation of the feasibility of using EDFA in the explored way is performed. A comparative analysis of the subcarrier-wave quantum key distribution system performance when integrated into an optical network is made in terms of the secure key generation rate for the cases when EDFA is either used or not. The results obtained demonstrate high efficiency of the scheme under study, i.e., the maximum achievable distance of the secure key distribution is increased while maintaining the efficiency of the information transmission.

KEYWORDS erbium-doped fiber amplifier, quantum key distribution, subcarrier-wave quantum key distribution

ACKNOWLEDGEMENTS The work was done by Leading Research Center “National Center for Quantum Internet” of ITMO University by the order of JSCo Russian Railways.

FOR CITATION Tupyakov D., Ivankov N., Vorontsova I., Kiselev F., Egorov V. Theoretical study of the EDFA optical amplifier implementation scheme improving the performance of a quantum key distribution system integrated with an WDM optical transport network. *Nanosystems: Phys. Chem. Math.*, 2023, **14** (2), 178–185.

1. Introduction

Quantum key distribution (QKD) can now be recognized as one of the most promising areas of quantum communications and cryptography in general [1, 2]. One advantage QKD features over classical encryption methods is that the security of the data transmission is based on the fundamental principles of quantum mechanics [3].

Significant interest is attracted to the possibility of introducing a QKD system into existing optical transport network based on wavelength division multiplexing (WDM) technology, practical convenience and economical benefits being the reason. Though it is a difficult task. The weak signal of a quantum channel is negatively affected by much more powerful information (classical) channels. Thus, noise signals fall into the spectral band of the quantum channel. The main reasons for their appearance include such nonlinear effects as spontaneous Raman scattering (SpRS), four-wave mixing (FWM), and linear channel crosstalk (LCXT) [4–6]. One method to minimize power of noise generated by classical channels corresponding to these effects is to reduce power of the classical channels. However, there is a reduction limit associated with the receiver’s requirement for minimum classical signal power and optical signal to noise ratio (OSNR). To use signals with a power below the limit, one can use an erbium doped fiber amplifier (EDFA) placed before a receiver. In this case, the power level of the classical channels will be restored to the limiting value, however, the amplifier will generate broadband amplified spontaneous emission (ASE) noise, leading to OSNR decrease. The power of the noise exceeds the power of quantum channels significantly, making it impossible for them to propagate through the amplifier. Therefore, the quantum channel is removed from the main fiber on the receiver side before entering the amplifier in the scheme under study.

This work is devoted to the study of the EDFA application scheme using numerical simulation methods based on the EDFA dynamics equations and the equations that determine the secure key generation rate in the case of subcarrier-wave (SCW) QKD protocol [7, 8]. Optimal parameters of the EDFA are evaluated, so that to achieve minimum allowable power per channel for 40 classical channels multiplexed using WDM technology with a frequency spacing of 100 MHz. To evaluate the efficiency of the scheme under study, we compare the maximum achievable distance of SCW QKD system in the presence of classical channels with and without EDFA. The results obtained make it possible to draw conclusions about the applicability of the scheme under study and to evaluate the parameters of EDFA necessary to increase the efficiency of the QKD session, when implemented in the existing fiber optical communication line (FOCL). The evaluated parameters

provide the maximum achievable distance of SCW QKD carried out simultaneously with the transmission of information via classical channels. By the expression "maximum achievable distance" we mean the maximum value of the fiber length at which the generation of a secure key is still possible, i.e. secure key generation rate is non-zero.

2. EDFA application scheme

Implementation of EDFA is one of possible ways to achieve the greatest attenuation of classical channels while maintaining the efficiency of information transmission. In order to avoid negative effect of an amplifier on the quantum channel, it is possible to use a scheme for integrating the QKD system into FOCL shown in Fig. 1.

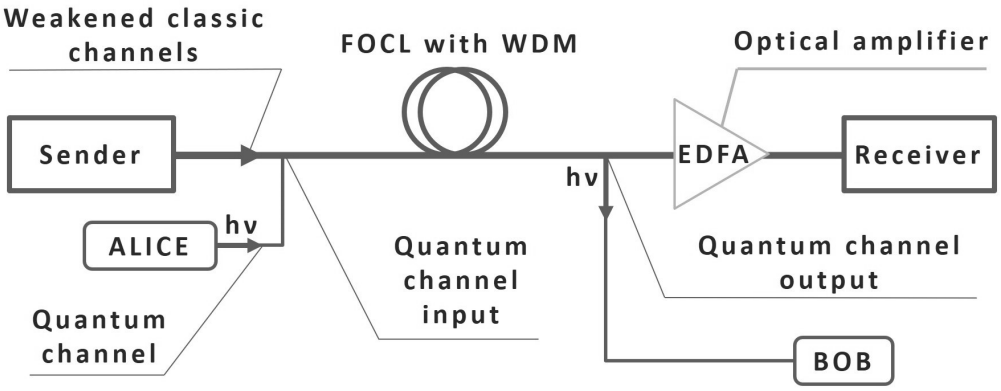

FIG. 1. Scheme of a QKD system integrated into a FOCL using an EDFA to restore the power of attenuated classical channels

On the sender side, weakened classical channels are combined with quantum channels using WDM technology and then enter the FOCL. On the receiver side, in turns, the quantum channel is diverted from the main line of the FOCL before it enters the amplifier, and then sent to the processing unit. The classical channels remaining in the FOCL are amplified with the help of EDFA and reach classical channel detectors after passing through the main demultiplexer. A similar solution was used when performing the experiment on the implementation of QKD through optical transport network in [9]. However, additionally to classical channel amplification, EDFA generates broadband noise, that is, so-called amplified spontaneous emission (ASE). It negatively affects such an information transmission efficiency parameter as OSNR. Therefore, it is necessary to carry out mathematical description of EDFA and numerical simulation of the explored circuit to determine the minimum allowable power of classical signals and the optimal parameters of the amplifier.

3. Mathematical model

3.1. Mathematical model of the EDFA

To simulate the EDFA dynamics, an ordinary nonlinear differential equation describing the relationship between the energy that enters the amplifier and the one absorbed by classical channels was used [10, 11]:

$$\frac{\partial N_2}{\partial t} = P_P\left(0,t\right)\left(1-G_P\right) + \sum_{\lambda_0}^{\lambda_n} P_S\left(0,t\right)\left(1-G_S\right) - \frac{N_2}{\tau}, \tag{1}$$

where N_2 is the number of ions at the metastable level, $P_{P(S)}\left(0,t\right)$ is the pump (signal) power value at the amplifier input, $G_{P(S)}$ is the pump (signal) gain value, and τ is the lifetime of the metastable level.

The signal power at the amplifier output $P_S\left(L,t\right)$ was determined by the formula [11]:

$$P_S\left(L,t\right) = P_S\left(0,t\right)G_S. \tag{2}$$

To calculate the channel gain G_S, the expression below was utilized [11]:

$$G_S = e^{B_S N_2 - C_S}. \tag{3}$$

In turns, the coefficients $B_{P(S)}$ and $C_{P(S)}$ used in 3 are calculated by the formula [11]:

$$B_{P(S)} = \Gamma_{P(S)}\frac{\alpha_{P(S)} + \beta_{P(S)}}{4.3429\rho A}, \tag{4}$$

$$C_{P(S)} = \Gamma_{P(S)}\frac{\alpha_{P(S)} L}{4.3429}, \tag{5}$$

where $\beta_{P(S)}$ is the absorption coefficient of the erbium-doped fiber at the pump (signal) wavelength, $\alpha_{P(S)}$ is the emission coefficient of the erbium-doped fiber for pump (signal) wavelength, ρ is the density of erbium ions, A is the cross-sectional

area of the amplifying fiber core, L is the length of the amplifying fiber, $\Gamma_{P(S)}$ is the overlap integral of the doped core and optical mode for pump (signal) radiation.

The overlap integrals $\Gamma_{P(S)}$ are calculated using the formulae [12]:

$$\Gamma_{P(S)} = 1 - e^{-\frac{b^2}{{w_{P(S)}}^2}}, \tag{6}$$

where b is the radius of the erbium-doped core and ${w_{P(S)}}^2$ is the radius of the effective area of the pump mode (signal).

To estimate the ASE noise power at the wavelength of the channel under study, the formula [11] can be used:

$$P_{ASE} = 2n_{sp}h\nu\Delta\nu\left(G_S - 1\right), \tag{7}$$

where n_{sp} is the population inversion coefficient between the metastable and ground levels, h is the Planck constant, ν is the frequency of the channel under study, $\Delta\nu$ is the detector bandwidth at the channel frequency.

Finally, the population inversion coefficient can be calculated using the following formula [10, 11]:

$$n_{sp} = \frac{1}{1 - \frac{\beta_P \alpha_S}{\beta_S \alpha_P}}. \tag{8}$$

In the case of simultaneous propagation of several channels, the energy is distributed among them unevenly. To study such a process, experimental values of the absorption and emission coefficients of the fiber for different wavelengths were used (see Fig. 2).

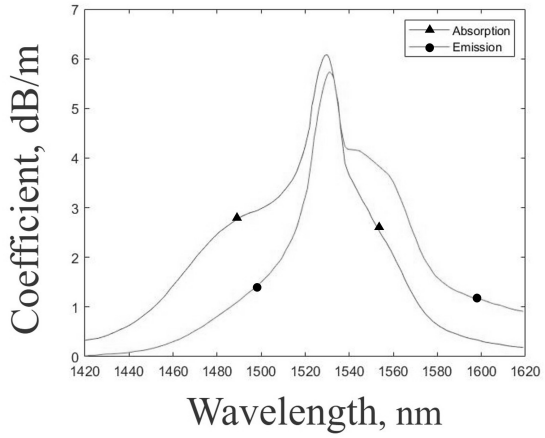

FIG. 2. Spectrum of emission (Emiss.) and absorption (Absorp.) of erbium ions doped fiber [11]

The mathematical model presented describes the dynamics of an optical amplifier in the approximation of weak information signals, which makes it possible to neglect the effect of gain saturation [13]. To describe the dynamics of EDFA with the considered parameters of the amplifying fiber under this approximation, the total power of classical channels should not exceed -2 dBm. In this work, the total power of information channels did not exceed -7 dBm, and thus, the requirement is fulfilled.

3.2. Mathematical model of noise

3.2.1. Spontaneous Raman scattering. The noise of forward spontaneous Raman scattering was determined by the formula [14]:

$$P_{\mathrm{ram,f}} = P_{\mathrm{out}} L \sum_{c=1}^{N_{\mathrm{ch}}} \rho(\lambda_{\mathrm{c}}, \lambda_{\mathrm{q}})\Delta\lambda, \tag{9}$$

where P_{out} is the output power of the fiber for one classical channel, L is the length of the optical fiber, N_{ch} is the number of information channels in the WDM system, $\rho(\lambda_{\mathrm{c}}, \lambda_{\mathrm{q}})$ is the normalized scattering cross section for the wavelengths of the information (λ_{c}) and quantum (λ_{q}) channels, $\Delta\lambda$ is the bandwidth of the filtering system quantum channels.

3.2.2. Four-wave mixing. The noise power of four-wave mixing (FWM) P_{ijk} for three pump signals featuring frequencies f_i, f_j and f_k at the new frequency $f_i + f_j - f_k$ was determined by the formula [14]:

$$P_{ijk} = \eta\gamma^2 D^2 p^2 e^{-\xi L} \frac{(1 - e^{-\xi L})^2}{9\xi^2} P_s P_l P_h, \tag{10}$$

where L is the interaction distance of the signals propagating along the fiber, D is the degeneracy parameter, ($D = 6$, $D = 3$), $P_{i(j,k)}$ and $f_{i(j,k)}$ are the input values of the power and optical frequencies of the interacting fields, respectively, γ is the third-order nonlinear coefficient, ξ is the loss factor, D_c and $dD_c/d\lambda$ are the dispersion parameters of the optical fiber, η is phase-matching efficiency, $\Delta\beta$ is the FWM parameter.

3.2.3. Linear channel crosstalk. The power leakage from the filter to the quantum channel was obtained as follows [14]:

$$P_{\mathrm{LCXT}} = P_{\mathrm{out}}\ (\mathrm{dBm}) - \mathrm{ISOL}\ (\mathrm{dB}). \tag{11}$$

where P_{out} is the output power of the fiber for one classical channel, ISOL is the inefficiency of the filter separating the quantum channel from the classical one.

3.3. Mathematical model of the secure key generation rate for a SCW QKD system

The quantum bit error rate $\mathrm{QBER}_{\mathrm{SCW}}$ was calculated by the formula [14]:

$$\mathrm{QBER}_{\mathrm{SCW}} = \frac{2\mu\tau\eta(1-\vartheta)\,(1 - cos(\delta\varphi)) + \tau\vartheta\mu_0\eta + p_{\mathrm{dark}} + p_{noise}}{4\mu\tau\eta(1-\vartheta) + 2\tau\vartheta\mu_0\eta + 2p_{\mathrm{dark}} + 2p_{\mathrm{noise}}}, \tag{12}$$

where $\eta \equiv \eta_{\mathrm{B}}\eta(L)\eta_{\mathrm{D}}$ is the value of the total optical transmission coefficient, $\mu = \mu_0 m^2$ is the average number of photons at side frequencies, m is the modulation constant, μ_0 is the average number of photons at the carrier frequency, $\tau \equiv \Delta t/T$ is the time parameter, η_{D} is the quantum detector efficiency, p_{dark} is the probability of quantum detector dark counts, p_{noise} is the probability of quantum detector noise counts, T is the time window, Δt is the gate opening time, $\eta(L) = 10^{-0.1\xi L}$ is the loss of the quantum signal in the fiber, ξ is the attenuation factor of the fiber, η_{B} is the loss in the receiver module, ϑ is the attenuation factor of the spectral filter, $\delta\phi$ is the phase shift caused by the imperfection of the equipment.

The quantum key rate K_{SCW} was calculated by the formula [14]:

$$K_{\mathrm{SCW}} = P_{\mathrm{B}}\nu_{\mathrm{S}}\left[1 - h(\mathrm{QBER}_{\mathrm{SCW}}) - h\left(\frac{1 - e^{-\mu_0 m^2}}{2}\right)\right], \tag{13}$$

where ν_{S} is the modulation frequency, $P_{\mathrm{B}} = (1 - G)/N$ is the probability of successful state detection if the receiver guesses the basis, N is the number of bases, $h(x)$ is the binary entropy function.

4. Results and discussions

The numerical simulation was performed in three stages. At the first stage, a model was developed to estimate the minimum allowable power of each of the classical channels and the length of the amplifier for a given pump power. At the second stage, the model obtained at the first stage was used to estimate the optimal pump power at which the lowest of all the minimum allowable powers of classical channels is achieved. At the third stage, the simulation of the SCW QKD session carried out simultaneously with the transmission of information via classical channels in a single optical fiber was performed. The EDFA parameters corresponding to the real ones used in transport optical networks were chosen for numerical simulation [11]. To evaluate the changes, we compare simulation results with the standard power of information channels and with their power values, optimized using the scheme under study. Let us now discuss the stages mentioned in a more detailed way.

4.1. First numerical simulation stage

The limiting value of the minimum power incident on the detector and the limiting value of the OSNR are determined by the sensitivity of the receiver. For the simulations, we used a power limiting value of -23 dBm. The lower limit of the OSNR was 9 dB. Such values correspond to the characteristics of detectors used in transport optical networks. To find the minimum allowable power value per channel, the amplification of 40 classical channels entering the amplifier at a time was simulated. The power of each information channel at the input of the amplifier varied from -15 to -25 dBm. The upper limit of the interval is the minimum required power, at which, taking into account the losses in the receiving module, no less than -23 dBm of power reaches the detector. The pump wavelength is 980 nm, which corresponds to the maximum of the absorption spectrum of erbium ions. The parameters used in our numerical simulations are given in the the Table 1

The simulation results of the gain spectrum for different signal powers are shown in Fig. 3. The simulation results of the detected power and OSNR of amplified classical channels are shown in Fig. 4.

The simulated gain exceeds 10 dB for each channel in the power range under consideration, which allows one, taking into account losses, to obtain a power at the receiver that significantly exceeds the threshold value (Fig. 4(a)). However,

TABLE 1. Parameters chosen for numerical simulations [11]

Parameter	Value	Units
ρ	$6.3 \cdot 10^{24}$	m^{-3}
A	4.52	$\mu\mathrm{m}^2$
β_P	3.31	dB/m
α_P	0	dB/m
β_S	Corresponds Fig. 2	dB/m
α_S	Corresponds Fig. 2	dB/m

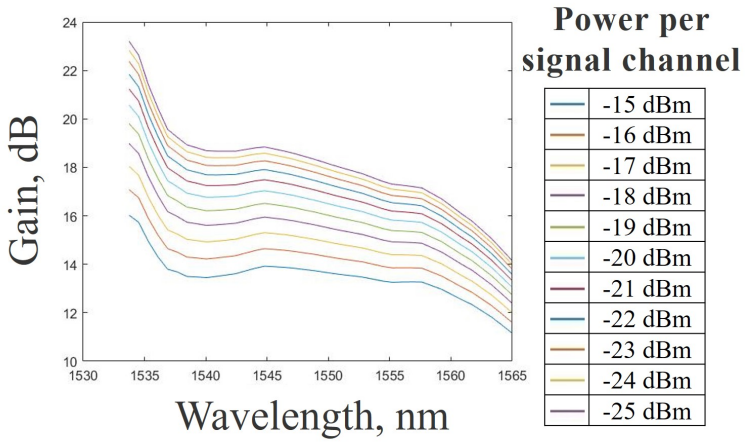

FIG. 3. Simulated gain of a classical channel versus wavelength of channel at different powers per channel

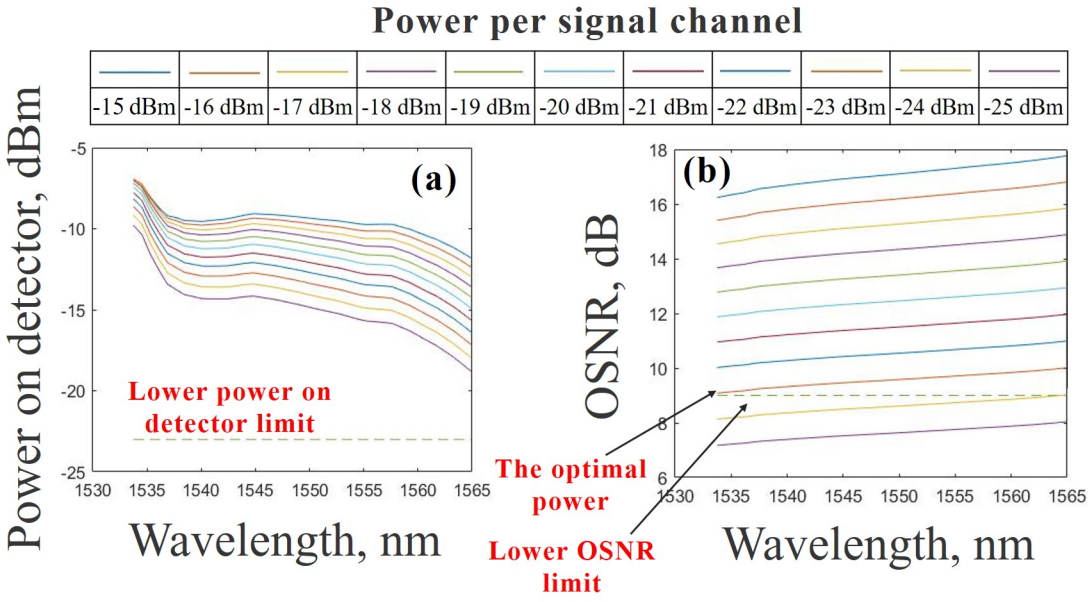

FIG. 4. Numerical simulation Results of a) Power of the amplified signal when it hits the detector versus wavelength of channel at different power per channel; b) OSNR versus wavelength of channel at different power per channel

the obtained OSNR values exceed the limit value only for powers not less than -23 dBm (Fig. 4(b)). Therefore, power of -23 dBm per channel is the minimum allowable for this system configuration and the amplifier performance.

4.2. Second numerical simulation stage

The EDFA dynamics was simulated using the above described algorithm for the pump power in the range of 10 to 40 dBm to determine the optimal pump power. Fig. 5 shows the dependence of the minimum allowable power per channel on the pump power.

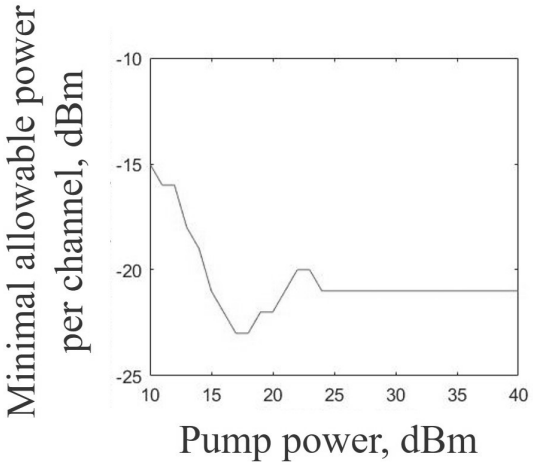

FIG. 5. Evaluated lowest allowable power per channel versus the pump power

The resulting dependence has a well-pronounced minimum in the pump power range from 17 to 18 dBm, the minimum value of power corresponding to -23 dBm per channel. We considered the behavior of characteristics depending on the pump power (Fig. 6) for the channel with the lowest OSNR (as can be seen from Fig. 4(b), this is the channel corresponding to the smallest value of the wavelength from the used range, that is 1533.7 nm) to understand the origin of the local minimum.

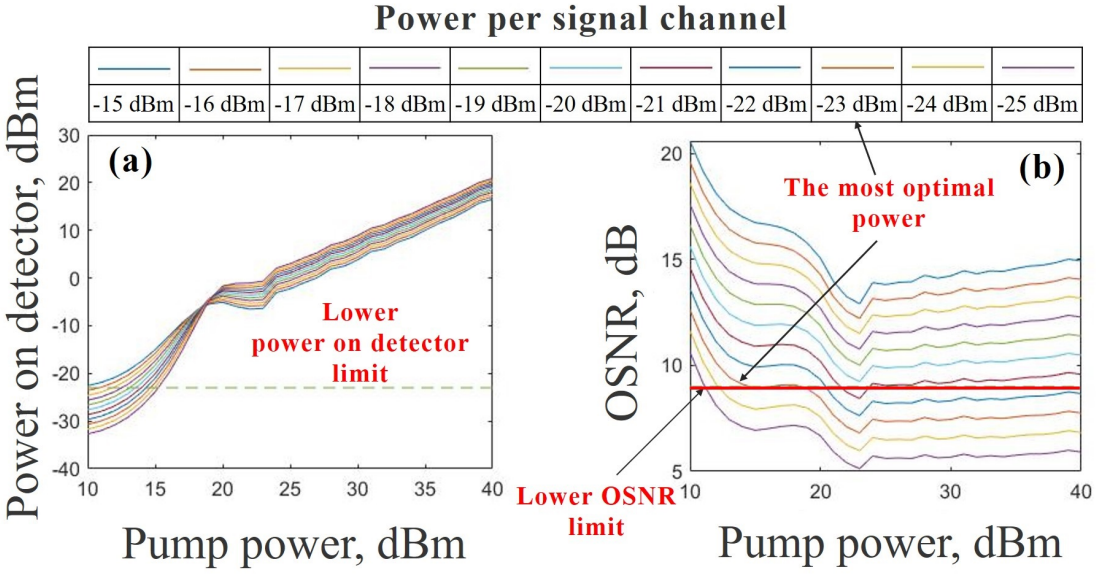

FIG. 6. Numerical simulation results for the channel at 1533.7 nm a) Power of the amplified signal when it hits the detector versus pump power at different power per channel; b) OSNR versus pump power at different power per channel

In the range from 10 to 15 dBm, the ASE noise power is much less than the signal power entering the amplifier, so the OSNR is high (Fig. 6(b)), and the minimum signal power is determined by the power hitting the detector (Fig. 6(a)). Starting from 15 dBm, the signal power at the detector begins to exceed the threshold value for almost all of the pump power values, and the minimum power value is then determined by the OSNR. Fig. 6(b) shows that in the pump power

range from 17 to 18 dBm, there is a slight increase in OSNR for the channel with its minimum value, which allows one to reach the minimum allowable power of -23 dBm. This phenomenon is associated with the nonlinearity of the processes of signal amplification and ASE noise generation. At the values greater than 18 dBm, the ASE power increases. Finally, at pump powers greater than 25 dBm, the ASE power and gain per channel reach constant value, since a doped fiber has a limit of the absorbed energy. This limitation is related to the finite number of absorbing centers. This leads to the fact that the excess pump power is not absorbed by the amplifier and the OSNR reaches a constant value and determines a constant minimum allowable power of -21 dBm per information channel.

4.3. Third numerical simulation stage

To evaluate the efficiency of the scheme under study, we calculated the secure key generation rate in the case of SCW QKD protocol, based on the equations (12,13) with standard parameters (without using EDFA) and with optimized parameters (calculated reduced power of classical channels with optimal EDFA parameters). The parameters of the SCW QKD system used for simulations are: $N_{ch} = 40$, $\Delta\nu = 100$ GHz, $R_X = -23$ dBm, $\lambda_q = 1535$ nm, $\delta\lambda = 15$ nm, $ISOL = 100$ dB, $\delta\phi = 5^\circ$, $\mu_0 = 4$, $m = 0.319$, $IL = 8$ dB, $D_e = 10\ \%$, $p_{dark} = 10^{-6}$, $\alpha = 0.18$ dB/km, $T = 1$ ns, $L = 0 - 50$ km, $N = 2$. The results are presented in Fig. 7.

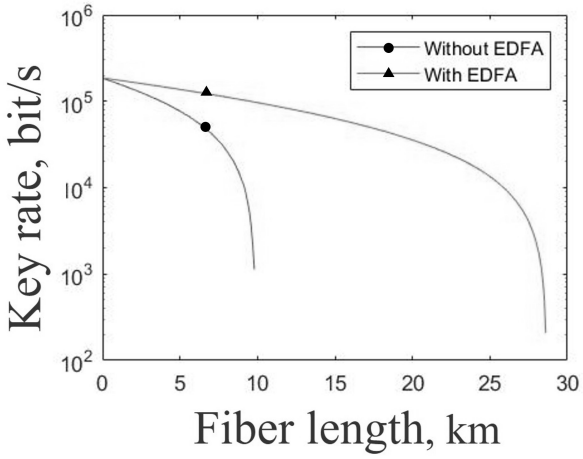

FIG. 7. Dependence of the secure key generation rate on the propagation distance for SCWQKD in the presence of classical channels with and without EDFA

The key generation rate axis is displayed on a logarithmic scale, the break in the graph corresponds to the key generation rate turning to zero. From the obtained numerical results presented in Fig. 7, it is clearly seen that, depending on whether EDFA is used or not, the distance at which successful QKD session is possible changes significantly. The use of an amplifier according to the scheme under study allows one to increase the maximum achievable distance at a non-zero key generation rate, as well as to increase the key generation rate at a fixed distance.

5. Conclusion

In this work, one of possible schemes for using EDFA to increase the performance of a QKD session was theoretically investigated. The presented scheme is quite simple to implement and has an extremely high efficiency, which was confirmed by numerical simulation. The calculated optimal parameters of the EDFA amplifier made it possible to simulate the most effective attenuation for a given number of classical channels, provided that the detector requirements are met. It was also shown, that for given characteristics of the amplifying fiber and given set of channels, the optimal pump power lies in the range from 17 dBm to 18 dBm. This is explained by the fact that the ASE power depends on the pump power and leads to the OSNR deterioration at high pump values. At lower pump powers, the OSNR is high, but there is not enough energy in the amplifier to restore the power of classical channels to the limiting value. Additionally, it was shown that for the discussed parameters the lowest power per channel to which classical channels can be attenuated is -23 dBm. In conclusion, the use of the considered scheme with these parameters, it was possible to increase the simulated maximum achievable distance of the secure key distribution session by the SCW QKD system. The presented scheme can be implemented in different ways. In the case of already existing and functioning FOCL, adding an extra amplifier to the line may not be an easy task. However, if it is possible from an engineering point of view, such a change will not lead to a deterioration in system performance, which is demonstrated in our work. Additionally, in most long-distance FOCLs, EDFA amplifiers are already used to compensate for fiber losses. In such a case the task is reduced to a mere reconfiguration of existing amplifiers, which also does not lead to a deterioration in system performance. Finally, it is

also possible to design FOCL equipped with an amplifier. Such FOCLs will not only be inferior to the ones without an amplifier but will outperform them in terms of the allowable range of information transmission [15].

References

[1] Scarani V., Bechmann-Pasquinucci H., Cerf J.N., Dušek M., Lütkenhaus N., Peev M. The security of practical quantum key distribution. *Reviews of Modern Physics*, 2009, **81** (3), P. 1301–1350.

[2] Pirandola S., Andersen U.L., Banchi L., Berta M., Bunandar D., Colbeck R., Englund D., Gehring T., Lupo C., Ottaviani C., Pereira J.L., Razavi M., Shamsul Shaari J., Tomamichel M., Usenko V.C., Vallone G., Villoresi P., Wallden P. Advances in quantum cryptography. *Advances in Optics and Photonics*, 2020, **12** (4), 1012.

[3] Gisin N., Ribordy G., Tittel W., Zbinden H. Quantum cryptography. *Reviews of Modern Physics*, 2002, **74** (1), P. 145–196.

[4] Mlejnek M., Kaliteevskiy N., Nolan D.A. Reducing spontaneous Raman scattering noise in high quantum bit rate QKD systems over optical fiber. 2017, URL: https://arxiv.org/ftp/arxiv/papers/1712/1712.05891.pdf.

[5] Niu J.-N., Sun Y.-M., Cai C., Ji-Y.-F. Optimized channel allocation scheme for jointly reducing four-wave mixing and Raman scattering in the DWDM-QKD system. *Applied Optics*, 2018, **57** (27), 7987.

[6] Kumar R., Qin H., Alléaume R. Coexistence of continuous variable QKD with intense DWDM classical channels. *New J. of Physics*, 2015, **17**, 043027.

[7] Gleim A.V., Egorov V.I., Nazarov Y.V., Smirnov S.V., Chistyakov V.V., Bannik O.I., Anisimov A.A., Kynev S.M., Ivanova A.E., Collins R.J., et al. Secure polarization-independent subcarrier quantum key distribution in optical fiber channel using BB84 protocol with a strong reference. *Optics Express*, 2016, **24** (3), P. 2619–2633.

[8] Merolla J., Mazurenko Y., Goedgebuer J.P. Quantum Gryptography using Frequency Modulation of Weak Ligh Pulses. *Proceedings of European Quantum Electronics Conference*. Glasgow, UK, Technical Digest of EQEC 1998, 1998, 101.

[9] Choi I., Zhou Y.R., F.-Dynes J., Yuan Z., Klar A., Sharpe A., Plews A., Lucamarini M., Radig C., Neubert J., Griesser H., Eiselt M., Chunnilall C., Lepert G., Sinclair A., Elbers Z.-P., Lord A., Shields A. Field trial of a quantum secured 10 Gb/s DWDM transmission system over a single installed fiber. *Optics Express*, 2014, **22** (19), 23121.

[10] Sharma R., Raghuwanshi S.K. Computer Model for EDFA Dynamics Over 1525-1560nm Band Using a Novel Multi-Wavelength MATLAB Simulink Test Bed for 8-Channels. *IETE J. of Research*, 2018, **64** (6), P. 814–831.

[11] Pinter S., Jean J., Fernando X. A dynamic multi-wavelength simulink model for EDFA. *Proceedings of Canadian Conference on Electrical and Computer Engineering 2004*, Niagara Falls, Ontario, Canada, IEEE, 2004, P. 2077–2080.

[12] Giles C.R., Desurvire E. Modeling erbium-doped fiber amplifiers. *J. of Lightwave Technology*, 1991, **9** (2), P. 271–283.

[13] Lebedev V.F., Serduk K.V., Fomenko I.N. *Laser Technology*. St. Petersburg State University of Aerospace Instrumentation, St. Petersburg, 2021, 45 p.

[14] Kiselev F., Veselkova N., Goncharov R., Egorov V. A theoretical study of subcarrier-wave quantum key distribution system integration with an optical transport network utilizing dense wavelength division multiplexing. *J. of Physics B: Atomic, Molecular and Optical Physics*, 2021, **54** (13), 135502.

[15] Pradhan D., Vivekanand M. Analysis and Review of EDFA. *Int. J. of Computer Science and Network*, 2015, **4** (6), P. 918–923.

Submitted 1 March 2023; revised 9 March 2023; accepted 10 March 2023

Information about the authors:

Daniil Tupyakov – ITMO University, Kronverkskiy, 49, St. Petersburg, 197101, Russia; ORCID 0000-0002-8804-6569; dvtupiakov@itmo.ru

Nikita Ivankov – ITMO University, Kronverkskiy, 49, St. Petersburg, 197101, Russia; ORCID 0000-0002-2024-9773; ivankov.nikita2014@gmail.com

Irina Vorontsova – ITMO University, Kronverkskiy, 49, St. Petersburg, 197101, Russia; ORCID 0000-0001-9861-0816; iovorontsova@itmo.ru

Fedor Kiselev – ITMO University, Kronverkskiy, 49, St. Petersburg, 197101, Russia; ORCID 0000-0002-3894-511X; fdkiselev@itmo.ru

Vladimir Egorov – ITMO University, Kronverkskiy, 49, St. Petersburg, 197101, Russia; ORCID 0000-0003-0767-0261; viegorov@itmo.ru

Conflict of interest: the authors declare no conflict of interest.

NANOSYSTEMS:
PHYSICS, CHEMISTRY, MATHEMATICS

Rudyak V.Ya., Lezhnev E.V. *Nanosystems: Phys. Chem. Math.*, 2023, **14** (2), 186–194.
http://nanojournal.ifmo.ru
DOI 10.17586/2220-8054-2023-14-2-186-194

Original article

Modeling the rarefied gas thermal conductivity in nanochannels

Valery Ya. Rudyak[1,2,a], Evgeny V. Lezhnev[2,b]

[1]Kutateladze Institute of Thermophysics of Siberian Branch of RAS, Novosibirsk, Russia
[2]Novosibirsk State University of Architecture and Civil Engineering, Novosibirsk, Russia

[a]valery.rudyak@mail.ru, [b]lionlev@yandex.ru

Corresponding author: Valery Ya. Rudyak, valery.rudyak@mail.ru

PACS 51.20.+d, 02.70.Ns

ABSTRACT In the paper, the thermal conductivity of rarefied gases in nanochannels and in bulk was studied. The following gases Ar, Kr, Ne, Xe, O_2, CH_4 were considered. The evolution of gas molecules in phase space was calculated by the method of the stochastic molecular modelling. It was established that the thermal conductivity coefficient of the gas in the nanochannel is anisotropic. Anisotropy of the thermal conductivity is caused by the interaction of gas molecules with the channel walls. This interaction is described by the specular or diffuse laws of molecules reflection. The thermal conductivity of gases across the channel is significantly lower than along it. The anisotropy of the thermal conductivity persists even in microchannels, but it decreases with the increasing of the gas density. In fact, the thermal conductivity coefficient is not a gas property only, but of a gas+channel wall system.

KEYWORDS nanochannel, rarefied gas, stochastic molecular simulation, thermal conductivity, transport processes.

ACKNOWLEDGEMENTS This paper was supported partly by the Mega-Grant from the Ministry of Science and Higher Education of the Russian Federation (Agreement no. 075-15-2021-575).

FOR CITATION Rudyak V.Ya., Lezhnev E.V. Modeling the rarefied gas thermal conductivity in nanochannels. *Nanosystems: Phys. Chem. Math.*, 2023, **14** (2), 186–194.

1. Introduction

In the last two decades, various devices and systems where flows in nanochannels take place have been rapidly developing. First of all, we can mention various biomedical systems, NEMS systems, nanomixers, etc. [1–5]. Thermophysical applications of nanoflows are of a great interest also, for example, thermoelectric energy conversion, thermal management of nanoscale electronics, creation of a chip-level cooling system, etc. For obvious reasons, the experimental study of heat transfer in nanochannels and the measurement of the thermal conductivity coefficient is extremely difficult. An alternative method for studying these properties is the molecular dynamics one. Thermal conductivity of liquid argon in plane channels with krypton walls was studied [6]. The channel height did not exceed 6 nm. It was found that the coefficient of thermal conductivity is slightly lower than in the bulk in small channels (2–3 nm high), but then it grows and reaches a value in the bulk.

Thermal conductivity of liquid argon in nanochannels was calculated in a wide range of fluid densities in paper [7]. The transverse size of the nanochannel varied from 2.25 to 15 nm. It was shown that the thermal conductivity weakly depends on the shape (square or round) of the nanochannel with the same cross-sectional area and it increases with the growth of the transverse size of the channel. In addition, the thermal conductivity coefficient reached values in the bulk for a certain characteristic channel size, which strongly depended on the fluid density and varied from 5 to 11 nm. Here, however, it should be noted that the interaction of argon molecules with the walls was described by a rather rough potential (power-law repulsion with an exponent equal to 96).

Pourali and Maghari [8] simulated the thermal conductivity of a binary mixture of methane and some n-alctanes in a fairly narrow channel using the nonequilibrium molecular dynamics method. In order to create a temperature gradient, the walls of a plane channel had different temperatures. It was indicated that the thermal conductivity of the mixture increased with the decreasing of the channel height.

In the recent paper [9], a significant anisotropy of thermal conductivity along and across channel was established. This also agrees with experimental data [10]. The presence of such anisotropy is a natural consequence, firstly, of anisotropy of the channel geometry, and, secondly, of a great influence of fluid molecules interaction with the channel walls.

It was shown [11, 12] by methods of nonequilibrium statistical mechanics that, under confined conditions, the constitutive relations are transformed. In particular, a contribution appears in the transport coefficients due to the interaction of fluid molecules with the channel walls. Thus, in particular, it was found that the fluid viscosity is a property of the entire

fluid+channel wall system. Therefore, by varying the material of the walls, the viscosity can be controlled, it can be either more than in the bulk or less [13].

Finally, we should mention paper [14], where the thermal conductivity of water in a plane nanochannel with graphene walls was studied by the method of molecular dynamics. The maximum channel height was about 15 nm. Anisotropy of thermal conductivity was also established there. The degree of this anisotropy decreased with increasing of the channel height.

In all the papers cited above, thermal conductivity of liquids was studied by the method of molecular dynamics. However, from a practical point of view, data on the thermal conductivity of rarefied gases in nanochannels are also necessary. In this case, the molecular dynamics method is not actually applicable, since it requires the use of a huge number of molecules (characteristic size of the simulation cell must be greater than the mean free path of gas molecules). A special algorithm was developed [15] called the smart wall molecular dynamics (SWMD) to reduce the required calculation time. Later, this method was used to solve a number of problems of rarefied gas dynamics in nanochannels [16–18]. In the last work, heat transfer of argon in a plane nanochannel 5.4 nm high was studied. The great importance of gas molecules interaction with the channel walls was noted.

The problem of heat transfer of rarefied gas in nanochannels continuously attracts attention of many researchers and many attempts have been made to solve it [19–21], but it has not been established yet, whether there is a difference between the thermal conductivity coefficient of rarefied gas in nanochannels and the corresponding values in the bulk. The study of the thermal conductivity coefficient of a rarefied gas in confined conditions is an important factor in solving many practical problems. The influence of gas rarefaction degree on the coefficient is known, however, rigorous formulas can be obtained in the case of small or, on the contrary, large (in free molecular limit) Knudsen numbers. In the last case, a semi-phenomenological formula was actually obtained, where the thermal conductivity coefficient depended on the so-called accommodation coefficients, which described the interaction of gas molecules with the channel walls. In this connection, an attempt to calculate the accommodation coefficients of argon in channels with platinum walls using the molecular dynamics method was made [22]. One can see that these coefficients increase with decreasing temperature and tend to unity. Nevertheless, it should be noted that with this approach it is not possible to understand how the anisotropy of the transport processes affects the effective coefficient of thermal conductivity.

Previously, the authors developed the method of stochastic molecular modeling (SMM) for simulation of the transport coefficients of rarefied gases [23–26]. This method has been used to simulate the coefficients of self-diffusion, diffusion and viscosity of various gases, including polyatomic and rarefied gas nanosuspensions with high accuracy [26] (with the accuracy of experimental measurements). The viscosity of rarefied gases in nanochannels was also studied [27] and its anisotropy was established. The purpose of this paper is to calculate the thermal conductivity coefficients of rarefied gases in nanochannels using SMM method. Thermal conductivity of argon, krypton, xenon, oxygen, and methane in nanochannels with a square cross section was studied, and the channel height varied from 8.5 to 1000 nm. The coefficient of thermal conductivity in the bulk was also preliminarily calculated, which value was compared with the known experimental data. The accuracy of such modeling is also discussed.

2. Algorithm of the SMM Method

In this paper, we are talking about modelling the thermal conductivity coefficient of rarefied gases in nanochannels. Usually, the transport coefficients of rarefied gases are calculated using the kinetic theory of gases. One of the main achievements of this theory is derivation of formulas for calculating these coefficients (see, for example [28, 29]). Their calculation, however, in the general case is not an easy task and requires implementation of many time-consuming procedures, in particular, solution of fairly complex integral equations. Nonequilibrium statistical mechanics makes it possible to construct universal generalized constitutive relations and deduce explicit formulas for the transport coefficients [30–32]. In this case, the transport coefficients are determined by the so-called fluctuation-dissipation theorems (FDTs). In the literature they are usually called Green–Kubo formulas. According to FDTs, the transport coefficients are time integrals of two-time correlation functions of the corresponding dynamic variables. The equivalence of the formulas for the transport coefficients of the kinetic theory of gases to the Green–Kubo formulas is proved [33, 34]. In particular, the thermal conductivity coefficient λ is determined by the formula:

$$\lambda = \frac{k}{3VT^2}\int\limits_0^{\tau_p} \langle \mathbf{j}(0)\cdot\mathbf{j}(t)\rangle dt = \frac{k}{3VT^2}\int\limits_0^{\tau_p} \chi(0,t)dt, \tag{1}$$

where k is Boltzmann's constant, V is system volume, $\mathbf{j}$ is microscopic vector of heat flux, τ_p is the so-called plateau value of the integration time. Actually, an experimentally measurable value of the transport coefficient is obtained by reaching this value [35]. During this time, the corresponding autocorrelation function of thermal conductivity (TCACF) $\chi(0,t)$ damps. The angle brackets in (1) mean ensemble averaging. It is important to emphasize that the averaging in (1) is carried out over the equilibrium ensemble, and the transport coefficients and thermal conductivity coefficient, in particular, are determined by the properties of thermal equilibrium molecular fluctuations. This also corresponds to the kinetic theory of rarefied gases, where the transport coefficients are calculated by the Maxwell distribution function [28, 29].

The calculation of correlation functions requires information about the dynamic variables of the system being modeled at successive moments of time. In a rarefied gas, the interaction of molecules does not contribute to the transport coefficients and to the equation of state. The corresponding contributions appear only in the so-called nonideal gas [36,37]. For this reason, to model the transport coefficients of a rarefied gas, it is sufficient to have data on its dynamic variables only in the velocity space. Therefore, the microscopic vector of the heat flux in formula (1) depends only on the velocities of the molecules. In confined conditions and in nanochannels, in particular, there is an intense interaction of gas molecules with the channel walls. This leads to the fluctuation motion of the center of mass of the considered equilibrium gas (the average velocity of the gas center of mass is equal to zero, of course). This fluctuation motion changes the energy transfer in the system, and this contribution should be excluded to calculate the true thermal conductivity of gas. Therefore, the microscopic vector of the heat flux of a rarefied gas in confined conditions is described by the following relation:

$$\mathbf{j}(t) = \sum_{i}^{N} [\mathbf{v}_i(t) - \mathbf{v}_c(t)] e_i(t), \quad \mathbf{v}_c(t) = \frac{1}{N} \sum_{i}^{N} \mathbf{v}_i(t), \tag{2}$$

where $\mathbf{v}_c$, $\mathbf{v}_i$ and e_i are, respectively, the velocity of the mass center, the velocity of the molecule i and its kinetic energy, and N is the number of molecules in the system.

Below, the contribution due to the energy transfer associated with fluctuations in the velocity of the center of mass of gas will be called the fluctuation contribution. Calculating the thermal conductivity coefficient, the velocity of the center of mass, of course, is equal to zero in the bulk.

So, in order to calculate TCACF and, consequently, the thermal conductivity coefficient, it is necessary to have data on all molecules velocities of the simulated system at successive moments of time. In confined conditions, in addition to the interaction of gas molecules with each other, they also interact with the channel walls. For this reason, SMM algorithm became more complicated, since information about the coordinates of all molecules was also required at each moment of time. The interaction of gas molecules with the channel walls is described in this work using specular or specular-diffuse reflection law. This approach is typical for rarefied gas dynamics [38, 39]. In specular reflection, the velocity of a molecule along surface does not change, but its normal component changes its sign. In diffuse mode, the velocity of the reflected molecule is played out according to the Maxwell distribution function. In specular-diffuse reflection, the fraction of molecules θ interacts with the wall diffusely, while $(1-\theta)$ interacts specularly, where θ is the so-called accommodation coefficient. The molecules interaction is described by Lennard-Jones potential:

$$U(r) = 4\varepsilon \left[\left(\frac{\sigma}{r}\right)^{12} - \left(\frac{\sigma}{r}\right)^{6} \right], \tag{3}$$

where σ and ε are the effective molecular size and the potential well depth, respectively.

The simulation cell is chosen in the form of a parallelepiped with a square cross section, along its axis periodic boundary conditions are set, which are usual for the method of molecular dynamics [40]. In accordance with the given mass density of gas ρ (or numerical one), the molecules are distributed uniformly over the simulation volume. Their velocities are played out according to the Maxwell distribution with a given temperature, but in such a way the total momentum of all N molecules is equal to zero (the corresponding procedure is described in [25]), since the equilibrium state of gas is simulated. Simulating the dynamics of gas in question begins with listing. At the initial time t, all molecules are listed in some arbitrary order. By changing the order of the particles in the list, we will get different phase trajectories. Thus, at time t, the particles have velocities $\mathbf{v}_1, \mathbf{v}_2, ..., \mathbf{v}_N$ and coordinates $\mathbf{r}_1, \mathbf{r}_2, ..., \mathbf{r}_N$.

In order to obtain the values of dynamic variables at successive time moments, their dynamics is split into processes, and the motion of molecules in the space of velocities and configurations is successively modeled. The phase trajectory calculation time t_s is divided into intervals of duration $\tau_\alpha = \sigma / v_\alpha(t)$ where σ is the effective molecular diameter, and v_α is the maximum velocities of the system molecules at a given time. The formation of the list at the first-time step $(t + \tau_1)$ begins with the consideration of molecule 1. First, the coordinate of this molecule is changed, $\mathbf{r}(t+\tau_1) = \mathbf{r}_1(t) + \mathbf{v}_1(t)\tau_1$, and its collision with the wall is checked. If the interaction with the wall has occurred, then the molecule velocity changes depending on the law of interaction with the wall used in this calculation (specular, diffuse or specular-diffuse) and the coordinate changes accordingly. If there is no interaction with the wall, then its collision with other gas molecules is played out. For this purpose, a random number u is generated, uniformly distributed over the interval (0;1). If it turns out to be less than or equal to the average collision probability [29] $P_{c1} = 4\tau_1 \rho \sigma^2 \sqrt{\pi RT/m}$, then a collision will occur. In this case, molecule j is randomly selected from the remaining $(N-1)$ molecules, with which the collision is realized. As a result, the molecules velocities 1 and j change in accordance with the conservation laws. If the played number u turns out to be greater than the average collision probability, then molecule 1 does not collide and its velocity does not change. This is how all molecules are sequentially processed and a complete list of dynamic variables at the moment $(t + \tau_1)$ is formed. After that, the next time interval $\tau_2 = \sigma / \mathrm{v}_\alpha(t + \tau_1)$ is selected, and the procedure is repeated. Then the same procedure is implemented for each time step until the specified calculation time t_s is over. Thus, a complete set of dynamic variables of all simulated system's molecules is obtained at successive time moments.

TABLE 1. Comparison of calculation data for the thermal conductivity coefficient of rarefied gases by SMM method λ with experimental [41] λ_e $\mathrm{Wm^{-1}K^{-1}}$

	Ar	Kr	Ne	Xe	O_2	CH_4
λ	0.0175	0.0098	0.0506	0.0055	0.0279	0.0329
λ_e	0.0177	0.0096	0.049	0.0057	0.0267	0.0342
Δ %	1.23	2.52	3.36	3.17	4.49	3.93

3. Thermal Conductivity of Rarefied Gas in the Bulk

Modeling gas thermal conductivity in a nanochannel requires, first of all, SMM method verification, which is used for this purpose. On the one hand, it is necessary to verify this method, calculating the transport coefficients in the bulk, and on the other hand, in nanochannels themselves. Previously [23–26], the efficiency and accuracy of SMM method were demonstrated, calculating the coefficients of self-diffusion, diffusion, and viscosity of rarefied gases, including polyatomic gases. In all cases, it is possible to achieve an accuracy of 1–2% using a relatively small number of molecules. The accuracy grows with an increase in the number of molecules used for modeling and phase trajectories over which the calculated data are averaged. There are no experimental data on measuring gases thermal conductivity in nanochannels. However, it is clear from physical considerations that the coefficient of gas thermal conductivity along a sufficiently long channel should be consistent with its value in the bulk (unless the channel is too narrow). Therefore, SMM method verification in this case consists of two parts, the thermal conductivity coefficients of rarefied gases in the bulk and along nanochannel are calculated.

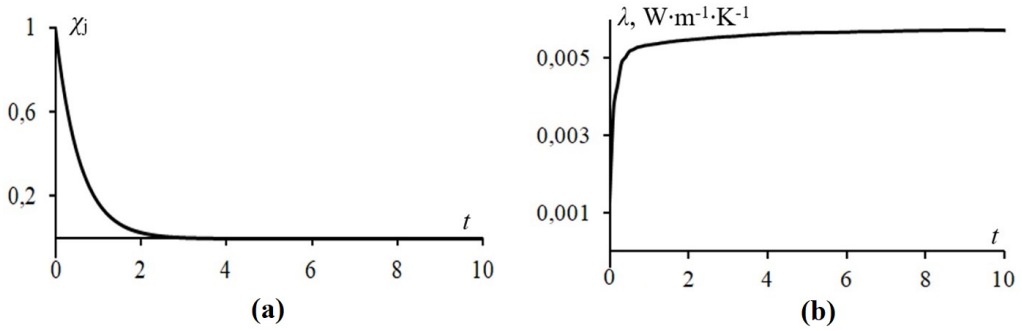

FIG. 1. Evolution of a) TCACF and b) thermal conductivity coefficient (1)

The calculation of the thermal conductivity of rarefied gases is still a rather complex problem in the kinetic theory of rarefied gases. If the first approximation of expansion in terms of Sonin polynomials is usually sufficient to calculate the diffusion and viscosity coefficients, then this is not the case for thermal conductivity. Therefore, direct numerical simulation of thermal conductivity is really relevant. Previously, such modeling was not performed by SMM method. This has been done for the first time below. Both monatomic (Ar, Kr, Ne, Xe) and polyatomic gases (CH_4, O_2) were considered. The thermal conductivity coefficient was calculated using FDT (1), but the velocity of the gas mass' center should be set equal to zero, calculating the correlation function (see formula (2)). Since gas is rarefied, TCACF χ should decay exponentially, which is shown by the calculation data presented in Fig. 1a. Here the calculation of the xenon TCACF is presented, the time is normalized to the mean free path time of the molecule. Indeed, over the time order of several free path times of molecules, TCACF relaxes. Exponential damping of the correlation function means a rather fast reaching of the plateau value of the corresponding transport coefficient, i.e., the thermal conductivity coefficient. Figure 1b illustrates this evolution.

Systematic data obtained for all the above gases are given in Table 1. All calculations were performed at atmospheric pressure and a temperature of 300 K. 3200 molecules were used, averaging was carried out over 1000 independent phase trajectories. The calculation data turn out to be quite comparable with the experimental ones. For argon, krypton, and xenon, they were obtained within the measurement accuracy (Δ is relative error), which is usually 2–3%. For the three remaining gases, the accuracy is slightly worse.

The accuracy of any molecular modeling, including SMM method, depends on several factors. First of all, it depends on the choice of the molecular interaction potential used. Strictly speaking, it is impossible to formulate universal recipes for their choice. Everything depends on the problem being solved. Situation is somewhat simplified, calculating the integral characteristics of fluids. Here we can choose rather simple potentials. However, success is largely determined by the choice of potential parameters. This should be treated very carefully. For example, it is difficult to expect high

accuracy of viscosity modeling, determining the parameters of the potential from diffusion data. Nevertheless, it can be stated that SMM method is quite conservative with respect to such a choice. High accuracy can be obtained even using the known parameters of Lennard-Jones potential, which are obtained from a variety of experimental data.

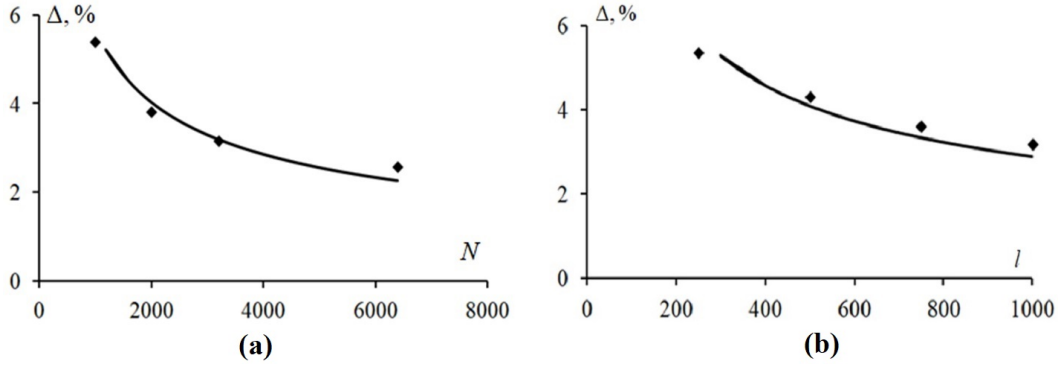

FIG. 2. Dependence of the relative error Δ for calculating the thermal conductivity coefficient of xenon on a) the number of molecules used and b) the number of trajectories

The calculation accuracy is affected both by the number of molecules used and by the number of independent trajectories over which the averaging is carried out. In this paper, the influence of both these factors is systematically studied. As an example, Figure 2a shows the dependence of the calculated values of xenon thermal conductivity on the number of molecules. 750, 1500, 3000 and 6400 molecules were used in the calculations; the calculated data in Fig. 2 correspond to the rhombuses. The calculation error Δ with an increase in the number of molecules systematically decreases and is well (the correlation coefficient is 0.97) described by the dependence: $\Delta = 175.17/\sqrt{N}$, which corresponds to a continuous curve in Fig. 2a. High accuracy in calculating the thermal conductivity coefficient can also be obtained for polyatomic molecules. For example, when 6400 molecules are used in calculations, the error in determining the thermal conductivity coefficient of oxygen is 0.93%, and that of methane is 0.67% (averaging was carried out over 1000 phase trajectories).

The second important circumstance that determines the accuracy and time of the calculation is the number of ensemble members (the number of independent phase trajectories) over which the obtained data are averaged. The ensemble, over which the averaging is carried out, is a typical Gibbs ensemble characterized by different initial phase states of molecules for given average values of macroscopic observables. The accuracy of modeling the thermal conductivity coefficient also increases with an increase in the number of ensemble members. Figure 2b shows the dependence of the relative error obtained, calculating xenon thermal conductivity. Here, the number of molecules used was 3000, and the number of trajectories varied from 250 to 1000 (the rhombuses). Together with an increase in the number of phase trajectories, the relative errors decrease monotonically and are well described by the dependence: $\Delta_1 = 91.29/\sqrt{L}$ (the correlation coefficient is 0.98). It is necessary to use about 8000 trajectories to obtain accuracy of the order of a percent, using 3000 molecules.

4. Thermal Conductivity of Gas in Nanochannels

In present paper, the thermal conductivity of argon, krypton, xenon, oxygen, and methane in nanochannels with a square cross section is studied, the channel height is varied from 8.5 to 1000 nm. The thermal conductivity coefficient was calculated using FDT (1). As it is already mentioned, there is a significant movement of the center of mass in the gas. In fact, some specific two-phase medium takes place. In order to calculate true gas thermal conductivity, the contribution due to the fluctuation motion of the mass center of gas should be excluded. In what follows, the contribution associated with energy transfer due to fluctuations in the velocity of the mass center of gas will be called the fluctuation contribution. The calculations were performed at a pressure from one to ten atmospheres and a temperature of 300 K.

First of all, it should be noted that with both the specular and diffuse laws of interaction of gas molecules with the walls, a significant anisotropy of thermal conductivity is recorded along and across the channel, the thermal conductivity across the channel is extremely low. As an example, Fig. 3a shows the dependence of the thermal conductivity coefficient along the channel with a fluctuation contribution (square marks) and without it (round marks) at atmospheric pressure in a channel with specular walls. The dotted line corresponds to the value of the thermal conductivity coefficient in the bulk. It should be noted that in the nanochannels presented here, the coefficient of longitudinal thermal conductivity (along the channel) is higher than in the bulk, although this excess is small. As the channel height increases, thermal conductivity along it tends to the thermal conductivity in the bulk. The coefficient of thermal conductivity in the bulk under these conditions is equal [42] to 0.01767 $\mathrm{Wm^{-1}K^{-1}}$. The difference in the thermal conductivity coefficient without fluctuation contribution along the channel at its height equal to 35 nm from the corresponding value in the bulk is already less than 1%. Thus, SMM method quite adequately predicts its value. It should be highlighted, however, that the accuracy of

modeling the thermal conductivity along a channel also depends on its length, despite the fact that periodic boundary conditions are used along it. In this case, this length is 100 nm.

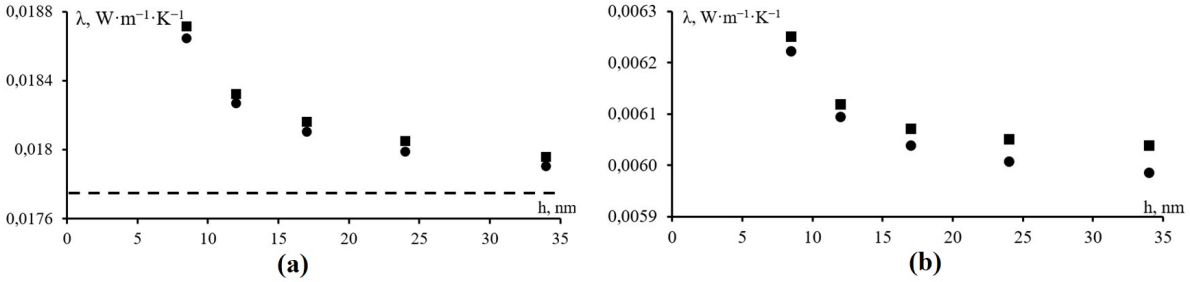

FIG. 3. Dependence of a) longitudinal and b) total thermal conductivity taking into account fluctuation contribution (square marks) and without it (round marks) on the channel height

The anisotropy of the thermal conductivity in a nanochannel is very large. The thermal conductivity coefficient across the channel (there are two such directions) in this case turns out to be three orders of magnitude smaller than the value fixed in the bulk. As a result, the total thermal conductivity coefficient is almost three times less than in volume. This is illustrated in Fig. 3b, which shows the dependence of the total thermal conductivity coefficient on the height of nanochannel. Here again, round marks correspond to the total thermal conductivity without a fluctuation contribution, and square marks correspond to a fluctuation one.

Two circumstances should be noted. First, the coefficient of thermal conductivity in the channels of minimum cross section is only a third of the corresponding value in the bulk, and then increases. However, the total thermal conductivity is almost two and a half times less than in the bulk even in a channel with a height of 35 nm. This means that although anisotropy weakens with increasing channel size, thermal conductivity across the channel is still quite low. The anisotropy is also preserved in sufficiently large channels. As a consequence, the total thermal conductivity in a nanochannel 500 nm high is slightly more than half of the value in the bulk (see Fig. 4). However, even in a channel with a height of 1 μm, thermal conductivity in the channel is approximately 40% lower than in the bulk (see Fig. 4).

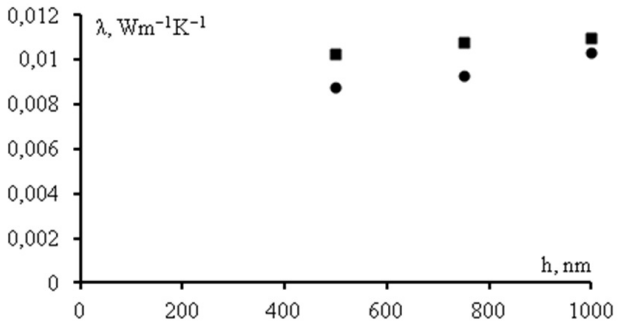

FIG. 4. Dependence of the total thermal conductivity with fluctuation contribution (square marks) and without it (round marks) at 300 K and atmospheric pressure from the channel height

The second aspect to note is the fluctuation component contribution, which somewhat increases with increasing channel cross section, although this contribution barely exceeds 1% in a channel with a height of $h = 35$ nm. Then it reaches maximum; at $h = 500$ nm, it is almost 17% here, but decreases with a further increase in the channel cross section: at $h = 750$ nm, it decreases to 15.7%, and at $h = 1$ μm, to 5.9%. It should also be kept in mind that the fluctuation contribution is especially large to the thermal conductivity across the channel. This contribution is especially noticeable in channels with a small cross section. For example, in a channel with a height of 35 nm, it is 183.4%. On the other hand, in a channel with a height of 1 μm, this contribution decreases to 13.5%.

So far, we have been talking about channels with specular walls. The character of the molecules interactions with walls significantly affects thermal conductivity, although the main qualitative characteristics remain unchanged. The dependence of the total thermal conductivity with fluctuation contribution λ_t and without it λ in a channel with diffuse walls on the channel height is presented in Table 2. Here again, gas temperature is 300 K. The last line shows relative difference between these two values of thermal conductivity. Thermal conductivity in a channel with diffuse walls is less than in the bulk and increases monotonically with increasing channel height. This applies to both longitudinal and transverse components. However, it remains 3 times less than in the bulk even in a channel with a height of 1000 nm. Such a low value of the thermal conductivity coefficient even in a channel with a height of 1 micron is associated with significant anisotropy of thermal conductivity. The thermal conductivity coefficient across the channel increases with

TABLE 2. Dependence of the total thermal conductivity with fluctuation contribution λt and without it λ in a channel with diffuse walls on the channel height

h, nm	8.5	17	34	500	750	1000
λ_t, W·m^{-1}·K^{-1}	$9.22{\cdot}10^{-5}$	$2.54{\cdot}10^{-4}$	$7.56{\cdot}10^{-4}$	0.00278	0.00328	0.00517
λ, W·m^{-1}·K^{-1}	$7.97{\cdot}10^{-5}$	$2.32{\cdot}10^{-4}$	$7.16{\cdot}10^{-4}$	0.00274	0.00324	0.00511
Δ, %	15.68	9.58	5.68	1.38	1.35	1.10

TABLE 3. The thermal conductivity coefficient with fluctuation contribution λ_t and without it λ in a channel with specular walls 500 nm high at a pressure of 10 atm

	λ_t, W·m^{-1}·K^{-1}	λ, W·m^{-1}·K^{-1}	Δ, %
OX	0.0146	0.0139	5
OY	0.0182	0.0181	0.5
OZ	0.0146	0.0139	5
λ_a, W·m^{-1}·K^{-1}	0.0158	0.0153	3

increasing channel height. If the transverse coefficient was 800 times less than in the bulk at a channel height of 8.5 nm, then it is only 8 times less than in the bulk at a channel height of 1000 nm.

It is important to emphasize that, thermal conductivity along the channel is close to thermal conductivity in the bulk (even somewhat exceeds it in channels of low height) under the specular law of interaction. On the contrary, in channels with a diffuse law of molecule interaction with walls in small channels, the longitudinal coefficient of thermal conductivity is always lower than in volume. In a channel with a height of 8.5 nm, it is less than in the bulk by about 80 times, and in a channel with a height of 1 μm, by 1.5 times.

In conclusion, we present the data of modeling the thermal conductivity coefficient by the SMM method at a temperature of 300 K and a pressure of 10 atm. A channel with specular walls 500 nm high was considered. This corresponds to Knudsen number Kn = 0.014. The thermal conductivity coefficient in the bulk in this case is [42] 0.01809. Simulation data are given in Table 3. Here, the longitudinal coefficient of thermal conductivity corresponds to OY axis, the other two are transverse. The bottom line shows the total coefficient of thermal conductivity, which is, in fact, the average in all three directions. In the last column, one can see the relative difference between thermal conductivity with and without the fluctuation contribution. The analysis of the table shows that the anisotropy of thermal conductivity is also preserved here, although it is significantly lower than at atmospheric pressure. The total thermal conductivity is only 3% lower than in bulk. In this case, the longitudinal coefficient of thermal conductivity practically coincides with the bulk value. Contribution of heat transfer caused by fluctuations in the velocity of the mass center of the system is almost absent in longitudinal direction and only 5% in transverse one.

5. Conclusion

In present paper, the thermal conductivity of rarefied gas in nanochannels has been studied. First, it is necessary to note its anisotropy. Previously, such anisotropy has already been observed in nanochannels with liquid [6–10]. In the case of rarefied gas, this anisotropy is much higher. As it is shown above, the thermal conductivity coefficients along and across the channel can differ by three orders of magnitude. As the channel height increases, the degree of anisotropy decreases, but it turns out to be significant even in microchannels. On the other hand, the rarefied gas thermal conductivity along the channel is consistent with the corresponding values in the bulk (if the channel is long enough). Finally, it should be noted that with an increase in gas density (pressure), the degree of anisotropy of thermal conductivity decreases.

The total (average) thermal conductivity value of a fluid in a nanochannel depends significantly on the interaction of its molecules with the channel walls. In fact, the thermal conductivity coefficient is not a gas property only, but of gas+channel wall system. For this reason, it is possible to change the effective coefficient of thermal conductivity by varying the walls' material, and hence heat transfer in nano and microchannels.

There is another important aspect. Fluid in nanochannels is some specific two-phase system. There is a fluctuation contribution to the thermal conductivity coefficient due to the presence of fluctuations in the velocity of the center of mass in equilibrium gas. It is clear that this contribution decreases with increasing channel height. This is confirmed by the performed calculations. However, this contribution still takes place even in microchannels. It should be understood that in real nanodevices, heat transfer will be determined by the total thermal conductivity coefficient, taking into account the fluctuation component. In this sense, fluctuation contribution in nanochannels is somewhat analogous to convective

heat conduction. Therefore, if there is a flow in the nanochannel, then along with the fluctuation component of thermal conductivity, there is also a convective one. Moreover, the convective component can be much larger than the fluctuation one.

References

[1] Li D. (Ed.) *Encyclopedia of Microfluidics and Nanofluidics*, Springer Science+Business Media, LLC, 2008, 2242 p.

[2] Mawatar K.I., Tsukahara T., Sugii Y., Kitamori T. Extended-nano fluidic systems for analytical and chemical technologies. *Nanoscale*, 2010, **2**(9), P. 1588–1595.

[3] Reisner W., Pedersen J.N., Austin R.H. DNA confinement in nanochannels: Physics and biological applications. *Reports Progress Phys.*, 2012, **75**, Article ID: 106601.

[4] David G.C., Paul V.B., Gang C., David R.C., Shanhui F., Kenneth E.G., Pawel K., William P.K., Gerald D.M., Arun M., Humphrey J.M., Simon R.P., Eric P., Li S. Nanoscale thermal transport. II. 2003–2012. *App. Phys. Rev.*, 2014, **1**, P. 011305.

[5] Rudyak V.Ya., Minakov A.V., *Modern Problems of Micro- and Nanofluidics*, Science, Novosibirsk, 2016, 260 p.

[6] Sofos F., Karakasidis T., Liakopoulos A. Transport properties of liquid argon in krypton nanochannels: Anisotropy and non-homogeneity introduced by the solid walls. *Int. J. Heat Mass Transfer*, 2009, **52**(3-4), P. 735–743.

[7] Hyzorek K., Tretiakov K.V. Thermal conductivity of liquid argon in nanochannels from molecular dynamics simulations. *J. Chem. Phys.*, 2016, **144**, P. 94507.

[8] Pourali M., Maghari A. Non-equilibrium molecular dynamics simulation of thermal conductivity and thermal diffusion of binary mixtures confined in a nanochannel. *J. Chem. Phys.*, 2014, **444**, P. 30–38.

[9] Zhao Z., Sun C., Zhou R. Thermal conductivity of confined-water in graphene nanochannels. *Int. J. Heat Mass Transfer*, 2020, **152**, P. 119502.

[10] Kima K., Murphy T.E. Strong anisotropic thermal conductivity of nanoporous silicon. *J. App. Phys.*, 2015, **118**, P. 154304.

[11] Rudyak V.Ya., Belkin A.A. Fluid viscosity under confined conditions. *Doklady Phys.*, 2014, **59**(12), P. 604–606.

[12] Rudyak V.Ya., Belkin A.A. Statistical mechanics of transport processes of fluids under confined conditions. *Nanosystems: Phys., Chem., Math.*, 2015, **6**(3), P. 366–377.

[13] Rudyak V.Ya., Belkin A.A. Molecular-dynamics simulation of fluid viscosity in nanochannels. *Nanosystems: Phys., Chem., Math.*, 2018, **9**(3), P. 349–355.

[14] Zhao Z., Sun C., Zhou R. Thermal conductivity of confined-water in graphene nanochannels International. *Int. J. Heat Mass Transfer*, 2020, **152**, P. 119502.

[15] Barisik M., Kim B., Beskok A. Smart wall model for molecular dynamics simulations of nanoscale gas flows. *Com. Comp. Phys.*, 2010, **7**(5), P. 977–993.

[16] Barisik M., Beskok A. Molecular dynamics simulations of shear-driven gas flows in nano-channels. *Microfluid Nanofluid*, 2011, **11**, P. 611–622.

[17] Barisik M., Beskok A. "Law of the nano-wall" in nano-channel gas flows. *Microfluidics Nanofluidics*, 2016, **20**, P. 46.

[18] Rabani R., Heidarinejad G., Harting J., Shirani E. Heat Conduction Characteristic of Rarefied Gas in Nanochannel. *J. App. Fluid Mech.*, 2020, **13**(1), P. 1-13.

[19] Frijns A.J.H., Nedea S.V., Markvoort A.J., van Steenhoven A.A., Hilbers P.A.J. Dynamics and Monte Carlo Simulations for Heat Transfer in Micro and Nano-channels. *ICCS*, 2004, **3039**, P. 661–666.

[20] Graur I., Sharipov F. Non-isothermal flow of rarefied gas through a long pipe with elliptic cross section. *Microfluid Nanofluid*, 2009, **6**, P. 267–275.

[21] Sharipov F. Gaseous mixtures in vacuum systems and microfluidics. *J. Vacuum Sci. Technology A*, 2013, **31**, P. 050806.

[22] Hwang G.S., Kaviany M.. Molecular dynamics simulation of effective thermal conductivity of vapor-filled nanogap and nanocavity. *J. App. Phys.*, 2009, **106**, P. 024317.

[23] Rudyak V.Ya., Lezhnev E.V.. Stochastic method for modeling rarefied gas transport coefficients. *J. Phys.: Conf. Series*, 2016, **738**, P. 012086.

[24] Rudyak V.Ya., Lezhnev E.V. Statistical simulation of the transport coefficients of the rarefied gases. *J. Phys.: Conf. Series*, 2018, **1105**, P. 012122.

[25] Rudyak V.Ya., Lezhnev E.V. Stochastic algorithm for simulating gas transport coefficients. *J. Comp. Physics*, 2018, **355**, P. 95–103.

[26] Rudyak V.Ya., Lezhnev E.V. Stochastic molecular modeling the transport coefficients of rarefied gas and gas nanosuspensions. *Nanosystems: Phys., Chem., Math.*, 2020, **46**, P. 51–54.

[27] Rudyak V.Ya., Lezhnev E.V. Viscosity of Gases in Nanochannels. *Tech. Phys. Lett.*, 2020, **46**(10), P. 1045–1048.

[28] Ferziger J., Kaper H. *Mathematical Theory of Transport Processes in gases*, Elsevier Science Publishing Co Inc., 1972, 579 p.

[29] Chapman S., Cowling T.G. *The Mathematical Theory of Non-uniform Gases*, Cambridge University Press, Cambridge, 1990, 423 p.

[30] Zubarev D.N., *Nonequilibrium Statistical Thermodynamics*, Consultants Bureau, N.Y., 1974, 489 p.

[31] Evans D.J., Morriss G.P. *Statistical Mechanics of Nonequilibrium Liquids*, Elsevier, 2013, 316 p.

[32] Allen M.P., Tildesley D.J. *Computer Simulation of Liquids, Oxford University Press*, Oxford, 2017. 640 p.

[33] Ernst M.H. Formal theory of transport coefficients to general order in the density. *Physica*, 1966, **32**(2), P. 209–243.

[34] Khon'kin A.D. Equations for space-time and time correlation functions and proof of the equivalence of results of the Chapman-Enskog and time correlation methods. *Theoretical Math. Phys.*, 1970, **5**, P. 1029–1037.

[35] Rudyak V.Ya., Belkin A.A., Ivanov D.A., Egorov V.V. The simulation of transport processes using the method of molecular dynamics. Self-diffusion coefficient. *High Temperature*, 2008, **46**(1), P. 30–39.

[36] Klimontovich Y.L. *Kinetic Theory of Nonideal Gases and Nonideal Plasmas*, Elsevier Ltd., 1982, 328 p.

[37] Rudyak V.Ya. *Statistical Theory of Dissipative Processes in Gases and Liquids*, Science, Novosibirsk, 1987, 269 p.

[38] Cercignani C. *Theory and Application of the Boltzmann Equation*, Scottish Academic Press, 1975, 415 p.

[39] Sone Y. *Molecular Gas Dynamics: Theory, Techniques, and Applications*, Birkhauser, 2007, 658 p.

[40] Rapaport D.C. *The Art of Molecular Dynamics Simulation*, Cambridge University Press, Cambridge, 1995, 549 p.

[41] Grigoriev I.S. et al. *Handbook of Physical Quantities*, CRC Press, 1997, 1548 p.

[42] Rabinovich V.A. *Thermophysical Properties of Neon, Argon, Krypton, and Xenon*, Hemisphere Publishing Corporation, 1988, 604 p.

Submitted 2 March 2023; accepted 16 March 2023

Information about the authors:

Valery Ya. Rudyak – Kutateladze Institute of Thermophysics of Siberian Branch of RAS, Lavrentiev Avenue, 1, 630090, Novosibirsk, Russia; Novosibirsk State University of Architecture and Civil Engineering, Leningradskaya Street, 113, 630008, Novosibirsk, Russia; ORCID 0000-0003-1335-4548; valery.rudyak@mail.ru

Evgeny V. Lezhnev – Novosibirsk State University of Architecture and Civil Engineering, Leningradskaya Street, 113, 630008, Novosibirsk, Russia; ORCID 0000-0003-3347-0781; lionlev@yandex.ru

Conflict of interest: the authors declare no conflict of interest.

NANOSYSTEMS:
PHYSICS, CHEMISTRY, MATHEMATICS

Diskaeva E.I., Vecher O.V., et al. *Nanosystems: Phys. Chem. Math.*, 2023, **14** (2), 195–201.
http://nanojournal.ifmo.ru
DOI 10.17586/2220-8054-2023-14-2-195-201

Original article

Experimental investigation of rheological properties of niosomal dispersions

Elena I. Diskaeva[1], Olga V. Vecher[1], Elena N. Diskaeva[2], Igor A. Bazikov[3], Karine S. Elbekyan[4]

[1]Department of Physics and Mathematics, Stavropol State Medical University, Stavropol, Russia

[2]Branch of the Federal State Budget Educational Institution of Higher Education "MIREA – Russian Technological University", Stavropol, Russia

[3]Department of Microbiology, Stavropol State Medical University, Stavropol, Russia

[4]Department of General and Biological Chemistry, Stavropol State Medical University, Stavropol, Russia

Corresponding author: Olga V. Vecher, vecher.olga@mail.ru

PACS 61.46.-w, 65.80.+n, 87.16.Dg

ABSTRACT In this work, the rheological properties of niosomal dispersions of various concentrations in the temperature range of 30 – 60 °C is investigated. The viscosity coefficient and the values of the activation energy were determined experimentally. It is found that the flow of niosomal dispersions exhibits the properties of Newtonian fluids in the studied range of temperatures and shear rates. Conditions were determined for obtaining stable homogeneous niosomal dispersions with an average vesicle size of 80 – 150 nm.

KEYWORDS nonionic surfactant vesicles, rheological properties, niosomal dispersion

ACKNOWLEDGEMENTS

FOR CITATION Diskaeva E.I., Vecher O.V., Diskaeva E.N., Bazikov I.A., Elbekyan K.S. Experimental investigation of rheological properties of niosomal dispersions. *Nanosystems: Phys. Chem. Math.*, 2023, **14** (2), 195–201.

1. Introduction

The creation of new pharmaceuticals using nanotechnology seems to be an urgent task. The direction of scientific research in this area is determined by the needs for modern medicine in highly active and safe pharmaceutical preparations.

Vesicular systems have attracted great attention in drug delivery because of their amphiphilic nature, biodegradability, non-toxicity, an increase in the duration of exposure and potential for increasing drug bioavailability. Furthermore, their structure can be manipulated in terms of shape, size, and rheological properties, in order to enhance their performance [1–4].

Modified release dosage forms are a group of drugs characterized by an altered release mechanism and pattern. Such dosage forms really affect the pharmacokinetics of drugs, leading to changes in the parameters of efficacy and tolerability in accordance with clinical needs [5–7]. Drug delivery systems using colloidal particulate carrier such as niosomes, ethosomes or liposomes have distinct advantages over conventional dosage forms.

Niosomes are thought to be better candidate's drug delivery system due to the various factor like cost, stability and less toxic. In contemporary times, niosomes have been extensively studied for their potential to serve as carrier for delivery of drugs, hormone, antigen and other bioactive agents [8–14].

Niosomal vesicles can be used to deliver a wide range of drugs due to the ability to retain hydro- lipo- and amphiphilic substances [15–17]. Further advantages provided by vesicular carriers include protection of the active agents against enzymatic and chemical degradation, and possibility minimization of side effects.

Investigation of the rheological properties of niosomal dispersions is necessary in designing targeted drug delivery systems because it allows one to substantiate and optimize effective technologies for increasing their bioavailability, stability and biodistribution in the body [18–24].

As known, the relation of viscosity with the structure of colloidal systems was revealed long ago and was well described in a literature [25–28]. However, many of the proposed rheological equations for description of the dispersed systems indicate the absence of unified approach. There are some rheological equations that describe disperse systems of different physical and chemical nature, and, conversely, one disperse system can be described by fundamentally different rheological equations.

In general case, the rheological equation can be presented in the form:

$$\tau^m = \tau_0^m + \eta^n \upsilon^n, \tag{1}$$

where τ is the shear stress, τ_0 is the ultimate shear stress, η is the dynamic viscosity coefficient, m and n are exponents, υ is the shear rate. Such equations make it possible to achieve the most accurate calculations of the flow of the dispersed

systems. But they are not informative for fundamental research, since there are no parameters characterizing colloidal systems at the level of intermolecular interactions. Nowadays, the universal equation that allows one to study the viscosity of dispersed systems taking into account intermolecular interactions is the Eyring–Frenkel equation:

$$\eta = A \exp\left(E/RT\right), \tag{2}$$

where A is a constant which has units of viscosity, R is the universal gas constant, T is the temperature, E is the activation energy of a viscous flow, which characterizes intermolecular and interparticle interactions, as well as the microstructural ordering and the stability of the dispersed systems. It can be concluded that the rheological behavior of niosomal dispersions is determined not only by the temperature and the volume concentrations of the dispersed phase, but also by the stress and the shear rate at which the flow occurs.

This study is aimed to the main structural and mechanical (rheological) properties of niosomal dispersions based on PEG-12 Dimethicone and to identification of factors that affect the rheological stability during their storage.

2. Material and methods

Structural and mechanical properties were evaluated for the samples of niosomal dispersions by using of rotational viscometer Rheotest RN 4.1, ("RHEOTEST Messgerate Medingen Gmbh", Germany). To obtain the flow curves of the samples study, the cylindrical system was used, which made it possible to achieve greater accuracy in measuring the viscosity. The temperature system operates in the temperature range (-10 °C; $+180$ °C). It allows one to quickly set and control the temperature of the test sample with an accuracy higher than 0.1 °C.

The niosomes were prepared by an original technology [29]. Niosomes vesicles consisted of PEG-12 Dimethicone ("Dow Corning", USA), which possesses amphiphilic properties. Its allow the water-soluble part (polyethylene glycol) to orient itself into water, and the fat-soluble part (dimethicone) into lipids (Fig. 1).

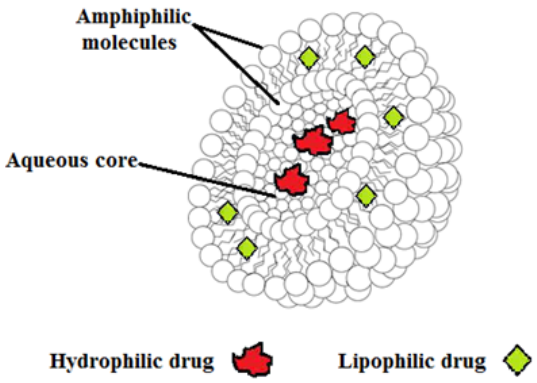

FIG. 1. Structure of a silicone-based niosome

In the hydrophilic part of dimethicone, there are functional groups of silicon oxide. The length of the Si–O bond is 1.6 Å, which is much longer than the C–C bond of 1.4 Å. The Si–O–Si bond angle is 130 degrees, in contrast to the 109 degrees of C–C–C bond. It leads to increase of the elasticity and the stability (Fig. 2). Due to this, the functional groups of the molecules are able to rotate with respect to each other. This gives one niosomes with greater elasticity than liposomes made up of phospholipids.

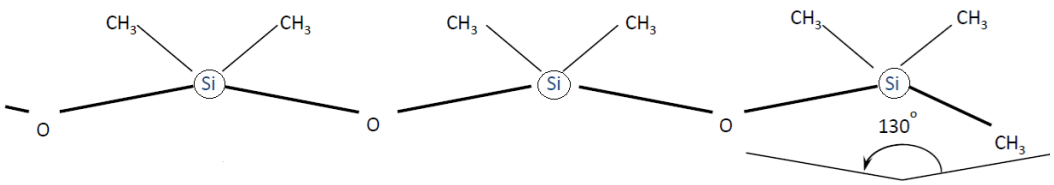

FIG. 2. Chemical structural PEG-12 Dimethicone

Using of PEG-12 Dimethicone led to the formation of vesicles without significant energy efforts. Stage of formation of vesicles occurred with intensive mechanical mixing using an automatic reclosure homogeniser. Dispersion was placed in a vessel for ultrasonic treatment. Ultrasonic sounding was carried out at frequency of 20 kHz, power of 200 W, the exposure time of 10 min. Monolamellar niosomes with 80 – 150 nm in size were formed. Then samples were diluted

with ultrapure water to the required concentrations. All the reagents and chemical used in present study were of the highest purity available and were used as received. For a degree estimation heterogeneous niosomal dispersions used the microphotos received by means of scanning electronic microscopy (Tescan Mira 3 Im). The particle size, determined by Image J, MS Excel statistical package program, was used to perform the analysis [30, 31].

3. Results and discussion

Niosomal dispersions with volumetric concentrations of 1, 5 or 10 % were selected for the research. It is clear that the rheological features of the behavior of niosomal dispersions with a change in temperature may indicate a change in indicators of both sedimentation and aggregative stability. Dependences of the viscosity on the temperature of niosomal vesicles of various concentrations were studied (Fig. 3). The viscosity at different temperatures was determined by changing the shear stress in the direction of increasing the shear rate.

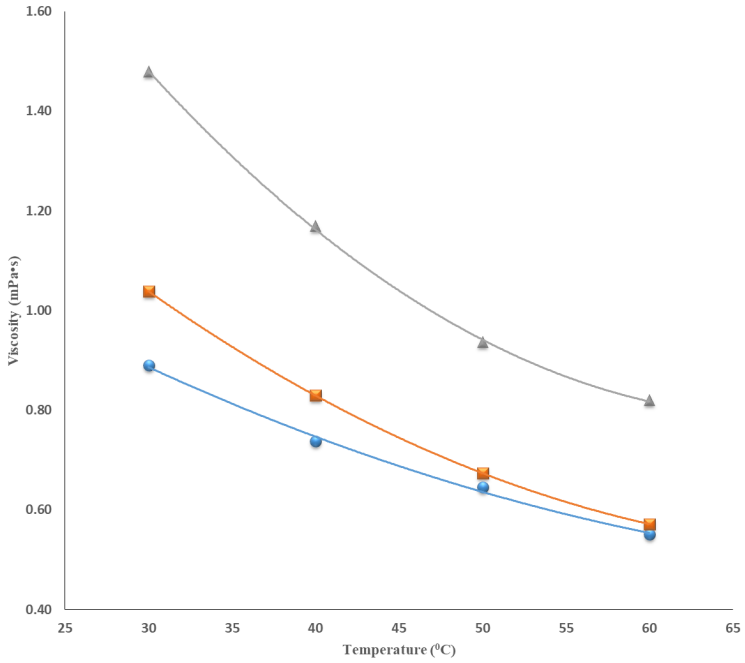

FIG. 3. Change in viscosity with rise in temperature for 1 % (circles), 5 % (squares) and 10 % (triangles) concentration

These curves illustrate a typical decrease in viscosity with increasing temperature for various concentrations, but with different degrees of intensity. This can be explained by a decrease in the forces of interaction between the niosomes vesicles with increasing temperature. As the volume concentration increases, a more pronounced dependence of the viscosity on temperature was observed. It can be assumed that further increase concentration of the dispersed phase will lead to the interaction of its particles, similar to the association of molecules and ions in true solutions up to the onset of coagulation.

To characterize the intensity of intervesicular interaction, it is necessary to estimate the value of the activation energy. In this connection, for the investigation of the behavior of niosomal dispersions of various concentrations, graphical dependences of the effective viscosity on the absolute temperature were plotted in coordinates $\ln \eta - 1/T$ (Fig. 4).

The energy of activation of the viscous flow was calculated based on the Arrhenius law. It can be presented of the form:

$$\Delta E = R \cdot \frac{d\left(\ln \eta\right)}{d\left(1/T\right)}, \tag{3}$$

where T is temperature, K; $R = 8.3144$, J/(mole·K) is the universal gas constant; E is the energy of activation of the viscous flow (J/mole) required for the transition of particle (flow unit) from one equilibrium position to another.

A typical electron micrograph of niosomes vesicles with an average size of 100 nm is shown in Fig. 5. The microphotograph shows that niosomes, for the most part, are spherical particles. Niosomal dispersion is heterogenous in volume [26, 27], but may be considered as a system consisting of separate particles each of which can move on free volume not occupied by other vesicles, but influencing it. In this case, we can consider the niosomal dispersion like a pseudohomogeneous system.

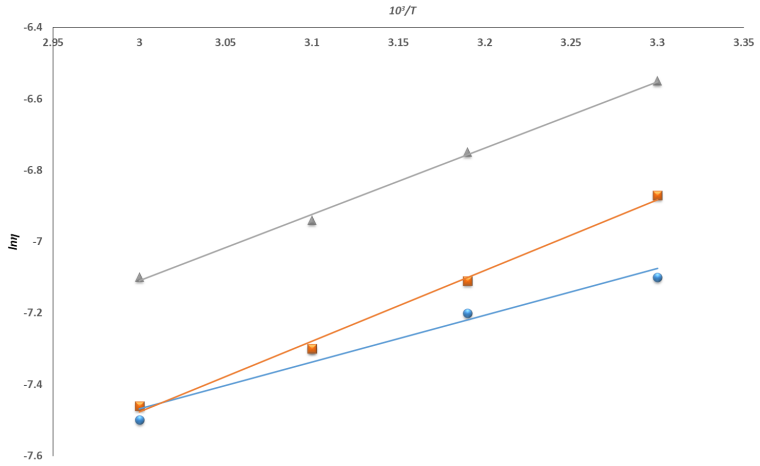

FIG. 4. Dependences of the logarithm of viscosity of niosomal dispersion on the inverse absolute temperature for different concentration: 1 % (circles), 5 % (squares) and 10 % (triangles)

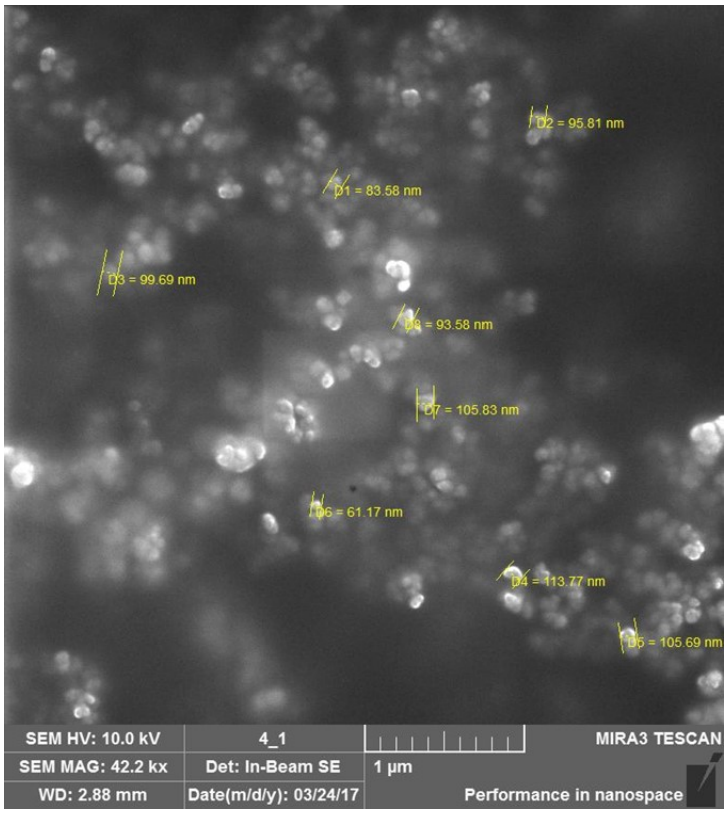

FIG. 5. Micrograph of niosomes obtained by Scanning Electron Microscopy (SEM)

The obtained dependencies are linear. In this case, the activation energy of the viscous flow of niosomal dispersions can be calculated from the slope of the plot of the logarithm of viscosity against the reciprocal temperature:

$$a = \tan\alpha = \frac{\left(\ln\eta^0\right)_1 - \left(\ln\eta^0\right)_2}{\left(\frac{10^3}{T}\right)_1 - \left(\frac{10^3}{T}\right)_2}. \tag{4}$$

Increase in the energy of activation of the viscous flow of niosomal dispersions in the concentration range of 1 – 10 % (Table 1) may indicate a decrease in the adsorption interaction and the transition of the system to a more structured (ordered) state. The obtained values of the energy of activation of the viscous flow can be used as a comparative characteristic of their stability during the long-term storage: the higher this indicator, the higher the stability.

To investigate the rheological behavior of niosomal dispersions in terms of stress and shear rate, the flow curves were studied (Fig. 6(a, b, c)).

TABLE 1. The energy of activation of the viscous flow of the niosomal dispersions for various volumetric concentrations

No.	φ, %	a	$E, kJ/(\text{mole} \cdot K)$
1	1.0	1.33	11.05
2	5.0	1.97	16.37
3	10.0	2.00	16.62

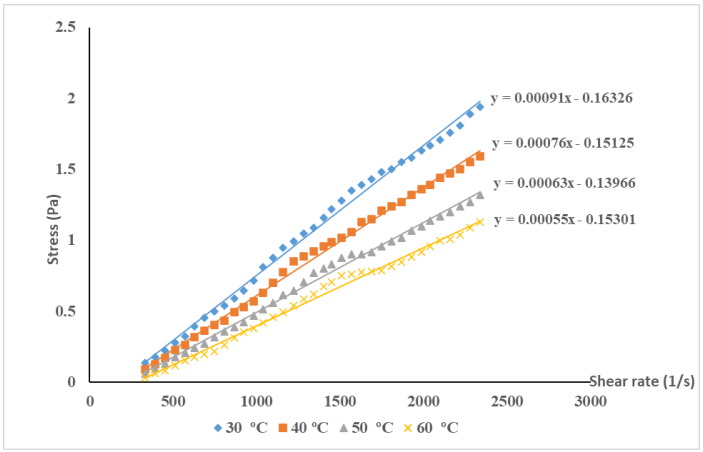

(a)

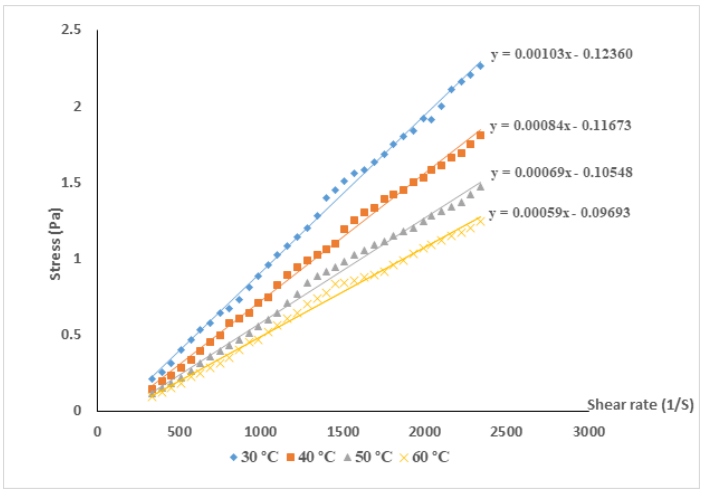

(b)

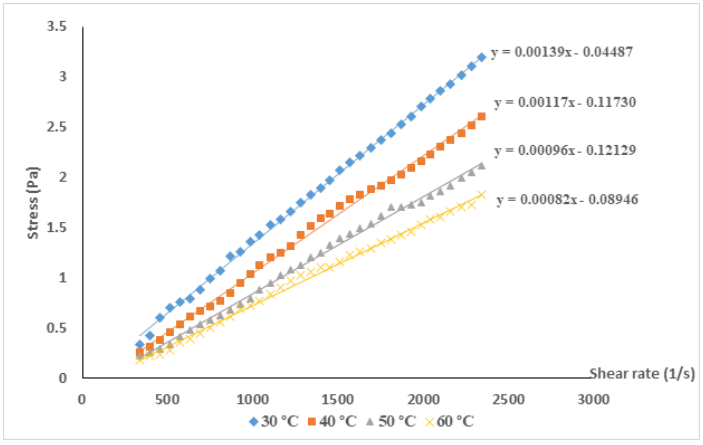

(c)

FIG. 6. Flow curves of the niosomal dispersions for different values of volumetric concentration: $\varphi = 1$ % (a), $\varphi = 5$ % (b), $\varphi = 10$ % (c)

As can be seen from the graphs, in the studied range of temperatures and shear rates, niosomal dispersions exhibit the properties of Newtonian fluids. It means that we can assume that in the studied colloidal system, there are no large aggregates of particles. The existing aggregates are smaller than the critical size in the given interval of velocities and they are not destroyed in the shear flow. Furthermore, with an increase in the shear rate, the viscosity does not change, which also indicates the constancy of the size of niosomal vesicles. However, the process of formation of some aggregates during interaction of individual vesicles and their subsequent rapid destruction cannot be excluding.

In order to study the stability of niosomal dispersions during their storage, experiments were repeated after 72 hours and the values of viscosity were determined at the same shear rates. Results obtained showed the absence of significant changes in the rheological parameters of the niosomal dispersions of the considered concentrations.

4. Conclusions

The use of niosomes based on PEG-12 Dimethicone as a targeted Drug Delivery System is expected to increase in foreseeable future. Silicon-based niosomes are promising drug carriers for the future with greater physical and chemical stability. Study of the rheological properties of niosomal dispersions based on PEG-12 Dimethicone and the ability to control the processes occurring in them are important for achieving optimal conditions for the development and storage of these nanocontainers.

The primary conclusions of this investigation are as follows:

(1) The niosomal dispersion of various concentrations shows a waiting decrease in viscosity with increasing temperature. This dependence was more significant if the volume concentration increases.
(2) The increases of the energy of activation of the viscous flow of niosomal dispersions with the growth of concentration indicates the pass into a more structured state.
(3) The flow of niosomal dispersions in the investigated temperature range obeys Newton's law.
(4) There are no significant changes in the rheological parameters of the niosomal dispersions with time in range up to 72 hours.

The results can give a better understanding of the mechanism of viscous flow of the niosomal dispersions.

References

[1] Pal'cev M.A. Nanotechnologies in medicine and pharmacology. *Remedium*, 2008, **9**, P. 6–11.
[2] Cho H.J., Yoon I.S., Yoon H.Y., et al. Polyethylene glycolconjugated hyaluronic acid-ceramide self-assembled nanoparticles for targeted delivery of doxorubicin. *Biomaterials*, 2012, **33**, P. 1190–1200.
[3] Dutta R.C. Drug carriers in pharmaceutical design: promises and progress. *Current Pharmaceutical Design*, 2007, **13** (7), 761.
[4] Martins S., Sarmento B., Ferreira D.C., Souto E.B. Lipid-based colloidal carriers for peptide and protein delivery—liposomes versus lipid nanoparticles. *Int. J. of Nanomedicine*, 2007, **2** (4), P. 595–607.
[5] Md. Sanower Hossain, Farahidah Mohamed,Mohd Affendi Mohd Shafri. Poly (trimethylene carbonate-co-caprolactone): An emerging drug delivery nanosystem in pharmaceutics. *Biomaterials and Biomechanics in Bioengineering*, 2020, **5** (1), P. 65–86.
[6] Naggar V.F., Elgamal S.S., Allam A.N. Proniosomes as a Stable Carrier for Oral Acyclovir: Formulation and Physicochemical Characterization. *J. of American Science*, 2012, **8** (9), P. 417–428.
[7] Dharashive V.M., Yelam K.V.N., Devine S.S. Niosomes: as a targeted drug delivery system. *Int. J. of Research in Pharmacy and Chemistry,* 2015, **5** (4), P. 582–589.
[8] Lombardo D., Kiselev M.A., Caccamo M.T. Smart nanoparticles for drug delivery application: development of versatile nanocarrier platforms in biotechnology and nanomedicine. *J. of Nanomaterials*, 2019, P. 1–26.
[9] Rajera R., Nagpal K., Singh S.K., Mishra D.N. Niosomes: a controlled and novel drug delivery system. *Biological and Pharmaceutical Bulletin,* 2011, **34** (7), P. 945–953.
[10] Pardakhty A., Moazeni E. Nano-niosomes in drug, vaccine and gene delivery: a rapid overview. *Nanomedicine J.*, 2013, **1** (1), P. 1–12.
[11] Madni A., Sarfraz M., Rehman M., Ahmad M., Akhtar N., Ahmad S., Tahir N., Ijaz S., Al-Kassas R., Löbenberg R. Liposomal drug delivery: a versatile platform for challenging clinical applications. *J. of Pharmacy and Pharmaceutical Sciences*, 2014, **17** (3), P. 401–426.
[12] Fofaria N.M., Quattal H.S.S., Liu X., Srivastava S.K. Nanoemulsion formulations for anti-cancer agent piplartine – characterization, toxicological, pharmacokinetics and efficacy studies. *Int. J. of Pharmaceutics*, 2016, **98**(1-2), P. 12–22.
[13] Kaur K., Jain S., Sapra B., Tiwary A.K. Niosomal gel for site-specific sustained delivery of anti-arthritic drug: in vitro-in vivo evaluation. *Current Drug Delivery*, 2007, **4** (4), P. 276–282.
[14] Sattuwar P.M., Khandare J.N., Nahde V.S. Niosomal delivery of Ketonozole. *Indian Drugs,* 2001, **38** (12), P. 620–623.
[15] Popova E.V., Beltyukov P.P., Radilov A.S. Modern trends in the development and production of nanoscale systems for the delivery of medicinal compounds. *Scientific and technical bulletin of information technologies, mechanics and optics*, 2020, **20** (2), P. 206–222.
[16] Yoshioka T., Sternberg B., Florence A.T. Preparation and properties of vesicles (niosomes) of sorbitan monoester (Span 20, 40, 60 and 80) and sorbitan trimester (Span 85). *Int. J. of Pharmaceutics*, 1994, **105** (1), P. 1–6.
[17] Ghafelehbashi R., Akbarzadeh I., Tavakkoli Yaraki M., Lajevardi A., Fatemizadeh M., Heidarpoor Saremi L. Preparation, physicochemical properties, in vitro evaluation and release behavior of cephalexin-loaded niosomes. *Int. J. of Pharmaceutics,* 2019, **569**, 118580.
[18] Anupriya Kapoor. An overview on niosomes. A novel vesicular approach for ophthalmic drug delivery. *Pharma Tutor*, 2016, **4** (2), P. 28–33.
[19] Vecher O.V., Diskaeva E.I., Bazikov I.A., Elbekyan K.S., Diskaeva E.N. Study of some rheological properties of niosomal dispersions based on PEG-12 dimethicone. *Advances in Natural Nanoscience and Nanotechnology*, 2020, **11** (4).
[20] Diskaeva E.I., Vecher O.V., Bazikov I.A., Elbekyan K.S., Diskaeva E.N. Dependence of the viscosity coefficient of the niosomal dispersion on the temperature and particle size of the dispersed phase. *Acta Polynechnica*, 2021, **61** (2), P. 336–341.
[21] Vasir J.K., Reddy M.K., Labhasetwar V.D. Nanosystems in drug targeting: opportunities and challenges. *Current Nanoscience*, 2005, **1** (1), P. 47–64.

[22] Paolino D., Muzzalupo R., Ricciardi A., Celia C., Picci N., Fresta M. In vitro and in vivo evaluation of Bola-surfactant containing niosomes for transdermal delivery. *Biomedical Microdevices*, 2007, **9** (4), P. 421–433.
[23] Godic A. New approaches to psoriasis treatment. A review. *Acta Dermatovenerologia* 2004, **13** (2), P. 50–57.
[24] Kazi Masud Karim, Asim Sattwa Mandal, Nikhil Biswas, Arijit Guha, Sugata Chatterjee, Mamata Behera. Niosome: A future of targeted drug delivery systems. *J. of Advanced Pharmaceutical Technology & Research*, 2011, **1** (4), P. 374–380.
[25] Bibik E.E. *Rheology of Dispersed Systems*. LGU, Leningrad, 1981, 171 p.
[26] Matveenko V.N., Kirsanov E.A. Viscosity and structure of dispersed systems. *Moscow University Chemistry Bulletin*, 2011, **66**, P. 199–201.
[27] Malkin A.Y., Isayev A.I. *Rheology: concepts, methods, and applications,* Elsevier Science, 2017, 500 p.
[28] Jhili Mishra, Jitendriya Swain , Ashok Kumar Mishra. Probing the temperature-dependent changes of the interfacial hydration and viscosity of Tween 20: cholesterol (1:1) niosome membrane using fisetin as a fluorescent molecular probe. *Physical Chemistry Chemical Physics*, 2018, **20**, P. 13279–13289.
[29] Bazikov I.A., Omelyanchuk P.A. The method of delivery of biologically active substances with the help of niosomes RF patent 2320323, 2008.
[30] Diskaeva E.I., Vecher O.V., Bazikov I.A., Vakalov D.S. Particle size analysis of niosomes as a function of temperature. *Nanosystems: Phys. Chem. Math.* 2018, **9** (2), P. 290–294.
[31] Diskaeva E.I., Vecher O.V., Bazikov I.A., Maltsev A.N. Dispersion analysis of niosomes different composition. *J. of Nanoparticle Research,* 2019, **21** (1), P. 21–23.

Submitted 14 March 2023; revised 29 March 2023; accepted 31 March 2023

Information about the authors:

Elena Igorevna Diskaeva – Department of Physics and Mathematics, Stavropol State Medical University, Mira, 310, Stavropol, 355017, Russia; ORCID 0000-0002-6095-7010; e_diskaeva@mail.ru

Olga Vladimirovna Vecher – Department of Physics and Mathematics, Stavropol State Medical University, Mira, 310, Stavropol, 355017, Russia; ORCID 0000-0002-6743-874X; vecher.olga@mail.ru

Elena Nikolaevna Diskaeva – Branch of the Federal State Budget Educational Institution of Higher Education "MIREA – Russian Technological University" in Stavropol, 355035, Stavropol, Kulakov Avenue, 8, Russia; ORCID 0000-0002-5185-6023; diskaevapes@mail.ru

Igor Alexandrovich Bazikov – Department of Microbiology, Stavropol State Medical University, Mira, 310, Stavropol, 355017, Russia; ORCID 0000-0001-9207-6552; bazikov@list.ru

Karine Sergeevna Elbekyan – Department of General and Biological Chemistry, Stavropol State Medical University, Mira, 310, Stavropol, 355017, Russia; ORCID 0000-0003-2403-8663; karinasgma@inbox.ru

Conflict of interest: the authors declare no conflict of interest.

NANOSYSTEMS:
PHYSICS, CHEMISTRY, MATHEMATICS

Glebova N.V., et al. *Nanosystems: Phys. Chem. Math.*, 2023, **14** (2), 202–207.
http://nanojournal.ifmo.ru
DOI 10.17586/2220-8054-2023-14-2-202-207

Original article

Investigation of stability of composite Nafion/nanocarbon material

Nadezhda V. Glebova[1,a], Anton S. Mazur[2,b], Anna O. Krasnova[1,c], Ivan V. Pleshakov[1,d], Andrey A. Nechitailov[1,e]

[1]Ioffe Institute, St. Petersburg, Russia

[2]St. Petersburg State University, St. Petersburg, Russia

[a]glebova@mail.ioffe.ru, [b]a.mazur@spbu.ru, [c]krasnova@mail.ioffe.ru, [d]inanple@yandex.ru, [e]aan.shuv@mail.ioffe.ru

Corresponding author: Nadezhda V. Glebova, glebova@mail.ioffe.ru

PACS 61.46.+w; 82.33.Pt; 68.35.Dv

ABSTRACT The article presents the results of a study of inorganic-polymer nanocomposites Nafion/thermally expanded graphite and Nafion/carbon black by nuclear magnetic resonance and thermogravimetry. The structure of carbon materials was characterized by electron microscopy and adsorption structural analysis by low-temperature nitrogen adsorption. The presence of the interaction of Nafion polymer and carbon material at the interface between the components leading to thermal stabilization of the composites is shown, and the differences between thermally expanded graphite and carbon black due to their morphology during interaction with Nafion are discussed.

KEYWORDS composite stability, Nafion migration, graphene, carbon black, NMR, thermogravimetry.

ACKNOWLEDGEMENTS The work was supported by the grant from the Russian Science Foundation No. 22-23-20127, https://rscf.ru/project/en/22-23-20127/ and the grant from the St. Petersburg Science Foundation in accordance with the agreement of 14.04.2022 No. 28/2022.

FOR CITATION Glebova N.V., Mazur A.S., Krasnova A.O., Pleshakov I.V., Nechitailov A.A. Investigation of stability of composite Nafion/nanocarbon material. *Nanosystems: Phys. Chem. Math.*, 2023, **14** (2), 202–207.

1. Introduction

Inorganic-polymer composites have recently been increasingly used in various fields of technology. One such application is the use of nanocomposites containing the Nafion proton-conducting polymer and a carbon material (usually carbon black) with catalyst nanoparticles on the surface for electrochemical energy conversion devices such as fuel cells, electrolyzers, etc. This is a fairly wide range of products, including various low-temperature fuel cells and water electrolyzers [1]. The reduction in cost and increase in the competitiveness of such devices is largely due to the solution of the problem of their durability. The related new knowledge about degradation mechanisms should serve both as a theoretical and practical basis for further development of membrane electrode assemblies (MEA).

A significant number of works have been devoted to the study of degradation processes in the MEA. Note that, despite the fact that the historical depth of publications is estimated at an impressive period of more than 10 years, the service life of modern MEAs is still not long enough and is about 5000 hours with a voltage loss of about 10% of the original one. Aging is associated with common electrochemical processes, such as electrochemical and chemical oxidation of the carbon and metal components of the electrode, recrystallization of metals, ingrowth of metal dendrites into the proton-conducting membrane, violation of the integrity of the membrane due to chemical and electrochemical oxidation-reduction processes [2–9].

One of the reasons for the deterioration of the characteristics of a fuel cell with a proton-conducting membrane is the migration of Nafion in the electrode, as a result of which inhomogeneity appears and the resistance to proton transfer increases [10]. The creation of new methods for extending the service life of electrochemical devices based on MEA containing Nafion is an urgent task.

Another promising field of application of inorganic-polymer composites is the elaboration of anti-radar coatings. In addition to the requirements associated with their functional properties, some of them are related to the microstructure and also physical and operational characteristics. For example, review [11] notes that an ideal shielding material should demonstrate high attenuation over a wide frequency range, low density, good thermal stability, and low cost. An important feature is the presence of good characteristics in high temperature conditions, which result from aerodynamic heating. Various carbon-based structures, having these properties and, in particular, the ability to strongly absorb electromagnetic waves, have attracted much attention as possible coatings of this kind. The use of substances such as carbon black [12], carbon nanotubes [13], carbon fibers [14], biomass carbon [15], graphite [16], and graphene-like materials [17, 18] has been considered. A possible way to create anti-radar coatings is utilizing of conducting polymers as matrices for the

embedded carbon nanoobjects [19, 20]. For example, in [19], a single-layer absorber based on a phenol resin reinforced with a polyaniline/expanded graphite composite, synthesized by *in situ* polymerization of aniline in an acidic medium, was studied. It was shown that attenuation in such a medium increases in the microwave range.

A negative factor in the synthesis of inorganic-polymer composites degrading their absorbing characteristics is the agglomeration of nanoparticles of the embedded material, which not only violates microhomogeneity, but also reduces the surface area of the dispersed component.

Composites based on the proton-conducting polymer Nafion and nanostructured carbon materials are relatively poorly studied [20], but they seem perspective both in terms of providing a stable homogeneous microstructure (since Nafion has pronounced surface-active properties and stabilizes nanosized carbon structural elements, preventing their agglomeration) and also because of their anti-corrosion performance [21]. In addition, the intercalation of carbon materials into the composite enhances the thermal stability of Nafion [22].

Thus, inorganic-polymer composites have great potential for practical application in various fields, although there is a problem of their stability. Due to the combination of ionic conductivity, surface active properties, and the ability to inhibit corrosion, Nafion is of particular interest for use in composites with carbon materials. Carbon nanomaterials have different formation at the micro level, which determines many of their structure-dependent properties. So, graphene is often considered as a pseudo-two-dimensional material, while carbon black is a conventional three-dimensional material. Due to this, different influence of these materials on the characteristics of the composite is expected.

The goal of this work is to study the causes and features of the stabilizing effect in a composite containing a dispersed phase of carbon nanostructured materials of various morphologies: pseudo-two-dimensional low-layer graphene and three-dimensional carbon black in the Nafion polymer medium.

2. Materials and experimental technique

In the work, thermally expanded graphite (TEG) obtained by the technology described in [23] (NP Tomsk Atomic Center) and commercial carbon black of the Vulcan XC-72 type were used as a carbon filler. The polymer matrix was obtained from a solution of Nafion brand DE1021 (DuPont). For the thermogravimetric study of Nafion, an aqueous isopropanol solution was prepared - isopropanol (99.80%, special purity, EKOS-1 JSC) with a content of 2 wt. % Nafion; the solution was dried on glass under normal conditions to an air-dry state (relative humidity ∼40–50%), and then the dry residue was removed with a spatula.

Nafion/TEG and Nafion/Vulcan two-component composites were made by mixing precise weights of the components in isopropanol/watermixture, taken in 1:1 volume ratio, followed by mechanical stirring and ultrasonic homogenization. The ratio of solid and liquid phases in the dispersion was maintained within (1:40)–(1:80) depending on the content of the carbon component. The higher the content of the latter, the more the liquid phase was added to ensure complete wetting of the solid components. The treatment was carried out in a Branson 3510 bath at an ultrasound operating frequency of 40 kHz and a power of 130 W for about 30–50 h until a visually homogeneous dispersion was obtained. The dispersion was dried on glass under normal conditions to an air-dry state (∼40–50% relative humidity) with subsequent removal of dry residue.

The carbon materials used in the work were characterized by electron microscopy and adsorption-structural analysis by low-temperature nitrogen adsorption.

Microscopic studies were carried out using electron microscopes Quanta 200 and JEM-2100F and at the Engineering Center of St. Petersburg State Institute of Technology on TESCAN and VEGA 3 SBH.

The morphology of carbon materials was studied using the ASAP 2020 specific surface analyzer. The specific surface area of the sample (S_{sp}), specific volume (V_{sp}) of pores, size, and pore size distribution were calculated using the BET method. Bulk density and specific pore volume were determined independently by gravimetric technique.

NMR experiments were performed on the equipment of the resource Center for Magnetic Resonance of St. Petersburg State University as follows. On a Bruker AVANCE III WB 400 spectrometer (magnetic field strength 9.4 T), the responses of ^{1}H, ^{19}F, and ^{13}C nuclei were recorded, the operating frequencies for which are 400, 376, and 104 MHz, respectively. The sample was placed in a probe - zirconium oxide rotor with an outer diameter of 4 mm, rotating at a magic angle with different frequencies (usually 12.5 kHz, although in some cases it was not possible to achieve this value due to the high conductivity of the substance). For the spectra of fluorine, several frequencies were used to determine the isotopic components of the spectrum. Tetramethylsilane was taken as an external reference for the ^{1}H and ^{13}C nuclei, and a one-molar aqueous solution of lithium fluoride was used for the ^{19}F nuclei. To excite the resonance, a single-pulse sequence with a pulse duration and a relaxation delay of 2.5 μs and 30 s for ^{1}H, 1.2 μs and 30 s for ^{13}C, and 2.9 μs and 2 s for ^{19}F, respectively, was used.

The thermal stability of the composites was studied on a Mettler-ToledoTGA/DSC 1 derivatograph with STAReSystem software. A sample of the material (2–3 mg) was placed in alundum crucible located in the instrument chamber. Registration of thermogravimetric curves (TG) was performed with air blowing through the chamber at a flow rate of 30 cm^3 min^{-1} in the mode of monotonic temperature rise at a rate of 5 K min^{-1} in the range of 35–1000°C.

TABLE 1. Structural characteristics of the investigated carbon materials

Material	Bulk density, g/cm^3	Porosity, %	Specific pore volume over the entire size range (including macropores), cm^3·g^{-1}	Specific surface area, m^3/g
TEG	0.002	99.9	500	143
Vulcan XC-72	0.26	88.0	1.7	200 – 250

3. Results and discussion

Micrographs of the studied carbon materials are shown in Fig. 1, from which it can be seen that they have a significantly different structure. Fig. 1a demonstrates the flakes of the initial TEG. It should be noted that this material has a very small bulk density (see Table 1), and after dispersion in isopropanol-water-Nafion medium, a homogeneous dispersion consisting of smaller graphene structures forms, up to graphene containing 1–3 layers [24]. The TEG (Fig. 1a, Fig. 1b) is built from graphene planes, while Vulcan (Fig. 1c, Fig. 1d) consists of spherical globules with a size in the range of about 60–100 nm.

Some structural characteristics of the carbon materials are given in Table 1. As follows from it, in the initial state both of them have a fairly close specific surface area, however, the porosity of TEG is significantly higher, which is explained by the peculiarities of its microcomposition: a system of flakes in the form of fused petals.

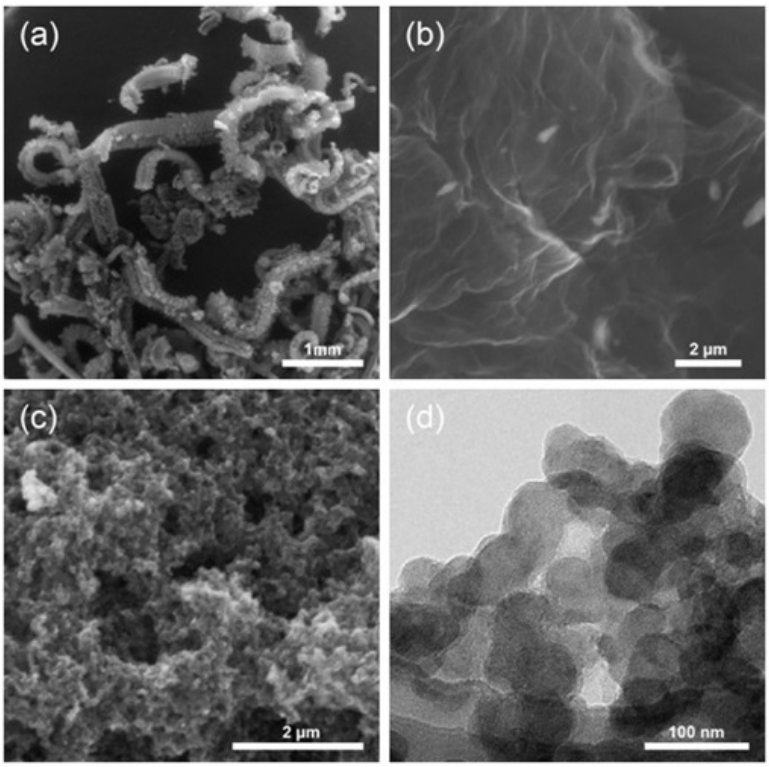

FIG. 1. Micrographs of the carbon materials: (a) SEM image of thermally expanded graphite flakes, (b) SEM image of the structure of thermally expanded graphite, (c) SEM image of Vulcan, (d) TEM image of Vulcan

The ^{1}H NMR spectra of the samples under study are shown in Fig. 2 (for Nafion/TEG, Nafion/Vulcan, and for pure Nafion in Figs. 2a, b and c respectively). Note that the signal-to-noise ratio for composites with carbon materials is much lower than for pure Nafion, which is owing to the presence of a conductive carbon phase and, consequently, a decrease in the Q-factor of the resonant circuit. It can be seen that the pure polymer Nafion has narrow intense inhomogeneously broadened spectral line with a chemical shift of 7.3 ppm (Fig. 2c), typical for water molecules in ionized pores of Nafion. This line is not observed in composites. Nafion/TEG exhibits a broad unresolved line with a maximum of about 1.7 ppm (Fig. 2a), which may be associated with a fast relaxation rate due to the presence of a highly conductive phase in the sample. The Nafion/Vulcan spectrum contains three broadened components with shifts of about 5.7, 1.3, and - 6.5 ppm, as well as a low-intensity peak of about 4.5 ppm (Fig. 2b). The narrow line is characteristic for free water, which could be

released from the sample mass under the influence of the rotation. The line of about 5.7 ppm most likely corresponds to the signal of water in the pores of Nafion with a lower degree of their intrapore ionization. A shift of the proton response to the negative region of the spectrum (as in the resonance near - 6.5 ppm) can be observed in cases when the hydrogen atom is additionally shielded (for example, it is located in a metal or other conductive matrix).

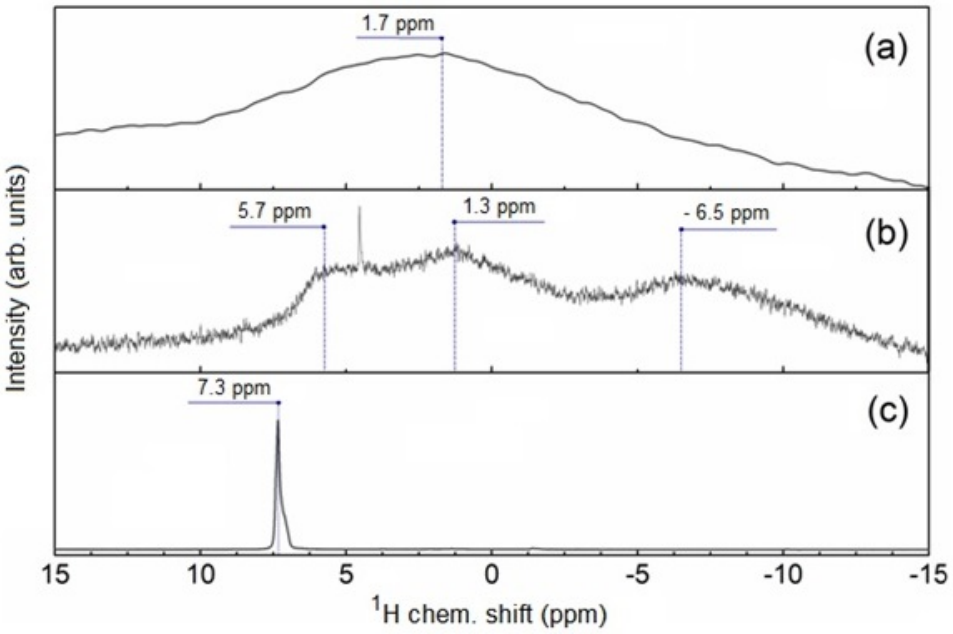

FIG. 2. Solid-state NMR spectra on the nuclei of ^{1}H of composite Nafion/carbon materials (wt. : wt.): a) Nafion/TEG 1 : 4; b) Nafion/Vulcan 1 : 4; c) Nafion 1 : 0

NMR spectra on ^{13}C nuclei have a wide unresolved line of about 111 ppm for pure Nafion and a broadened line in the region of the same chemical shift for the composition of Nafion/Vulcan. For the Nafion/TEG sample, the ^{13}C NMR spectrum could not be registered.

In all samples, the signals of ^{19}F were registered with a set of spectral components characteristic of Nafion. For Nafion and Nafion/Vulcan, the components – 80 ppm (OCF_2 and CF_3), – 117 ppm (SCF_2), – 122 ppm ((CF_2)n), – 138 ppm(CF(b)) and – 144 ppm (CF(s)) were resolved [25]. In Nafion/TEG, one unresolved broadened line was observed with a maximum of about – 122 ppm.

A significant broadening of the NMR lines from the ^{1}H and ^{19}F nuclei, as well as the impossibility of registering the ^{13}C spectrum for the Nafion/TEG sample, is associated with the high conductivity of TEG, which leads to a decrease in the Q-factor of the resonant circuit and/or to acceleration of relaxation processes. On the other hand, the presence of Vulcan particles in the Nafion/Vulcan sample does not cause a similar cardinal suppression of the spectrum, which seems to be due to the lower conductivity of this composite.

The absence of ^{1}H lines in the region of 7.3 ppm for composites with TEG and Vulcan may indicate the disappearance of a large number of pores inside the Nafion matrix because of their filling with particles of modifying materials, or monomolecular enveloping of these particles with Nafion polymer fibers [26].

Fig. 3 shows the results of thermogravimetric analysis of composites. It can be seen that the thermal destruction of Nafion for the Nafion/TEG composite occurs in one stage – there is one stage of mass loss on the TG dependence, which corresponds to one pronounced peak on the differential termogravimetric curve (DTG). In the case of the Nafion/Vulcan composite, three areas of mass loss can be noted on the TG with three resolved peaks on the DTG (Peak temperatures are summarized in Table 2). This behavior may indicate the formation of a part of Nafion in the composite without the formation of spherical clusters containing sulfogroups on the inner surface, which is also confirmed by NMR data. Such structural features may be the reason for the increase in thermal stability.

The data in Fig. 3 and Table 2 demonstrate higher thermal stability of the Nafion/TEG composite compared to Nafion/Vulcan. The temperatures of the destruction peaks of these composites are still quite close, which is consistent with the proximity of the resonance frequencies in the NMR spectra.

4. Conclusion

Thus, the NMR studies of Nafion/carbon composites supplemented with thermogravimetry showed a strong influence of the carbon filler on the polymer. The presence of TEG and Vulcan leads to a change in the structural and physico-chemical characteristics of Nafion and increases its thermal stability due to the possible disappearance of a large number

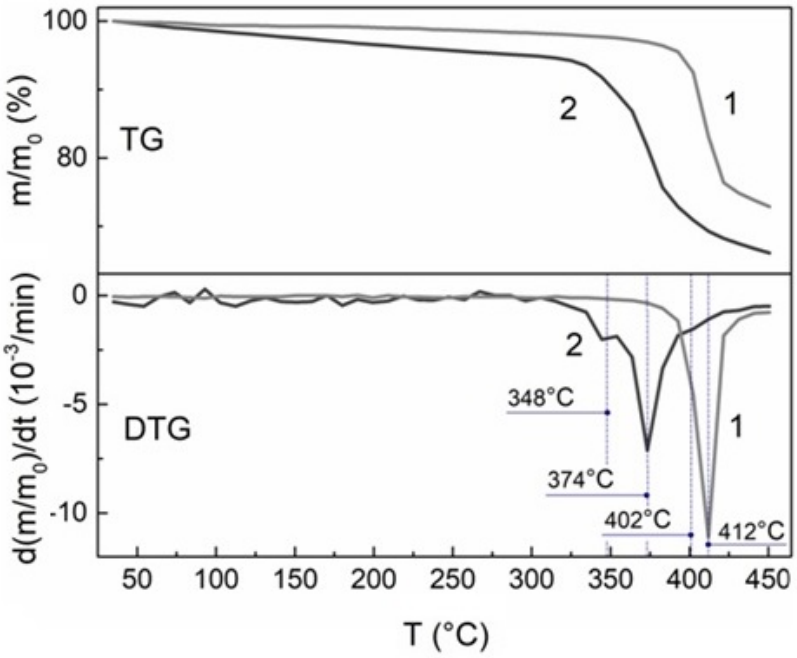

FIG. 3. Thermogravimetric and differential thermogravimetric destruction curves of Nafion when heated of composites Nafion/carbon material (wt. : wt.): 1 – Nafion/TEG 1:4; 2 – Nafion/Vulcan 1:4

TABLE 2. Nafion thermal destruction peak temperatures in Nafion/carbon composites (wt. : wt.): 1:4

Composite	Peak number	T, °C
Nafion/TEG	1	412
Nafion/Vulcan	1	348
	2	374
	3	402

of pores inside the Nafion matrix from - with particles of modifying materials or monomolecular coverage of these particles by polymer fibers Nafion. Besides, it was found that different carbon materials have different influence on the properties of Nafion.

References

[1] Tellez-Cruz M.M., Escorihuela J., Solorza-Feria O., Compañ V. Proton exchange m membrane fuel cells (PEMFCs): advancesand challenges. *Polymers*, 2021, **13**(18), P. 3064.

[2] Zatoń M., Rozière J., Jones D.J. Current understanding of chemical degradation mechanisms of perfluorosulfonic acid membranes and their mitigation strategies: a review. *Sustainable Energy Fuels*, 2017, **1**, P. 409–438.

[3] Bruijn F.A. de, Dam V.A.T., Janssen G.J.M. Durability and degradation issues of PEM fuel cell components. *Fuel Cells*, 2008, **8**(1), P. 3–22.

[4] Nechitailov A.A., Glebova N.V. Investigation of the stability of a nanocomposite of platinum carbon black and carbon nanotubes as an electrocatalyst of fuel cells. *Electrochemical energy*, 2013, **13**(4), P. 192–200 (in Russian).

[5] Nechitailov A.A., Glebova N.V. Mechanism of the effect of oxygen-modified carbon nanotubes on the kinetics of oxygen electroreduction on platinum. *Russian Journal of Electrochemistry*, 2014, **50**(8), P. 751–755.

[6] Grigoriev S.A., Bessarabov D.G. Fateev V.N. Degradation mechanisms of MEA characteristics during water electrolysis in solid polymer electrolyte cells. *Russian Journal of Electrochemistry*, 2017, **53**, P. 318–323.

[7] Siracusano S., Baglio V., Aricò A.S., Grigoriev S.A., Merlo L., Fateev V.N. The influence of iridium chemical oxidation state on the performance and durability of oxygen evolution catalysts in PEM electrolysis. *Journal of Power Sources*, 2017, **366**, P. 105–114.

[8] Pavlov V.I., Gerasimova E.V., Zolotukhina E.V., Don G.M., Dobrovolsky Yu.A., Yaroslavtsev A. B. Degradation of Pt/C electrocatalysts having different morphology in low-temperature PEM fuel cells. *Nanotechnologies in Russia*, 2016, **11**(11-12), P. 743–750.

[9] Moguchikh E.A., Alekseenko A.A., Guterman V.E. Novikovsky N.M., Tabachkova N.Yu., Menshchikov V.S. Effect of the composition and structure of Pt(Cu)/C electrocatalysts on their stability under different stress test conditions. *Russian Journal of Electrochemistry*, 2018, **54**, P. 979–989.

[10] Nechitailov A.A., Glebova N.V., Tomasov A.A., Krasnova A.O., Zelenina N.K. Study of the heterogeneity of a mixed-conducting electrochemical electrode. Technical Physics, 2019, **64**(6), P. 839–847.

[11] Ruiz-Perez F., López-Estrada S.M., Tolentino-Hernández R.V., Caballero-Briones F. Carbon-based radar absorbing materials: a critical review. *Journal of Science: Advanced Materials and Devices*, 2022, **7**(3), P. 100454.
[12] Ansari A., Akhtar M.J. High porous carbon black based flexible nanocomposite as efficient absorber for X-band applications. *Materials Research Express*, 2018, **5**(10), P. 105017.
[13] Wang Y., Gao X., Wu X., Luo C. Facile synthesis of Mn_3O_4 hollow polyhedron wrapped by multiwalled carbon nanotubes as a high-efficiency microwave absorber. Ceramics International, 2020, 46(2), P. 1560–1568.
[14] Min D., Zhou W., Qing Y., Luo F., Zhu D. Highly oriented flake carbonyl iron/carbon fiber composite as thin-thickness and wide-bandwidth microwave absorber. *J. Alloys Compd.*, 2018, **744**, P. 629–636.
[15] Cheng Y., Seow J.Z.Y., Zhao H., Xu Z.J., Ji G. A flexible and lightweight biomass-reinforced microwave absorber. *Nano-Micro Lett.*, 2020, **12**(1), P. 125.
[16] Du X., Wang B., Mu C., Wen F., Xiang J., Nie A., Liu Z. Facile synthesis of carbon-encapsulated Ni nanoparticles embedded into porous graphite sheets as high-performance microwave absorber. ACS Sustainable Chemistry and Engineering, 2018, **6**(12), P. 16179–16185.
[17] Zhao H., Han X., Li Z., Liu D., Wang Y., Wang Y., Zhou W., Du Y. Reduced graphene oxide decorated with carbon nanopolyhedrons as an efficient and lightweight microwave absorber. *J. Colloid Interface Sci.*, 2018, **528**, P. 174–183.
[18] Lu W.B., Wang J.W., Zhang J., Liu Z.G., Chen H., Song W.J., Jiang Z.H. Flexible and optically transparent microwave absorber with wide bandwidth based on grapheme. *Carbon*, 2019, **152**, P. 70–76.
[19] Mahanta U.J., Gogoi J.P., Borah D., Bhattacharyya N.S. Dielectric characterization and microwave absorption of expanded graphite integrated polyaniline multiphase nanocomposites in X-band. *IEEE Trans. Dielectr. Electr. Insul.*, 2019, **26**(1), P. 194–201.
[20] Zixuan Lei, Yuxi Song, Mingze Li, Shuaizhen Li, DianyuGeng, Wei Liu, Yu Cui, Haichang Jiang, Song Ma, Zhidong Zhang. Multi-carbon encapsulating soft-magnetic nanocomposite with environmentally adaptive wideband electromagnetic wave absorption, *J. Alloys Compd.*, 2023, **936**, P. 168216.
[21] Jiheng Ding, Panlin Liu, Min Zhou, Haibin Yu. Nafion-endowed graphene super-anticorrosion performance. *ACS Sustainable Chemistry and Engineering*, 2020, **8**(40), P. 15344–15353.
[22] Glebova N.V., Nechitailov A.A., Krasnova A.O. Thermal degradation of Nafion in the presence of nanostructured materials: thermally expanded graphite, carbon black, and platinum. *Russ. J. Appl. Chem.*, 2020, **93**(7), P. 1034–1041.
[23] Method of producing porous carbon material based on highly disintegrated graphite, Patent 2014116365/05 Russia: IPC C01B 31/04, Mazin V.I., N 2581382, Bull. N 11, 2016, 9 p.
[24] Kastsova A.G., Glebova N.V., Nechitailov A.A., Krasnova A.O., Pelageikina A.O., Eliseyev I.A. Electronic spectroscopy of graphene obtained by ultrasonic dispersion. *Tech. Phys. Lett.*, 2022, **48**(12), P. 60–62.
[25] Chen Q., Schmidt-Rohr K. 19F and 13C NMR signal assignment and analysis in a perfluorinated ionomer (Nafion) by two-dimensional solid-state NMR. *Macromolecules*, 2004, **37**(16), P. 5995.
[26] Lee W.-J., Bera S., Kim C.M., Koh E.-K., Hong W.-P., Oh S.-J., Cho E., Kwon S.-H. Synthesis of highly dispersed Pt nanoparticles into carbon supports by fluidized bed reactor atomic layer deposition to boost PEMFC performance. *NPG Asia Materials*, 2020, **12**(1), P. 40.

Submitted 22 March 2023; revised 28 March 2023; accepted 29 March 2023

Information about the authors:

Nadezhda V. Glebova – Ioffe Institute, 26 Politechnicheskaya str., St. Petersburg, 194021, Russia; ORCID 0000-0003-4519-0111; glebova@mail.ioffe.ru

Anton S. Mazur – St. Petersburg State University, 7-9 Universitetskaya emb., St. Petersburg, 199034, Russia; ORCID 0000-0002-2746-6762; a.mazur@spbu.ru

Anna O. Krasnova – Ioffe Institute, 26 Politechnicheskaya str., St. Petersburg, 194021, Russia; ORCID 0000-0001-6709-5559; krasnova@mail.ioffe.ru

Ivan V. Pleshakov – Ioffe Institute, 26 Politechnicheskaya str., St. Petersburg, 194021, Russia; ORCID 0000-0002-6707-6216; inanple@yandex.ru

Andrey A. Nechitailov – Ioffe Institute, 26 Politechnicheskaya str., St. Petersburg, 194021, Russia; ORCID 0000-0002-9895-6822; aan.shuv@mail.ioffe.ru

Conflict of interest: the authors declare no conflict of interest.

NANOSYSTEMS:
PHYSICS, CHEMISTRY, MATHEMATICS

Talanov V.M., et al. *Nanosystems: Phys. Chem. Math.*, 2023, **14** (2), 208–215.
http://nanojournal.ifmo.ru
DOI 10.17586/2220-8054-2023-14-2-208-215

Original article

Symmetry-based prediction of the type-II multiferroics with pyrochlore structure

Valeriy M. Talanov[1,a], Mikhail V. Talanov[1,2,b], Vladimir B. Shirokov[1,2,3,c]

[1]Platov South-Russian State Polytechnic University, Novocherkassk, Russia

[2]Southern Federal University, Rostov-on-Don, Russia

[3]Southern Scientific Center of Russian Academy of Sciences, Rostov-on-Don, Russia

[a]valtalanov@mail.ru, [b]mvtalanov@gmail.com, [c]shirokov.ssc@gmail.com

Corresponding author: Valeriy M. Talanov, valtalanov@mail.ru

PACS 05.70.Fh; 61.50.Ah; 61.50.Ks; 61.66.Fn

ABSTRACT Based on the symmetry related concept of the group theory we predict two structures with enantiomorphic space groups P_I4_3 and P_I4_1. These phases arise as a result of spin ordering on 16d Wyckoff position in crystals with space group $Fd\bar{3}m$. It is shown that P_I4_3 and P_I4_1 hypothetical magnetic structures are multiferroics of type II. The ferroelectric polarization emerges through a mechanism of the hybrid improper ferroelectricity allowing trilinear coupling of polarization and two other antiferromagnetic order parameters. In addition to improper ferroelectricity, the symmetry analysis proves the possible coexistence of other improper ferroic orders including orbital, ferroelastic, ferroelastoelectric, ferrobielastic, optical, ferroaxial, ferrotoroidic, gyrotropic and other crystal freedom degrees.

KEYWORDS spin order, multiferroics, improper ferroelectrics, trilinear coupling, multi-order state, secondary ferroics.

ACKNOWLEDGEMENTS The reported study was funded by Russian Science Foundation (RSF)-research projects No. 22-22- 00183, https://rscf.ru/project/22-22-00183/

FOR CITATION Talanov V.M., Talanov M.V., Shirokov V.B. Symmetry-based prediction of the type-II multiferroics with pyrochlore structure. *Nanosystems: Phys. Chem. Math.*, 2023, **14** (2), 208–215.

1. Introduction

Magnetoelectric multiferroics demonstrate both magnetic and ferroelectric order with the mutual influence of the corresponding properties on each other. Thus, the electric field control of magnetization or vice versa magnetic field tunable electric polarization are possible that opens up a wide range of practical applications including magnetic field sensors, electrically tunable microwave resonators, random access multi-state memories and many others [1]. The classification by Khomskii distinguishes two types of multiferroics [2]. In a type-I multiferroics, ferroelectricity and magnetism appear independently and, most often, different subsystems and ions are responsible for them. Classical examples are oxides with the perovskite structure $BiFeO_3$ and $BiMnO_3$, in which ferroelectricity is due to Bi^{3+} ions with a lone pair of electrons in the A sublattice, and magnetism is associated with ions with a partially filled d shell in the B sublattice [3–5]. The magnetic and ferroelectric degrees of freedom in these systems are coupled, but the magnetoelectric coefficients are rather low that hinders many applications. In a type-II multiferroics, ferroelectric polarization arises due to magnetic ordering, which usually leads to a stronger magnetoelectric interaction. Typical examples are $TbMnO_3$ [6], $Tb_2Mn_2O_5$ [7] and many other structures, where spin order induces electrical polarization [8].

Approaches to the design of magnetoelectric materials and corresponding nanosystems differ significantly for type -I and type-II multiferroics. For a long time, it was believed that magnetism and ferroelectricity in one substance should not coexist due to the so-called "d^n–d^0 separation" [9]. The meaning of this rule is very simple: substances containing partially filled d-shells are magnetic, while substances with an unfilled d^0-configuration will be non-magnetic but may turn out to be ferroelectric as a result of the pseudo Jahn-Teller effect (similar to $BaTiO_3$) [10]. Thus, there is a contradictory requirement for the electronic structure of the single ions responsible for ferroelectricity and magnetism.

One of the main directions in solving the problem of "d^n–d^0 separation" was the design of materials in which different sublattices were "responsible" for magnetic or ferroelectric properties. Such materials are type-I multiferroics or ferromagnetics [11]. In addition to the already mentioned $BiFeO_3$ and $BiMnO_3$, type-I multiferroics include $PbFe_{2/3}W_{1/3}O_3$, $PbFe_{1/2}Nb_{1/2}O_3$, various solid solutions based on them, as well as many other complex perovskites of the Pb(B'B'')O_3 type. In these cases, magnetic and ferroactive ions occupy different sublattices of the perovskite structure and/or are randomly mixed in one of the sublattices [3–5].

Another approach to the creation of magnetoelectric materials are composites (two-phase multiferroics) based on piezoelectric and magnetostrictive components, which often belong to different structural types, as, for example, in the case of widely studied nano- and bulk composites based on $PbZr_{0.5}Ti_{0.5}O_3$ (perovskite) and $NiFe_2O_4$ (spinel) and many

others [12]. Under the action of a magnetic field, the ferrite is deformed due to magnetostriction. This deformation, in turn, induces the appearance of an electric charge at the boundaries of the ferroelectric phase as a result of the direct piezoelectric effect. Thus, the magnetoelectric interaction is carried out due to the magnetic subsystem, which has been confirmed in various forms of connectivity of the mechanical and ferroelectric components of composites: mixed, layered, etc. [12].

In recent years, a new line of research has appeared in the field of creating the multiferroics. This line is associated with the discovery of a hybrid mechanism of improper ferroelectricity in the superlattices of various perovskites, for example, $PbTiO_3/SrTiO_3$ [13–16]. The polarization is possible due to the interaction of several nonferroelectric order parameters (in the case of the above superlattices, these are different types of oxygen octahedra tilts), which are described by a trilinear term of the $\eta_1\eta_2 P$ form (where η_1, η_2 are nonpolar distortions, and P is polarization) in the thermodynamic potential [17]. Later, hybrid improper ferroelectricity was also discovered in single-phase materials, including ordered perovskites [17–20], Ruddlesden–Popper phases [16, 19–27], molecular perovskites [28, 29], metal-organic frameworks [23] and other materials, including multiferroics (for example, [16,30]). Thus, the problem of "d^n–d^0 separation" can also be solved by creating artificial nanosystems - superlattices consisting of magnetic nonpolar layers, in which polarization occurs as an integral effect.

In the case of type-II multiferroics, the occurrence of ferroelectric polarization is due to magnetic ordering, which leads to the loss of the inversion center. In this case, the problem of "d^n–d^0 separation" is not relevant. To date, the main microscopic mechanisms of violation of the inversion center because of the specific geometry of both collinear and noncollinear spin-ordered structures have been identified [3,31]. Thus, in collinear magnetic structures with different types of magnetic ions (for example, chains of nonequivalent spins directed alternately downward - upward), the occurrence of polarization is caused by the mechanism of exchange striction [33]. In noncollinear magnets, magnetically induced ferroelectricity is possible due to the spin-current mechanism or reverse Dzyaloshinsky-Moriya model for canted spins or spiral magnetic structures [34] including cycloid and transverse conical ones [32].

One of the promising atomic architectures for the implementation of various magnetic orders and, as a result, magnetically induced ferroelectricity is the pyrochlore lattice [35,36], which is a part of the structures of pyrochlores, spinels, and C15 Laves phases (Fig. 1).

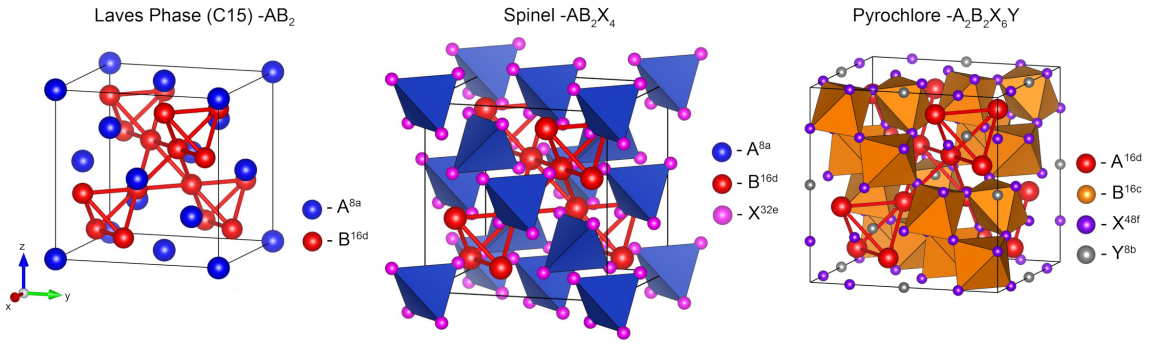

FIG. 1. Main structural types of materials with pyrochlore sublattice. Pyrochlore sublattice in Laves phases (C15) AB_2 (a), normal spinel AB_2X_4 (c), $A_2B_2X_6Y$ pyrochlore (c). In all figures, this sublattice is shown in red

To date, a huge number of various magnetic materials with a pyrochlore lattice are known, which are characterized by a diversity of spin-ordered structures [32, 35]. This lattice is a platform for the implementation of various types of competing and coexisting interactions, which is due to strong geometric frustration. Materials with pyrochlore lattices tend to exhibit a very complex relationship of interacting structural, orbital, charge, and spin degrees of freedom. The nature of such multi-order determining the unique physical properties of this class of materials cannot be understood without profound knowledge of group-theoretical symmetry principles. The aim of this work is to make a group-theoretical prediction of some types of the complex multi-orders, similar to improper ferroelectricity in type II multiferroics, and generated by ordering the spins of magnetic cations on the pyrochlore lattice.

2. Methods

We will consider the case of the formation of spin-ordered structures that is not accompanied by the splitting of the $16d$ Wyckoff positions of the $Fd\bar{3}m$ space group. If we take this limitation, within the framework of Landau phase transition theory, it is sufficient only to consider the magnetic order parameters (OPs) with two propagation vectors $k = (0, 0, 0)$ and $k = (0, 0, 1)$. For irreducible representations (*irreps*) of these wave vectors, the magnetic representations are as follow:

$$T_{mag} = \left(m\Gamma_2^+\right) \oplus \left(m\Gamma_3^+\right) \oplus \left(m\Gamma_5^+\right) \oplus 2\left(m\Gamma_4^+\right) \quad for \quad k = (0, 0, 0), \tag{1}$$

TABLE 1. Theoretically predicted structures of the type-II multiferroics derived from cubic pyrochlore lattice without splitting of the initial 16d Wyckoff crystallographic positions of $Fd\bar{3}m$ space group

Primary OPs	Secondary OPs	Magnetic space group	Basis vectors	Origin	Size
	$\Gamma_1^+(a)$				
	$\Gamma_1^-(a)$	P_I4_3			
$mX_3\ (0,0;0,0;a,0)$	$\Gamma_3^-(0,a)$	(No. 78.24)	(1/2,1/2,0)		
$mX_4\ (0,0;0,0;a,0)$	$\Gamma_4^-(0,0,a)$	UNI:	(-1/2,1/2,0)	(-3/8,3/8,0)	2
	$\Gamma_3^+(a,0)$	$P4_3.1'_I[I4_1]$	(0,0,1)		
	$\Gamma_4^+(0,0,a)$				
	$\Gamma_1^+(a)$				
	$\Gamma_1^-(a)$	P_I4_1			
$mX_3\ (0,0;0,0;0,a)$	$\Gamma_3^-(0,a)$	(No. 76.12)	(1/2,1/2,0)		
$mX_4\ (0,0;0,0;0,a)$	$\Gamma_4^-(0,0,a)$	UNI:	(-1/2,1/2,0)	(-1/8,1/8,0)	2
	$\Gamma_3^+(a,0)$	$P4_1.1'_I[I4_1]$	(0,0,1)		
	$\Gamma_4^+(0,0,a)$				

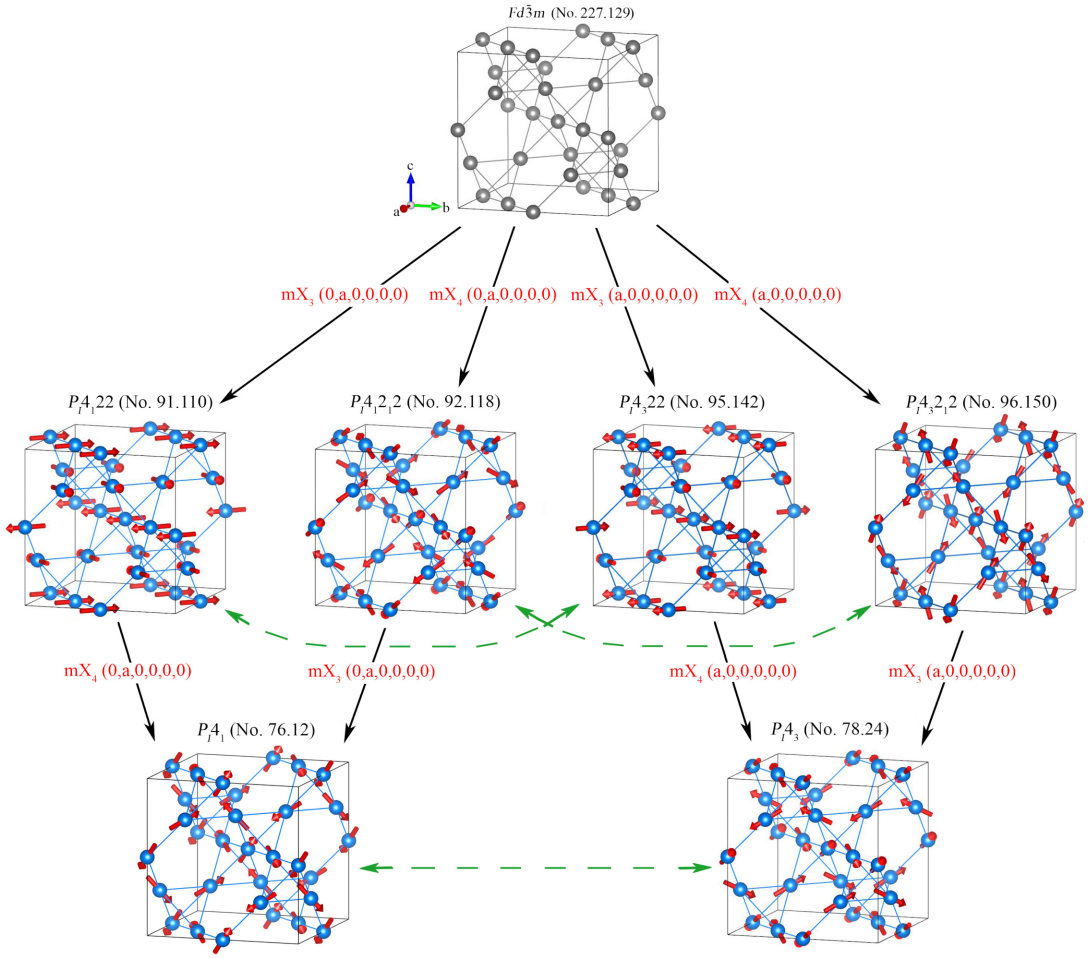

FIG. 2. Symmetric ways of formation of enantiomorphic structures with space groups P_I4_3 and P_I4_1 from the initial symmetry group $Fd\bar{3}m$. The OPs that generate transformations of structures are marked in red. Enantiomorphic pairs of structures are connected by green dotted arrows

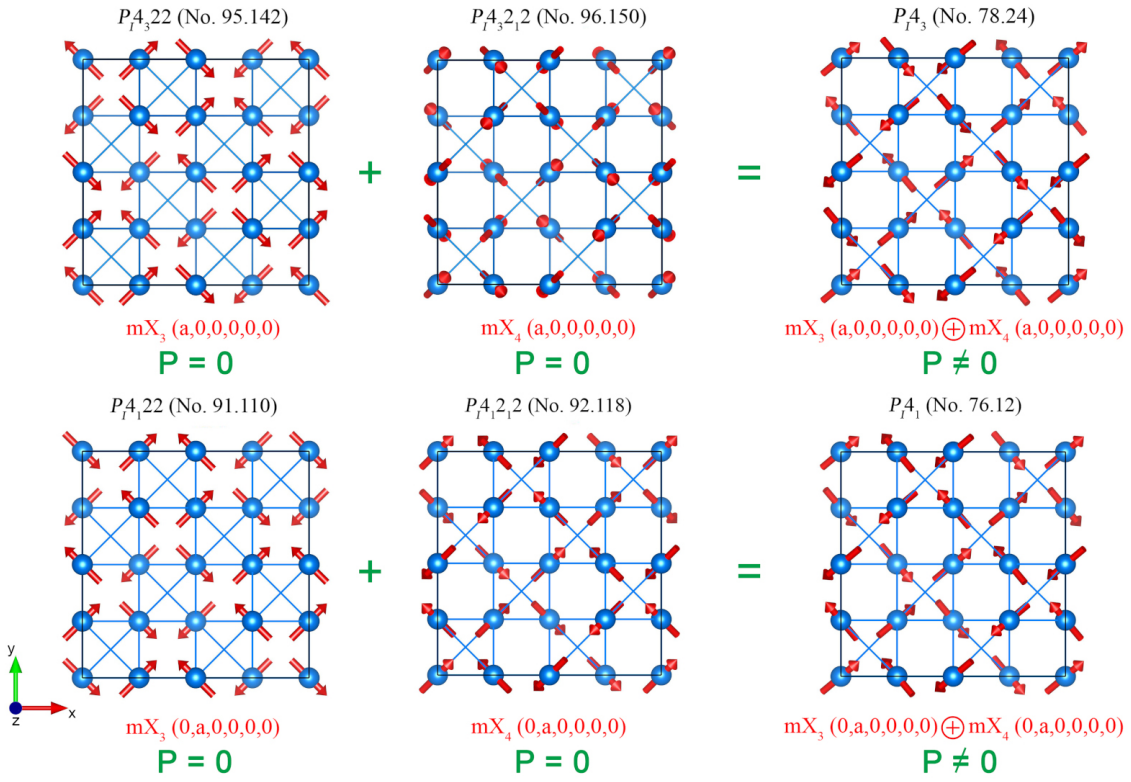

FIG. 3. Mechanism of the spin-induced polarization formation via trilinear coupling on the examples of an improper ferroelectric phases with space groups P_I4_3 (No. 78.24) and P_I4_1 (No. 76.12)

$$T_{mag} = (mX_3) \oplus 2\,(mX_4) \oplus (mX_1) \oplus 2(mX_2) \quad for \quad k = (0,0,1), \tag{2}$$

The compositions of the magnetic representations (1 and 2) determine the variety of magnetically ordered phases, possible types of phase diagrams and physical properties.

At present, some group-theoretical tasks of the magnetic phase transitions theory can be solved using computer programs (ISOTROPY Software Suite [37] and Bilbao Crystallographic Server [38]). In our work, we used ISODISTORT [37], k-Subgroupsmag/Get_mirreps [38], MAGMODELIZE programs [38]. Magnetic structure visualization was made by VESTA [39].

3. Results and discussion

According to our calculations, the magnetic representations (1 and 2) determine the possibility of the existence of 25 phases [32]. In the context of possible multiferroic phases, we underline two structures P_I4_3 (No. 78.24) and P_I4_1 (No. 76.12) which are induced by two OPs transformed by *irreps* mX_3 and mX_4 (with different OPs direction for these phases). Table 1 shows the sets of OPs that determine the magnetic structure, magnetic space group (Belov–Neronova–Smirnova [40] and new unified (UNI) [41] designation), secondary OPs, basis vectors of the primitive cell and the change in the volume of a primitive cell (column "size"). Note that the sets of secondary OPs in the formation of P_I4_3 and P_I4_1 structures are the same. Symmetry analysis makes it possible to establish the physical realization of the secondary OPs: ferroelastic (*irrep* Γ_3^+) and nonferroelastic (*irreps* Γ_3^- and Γ_4^-) displacements of atoms [36, 42], as well as ordering (*irreps* Γ_3^+ and Γ_4^+) of d-orbitals [43].

The symmetry of predicted spin-ordered structures allows physical properties described by tensors of different orders (secondary ferroics) [32]. Table 2 lists some of these simple tensor properties, the irreducible representations by which they are converted, as well as the secondary order parameters from Table 1. Therefore, the predicted crystals are improper ferroics or type-II multiferroic materials. The analysis of the secondary OP (Table 1 and Table 2) shows that the improper ferroelectrics with the P_I4_3 and P_I4_1 structure can also be ferroelastic, ferroelastoelectric, ferrobielastic, ferrotoroidic and gyrotropic phases [44–47].

Spin ordering led to the formation of enantiomorphic (chiral) structures with P_I4_3 – and P_I4_1 – symmetries. They form an enantiomorphic pair. We see (Fig. 2) that the final P_I4_3 – and P_I4_1 – phases can be obtained in various symmetry ways from the initial phase. This conclusion corresponds to the so-called variable principle, which was first established in work [48]. From the initial structure with the $Fd\bar{3}m$ space group, this enantiomorphic pair is obtained through intermediate structures (Fig. 2). The intermediate structures, in turn, form two enantiomorphic pairs: $P4_122$ – $P4_322$ and $P4_12_12$ – $P4_32_12$. Enantiomorphic crystals modify one into another in mirror reflection. One of these modifications is

TABLE 2. Predicted improper physical properties of the crystals with P_I4_3 and P_I4_1 space group

Examples of physical properties or phenomena	Macro-parameters	Decomposition of reducible presentation	Secondary OPs from Table 1
Ferroelectric, polarization	Γ_4^-	Γ_4^-	$\Gamma_4^-\ (0,0,a)$
Ferroelastic, strain, stress, permitivity	$\left[\left(\Gamma_4^-\right)^2\right]$	$\Gamma_1^+ + \Gamma_3^+ + \Gamma_5^+$	$\Gamma_3^+(a,0)$
Longitudinal piezoelectric effect tensor	$\left[\left(\Gamma_4^-\right)^3\right]$	$\Gamma_2^- + 2\Gamma_4^- + \Gamma_5^-$	$\Gamma_4^-\ (0,0,a)$
Symmetric in all indices fourth-rank tensor, cubic susceptibility tensor neglecting dispersion	$\left[\left(\Gamma_4^-\right)^4\right]$	$2\Gamma_1^+ + 2\Gamma_3^+ + 2\Gamma_5^+ + \Gamma_4^+$	$\Gamma_3^+\ (a,0)$ $\Gamma_4^+\ (0,0,a)$
Ferroelastoelectric, piezoelectric tensor, electro-optic coefficient	$\left[\left(\Gamma_4^-\right)^2\right]\left(\Gamma_4^-\right)$	$\Gamma_2^- + \Gamma_3^- + 3\Gamma_4^- + 2\Gamma_5^-$	$\Gamma_3^-(0,a)$ $\Gamma_4^-\ (0,0,a)$
Ferrobielastic, electrostriction, elastooptic or piezooptic tensor	$\left[\left(\Gamma_4^-\right)^2\right]^2$	$3\Gamma_1^+ + \Gamma_2^+ + 4\Gamma_3^+ + 3\Gamma_4^+ + 5\Gamma_5^+$	$\Gamma_3^+\ (a,0)$ $\Gamma_4^+\ (0,0,a)$
Axial crystal	A	Γ_4^+	$\Gamma_4^+\ (0,0,a)$
Ferrotoroidic	$A\left(\Gamma_4^+\right)$	Γ_4^+	$\Gamma_4^+\ (0,0,a)$
Optical activity, gyration tensor	$\varepsilon\left[\left(\Gamma_4^-\right)^2\right]$	$\Gamma_1^- + \Gamma_3^- + \Gamma_5^-$	$\Gamma_1^-(a)$ $\Gamma_3^-(0,a)$
Enanthiomorphism, Pure gyrotropic phase	ε	Γ_1^-	$\Gamma_1^-(a)$
Gyrotropic ferroelastic	Γ_3^-	Γ_3^-	$\Gamma_3^-(0,a)$
Gyrotropic ferroelectric	Γ_4^-	Γ_4^-	$\Gamma_4^-\ (0,0,a)$

Explanations for Table 2. Γ_4^- – the vector representation of the $Fd\bar{3}m$ symmetry group, A – the axial representation of the $Fd\bar{3}m$ symmetry group, ε– pseudo scalar. Secondary OPs from Table 1 for primary OPs: $mX_3(0,0;0,0;a,0)$ + $mX_4(0,0;0,0;a,0)$ and $mX_3(0,0;0,0;0,a)$ +$mX_4(0,0;0,0;0,a)$ are the same.

conventionally called “right”, and the other - “left”. Enanthiomorphic objects are described by a point symmetry group containing only symmetry axes. Both forms of enantiomorphic crystals have optical activity (gyrotropes), but the crystal rotates the plane of polarization of light propagating along the optical axis, either along the left screw for one modification or the right screw for the other modification to the same angle.

However, the conditions for the existence of enaniomorphism do not completely coincide with the those for the existence of the optical activity. A novel functionality of enantiomorphic (chiral) materials is discovered in spintronics, which is known as “Chirality Induced Spin Selectivity” effect [49–52]. In our study, we established the opposite effect - the emergence of enantiomorphic (chiral) structures as a result of spin ordering associated with the lattice deformations and orbital ordering.

The symmetry allows trilinear coupling through mixed invariant $\gamma M_{mX_3} M_{mX_4} P_{\Gamma_4^-}$ in the thermodynamic potential, where γ is a coefficient characterizing the strength of the magnetoelectric coupling (by this invariant); M_{mX_3}, M_{mX_4} and $P_{\Gamma_4^-}$ are antiferromagnetic (M_{mX_3} and M_{mX_4}) and ferroelectric ($P_{\Gamma_4^-}$) OPs transformed according *irrep*s mX_3, mX_4

and Γ_4^-, respectively. Thus, space-inversion symmetry breaking the emergence of the spontaneous polarization results from the interaction between two antiferromagnetic orders, which do not separately lead to the ferroelectric distortion (Fig. 3). From the symmetry consideration, the emergence of spin-induced polarization in these phases is similar to the mechanism of the hybrid improper ferroelectricity in artificial superlattices ($PbTiO_3$/$SrTiO_3$ [13]) and Ruddlesden–Popper perovskite-like phases ($Ca_3Mn_2O_7$ [16]). But in these examples the linear polarization is the product of interaction between two types of the octahedron rotational modes (instead of the two types of antiferromagnetic OPs) through trilinear coupling term in the Landau thermodynamic potential. Thus, these theoretically predicted phases can be attributed to the multiferroics of type-II according to the Khomskii classification [2].

Considering a variety of spin-ordered pyrochlore-like compounds, we expect that they may be a potential arena for ferroaxial materials. Ferroaxial order is discussed as a new class of ferroic states in recent years [46, 53–55]. The so-called ferroaxial transitions (a transition from nonferroaxial to ferroaxial phases) are characterized by rotational structural distortions that break the mirror symmetry. Among the 32 crystallographic point groups, there are 13 ferroaxial (or pyroaxial) groups (1, $\overline{1}$, 2, m, $2/m$, 3, $\overline{3}$, 4, $\overline{4}$, $4/m$, 6, $\overline{6}$, and $6/m$ [56], among which there is a point group 4. In the ferroaxial state, clockwise and counterclockwise rotational distortions are energetically equivalent and form domain states whose spatial distributions have been reported recently [54–59]. However, transition $m\overline{3}m \rightarrow 4$ is not pure ferroaxial species because it accompanies ferroelectric, ferroelastic, gyrotropic transitions. Only a few ferroaxial materials that show a pure ferroaxial transition are reported to date [e.g., $RbFe(MoO_4)_2$ ($\overline{3}m \rightarrow \overline{3}$ at 190 K [60]) and $NiTiO_3$ ($\overline{3}m \rightarrow \overline{3}$ at 1560 K [61])].

We consider also gyrotropic phase transitions in which the initial phase is optically inactive or non-gyrotropic; Therefore, the ferroic optically active phase will be called the gyrotropic phase. The appearance of a spontaneous gyrotropic phase, which is not accompanied by either ferroelectricity or ferroelasticity, corresponds to the formation of so-called pure gyrotropic phase [47]. If the formation of a gyrotropic phase is accompanied by the appearance of polarization or deformation in the ferroic phase, then the optically active phase will be called gyrotropic ferroelectric or gyrotropic ferroelastic, respectively.

Thus, the predicted pyrochlore-like phases with P_I4_3 and P_I4_1 space symmetry are characterized by a complex and multi-order, including the structural, orbital, spin, optical, ferroaxial, ferrotoroidic, ferroelastoelectric, ferrobielastic, gyrotropic, electrical and other crystal freedom degrees.

4. Conclusions

In our work, we predict the possibility of the existence of two enantiomorphic multiferroics of type II with P_I4_3- and P_I4_1- symmetries, whose ferroelectrical properties appear as a result of magnetic ordering on the $16d$ Wyckoff positions in the initial $Fd\overline{3}m$ phase with pyrochlore sublattice(s). These multiferroics are objects to be searched and studied, since they can have not only magnetic and electrical properties, but, at the same time, they can have other above mentioned physical properties. This complex multi-order may result in unusual physical properties of the above materials.

References

[1] Vopson M.M. Fundamentals of Multiferroic Materials and Their Possible Applications. *Critical Reviews in Solid State and Materials Sciences*, 2014, **201**, P. 1–28.

[2] Khomskii D. Classifying multiferroics: Mechanisms and effects. *Physics*, 2009, **2**(20), P. 1-8.

[3] Selbach S.M., Tybell T., et al. The Ferroic Phase Transitions of $BiFeO_3$. *Adv. Mater.*, 2008, **20**, P. 3692–3696.

[4] Kimura T., Kawamoto S., et al. Magnetocapacitance effect in multiferroic $BiMnO_3$. *Phys. Rev. B*, 2003, **67**, P. 180401(1-4) (R).

[5] Seshadri R., Hill N. A. Visualizing the role of Bi $6s$ "lone pairs" in the off-center distortion in ferromagnetic $BiMnO_3$. *Chem. Mater.*, 2001, **13**, P. 2892–2899.

[6] Kimura T., Goto T., et al. Magnetic control of ferroelectic polarization. *Nature*, 2003, **426**, P. 55–58.

[7] Hur N., Park S., et al. Electric polarization reversal and memory in a multiferroic material induced by magnetic fields. *Nature*, 2004, **429**, P. 392–395.

[8] Cheong S.W., Mostovoy M. Multiferroics: a magnetic twist for ferroelectricity. *Nature Mater*, 2007, **6**, P. 13–20.

[9] Hill N. A. Why there are so few multiferroics with the perovskites structure? *J. Phys. Chem. B*, 2000, **104**(29), P. 6694–6709.

[10] Polinger V., Garcia-Fernandez P., et al. Pseudo Jahn–Teller origin of ferroelectric instability in $BaTiO_3$ type perovskites: The Green's function approach and beyond. *Physica B: Condensed Matter*, 2015, **457**, P. 296–309.

[11] Smolenskii G. A., Chupis I. E. Ferroelectromagnets. *Physics–Uspekhi*, 1982, **25**, P. 475–493.

[12] Nan C.-W. Multiferroic magnetoelectric composites: Historical perspective, status, and future directions. *J. Appl. Phys.*, 2008, **103**, P. 031101(1-35).

[13] Bousquet E., Dawber M., et al. Improper ferroelectricity in perovskite oxide artificial superlattices. *Nature*, 2008, **452**, P. 732–736.

[14] Sim H., Cheong S.W., et al. Octahedral tilting-induced ferroelectricity in $ASnO_3$/A'SnO_3 superlattices (A, A'=Ca, Sr, and Ba). *Phys. Rev. B*, 2013, **88**, P. 014101(1-7).

[15] Zhao H.J., Íñiguez J., et al. Atomistic theory of hybrid improper ferroelectricity in perovskites. *Phys. Rev. B*, 2014, **89**, P. 174101(1-7).

[16] Benedek N. A., Fennie C.J. Hybrid Improper Ferroelectricity: A Mechanism for Controllable Polarization-Magnetization Coupling. *Phys. Rev. Lett.*, 2011, **106**, P. 107204(1-4).

[17] Rondinelli J.M., Fennie C.J. Octahedral Rotation-Induced Ferroelectricity in Cation Ordered Perovskites. *Adv. Mater.*, 2012, **24**, P. 1961–1968.

[18] Mulder A.T., Benedek N.A., et al. Turning ABO_3 Antiferroelectrics into Ferroelectrics: Design Rules for Practical Rotation-Driven Ferroelectricity in Double Perovskites and $A_3B_2O_7$ Ruddlesden-Popper Compounds. *Adv. Func. Mater.*, 2013, **23**, P. 4810–4820.

[19] Benedek N.A., Rondinelli J.M., et al. Understanding ferroelectricity in layered perovskites: new ideas and insights from theory and experiments. *Dalton Trans.*, 2015, **44**, P. 10543–10558.
[20] Santos S.S.M., Marcondes M.L., et al. Spontaneous electric polarization and electric field gradient in hybrid improper ferroelectrics: insights and correlations. *J. Mater. Chem. C*, 2021, **22**, P. 15074–15082.
[21] Oh Y.S., Luo X., et al. Experimental demonstration of hybrid improper ferroelectricity and the presence of abundant charged walls in (Ca, Sr)$_3$Ti$_2$O$_7$ crystals. *Nature Mater.*, 2015, **14**, P. 407–413.
[22] Liu X.Q., Wu J.W., et al Direct observation of ferroelectricity in $Ca_3Mn_2O_7$ and its prominent light absorption. *Appl. Phys. Lett.*, 2015, **106**, P. 202903(1-5).
[23] Yoshida S., Akamatsu H., et al. Hybrid Improper Ferroelectricity in (Sr,Ca)$_3$Sn$_2$O$_7$ and Beyond: Universal Relationship between Ferroelectric Transition Temperature and Tolerance Factor in n = 2 Ruddlesden–Popper Phases. *J. Am. Chem. Soc.*, 2018, **140**, P. 15690–15700.
[24] Yoshida S., Fujita K., et al. Ferroelectric $Sr_3Zr_2O_7$: Competition between Hybrid Improper Ferroelectric and Antiferroelectric Mechanisms. *Adv. Funct. Mater.*, 2018, **30**, P. 1801856(1-12).
[25] Hu Z.Z., Lu J.J., et al First-order phase transition and unexpected rigid rotation mode in hybrid improper ferroelectric (La, Al) co-substituted $Ca_3Ti_2O_7$ ceramics. *J. Materiomics*, 2019, **5**, P. 618–625.
[26] Lee M.H., Chang C.-P., et al. Hidden Antipolar Order Parameter and Entangled Néel-Type Charged Domain Walls in Hybrid Improper Ferroelectrics. *Phys. Rev. Lett.*, 2017, **119**, P. 157601(1-6).
[27] Smith K.A., Nowadnick E.A., et al. Infrared nano-spectroscopy of ferroelastic domain walls in hybrid improper ferroelectric $Ca_3Ti_2O_7$. *Nature Commun.*, 2019, **10**, P. 5235(1-9).
[28] Boström H.L.B., Senn M.S., Goodwin A.L. Recipes for improper ferroelectricity in molecular perovskites. Nature Commun., 2018, **9**, P. 2380(1-7).
[29] Boström H.L.B., Goodwin A.L. Hybrid Perovskites, Metal–Organic Frameworks, and Beyond: Unconventional Degrees of Freedom in Molecular Frameworks. *Acc.Chem.Res.*, 2021, **54**, P. 1288–1297.
[30] Stroppa A., Barone P., et al. Hybrid Improper Ferroelectricity in a Multiferroic and Magnetoelectric Metal-Organic Framework. *Adv. Mater.*, 2013, **25**, P. 2284–2290.
[31] Tokura Y., Seki S. Multiferroics with Spiral Spin Orders. *Advanced Materials*, 2010, **22**(14), P. 1554–1565.
[32] Talanov M.V., Shirokov V.B., Pimenov M.S., Talanov V.M. Magnetic phase diagrams of the pyrochlore-based magnets: Landau theory. *J. Magn. Magn. Mat*, 2023 (in press).
[33] Choi Y.J., Yi H.T., et al. Ferroelectricity in an Ising Chain Magnet. *Phys. Rev. Lett.*, 2008, **100**, P. 047601(1-4).
[34] Arima T. Ferroelectricity induced by proper-screw type magnetic order, *J. Phys. Soc. Jpn.*, 2007, **76**, P. 073702(1-4).
[35] Talanov M.V., Talanov V.M. Structural Diversity of Ordered Pyrochlores. *Chem Mater.*, 2021, **33**, P. 2706–2725.
[36] Talanov M.V., Talanov V.M. Formation of Breathing Pyrochlore Lattices: Structural, Thermodynamic and Crystal Chemical Aspects. *CrystEngComm.*, 2020, **22**, P. 1176–1187.
[37] Campbell B.J., Stokes H.T., et al., ISODISPLACE: a web-based tool for exploring structural distortions. *J. Appl. Cryst.*, 2006, **39**, P. 607–614.
[38] Perez-Mato J., Gallego S., et al. Symmetry-Based Computational Tools for Magnetic Crystallography. *Annu. Rev. Mater. Res.*, 2015, **45**, P. 217–248.
[39] Momma K., Izumi F. VESTA: a three-dimensional visualization system for electronic and structural analysis. *J. Appl. Cryst*, 2008, **41**, P. 653–658.
[40] Belov N.V., Neronova N.N., Smirnova T.S. *Tr. Inst. Krist. Akad. SSSR.*, 1955, **11**, P. 33–67, English translation in *Sov. Phys. Crystallogr*., 1957, **1**, P. 487–488.
[41] Campbell B.J., Stokes H.T., et al. Introducing a unified magnetic space-group symbol, *Acta Cryst. A*, 2022, **78**, P. 99–106.
[42] Talanov M.V., Talanov V.M. Order parameters and phase diagrams of ferroelastics with pyrochlore structure, *Ferroelectrics*, 2019, **543**, P. 1–11.
[43] Talanov M.V., Shirokov V.B., et al., Vanadium clusters formation in geometrically frustrated spinel oxide AlV_2O_4, *Acta Crystallogr. B*, 2018, **74**, P. 337–353.
[44] Sirotin Y.I. *Shaskol'skaya M.P. Foundations of Crystal Physics*. Nauka, Moscow, 1979.
[45] Tagantsev A.K., Cross L.E., Fousek J. *Domains in Ferroic Crystals and Thin Films*. Springer Science+Business Media, LLC, 2010, 821 p.
[46] Hlinka J., Privratska J., et al. Symmetry Guide to Ferroaxial Transitions. *Phys. Rev. Lett.*, 2016, **116**, P. 177602(1-6).
[47] Koňák Č., Kopský V., Smutný F. Gyrotropic phase transitions. *J. Phys. C: Solid State Phys.*, 1978, 11, P. 2493–2518.
[48] Talanov M.V. Group-theoretical analysis of 1:3 A-site-ordered perovskite formation. *Acta Cryst. A*, 2019, **75**, P. 379–397.
[49] Göhler B., Hamelbeck V., et al. Spin selectivity in electron transmission through self-assembled monolayers of double-stranded DNA. *Science*, 2011, **331**, P. 894–897.
[50] O. Ben Dor S. Yochelis, et al. Magnetization switching in ferromagnets by adsorbed chiral molecules without current or external magnetic field. *Nat. Commun.*, 2017, **8**, P. 14567(1-7).
[51] Naaman R., Paltiel Y., et al. Chiral Induced Spin Selectivity Gives a New Twist on Spin-Control in Chemistry. *Acc. Chem. Res.*, 2020, **53**, P. 2659–2667.
[52] Suda M., Thathong Y., et al. Light-driven molecular switch for reconfigurable spin filters. *Nat. Commun.*, 2019, **10**, P. 2455(1-7).
[53] Cheong S.-W., Talbayev, et al. Broken Symmetries. Non-reciprocity, and Multiferroicity. *npj Quantum Mater.*, 2018, **3**, P. 19.
[54] Jin, W., Drueke, E., et al. Observation of a Ferro-Rotational Order Coupled with Second-Order Nonlinear Optical Fields. *Nat. Phys.*, 2020, **16**, P. 42–46.
[55] Hayashida T., Uemura, et al. Visualization of Ferroaxial Domains in an Order-Disorder Type Ferroaxial Crystal. *Nat. Commun.*, 2020, **11**, P. 4582.
[56] Cheong S.-W., Lim S., et al. Permutable SOS (Symmetry Operational Similarity). *npj Quantum Mater*, 2021, *6*, P. 58.
[57] Hayami S., Oiwa R., Kusunose H. Electric Ferro-axial Moment as Nanometric Rotator as Source of Longitudinal Spin Current. *J. Phys. Soc. Jpn.*, 2022, **91**, P. 113702.
[58] Hayashida T., Uemura Y., et al. Phase Transition and Domain Formation in Ferroaxial Crystals. *Phys. Rev. Mater.*, 2021, *5*, P. 124409.
[59] Yokota H., Hayashida T., et al. Three dimensional Imaging of Ferroaxial Domains Using Circularly Polarized Second Harmonic Generation Microscopy. *npj Quantum Mater.*, 2022, *7*, P. 106.
[60] Waśkowska A. Gerward L., et al. Temperature-and pressure-dependent lattice behaviour of $RbFe(MoO_4)_2$. *J. Phys. Condens. Matter.*, 2010, *22*, P. 055406.
[61] Boysen H., Frey F., et al. Neutron Powder Investigation of the High-temperature Phase Transition in $NiTiO_3$. *Z. Kristallogr. – Cryst. Mater.*, 1995, *210*, P. 328–337.

Submitted 24 March 2023; revised 28 March 2023; accepted 29 March 2023

Information about the authors:

Valeriy M. Talanov – Platov South-Russian State Polytechnic University, Novocherkassk, Rostov region, 346428, Russia; ORCID 0000-0002-1269-2521; valtalanov@mail.ru

Mikhail V. Talanov – Platov South-Russian State Polytechnic University, Novocherkassk, Rostov region, 346428, Russia; Southern Federal University, Rostov-on-Don,344090, Russia; ORCID 0000-0002-5416-9579; mvtalanov@gmail.com

Vladimir B. Shirokov – Platov South-Russian State Polytechnic University, Novocherkassk, Rostov region, 346428, Russia; Southern Federal University, Rostov-on-Don,344090, Russia; Southern Scientific Center of Russian Academy of Sciences, Rostov-on-Don, 344006, Russia; ORCID 0000-0002-5267-2226; shirokov.ssc@gmail.com

Conflict of interest: the authors declare no conflict of interest.

NANOSYSTEMS:
PHYSICS, CHEMISTRY, MATHEMATICS

Potkina M.N., et al. *Nanosystems: Phys. Chem. Math.*, 2023, **14** (2), 216–222.
http://nanojournal.ifmo.ru
DOI 10.17586/2220-8054-2023-14-2-216-222

Original article

Nucleation and collapse of magnetic topological solitons in external magnetic field

Maria N. Potkina[a], Igor S. Lobanov[b], Valery M. Uzdin[c]

ITMO University, St. Petersburg, 197101, Russia

[a]potkina.maria@yandex.ru, [b]lobanov.igor@gmail.com, [c]v_uzdin@mail.ru

Corresponding author: M. N. Potkina, potkina.maria@yandex.ru

ABSTRACT The dependence of the lifetimes and rates of spontaneous nucleation of topological magnetic solitons on the external magnetic field is calculated within the framework of the harmonic transition state theory for magnetic degrees of freedom. For two-dimensional magnetic skyrmions, the influence of the magnetic field on the collapse rate was found to be greater than on the nucleation rate. This is explained by the weaker dependence of the energy of the transition state on the external field compared to the energy of the metastable skyrmion. The balance of the nucleation and collapse of skyrmion rates makes it possible to determine the average equilibrium concentration of skyrmions in a thin film as a function of the external field and temperature. It is shown that skyrmion and antiskyrmion states can exist simultaneously in quasi-two-dimensional thin films in tilted external magnetic field. The minimum energy paths for the collapse of these topological solitons and magnetic configurations in the vicinity of saddle point have been found and compared.

KEYWORDS transition state theory, topological magnetic solitons, nucleation, collapse, lifetime.

ACKNOWLEDGEMENTS The study was supported by the Russian Science Foundation grant No. 22-72-00059, https://rscf.ru/en/project/22-72-00059/.

FOR CITATION Potkina M.N., Lobanov I.S., Uzdin V.M. Nucleation and collapse of magnetic topological solitons in external magnetic field. *Nanosystems: Phys. Chem. Math.*, 2023, **14** (2), 216–222.

1. Introduction

Magnetic skyrmions, antiskyrmions and other structures with a topological charge are currently considered as promising elements for creating a new generation of magnetic racetrack memory [1]. This technology assumes that information is encoded in localized magnetic structures that can move at speeds of up to several kilometers per second along magnetic tracks. Devices for writing and reading information do not move, which increases the performance and energy efficiency of magnetic memory. The small size of the information carriers makes it possible to achieve high density of information storage [2–4].

The fundamental issues of using topological solitons as bits of magnetic memory are their stability with respect to thermal fluctuations and the ability to write, read, delete and move information contained in a sequence of magnetic structures.

The problem of stability becomes especially relevant as the size of magnetic elements, which determine the density of information storage, decreases. From a theoretical point of view, the quantitative estimate of the stability and calculation of the lifetime of magnetic states are complex problems associated with the fundamental problem of "rare events". The rate of magnetic transitions associated with the nucleation and collapse of localized topological magnetic structures as a whole is 10–12 orders of magnitude lower than the frequency of oscillations of individual magnetic moments in the system. Therefore, stochastic modeling can be carried out in a very limited range of high temperatures, and standard stochastic methods do not allow one to determine quantitative characteristics of stability, such as the lifetimes of long-lived topological magnetic states. However, due to the difference in the time scales of the collective and individual motion of magnetic moments, statistical approaches such as the transition state theory (TST) [5] or the Kramers-Langer method can be used to analyze the rates of magnetic transitions [6].

These approaches are based on the analysis of the multidimensional energy surface of the system, the search for minimal energy paths (MEP) between states corresponding to certain magnetic configurations, the calculation of energy barriers between such states and the rates of overcoming these barriers [7]. Methods of statistical physics have shown their effectiveness for describing the thermal stability of a wide class of magnetic systems from clusters of several atoms [8] to micromagnetic structures [9]. The TST was used to estimate the activation barriers for the decay of skyrmions in thin chiral films under conditions of restricted sample geometry, in an external magnetic field, and in the presence of impurities [10–12]. This theory has also been used to evaluate the lifetime of three-dimensional hopfions [13], as well as quasi-two-dimensional skyrmions in antiferromagnets [14] and synthetic antiferromagnets [15].

The task and technology of recording information by creating specific topological magnetic configurations is even more difficult, since it is necessary to take into account both thermal fluctuations and certain external impacts that should

cause the transition [16]. The process of nucleation of topological structures can be induced by an additional magnetic field [17], polarized spin current [18] or electric field impulses [19]. Furthermore, for any practical application of topological solitons, it is necessary to take into account thermal fluctuations, the presence of impurities and structural defects [20]. Therefore, TST for magnetic degrees of freedom, which was used to quantify the lifetime of magnetic states at an arbitrary temperature, is an adequate method for describing such effects.

The problem of nucleation of topological structures under the influence of thermal fluctuations has much in common with the TST-estimation of the stability of such structures. In this case, the topologically trivial ground state of the system should be chosen as the initial state, and the metastable state with a magnetic skyrmion should be considered as the final state. After finding the MEP, the activation barrier is determined by the energy difference between the transition and ground states of the system. If a skyrmion is metastable, the activation barrier for nucleation is higher than for its collapse. The pre-exponential factor in the Arrhenius law for the nucleation of skyrmions can be computed in harmonic approximation to TST if the energy surface near the initial ferromagnetic (FM) state and near the saddle point (SP) on the energy surface corresponding to the transition state is approximated by a quadratic expansions.

Of particular interest are the effects associated with a change in the topological charge during the nucleation of localized topological solitons. As in the case of collapse, topological protection on a discrete lattice should manifest itself through the magnitude of the energy barrier separating a spatially homogeneous state and a state with a nonzero topological charge. A decrease in the lattice constant with respect to the size of a topological soliton, while maintaining its shape, corresponds to the transition to a continuous distribution of magnetization and should shed light on the nature of topological effects in such systems. For magnetic skyrmions, such a transition gives the energy of the transition state corresponding to the minimum energy ($8\pi A$) of the topological soliton in the σ-model with the exchange stiffness A [21], regardless of other magnetic parameters – anisotropy, magnetization, and Dzyaloshinskii-Moriya interaction (DMI) [22]. Therefore, the barrier for the nucleation of a skyrmion must be the same in the continuous limit, regardless of all interactions, except for the symmetric exchange.

For skyrmions with sizes on the order of several lattice constants, the nucleation barriers depend on the entire set of magnetic parameters. The size of a skyrmion and, consequently, the processes of nucleation can be controlled by applying an external magnetic field [23, 24]. In thin films in an inclined magnetic field, solitons of different types with different topological charges can be nucleated. In particular, skyrmions and anti-skyrmions were simultaneously observed in quasi-two-dimensional films of Heusler alloys, and transitions between these states were stimulated by changing the magnetic field in the film plane [25, 26].

In the present work, we study the dependence of the nucleation rate of topological magnetic solitons on an external magnetic field, taking into account thermal fluctuations. The next section describes the model and method for calculating the intensity of the nucleation process at a given temperature and external magnetic field. Next, we present the results of calculations of the rate of spontaneous generation of magnetic skyrmions and their equilibrium concentration in magnetic fields perpendicular to the film, and study the stability of coexisting skyrmions and anti-skyrmions in an inclined field.

2. Methodology of calculations and simulated system

We consider quasi-two-dimensional topological solitons in the system described by the generalized Heisenberg model with the energy

$$E = -J\sum_{\langle i,j\rangle}\mathbf{S}_i\cdot\mathbf{S}_j - \sum_{\langle i,j\rangle}\mathbf{D}_{ij}\cdot(\mathbf{S}_i\times\mathbf{S}_j) - \mu\sum_i\mathbf{B}\cdot\mathbf{S}_i - K\sum_i(\mathrm{S}_i^{\mathrm{z}})^2, \tag{1}$$

where $\mathbf{S}_i$ is a three-dimensional vector of unit length in the direction of the magnetic moment at site i of a two-dimensional lattice. The first term describes the Heisenberg exchange with the parameter J for the magnetic moments of the nearest neighbors, the second term takes into account the DMI with the Dzyaloshinskii-Moriya vector $\mathbf{D}_{ij}$ lying in the plane of the sample perpendicular to the vector connecting the nodes of atoms i and j. The third and fourth terms correspond to the interaction with the magnetic field and the contribution of magnetic anisotropy with an easy axis along the z-axis perpendicular to the film plane. The magnetic moments μ, external field $\mathbf{B}$ and anisotropy parameters K are assumed to be the same for all lattice sites. The summation $\langle i,j\rangle$ in (1) runs over all pairs of nearest neighbor sites.

We will use two sets of parameters: the first of them corresponds to the experimentally observed skyrmions in the Pd/Fe bilayer on the Ir(111) [27] substrate: $\mu B = 0.093J$, $K = 0.07J$, D=$|\mathbf{D}_{ij}|$ = $0.32J$, J = 7 meV. Skyrmions are placed on a two-dimensional triangular lattice and have a size of the order of several nanometers. The second set describes stable at room temperature antiskyrmions 150 nm in diameter in Mn-Pt-Pd-Sn Heusler alloys [28, 29]. The numerical values of the parameters are $\mu B = 2.2\times10^{-4}J$, K=0, D=0.016 J, J = 1.83 eV.

Note that the value of the exchange parameter J is proportional to the film thickness, which was several tens of nm. Calculations with these parameters were carried out for magnetic moments at the nodes of a two-dimensional square lattice. To reduce computational costs, we used the scaling method, which allowed us to reduce the size of the system while maintaining the shape and energy of topological solitons [29]. The system under consideration was taken $N = 20$ times less dense and the model parameters were changed accordingly ($D' = ND, \mu' = \mu N^2$) [22].

The multidimensional energy surface of the system is a functional of variables that uniquely determine the magnetic configuration. As such variables for model (1), one can use the angles that specify the directions of the magnetic moments.

Then, the "geodesic nudged elastic band method" [30] can be used to find a MEP between locally stable states. Instead we will use here the Cartesian coordinates for the vectors of magnetic moments, and the condition of the constancy of the magnitude of the magnetic moments at each site will be taken into account by introducing Lagrange multipliers. This approach allows to avoid singularities and simplifies computations of Hessians of energy [7,31]. For the rate of nucleation processes k_{nuc} in the harmonic approximation of TST, one can obtain an expression corresponding to the Arrhenius law

$$k_{nuc} = k_0 \exp\left(-\frac{E_{SP}}{k_B T}\right). \tag{2}$$

The activation energy of the skyrmion nucleation process is equal to the energy of the SP on the MEP E_{SP} relative to the FM state.

The pre-exponential factor, as in the case of collapse, can be written as the product of the dynamic and entropy parts:

$$k_0 = \frac{1}{2\pi} k_{dyn} k_{ent}. \tag{3}$$

The dynamic prefactor k_{dyn} depends only on the shape of the energy surface near the transition state. In the framework of TST, this contribution arises from the calculation of the rate of crossing the transition state from FM to the skyrmion state. Within the harmonic approximation, the dynamic prefactor for nucleation and collapse of skyrmion is the same. This factor can be calculated as follows [13]:

$$k_{dyn} = \sqrt{\frac{\boldsymbol{b} \cdot \mathcal{H}^{SP} \boldsymbol{b}}{|\zeta_s^1|}}, \quad b_i = \frac{\gamma}{\mu} \zeta_s^1 S_i^{SP} \times e_i. \tag{4}$$

Here S_i^{SP} is the spin configuration at the SP, $\mathcal{H}^{SP}$ is the Hessian of energy in this point, and $\boldsymbol{e}$ is the unit eigenvector corresponding to the only negative eigenvalue ζ_s^1 of the operator $\mathcal{H}^{SP}$. The constant γ is the gyromagnetic ratio. The entropy prefactor is the square root of the ratio of the modulus of determinants of Hessians $\mathcal{H}^{FM}$ and $\mathcal{H}^{SP}$ at homogeneous FM state and the SP respectively.

$$k_{ent} = \sqrt{\frac{\det \mathcal{H}^{FM}}{|\det \mathcal{H}^{SP}|}}. \tag{5}$$

If the harmonic expansion of energy near the saddle point contains zero modes corresponding to degrees of freedom for which the energy does not change significantly, then the entropy prefactor contains an additional factor k_{ZM} depending on temperature:

$$k_{ZM} = \frac{V_{SP}}{(2\pi k_B T)^{\frac{P_{SP}}{2}}}, \tag{6}$$

where V_{SP} give the volume corresponding to zero modes while P_{SP} the number of such modes. The dimensionality of $\mathcal{H}^{SP}$ in this case decreases by P_{sk}. It is worth noting that for the reverse process corresponding to the collapse of a topological soliton into a FM state, zero modes can also exist in the initial state. In this case, a factor similar to (6) will appear in the denominator of the expression for the entropy factor (5).

Knowing the rate of collapse k_{col} and nucleation k_{nuc} of skyrmion states makes it possible to estimate the equilibrium concentration of skyrmions n at arbitrary temperatures. In the equilibrium, the number of generated and decayed skyrmions per unit time should be the same. A skyrmion can be nucleated at any site of the lattice, and can be destroyed only where it was. The concentration is governed by the balance equation:

$$n k_{col} = n_s k_{nuc}. \tag{7}$$

where n_s is the density of sites in the lattice. Substituting the values of the rates and taking into account that the dynamic prefactor for decay and nucleation are the same, we obtain

$$n = n_s \frac{V_{SK}}{(2\pi k_B T)^{\frac{P_{SK}}{2}}} \exp\left(-\frac{E_{SK}}{k_B T}\right) \cdot \sqrt{\frac{\det \mathcal{H}^{FM}}{\det \mathcal{H}^{SK}}}, \tag{8}$$

where E_{SK} is the energy of the skyrmion state relative to the FM state. By P_{SK} and V_{SK} we have denoted, respectively, the number of zero modes and their volume for the equilibrium skyrmion state. The equilibrium concentration does not depend on the shape of the surface near the SP and the height of the energy barrier between the states. Only the time of equilibrium establishment depends on these quantities.

3. Results

Let us first consider the possibility of controlling the process of skyrmion nucleation due to thermal fluctuations in the PdFe bilayer on the Ir(111) surface. Tunneling microscopy methods have shown that in this system the equilibrium size of skyrmions and their lifetime depend on the strength of the external magnetic field. At a temperature of 4.2 K, the skyrmion structure remains stable up to fields of 5–6 T [27] . This means that skyrmions do not appear or disappear during the observation time if the current from the tip of the tunneling microscope used to observe the skyrmions is small enough [17]. As the temperature rises, the nucleation and collapse of skyrmions occur more and more often, and then the

system passes into a fluctuation-disordered state, in which, along with skyrmions, there are also high-energy non-collinear localized and delocalized magnetic states [32].

Fig. 1 shows the temperature dependence of the average lifetime of skyrmion states, the average waiting time for the nucleation of a skyrmion at a selected lattice site, and the equilibrium concentration of skyrmions after the establishment of thermodynamic equilibrium. Circles and squares correspond to external magnetic fields $B = 3.75$ T and $B = 4.6$ T, respectively.

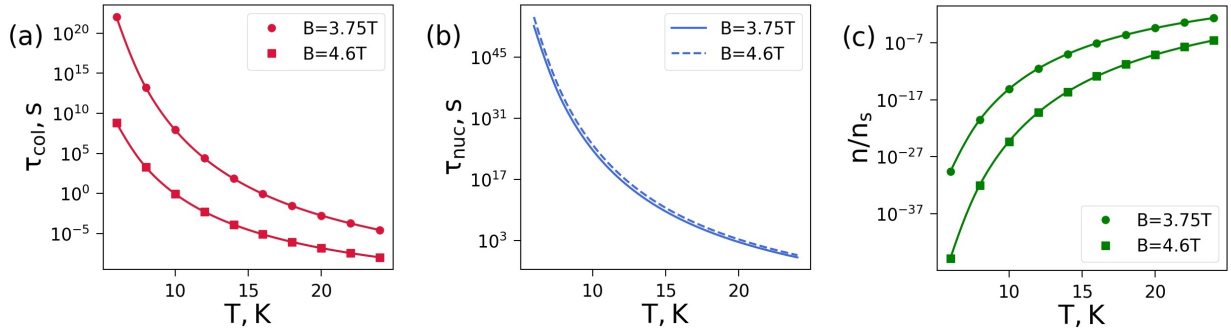

FIG. 1. Temperature dependence of the average waiting time for the collapse of a skyrmion τ_{col} (a), its nucleation τ_{nuc} (b) and the equilibrium number of skyrmions per lattice site (c) for two values of the external magnetic field $B = 3.75$ T (circles) and $B = 4.6$ T (squares)

At low temperatures up to 10 K, the spontaneous nucleation of skyrmions due to thermal fluctuations is practically impossible. The lifetime of already existing skyrmions ranges from a few seconds at a field of 3.75 T to several years at 4.6 T, as seen in Fig. 1a. In this case, the equilibrium concentration of skyrmions is negligible. As the temperature rises, the probability of collapse and nucleation also increases, but for nucleation it occurs faster in accordance with Fig. 1b. As a result, the equilibrium concentration of skyrmions increases, and in the region of 1000×1000 lattice sites, one can expect the appearance of several skyrmions in moderate magnetic fields and temperature 15–20 K, as follows from Fig. 1c.

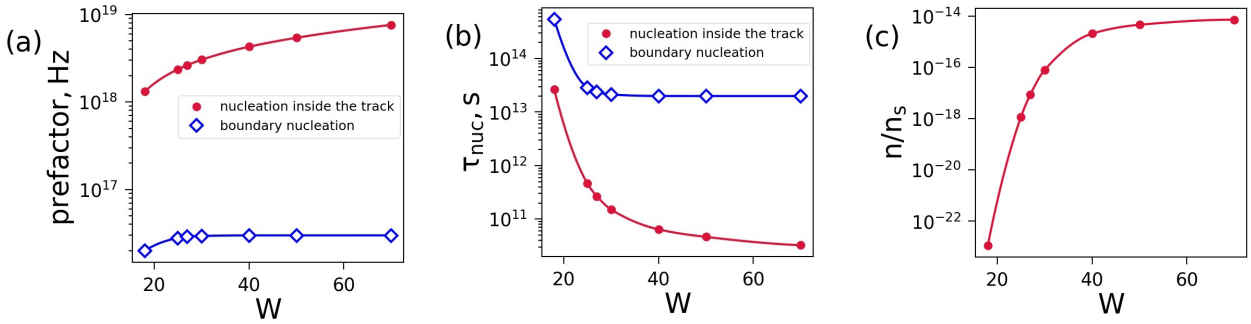

FIG. 2. The pre-exponential factor k_{nuc} for the rate of skyrmion nucleation on the magnetic track (a) and the average waiting time τ_{nuc} for nucleation at a particular lattice site (b) depending on the track width W. Filled red circles and empty blue rhombuses correspond to nucleation in the middle and at the border of the track, respectively. Equilibrium skyrmion concentration inside the track n/n_s as function of track width (c). T=15 K, B =4.6 T

The increase in concentration with temperature is associated with both energy and entropy effects. Note that the skyrmion and the transition state for collapse (nucleation) are metastable. As the temperature increases, the exponential factor in the Arrhenius law for the lifetime decreases, and the entropy factor $1/k_{ent}$ plays an increasingly important role. The entropy of the skyrmion state is greater than that of the transition state, and in the transition state it is greater than that of the ground state. This leads to the relation $k_{nuc} \gg k_{col}$. Therefore, with an increase in temperature, the rate of nucleation processes rapidly increases and can be comparable with the rate of skyrmion collapses and even exceed it. In which state it is more likely to detect a system at a fixed temperature depends on the magnitude of the external magnetic field. This has been done to write and delete single magnetic skyrmions using current injection from the tip of tunnel microscope [17].

In the practical development of technologies based on the use of topological solitons, it is necessary to take into account structural defects and the influence of boundaries on the stability, collapse, and nucleation of localized topological states [10, 12]. The nucleation of skyrmions under the action of the current from the tip of tunneling microscope occurs usually near local defects [17]. Such defects and the proximity of the sample boundary reduce the energy of the transition

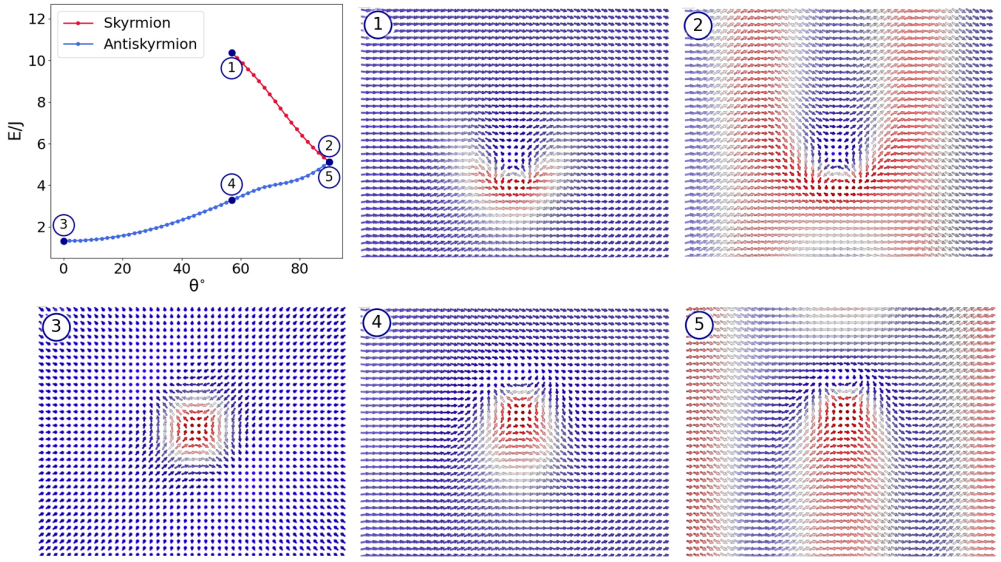

FIG. 3. Energy of antiskyrmion and skyrmion states as a function of the angle θ of inclination of the magnetic field. Configurations (1), (2), (3), (4) and (5) correspond to the marked points on the graph and show the evolution of the skyrmion and antiskyrmion states with an increase in angle θ

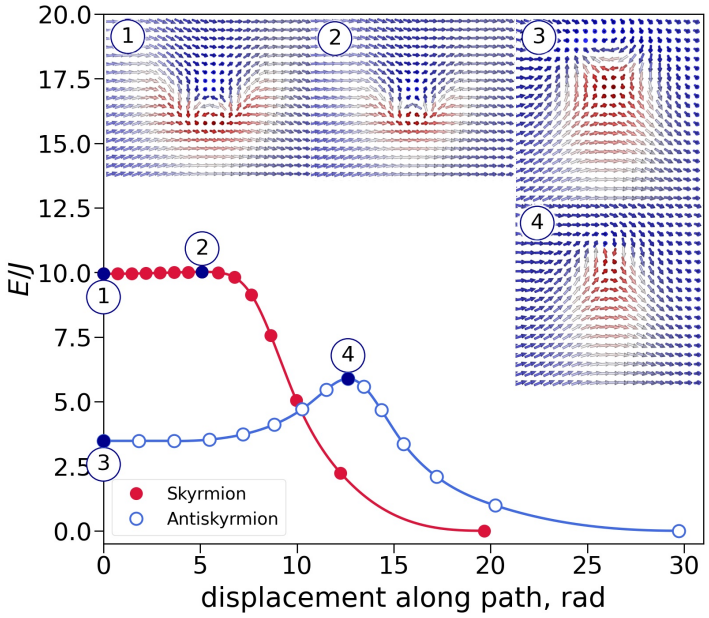

FIG. 4. MEPs for the collapse of a skyrmion (solid red circles) and an antiskyrmion (empty blue circles) in an inclined magnetic field (angle of inclination 60°). The insets show the magnetic configurations corresponding to equilibrium skyrmion (1), transition state during the decay of a skyrmion (2), equilibrium antiskyrmion (3), and the transition state during the decay of the antiskyrmion

state and, consequently, the activation barrier for collapse and nucleation of skyrmions. In addition, another way for the creation (annihilation) of skyrmions at the border has appeared [7, 22]. Therefore, nucleation processes, taking into account the finite size of the system, such as magnetic track of finite width, are of particular interest.

Fig. 2a shows the dependence of the pre-exponential factor for skyrmion nucleation inside the magnetic track and at its boundary on the track width W. It can be seen that the prefactor for nucleation at the boundary is significantly lower than for such a process inside the sample, and the characteristic waiting time for nucleation at the boundary is much longer, as can be seen in Fig. 2b. Besides, there are fewer atoms at the border of the track than inside it. Therefore, when calculating the average concentration, nucleation at the boundary can be neglected. Fig. 2c shows the equilibrium concentration of skyrmions localized in the magnetic track. It is negligibly small for narrow layers, but with increasing width it reaches a value corresponding to the concentration in an unlimited sample.

Let us now turn to the behavior of topological solitons in an inclined magnetic field. Here, we study the antiskyrmion state in magnetic field tilted with respect to the normal of the sample surface of Heusler alloy [28]. Plot in Fig. 3 (top left) shows the energy of antiskyrmion state as a function of slope angle θ (blue curve). When θ reaches a value of about 57°, the coexistence of the skyrmion state with the antiskyrmion state is observed (red curve). Fig. 3 (1)-(5) show the evolution of skyrmion and antiskyrmion state with an increase in the angle of inclination of the magnetic field. Coexisting particles with opposite topological charges were discovered in experimental works [25, 26]. There, counterpart state was obtained from antiskyrmion by tilting the magnetic field, which is in agreement with our simulation.

Fig. 4 shows the MEPs for the collapse of an antiskyrmion and a skyrmion into a homogenious FM ground state. These topological solitons simultaneously exist in a tilted magnetic field with inclination angle $\theta = 60^\circ$ but the energy of a skyrmion is greater than that of an antiskyrmion, and the barrier for the collapse of the skyrmion is much lower. However, increasing θ to 90° which correspond to an in-plane magnetic field leads to the identic MEPs and barriers. In the inserts of Fig. 4 the magnetic configurations in the initial states and at saddle points are shown. It is worth to note that the size of a noncollinear structure in the saddle point in an inclined magnetic field does not decrease significantly, in contrast to the case of a field perpendicular to the surface. This may be important for the value of entropy prefactor in Arrhenius law for lifetime and therefore affect the stability of the states [33].

4. Conclusion

The possibility of controlling the processes of spontaneous nucleation and collapse of topological magnetic solitons can be implemented by choosing the temperature regime and the external magnetic field. This allows writing and deleting information encoded in a sequence of topological magnetic structures. In an inclined magnetic field, localized magnetic configurations with different topological charges can simultaneously exist. Their stability and the activation energy of the nucleation and collapse can be operated by changing the angle of inclination of the magnetic field.

References

[1] Parkin S.S.P., Hayashi M., Thomas L. Magnetic Domain-Wall Racetrack Memory. *Science*, 2008, **320**, **5837**, P. 190–194.

[2] Wiesendanger R. Nanoscale magnetic skyrmions in metallic films and multilayers: A new twist for spintronics. *Nat. Rev. Mater.*, 2016, **1**, P. 16044.

[3] Finocchio G., Büttner F., Tomasello R., Carpentieri M., Kläu M. Magnetic skyrmions: from fundamental to applications. *J Phys. D: Appl. Phys.*, 2016, **49**, P. 423001.

[4] Fert A., Reyren N., Cros V. Magnetic skyrmions: Advances in physics and potential applications. *Nat. Rev. Mater.*, 2017, **2**, P. 17031.

[5] Bessarab P.F., Uzdin V.M., Jónsson H. Harmonic transition-state theory of thermal spin transitions. *Phys. Rev. B*, 2012, **85**, P. 184409.

[6] Coffey W.T., Garanin D.A., Mccarthy D.J. Crossover formulas in the Kramers theory of thermally activated escape rates—application to spin systems. *Adv. Chem. Phys.*, 2001, **117**, P. 483–765.

[7] Lobanov I.S., Potkina M.N., Uzdin V.M. Stability and lifetimes of magnetic states of nano- and microstructures (Brief review) *JETP Lett.*, 2021 **113**, P. 833–847.

[8] Bessarab P.F., Uzdin V.M., Jónsson H. Size and Shape Dependence of Thermal Spin Transitions in Nanoislands. *Phys. Rev. Lett.*, 2013, **110**, P. 020604.

[9] Suess D., Vogler C., Bruckner F., Heistracher P., Slanovc F., Abert, C. Spin torque efficiency and analytic error rate estimates of skyrmion racetrack memory. *Sci. Rep.*, 2019, **9**, P. 4827.

[10] Uzdin V.M., Potkina M.N., Lobanov I.S., Bessarab P.F., Jónsson H. The effect of confinement and defects on the thermal stability of skyrmions. *Physica B: Condens. Matter.*, 2018, **549**, 15, P. 6–9.

[11] Uzdin V.M., Potkina M.N., Lobanov I.S., Bessarab P.F., Jónsson H. Energy surface and lifetime of magnetic skyrmions. *J. Magn. Magn. Mater.*, 2018, **459**, P. 236–240.

[12] Potkina M.N., Lobanov I.S., Uzdin V.M. Nonmagnetic impurities in skyrmion racetrack memory *Nanosystems: phys., chem., math.*, 2020, **11** (6), P. 628–635.

[13] Lobanov I.S., Uzdin V.M. Lifetime, collapse, and escape paths for hopfions in bulk magnets with competing exchange interactions. *Phys. Rev. B*, 2023, **107**, P. 104405.

[14] Potkina M.N., Lobanov I.S., Jónsson H., Uzdin V.M. Skyrmions in antiferromagnets: Thermal stability and the effect of external field and impurities. *J. Appl. Phys.*, 2020, **127**, P. 213906.

[15] Voronin K.V. Lobanov I.S., Uzdin V.M. Activation Energy and Mechanisms for Skyrmion Collapse in Synthetic Antiferromagnets *JETP Lett.*, 2022 **116**, P. 242–248.

[16] Sampaio J., Cros V., Rohart S., Thiaville A., Fert A., Nucleation, stability and current-induced motion of isolated magnetic skyrmions in nanostructures. *Nat. Nanotech.*, 2013. **8**, P. 839

[17] Romming N., Hanneken C., Menzel M., Bickel J.E., Wolter B., von Bergmann K., Kubetzka A., Wiesendanger R. Writing and Deleting Single Magnetic Skyrmions. *Science*, 2013, **341**, 6146, P. 636–639.

[18] Iwasaki J., Mochizuki M., Nagaosa N. Current-induced skyrmion dynamics in constricted geometries. *Nat. nanotech.*, 2013, **8**, P. 742–747.
[19] Desplat, L., Meyer, S., Bouaziz, J., Buhl, P.M., Lounis, S., Dupé, B. and Hervieux, P.A. Mechanism for ultrafast electric-field driven skyrmion nucleation. *Phys. Rev. B*, 2021, **104**, P. L060409.
[20] Zhang X., Zhou Y., Song K.M., Park T.E., Xia J., Ezawa M., Liu X., Zhao W., Zhao G., Woo S. Skyrmion-electronics: writing, deleting, reading and processing magnetic skyrmions toward spintronic applications. *J. Phys.: Cond. Mat.*, 2020, **14**, P. 143001.
[21] Belavin A.A. , Polyakov A.M. Metastable states of two-dimensional isotropic ferromagnets. *JETP Lett.*, 1975 **22**, P. 503–506. [JETP Lett. **22**, 245 (1975)].
[22] Potkina, M.N., Lobanov, I.S., Jónsson, H., Uzdin, V.M. Lifetime of skyrmions in discrete systems with infinitesimal lattice constant. *J. Magn. Magn. Mater.*, 2022, **549**, P. 168974.
[23] von Malottki S., Bessarab P.F., Haldar S., Delin A. and Heinze S. Skyrmion lifetime in ultrathin films. *Phys. Rev. B*, 2019, **99**, P. 060409.
[24] Capic D., Garanin D.A., Chudnovsky E.M., Skyrmions in an oblique field. *J. Magn. Magn. Mater.*, 2021, **537**, P. 168215.
[25] Peng L., Takagi R., Koshibae W., Shibata K., Nakajima K., Arima T.H., Nagaosa N., Seki S., Yu X. Tokura, Y., Controlled transformation of skyrmions and antiskyrmions in a non-centrosymmetric magnet. *Nat. nanotech.*, 2020, **15**, P. 181–186.
[26] Jena J., Göbel B., Ma T., Kumar V., Saha R., Mertig I., Felser C., Parkin, S.S.P. Elliptical Bloch skyrmion chiral twins in an antiskyrmion system. *Nat. Commun.*, 2020, **11**, P. 1115.
[27] Hagemeister J., Romming N., von Bergmann K., Vedmedenko E.Y., Wiesendanger R. Stability of single skyrmionic bits. *Nat. Commun.*, 2015, **6**, P. 8455.
[28] Nayak A.K., Kumar V., Ma T., Werner P., Pippel E., Sahoo R., Damay F., Rößler U.K., Felser C., Parkin, S.S.P. Magnetic antiskyrmions above room temperature in tetragonal Heusler materials. *Nature*, 2017, **548**(7669), P. 561–566.
[29] Potkina M.N., Lobanov I.S., Tretiakov O.A., Jónsson H., Uzdin, V.M. Stability of long-lived antiskyrmions in the Mn-Pt-Sn tetragonal Heusler material. *Phys. Rev. B*, 2020, **102**, P. 134430.
[30] Bessarab P. F., Uzdin V. M., Jónsson H. Method for finding mechanism and activation energy of magnetic transitions, applied to skyrmion and antivortex annihilation. *Comp. Phys. Commun.*, 2015, **196**, P. 335.
[31] Lobanov, I. S., Uzdin, V. M. The lifetime of micron scale topological chiral magnetic states with atomic resolution. *Comp. Phys. Commun.*, 2021, **269**, P. 108136.
[32] Rózsa L., Simon E., Palotás K., Udvardi L., Szunyogh L. Complex magnetic phase diagram and skyrmion lifetime in an ultrathin film from atomistic simulations. *Phys. Rev. B*, 2016, **93**, P. 024417.
[33] Wang C., Du H., Zhao X., Jin C., Tian M., Zhang Y., Che R. Enhanced stability of the magnetic skyrmion lattice phase under a tilted magnetic field in a two-dimensional chiral magnet. *Nano lett.*, 2017 **17**, P. 2921.

Submitted 15 March 2023; revised 14 April 2023; accepted 15 April 2023

Information about the authors:

Maria N. Potkina – Faculty of Physics, ITMO University, 197101 St. Petersburg, Russia; ORCID 0000-0002-1380-2454; potkina.maria@yandex.ru

Igor S. Lobanov, – Faculty of Physics, ITMO University, 197101 St. Petersburg, Russia; ORCID 0000-0001-8789-3267; lobanov.igor@gmail.com

Valery M. Uzdin – Faculty of Physics, ITMO University, 197101 St. Petersburg, Russia; ORCID 0000-0002-9505-0996; v_uzdin@mail.ru

Conflict of interest: the authors declare no conflict of interest.

NANOSYSTEMS:
PHYSICS, CHEMISTRY, MATHEMATICS

Original article

Kozlova T.O., et al. *Nanosystems: Phys. Chem. Math.*, 2023, **14** (2), 223–230.
http://nanojournal.ifmo.ru
DOI 10.17586/2220-8054-2023-14-2-223-230

Ceric phosphates and nanocrystalline ceria: selective toxicity to melanoma cells

Taisiya O. Kozlova[1,a], Anton L. Popov[2,b], Mikhail V. Romanov[2,c], Irina V. Savintseva[2,d], Darya N. Vasilyeva[1,3,e], Alexander E. Baranchikov[1,f], Vladimir K. Ivanov[1,g]

[1]Kurnakov Institute of General and Inorganic Chemistry of the Russian Academy of Sciences, Moscow, Russia
[2]Institute of Theoretical and Experimental Biophysics of the Russian Academy of Sciences, Pushchino, Russia
[3]National Research University Higher School of Economics, Moscow, Russia

[a]taisia.shekunova@yandex.ru, [b]antonpopovleonid@gmail.com, [c]rmvya@yandex.ru, [d]savintseva_irina@mail.ru, [e]dnvasileva_1@edu.hse.ru, [f]a.baranchikov@yandex.ru, [g]van@igic.ras.ru

Corresponding author: Taisiya O. Kozlova, taisia.shekunova@yandex.ru

PACS 61.66.Fn; 81.70.-q; 87.17.-d

ABSTRACT Nanocrystalline cerium dioxide is a promising inorganic UV filter for sunscreen applications due to its high UV absorbance and non-toxicity to normal cells. Nanoscale CeO_2 also showed selective cytotoxicity to cancer cells, thus ceria-containing materials are now regarded for the creation of both preventive and therapeutic compositions. At the same time, the interaction of ceria nanoparticles with cell membranes and phosphate-rich components of sunscreen compositions arise the interest to biocompatibility of ceric phosphates. Crystalline cerium(IV) phosphates can be a promising alternative for nanoscale CeO_2 due to their low solubility, high redox stability and UV protective property. However, to date, there is no information on their toxicity to cancer cells. In this work, using the MTT, Live/Dead and MMP assays, we demonstrated for the first time that the inhibitory impact of ceric phosphates $Ce(PO_4)(HPO_4)_{0.5}(H_2O)_{0.5}$ and $NH_4Ce_2(PO_4)_3$ on murine melanoma B16/F10 cell line *in vitro* is comparable to that of nanoscale CeO_2, at high (500–1000 μg/ml) concentrations.

KEYWORDS ceric phosphates, ceria, metabolic activity, reactive oxygen species, UV protectors.

ACKNOWLEDGEMENTS This work was supported by Russian Science Foundation (Grant no. 21-73-00294, https://rscf.ru/en/project/21-73-00294/) using the equipment of the JRC PMR IGIC RAS.

FOR CITATION Kozlova T.O., Popov A.L., Romanov M.V., Savintseva I.V., Vasilyeva D.N., Baranchikov A.E., Ivanov V.K. Ceric phosphates and nanocrystalline ceria: selective toxicity to melanoma cells. *Nanosystems: Phys. Chem. Math.*, 2023, **14** (2), 223–230.

1. Introduction

Cerium is one of the most common elements among rare earth metals, and, unlike most representatives of this group, is stable in two oxidation states, +3 and +4 [1,2]. Among the inorganic cerium compounds, ceria (CeO_2) is regarded as the most promising for practical uses [3]. In particular, cerium dioxide is a part of automotive three-way catalysts, it is used as the main component of polishing mixtures and abrasives, solid oxide fuel cells and protective anticorrosion coatings, it possesses high activity in a wide range of catalytic applications [4–7].

In the nanodispersed state, CeO_2 exhibits unique redox activity, acts as an inorganic antioxidant capable of protecting living systems from oxidative stress, and can perform the functions of certain enzymes – oxidoreductases, phosphatases, etc. [8–10].

In addition to outstanding biological activity, nanodispersed CeO_2 shows high light absorption in the UV range, which allows one to consider it as a promising component of sunscreen cosmetics instead of photocatalytically active nanocrystalline TiO_2 and ZnO [11–14]. Excessive exposure to sunlight, especially ultraviolet light, has been found to be harmful to the skin and can lead to photosensitivity, erythema and burns, premature aging, and even cancer [15]. A number of studies have shown that nanosized cerium dioxide exhibits selective cytotoxicity with respect to cancer cells [16–18], including skin cancer cells (e.g. melanoma) [19–21], which makes it attractive not only as a prophylactic agent, but also as a therapeutic. However, the use of nanodispersed CeO_2 in sunscreens has certain disadvantages. At a natural skin pH ($\sim$5), CeO_2 can act as prooxidant [22,23], negatively affecting the skin health. Moreover, even if the beneficial antioxidant properties of nanodispersed cerium dioxide are retained on skin surface, they can be lost due to the interaction of CeO_2 with phosphate groups presented in sunscreen components or in cell membranes [24–26]. Cerium dioxide is extremely prone to catalytic oxidation of organic compounds [27–29].

In turn, due to their low solubility and high redox stability, cerium phosphates are not expected to interact with organic compounds presented in sunscreens, thus allowing to obtain highly stable formulations with long shelf life [30,31]. High

biocompatibility of the phosphate matrix, along with high ultraviolet absorption and low photocatalytic activity of cerium phosphates, provide interest in these compounds as promising inorganic UV filters [32–38].

In our previous report [39], a comprehensive study of the sun protection characteristics and cytotoxicity of amorphous and crystalline cerium(IV) phosphates $Ce(PO_4)(HPO_4)_{0.5}(H_2O)_{0.5}$ and $NH_4Ce_2(PO_4)_3$ was performed for the first time. It was shown that $NH_4Ce_2(PO_4)_3$ is characterised by SPF (2.7) and UVAPF (2.5) values close to the corresponding characteristics of the well-known inorganic UV filters, nanocrystalline CeO_2 and TiO_2. Moreover, in a wide range of concentrations, crystalline cerium (IV) phosphates were found to be not toxic to NCTC L929 mouse fibroblast cells and human mesenchymal stem cells, and even enhanced the proliferative activity of the latter.

In this work, we studied the effect of the same crystalline cerium(IV) phosphates, $Ce(PO_4)(HPO_4)_{0.5}(H_2O)_{0.5}$ and $NH_4Ce_2(PO_4)_3$, on skin cancer cells (melanoma) in order to detect their possible selective cytotoxicity with respect to transformed cells. The toxicity evaluation of ceric phosphates to the cells is of primary importance for understanding the cytotoxicity mechanisms of CeO_2 nanoparticles, especially in biological phosphate-rich media.

2. Experimental Section

The following materials were used as received, without further purification: $Ce(NO_3)_3 \cdot 6H_2O$ (pure grade, Lanhit Russia), phosphoric acid (85 wt.% aq, $\rho = 1.689$ g/cm^3, extra-pure grade, Komponent-Reaktiv Russia), aqueous ammonia (25 wt.%, extra-pure grade, Khimmed Russia), isopropanol (extra-pure grade, Khimmed Russia), distilled water.

First, nanocrystalline CeO_2, which was also further used for the synthesis of cerium(IV) phosphates, was obtained in accordance with previously published procedure [40]. Briefly, 0.08 M cerium(III) nitrate solution in aqueous isopropanol (water : isopropanol = 1 : 1 v/v) was mixed with 3 M aqueous ammonia. The obtained yellow precipitate was washed with distilled water to a neutral pH and dried at 60°C.

To obtain crystalline ceric phosphates, 0.1 g of nanocrystalline cerium dioxide was dissolved in concentrated phosphoric acid (5 ml) at 80°C. For the synthesis of $Ce(PO_4)(HPO_4)_{0.5}(H_2O)_{0.5}$ or $NH_4Ce_2(PO_4)_3$, to the cooled solution, 35 ml of distilled water or 1.5 M aqueous ammonia was added under vigorous stirring. The resulting gel-like precipitates (∼40 ml) were placed in 100 ml Teflon autoclave and subjected to hydrothermal treatment at 180°C for 24 h. After cooling the autoclave, the precipitates were repeatedly washed using distilled water and dried at 60°C in air.

Powder X-ray diffraction (PXRD) patterns were acquired on a Bruker D8 Advance diffractometer, using Cu $K_{\alpha 1,2}$ radiation in the 2θ range of 5°–80° with 0.02° 2θ step and a signal accumulation time of no less than 0.2 s per point.

Scanning electron microscopy (SEM) images were obtained using a Carl Zeiss NVision 40 high-resolution electron microscope equipped with an Oxford Instruments X-MAX detector (80 mm^2) at an accelerating voltage of 1–2 kV.

Transmission electron microscopy (TEM) images were collected using a Leo912 AB Omega microscope. The images were obtained at an accelerating voltage of 100 kV in a bright field mode with magnifications up to ×500 000.

The cytotoxicity of nanoscale ceria and crystalline cerium(IV) phosphates were assessed *in vitro* using a murine melanoma B16/F10 cell line. The cells were seeded in 96-well plates at a density of 30 000 cells per cm^2 in a DMEM/F12 nutrient (culture) medium containing 10% fetal bovine serum. After 12 h of cultivation, the culture medium was completely replaced with an identical medium containing the suspension of cerium(IV) phosphates or CeO_2 prepared under intense magnetic stirring for 30 min. The concentration of the solid particles in DMEM/F12 medium was fairly high, 500 or 1000 μg/ml to test their acute toxicity and to be close to the concentrations of inorganic UV filters used in sunscreen formulations. In a control experiment, the culture medium was replaced with a fresh medium that did not contain either cerium(IV) phosphates or ceria. After 24, 48 or 72 h of incubation, the nutrient medium with the test substances was replaced with a serium-free culture medium DMEM/F12 containing 3-[4,5-dimethylthiazol-2-yl]-2,5-diphenyltetrazolium bromide (MTT) at a concentration of 500 μg/ml. After 3 h, the medium with MTT was removed and dimethyl sulfoxide (DMSO) was added. The plates were shaken at room temperature for 10 min to dissolve formazan crystals. The optical density of the formazan was measured on a BIO-RAD 680 photometer at 540 nm. The optical density values were recalculated as percentages of the control group. Statistical data processing was performed using GraphPad Prism software. Statistically significant differences were determined in accordance with the Welch's t-test at $0.01 < p < 0.05$ (*), $0.001 < p < 0.01$ (**), $0.0001 < p < 0.001$ (***) and $p < 0.0001$ (****). The IC_{50} value (half maximal inhibitory concentration) was used as the boundary for determining the cytotoxicity of the samples.

To assess the proportion of dead cells after incubation with the tested substances, Live/Dead assay was conducted. After 24, 48 or 72 h culture medium containing ceric phosphates or ceria was replaced with Hanks' balanced salt solution containing a mixture of fluorescent dyes Hoechst 33342 (binds to the DNA of all cells, $\lambda_{ex} = 350$ nm, $\lambda_{em} = 460$ nm) and propidium iodide (binds to the DNA of dead cells, $\lambda_{ex} = 535$ nm, $\lambda_{em} = 615$ nm). After 15 min, the cells were washed with Hanks' balanced salt solution and then analysed using a BioRad Zoe fluorescence microscope. The micrographs were further processed with ImageJ software.

To analyze the level of membrane mitochondrial potential (MMP), mitochondria were stained using a voltage-sensitive dye tetramethylrhodamine (TMRE; Lumiprobe, Russia). After 24, 48 or 72 h, the culture medium containing the tested substances was replaced with TMRE solution at 500 nM concentration ($\lambda_{ex} = 552$ nm, $\lambda_{em} = 574$ nm), then the cells were twice washed by Hanks' balanced salt solution. The analysis of the cells was performed using a BioRad Zoe fluorescence microscope and micrographs were further processed with ImageJ software. The fluorescence intensity values

were recalculated as percentages of the control group. Statistically significant differences were determined in accordance with the Welch's *t*-test at $0.01 < p < 0.05$ (*), $0.001 < p < 0.01$ (**), $0.0001 < p < 0.001$ (***) and $p < 0.0001$ (****) using GraphPad Prism software.

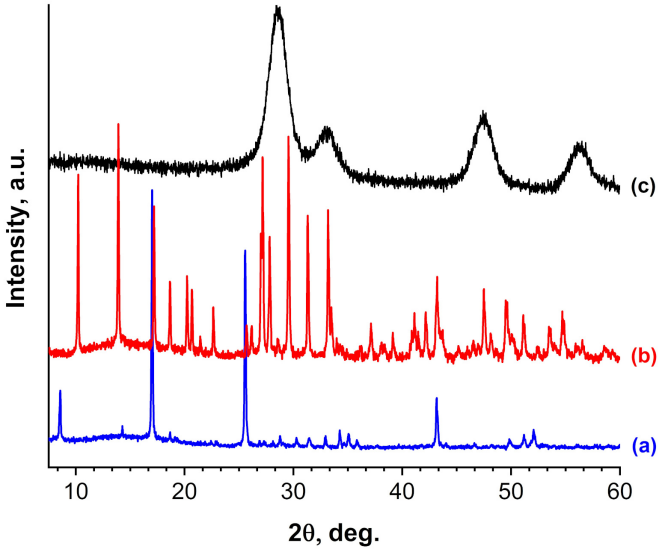

FIG. 1. Diffraction patterns for a) $Ce(PO_4)(HPO_4)_{0.5}(H_2O)_{0.5}$, b) $NH_4Ce_2(PO_4)_3$, c) CeO_2

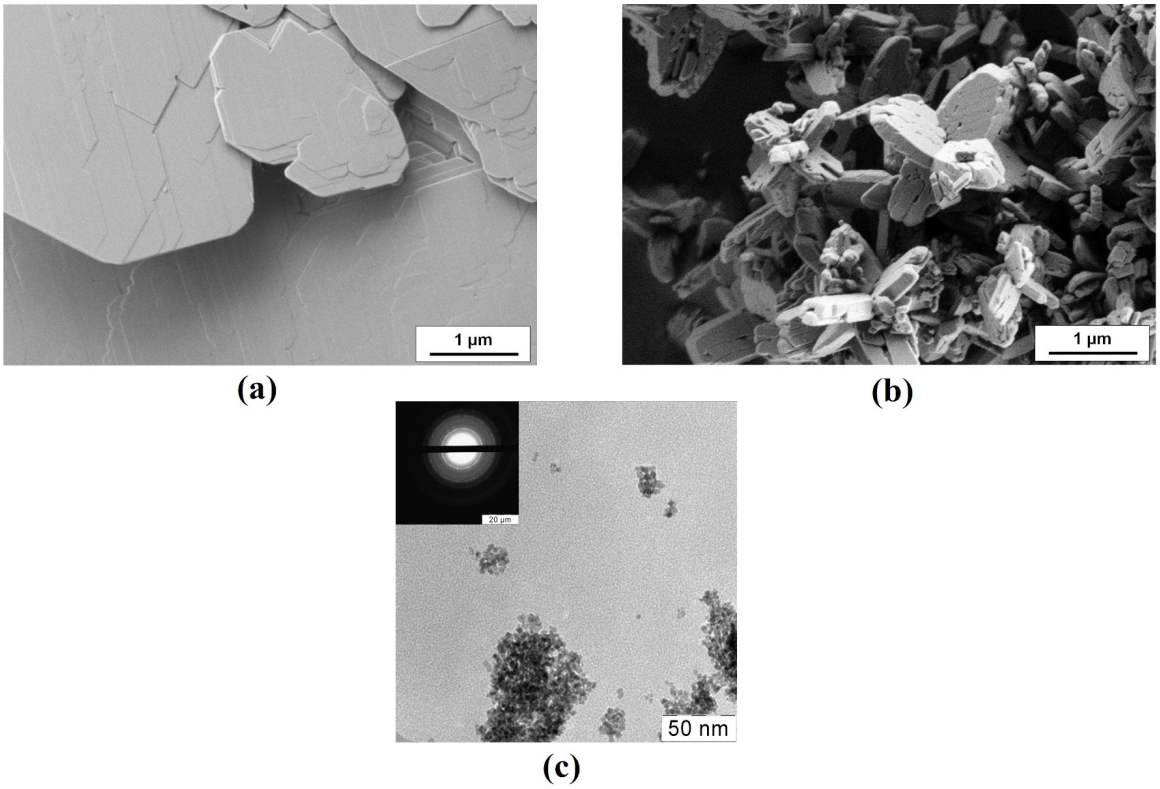

FIG. 2. SEM images for a) $Ce(PO_4)(HPO_4)_{0.5}(H_2O)_{0.5}$, b) $NH_4Ce_2(PO_4)_3$, and TEM image for c) CeO_2

3. Results and discussion

The diffraction patterns of the obtained crystalline cerium(IV) phosphates show the sets of reflections corresponding to single-phase $Ce(PO_4)(HPO_4)_{0.5}(H_2O)_{0.5}$ or $NH_4Ce_2(PO_4)_3$ (Fig. 1a,b) [41, 42]. The diffraction pattern of cerium oxide is typical to this compound in a nanocrystalline state and shows phase purity of the material (Fig. 1c). According to SEM data, $Ce(PO_4)(HPO_4)_{0.5}(H_2O)_{0.5}$ phase consisted of lamellar thin (∼100 nm) aggregates, while $NH_4Ce_2(PO_4)_3$

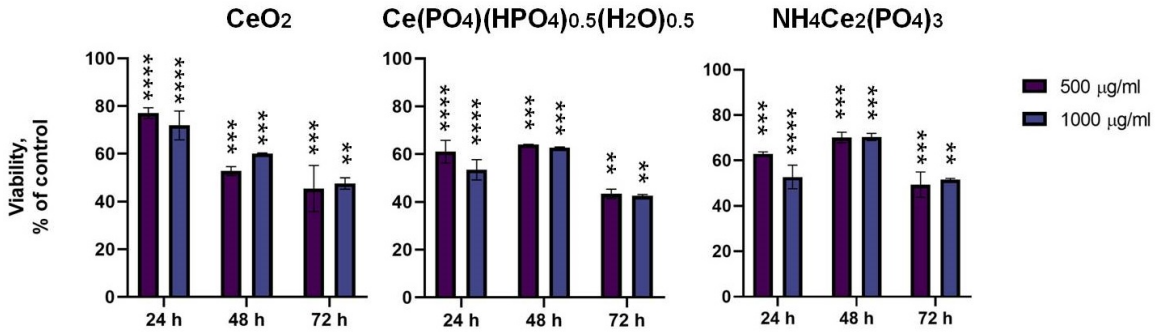

FIG. 3. The metabolic activity of B16/F10 murine melanoma cell line after 24–72 h of cultivation with cerium(IV) phosphates and ceria in concentrations of 500 or 1000 μg/ml. The data are presented as mean $\pm$ standard deviation, $0.001 < p < 0.01$ (**), $0.0001 < p < 0.001$ (***) and $p < 0.0001$ (****) via Welch's t-test

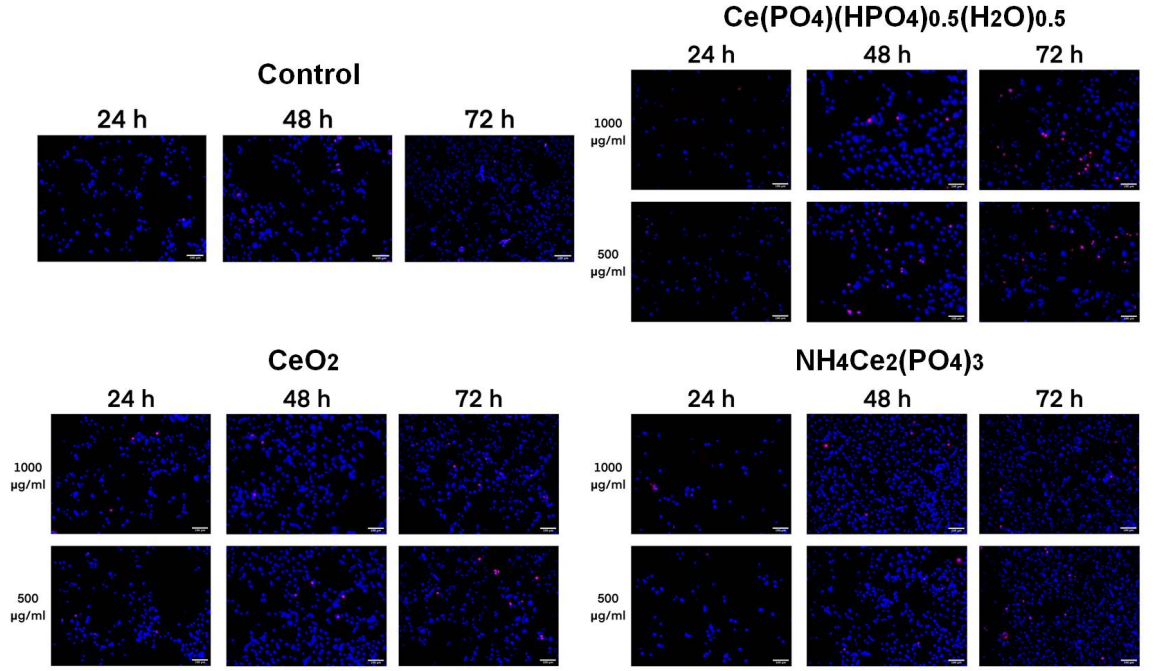

FIG. 4. Live/Dead assay of B16/F10 murine melanoma cells in the presence of ceria or cerium(IV) phosphates. Hoechst 33342 (blue) and propidium iodide (red) staining. Scale bar – 100 μm

phase consisted of elongated microparticles (Fig. 2a,b). The TEM images of CeO_2 show nanoparticles with a size of about 5 nm (Fig. 2c), which is in a good agreement with the estimates made from the results of PXRD data.

The study of the metabolic activity of B16/F10 murine melanoma cells using the MTT assay showed that the activity of NADPH-dependent oxidoreductases after 24 h of co-incubation with ceria nanoparticles decreased to 70–80% in comparison with the control group, while co-incubation of the cells with $Ce(PO_4)(HPO_4)_{0.5}(H_2O)_{0.5}$ and $NH_4Ce_2(PO_4)_3$ reduced in to 60% (Fig. 3). After 48 h co-incubation of melanoma cells with nanocrystalline cerium dioxide, their viability level reached 60% relatively to the control group, while in the case of cerium(IV) phosphates, there was no additional decrease in metabolic activity compared to the 24 h experiment. After 72 h, the metabolic activity of B16/F10 murine melanoma cells decreased to the IC_{50} value for all the test samples. Thus, $Ce(PO_4)(HPO_4)_{0.5}(H_2O)_{0.5}$ and $NH_4Ce_2(PO_4)_3$, along with cerium dioxide, significantly inhibit the viability of B16/F10 cancer cells. At the same time, the inhibitory effect of both of the cerium(IV) phosphates is almost identical, which indirectly indicates that their cytotoxicity is not due to the microstructure and microenvironment of Ce(IV) in crystal lattice.

The results of the Live/Dead assay (Fig. 4) demonstrate that co-incubation of B16/F10 murine melanoma cells with nanocrystalline CeO_2 or cerium(IV) phosphates at concentrations of 500 or 1000 μg/ml for 24–72 h does not cause a significant increase in the proportion of dead cells. This indicates that the studied samples have a toxic, but not lethal effect on the cells.

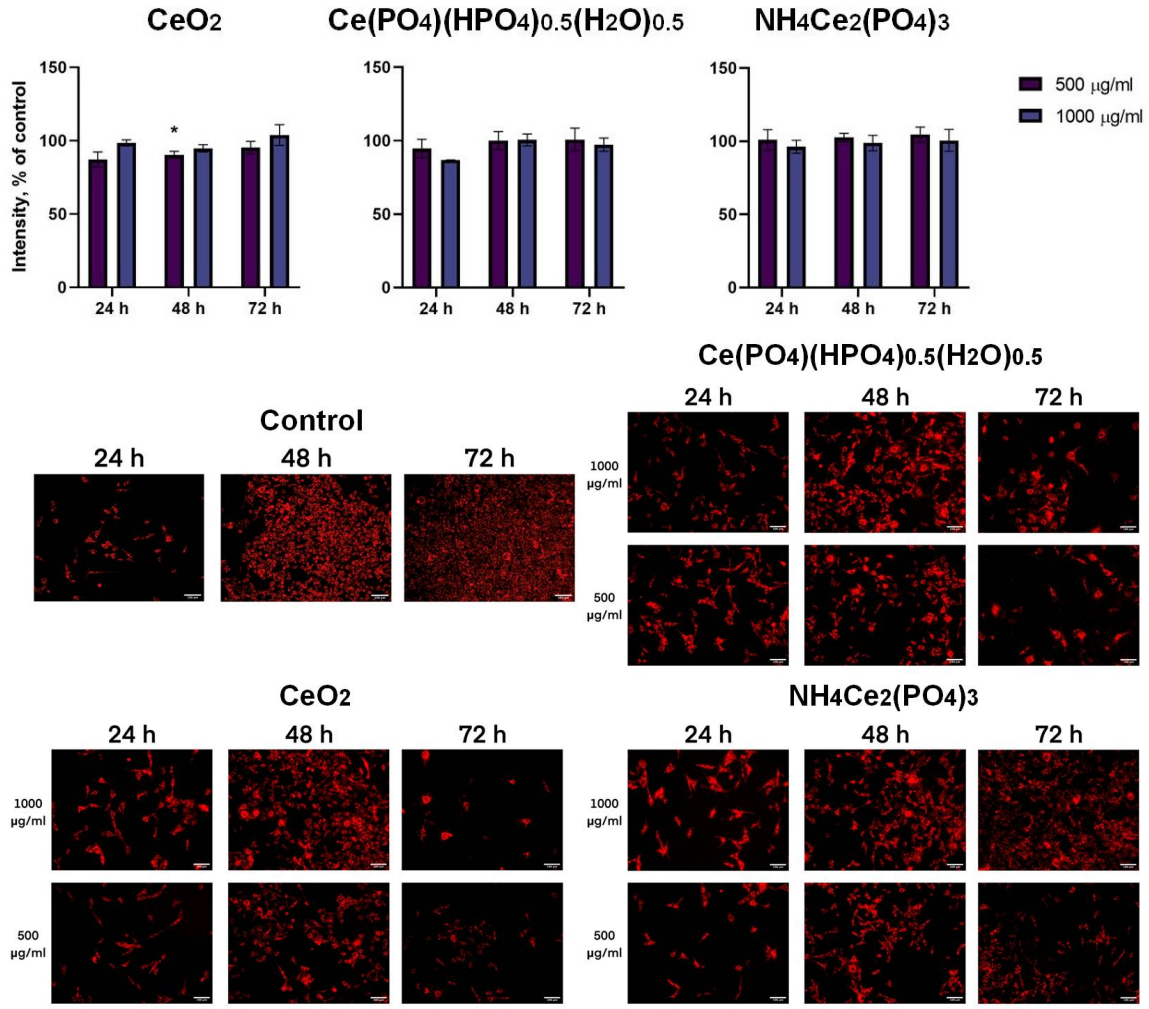

FIG. 5. Quantitative (top) and qualitative (bottom) analysis of the mitochondrial membrane potential level of B16/F10 murine melanoma cells *in vitro*. The assay was carried out after 24, 48 or 72 h of co-incubation of the cells with CeO_2 or cerium(IV) phosphates at concentrations of 500 and 1000 μg/ml. Scale bar – 100 μm

Cerium-containing nanobiomaterials are redox-active and can actively participate in redox reactions, exhibiting pro- or antioxidant properties depending on their microenvironment [43]. To establish the possible mechanism of the cytotoxic effect of cerium(IV) phosphates and nanocrystalline cerium dioxide on B16/F10 murine melanoma cells, we studied the mitochondrial membrane potential using the voltage-sensitive dye tetramethylrhodamine. The MMP level is inversely connected with the level of intracellular reactive oxygen species and oxidative stress state of the cells [44]. The data obtained indicate that the co-incubation of nanocrystalline ceria or cerium(IV) phosphates at concentrations of 500 and 1000 μg/ml with B16/F10 murine melanoma cells did not resulted in a significant decrease in the MMP level of the cells (Fig. 5a). At the same time, a qualitative assessment (Fig. 5b) shows that in the presence of CeO_2, $Ce(PO_4)(HPO_4)_{0.5}(H_2O)_{0.5}$ or $NH_4Ce_2(PO_4)_3$ crystalline particles, the appearance of the cells changed. The increase in the size of the cells, changes in the number of outgrowths, and hypervascularization was observed. Such morphological changes are characteristic of apoptotic or senescent cells [45], being the markers of the toxicity.

Thus, within the framework of this work, the selective cytotoxicity of cerium(IV) phosphates to melanoma cells was assessed for the first time. It should be noted that, to date, selective cytotoxicity of nanocrystalline cerium dioxide to various types of cancer cells along with its protective action to normal cells was abundantly exemplified [46], but the mechanisms of such an effect are still under debates. Lysosomal injury [47], oxidative stress induction [48], interference with the nutrient transport functions of the membrane [49], and mechanical membrane disruption [50] are considered as the most probable reasons for the suppression of cancer cells viability by cerium dioxide. At the same time, there is no consensus on the factors initiating the cytotoxic effect, it can be associated with both the unique redox properties of nanosized CeO_2 [51] and redox-independent mechanisms involving the effect of free cerium ions in the cells microenvironment [52, 53]. In the latter case, the problem of solubility of ceric compounds in biological media is of high importance, but it is poorly discussed. In particular, Schwabe et al. [54] found that ceria nanoparticles release free cerium

species at pH below 4.6 and, in the presence of strong chelating agents, even at pH 8. Dahle et al. [55] showed that CeO_2 dissolution effect is significant at pH < 5 and is inversely proportional to surface area of the nanoparticles. Plakhova et al. [56] calculated the solubility product constant for ceria nanoparticles ($\log K_{sp} = -59.3 \pm 0.3$ in 0.01 M $NaClO_4$) and demonstrated that solubility behavior of CeO_2 in neutral and alkaline media is mostly pH independent, $Ce(OH)_{4(aq)}$ being a predominant cerium form in aqueous solutions. Avramescu et al. [57] detected that solubility of CeO_2 nanoparticles at the 10 mg/l concentration in DMEM cell culture medium is significantly higher than in water.

Note that, for cerium(IV) phosphates, the data is even more scarce, the solubility of $Ce(PO_4)(HPO_4)_{0.5}(H_2O)_{0.5}$ was reported to be lower than 1 mg/l in an aqueous medium at pH 1.3 [58], while in 1 M alkaline aqueous solution, the structure of this compound was reported to degrade completely due to the hydrolysis and the formation of Ce–O–Ce bonds [59].

Thus, it is obvious that in order to find the reasons for the selective cytotoxicity of different cerium(IV) phosphates, it is necessary to conduct comprehensive and detailed studies, including analysis of the chemical stability of cerium(IV) phosphates in biological media at various pH levels. However, the results obtained in this work can become a starting point for further studies of cerium(IV) phosphates, their possible inorganic UV filter applications, as well as their ability to counteract the negative delayed effects of ultraviolet irradiation associated with skin melanoma.

4. Conclusions

In this paper, we compared the cytotoxicity of nanoscale ceria and crystalline cerium(IV) phosphates $Ce(PO_4)(HPO_4)_{0.5}(H_2O)_{0.5}$ or $NH_4Ce_2(PO_4)_3$ to B16/F10 murine melanoma cells *in vitro*. The toxicity was assessed at high concentrations of the solid particles, relevant to the content of inorganic components in sunscreen compositions. The MTT assay showed that the metabolic activity of B16/F10 murine melanoma cells decreases by about 40% after their contact with cerium(IV) phosphates, being even higher than for the CeO_2 nanoparticles. The IC_{50} value was reached after 72 h of co-incubation of B16/F10 murine melanoma cells with ceria or ceric phosphates. The co-incubation of $Ce(PO_4)(HPO_4)_{0.5}(H_2O)_{0.5}$, $NH_4Ce_2(PO_4)_3$ or CeO_2 with cancer cells resulted in the changes in their morphology supporting the toxic effect of cerium-based materials to cancer cells. We believe that our results can also contribute to the understanding of the cytotoxicity of nanoscale CeO_2 in phosphate-rich biological media.

References

[1] Achary S.N., Bevara S., Tyagi A.K. Recent progress on synthesis and structural aspects of rare-earth phosphates. *Coord. Chem. Rev.*, 2017, **340**, P. 266–297.

[2] Behrsing T., Deacon G.B., Junk P.C. The chemistry of rare earth metals, compounds, and corrosion inhibitors. *Rare Earth-Based Corrosion Inhibitors*, Elsevier, Amsterdam, 2015, 1–37 p.

[3] Sroor F.M.A., Edelmannand F.T. Tetravalent chemistry: Inorganic. *Rare Earth Elem. Fundam. Appl.*, John Wiley & Sons Ltd, Chichester, 2012, P. 313–320.

[4] Scirè S., Palmisano L. *Cerium and cerium oxide: A brief introduction. Cerium Oxide (CeO_2): Synthesis, Properties and Applications*, Elsevier, Amsterdam, 2019, 1–12 p.

[5] Montini T., Melchionna M., Monai M., Fornasiero P. Fundamentals and Catalytic Applications of CeO_2-Based Materials. *Chem. Rev.*, 2016, **116**(10), P. 5987–6041.

[6] Mishra U.K., Chandel V.S., Singh O.P. A review on cerium oxide–based catalysts for the removal of contaminants. *Emergent Mater.*, 2022, **5**(5), P. 1443–1476.

[7] Voncken J.H.L. *The Rare Earth Elements*. Springer International Publishing, Switzerland, 2016, 1–127 p.

[8] Ermakov A., Popov A., Ermakova O., Ivanova O., Baranchikov A., Kamenskikh K., Shekunova T., Shcherbakov A., Popova N., Ivanov V. The first inorganic mitogens: Cerium oxide and cerium fluoride nanoparticles stimulate planarian regeneration via neoblastic activation. *Mater. Sci. Eng. C*, 2019, **104**, P. 109924.

[9] Shcherbakov A.B., Reukov V.V., Yakimansky A.V., Krasnopeeva E.L., Ivanova O.S., Popov A.L., Ivanov V.K. CeO_2 Nanoparticle-Containing Polymers for Biomedical Applications: A Review. *Polymers*, 2021, **13**(6), P. 924.

[10] Rajeshkumar S., Naik P. Synthesis and biomedical applications of Cerium oxide nanoparticles – A Review. *Biotechnol. Reports*, 2018, **17**, P. 1–5.

[11] Egambaram O.P., Kesavan P.S., Ray S.S. Materials Science Challenges in Skin UV Protection: A Review. *Photochem. Photobiol.*, 2020, **96**(4), P. 779–797.

[12] Parwaiz S., Khan M.M., Pradhan D. CeO_2-based nanocomposites: An advanced alternative to TiO_2 and ZnO in sunscreens. *Mater. Express*, 2019, **9**(3), P. 185–202.

[13] Zholobak N.M., Shcherbakov A.B., Bogorad-Kobelska A.S., Ivanova O.S., Baranchikov A.Y., Spivak N.Y., Ivanov V.K. Panthenol-stabilized cerium dioxide nanoparticles for cosmeceutic formulations against ROS-induced and UV-induced damage. *J. Photochem. Photobiol. B*, 2014, **130**, P. 102–108.

[14] Kolesnik I.V., Shcherbakov A.B., Kozlova T.O., Kozlov D.A., Ivanov V.K. Comparative Analysis of Sun Protection Characteristics of Nanocrystalline Cerium Dioxide. *Russ. J. Inorg. Chem.*, 2020, **65**(7), P. 960–966.

[15] Gallagher R.P., Lee T.K. Adverse effects of ultraviolet radiation: A brief review. *Prog. Biophys. Mol. Biol.*, 2006, **92**(1), P. 119–131.

[16] Gao Y., Chen K., Ma J.L., Gao F. Cerium oxide nanoparticles in cancer. *Onco. Targets. Ther.*, 2014, **7**, P. 835–840.

[17] Shcherbakov A.B., Zholobak N.M., Spivak N.Y., Ivanov V.K. Advances and prospects of using nanocrystalline ceria in cancer theranostics. *Russ. J. Inorg. Chem.*, 2014, **59**(13), P. 1556–1575.

[18] Mihai M.M., Holban A.M., Călugăreanu A., Orzan O.A. Recent advances in diagnosis and therapy of skin cancers through nanotechnological approaches. *Nanostructures Cancer Ther.*, 2017, P. 285–305.

[19] Ali D., Alarifi S., Alkahtani S., AlKahtane A.A., Almalik A. Cerium Oxide Nanoparticles Induce Oxidative Stress and Genotoxicity in Human Skin Melanoma Cells. *Cell Biochem. Biophys.*, 2015, **71**(3), P. 1643–1651.

[20] Aplak E., Von Montfort C., Haasler L., Stucki D., Steckel B., Reichert A.S., Stahl W., Brenneisen P. CNP mediated selective toxicity on melanoma cells is accompanied by mitochondrial dysfunction. *PLoS One*, 2020, **15**(1), P. e0227926.

[21] Yong J.M., Fu L., Tang F., Yu P., Kuchel R.P. Whitelock J.M., Lord M.S. ROS-Mediated Anti-Angiogenic Activity of Cerium Oxide Nanoparticles in Melanoma Cells. *ACS Biomater. Sci. Eng.*, 2022, **8**(2), P. 512–525.

[22] Ni P., Wei X., Guo J., Ye X., Yang S. On the origin of the oxidizing ability of ceria nanoparticles. *RSC Adv.*, 2015, **5**(118), P. 97512–97519.

[23] De Marzi L., Monaco A., De Lapuente J., Ramos D., Borras M., Di Gioacchino M., Santucci S., Poma A. Cytotoxicity and Genotoxicity of Ceria Nanoparticles on Different Cell Lines in Vitro. *Int. J. Mol. Sci.*, 2013, **14**(2), P. 3065–3077.

[24] Singh S., Dosani T., Karakoti A.S., Kumar A., Seal S. Self W.T. A phosphate-dependent shift in redox state of cerium oxide nanoparticles and its effects on catalytic properties. *Biomaterials*, 2011, **32**(28), P. 6745–6753.

[25] Rozhin P., Melchionna M., Fornasiero P., Marchesan S. Nanostructured Ceria: Biomolecular Templates and (Bio)applications. *Nanomaterials*, 2021, **11**(9), P. 2259.

[26] Walther R., Huynh T.H., Monge P., Fruergaard A.S., Mamakhel A. Zelikin A.N. Ceria Nanozyme and Phosphate Prodrugs: Drug Synthesis through Enzyme Mimicry. *ACS Appl. Mater. Interfaces*, 2021, **13**(22), P. 25685–25693.

[27] Yabe S., Sato T. Cerium oxide for sunscreen cosmetics. *J. Solid State Chem.*, 2003, **171**(1–2), P. 7–11.

[28] Onoda H., Iwashita M. Synthesis of novel white pigments by shaking cerium compounds with phosphoric acid. *Emergent Mater.*, 2022.

[29] Masui T., Hirai H., Imanaka N., Adachi G. New sunscreen materials based on amorphous cerium and titanium phosphate. *J. Alloys Compd.*, 2006, **408–412**, P. 1141–1144.

[30] Wawrzynczak A., Feliczak-Guzik A., Nowak I. Nanosunscreens: From nanoencapsulated to nanosized cosmetic active forms. *Nanobiomaterials Galen. Formul. Cosmet. Appl. Nanobiomaterials*, 2016, P. 25–46.

[31] Seixas V.C., Serra O.A. Stability of sunscreens containing $CePO_4$: Proposal for a new inorganic UV filter. *Molecules*, 2014, **19**(7), P. 9907–9925.

[32] De Lima J.F., Serra O.A. Cerium phosphate nanoparticles with low photocatalytic activity for UV light absorption application in photoprotection. *Dyes Pigm.*, 2013, **97**(2), P. 291–296.

[33] Lima J.F., De Sousa Filho P.C., Serra O.A. Single crystalline rhabdophane-type $CePO_4$ nanoparticles as efficient UV filters. *Ceram. Int.*, 2016, **42**(6), P. 7422–7431.

[34] Onoda H., Tanaka R. Synthesis of cerium phosphate white pigments from cerium carbonate for cosmetics. *J. Mater. Res. Technol.*, 2019, **8**(6), P. 5524–5528.

[35] Sato T., Yin S. Morphology Control of Cerium Phosphates for Uv-Shielding Application. *Phosphorus Res. Bull.*, 2010, **24**, P. 43–48.

[36] Yin S., Saito M., Liu X., Sato T. Preparation and Characterization of Plate-like Cerium Phosphate / Nanosize Calcia Doped Ceria Composites by Precipitation Method. *Phosphorus Res. Bull.*, 2011, **25**, P. 68–71.

[37] Sato T., Sato C., Yin S. Optimization of Hydrothermal Synthesis of Plate-Like Hydrated Cerium Phosphates and Their Photochemical Properties. *Phosphorus Res. Bull.*, 2008, **22**, P. 17–21.

[38] Sato T., Li R., Sato C., Yin S. Synthesis and Photochemical Properties of Micaceous Cerium Phosphates. *Phosphorus Res. Bull.*, 2007, **21**, P. 44–47.

[39] Kozlova T.O., Popov A.L., Kolesnik I.V., Kolmanovich D.D., Baranchikov A.E., Shcherbakov A.B., Ivanov V.K. Amorphous and crystalline cerium(iv) phosphates: biocompatible ROS-scavenging sunscreens. *J. Mater. Chem. B*, 2022, **10**(11), P. 1775–1785.

[40] Baranchikov A.E., Polezhaeva O.S., Ivanov V.K., Tretyakov Y.D. Lattice expansion and oxygen non-stoichiometry of nanocrystalline ceria. *CrystEngComm.*, 2010, **12**(11), P. 3531–3533.

[41] Nazaraly M., Wallez G., Chanéac C., Tronc E., Ribot F., Quarton M., Jolivet J.P. The first structure of a cerium(IV) phosphate: Ab initio rietveld analysis of $Ce^{IV}(PO_4)(HPO_4)_{0.5}(H_4O)_{0.5}$. *Angew. Chemie - Int. Ed.*, 2005, **44**, P. 5691–5694.

[42] Shekunova T.O., Istomin S.Y., Mironov A.V., Baranchikov A.E., Yapryntsev A.D., Galstyan A.A., Simonenko N.P., Gippius A.A., Zhurenko S.V., Shatalova T.B., Skogareva L.S., Ivanov V.K. Crystallization Pathways of Cerium(IV) Phosphates Under Hydrothermal Conditions: A Search for New Phases with a Tunnel Structure. *Eur. J. Inorg. Chem.*, 2019, **2019**(27), P. 3242–3248.

[43] Yang Y., Mao Z., Huang W., Liu L., Li J., Li J., Wu Q. Redox enzyme-mimicking activities of CeO_2 nanostructures: Intrinsic influence of exposed facets. *Sci. Rep.*, 2016, **6**(1), P. 35344.

[44] Suski J.M., Lebiedzinska M., Bonora M., Pinton P., Duszynski J., Wieckowski M.R. Relation Between Mitochondrial Membrane Potential and ROS Formation. *Methods Mol. Biol.*, 2012, **810**, P. 183–205.

[45] Kumari R., Jat P. Mechanisms of Cellular Senescence: Cell Cycle Arrest and Senescence Associated Secretory Phenotype. *Front. Cell Dev. Biol.*, 2021, **9**, P. 645593.

[46] Shcherbakov A.B., Zholobak N.M., Ivanov V.K. Biological, biomedical and pharmaceutical applications of cerium oxide. *Cerium Oxide (CeO_2): Synthesis, Properties and Applications*, Elsevier, Amsterdam, 2020, P. 279–358.

[47] Lin S., Wang X., Ji Z., Chang C.H., Dong Y., Meng H., Liao Y.-P., Wang M., Song T.-B., Kohan S., Xia T., Zink J.I., Lin S., Nel A.E. Aspect Ratio Plays a Role in the Hazard Potential of CeO_2 Nanoparticles in Mouse Lung and Zebrafish Gastrointestinal Tract. *ACS Nano*, 2014, **8**(5), P. 4450–4464.

[48] Lin W., Huang Y., Zhou X.-D., Ma, Y. Toxicity of Cerium Oxide Nanoparticles in Human Lung Cancer Cells. *Int. J. Toxicol.*, 2006, **25**(6), P. 451–457.

[49] Zeyons O., Thill A., Chauvat F., Menguy N., Cassier-Chauvat C., Oréar C., Daraspe J., Auffan M., Rose J., Spalla O. Direct and indirect CeO_2 nanoparticles toxicity for Escherichia coli and Synechocystis. *Nanotoxicology*, 2009, **3**(4), P. 284–295.

[50] Rogers N.J., Franklin N.M., Apte S.C., Batley G.E., Angel B.M., Lead J.R., Baalousha M. Physico-chemical behaviour and algal toxicity of nanoparticulate CeO_2 in freshwater. *Environ. Chem.*, 2010, **7**(1), P. 50–60.

[51] Pulido-Reyes G., Rodea-Palomares I., Das S., Sakthivel T.S., Leganes F., Rosal R., Seal S., Fernández-Pinãs F. Untangling the biological effects of cerium oxide nanoparticles: The role of surface valence states. *Sci. Rep.*, 2015, **5**, P. 15613.

[52] Caputo F., Giovanetti A., Corsi F., Maresca V., Briganti S., Licoccia S., Traversa E., Ghibelli L. Cerium oxide nanoparticles reestablish cell integrity checkpoints and apoptosis competence in irradiated HaCaT cells via novel redox-independent activity. *Front. Pharmacol.*, 2018, **9**, P. 1183.

[53] Corsi F., Caputo F., Traversa E., Ghibelli L. Not only redox: The multifaceted activity of cerium oxide nanoparticles in cancer prevention and therapy. *Front. Oncol.*, 2018, **8**, P. 1–7.

[54] Schwabe F., Schulin R., Rupper P., Rotzetter A., Stark W. Nowack B. Dissolution and transformation of cerium oxide nanoparticles in plant growth media. *J. Nanopart. Res.*, 2014, **16**, P. 2668.

[55] Dahle J.T., Livi K., Arai Y. Effects of pH and phosphate on CeO_2 nanoparticle dissolution. *Chemosphere*, 2015, **119**, P. 1365–1371.

[56] Plakhova T.V., Romanchuk A.Y., Yakunin S.N., Dumas T., Demir S., Wang S., Minasian S.G., Shuh D.K., Tyliszczak T., Shiryaev A.A., Egorov A.V., Ivanov V.K., Kalmykov S. N. Solubility of nanocrystalline cerium dioxide: Experimental data and thermodynamic modeling. *J. Phys. Chem. C.*, 2016, **120**(39), P. 22615–22626.

[57] Avramescu M.L., Chénier M., Beauchemin S., Rasmussen P. Dissolution Behaviour of Metal-Oxide Nanomaterials in Various Biological Media. *Nanomaterials*, 2023, **13**(1), P. 26.

[58] Romanchuk A.Y., Shekunova T.O., Larina A.I., Ivanova O.S., Baranchikov A.E., Ivanov V.K., Kalmykov S.N. Sorption of Radionuclides onto Cerium(IV) Hydrogen Phosphate $Ce(PO_4)(HPO_4)_{0.5}(H_2O)_{0.5}$. *Radiochemistry*, 2019, **61**(6), P. 719–723.

[59] Kozlova T.O., Vasil'eva D.N., Kozlov D.A., Teplonogova M.A., Birichevskaya K.V., Baranchikov A.E., Gavrikov A.V., Ivanov V.K. On the Chemical Stability of $Ce^{IV}(PO_4)(HPO_4)_{0.5}(H_2O)_{0.5}$ in Alkaline Media. *Russ. J. Inorg. Chem.*, 2022, **67**(12), P. 1901–1907.

Submitted 6 February 2023; accepted 31 March 2023

Information about the authors:

Taisiya O. Kozlova – Kurnakov Institute of General and Inorganic Chemistry of the Russian Academy of Sciences, Moscow, Russia; ORCID 0000-0002-9757-9148; taisia.shekunova@yandex.ru

Anton L. Popov – Institute of Theoretical and Experimental Biophysics of the Russian Academy of Sciences, Pushchino, Russia; ORCID 0000-0003-2643-4846; antonpopovleonid@gmail.com

Mikhail V. Romanov – Institute of Theoretical and Experimental Biophysics of the Russian Academy of Sciences, Pushchino, Russia; rmvya@yandex.ru

Irina V. Savintseva – Institute of Theoretical and Experimental Biophysics of the Russian Academy of Sciences, Pushchino, Russia; savintseva_irina@mail.ru

Darya N. Vasilyeva – Kurnakov Institute of General and Inorganic Chemistry of the Russian Academy of Sciences, Moscow, Russia; National Research University Higher School of Economics, Moscow, Russia; dnvasileva_1@edu.hse.ru

Alexander E. Baranchikov – Kurnakov Institute of General and Inorganic Chemistry of the Russian Academy of Sciences, Moscow, Russia; ORCID 0000-0002-2378-7446; a.baranchikov@yandex.ru

Vladimir K. Ivanov – Kurnakov Institute of General and Inorganic Chemistry of the Russian Academy of Sciences, Moscow, Russia; ORCID 0000-0003-2343-2140; van@igic.ras.ru

Conflict of interest: the authors declare no conflict of interest.

NANOSYSTEMS:
PHYSICS, CHEMISTRY, MATHEMATICS

Polyakov E.V., Maksimova M.A., et al. *Nanosystems: Phys. Chem. Math.*, 2023, **14** (2), 231–241.
http://nanojournal.ifmo.ru
DOI 10.17586/2220-8054-2023-14-2-231-241

Original article

Colloidal-chemical mechanism of $Zn(OH)_2$–ZnO layer formation at the glass – ammonia solution – Zn(II) interface

Evgeny V. Polyakov, Maria A. Maksimova, Julia V. Kuznetsova, Larisa Yu. Buldakova

Institute of Solid State Chemistry of Ural Branch of Russian Academy of Sciences, Ekaterinburg, Russia

Corresponding author: Evgeny V. Polyakov, polyakov@ihim.uran.ru

PACS 81.15.-z

ABSTRACT Thermodynamic and experimental studies of $Zn(OH)_2$/ZnO particle formation conditions in the model of closed system Zn^{2+}–$NH_{3,aq}$–$NH_{3,gas}$–H^+–OH^-–H_2O–$N_{2,gas}$ (1), which often occurs in the process of synthesis of zinc oxide nanoparticles and films by chemical bath deposition (CBD) methods, were carried out. It was shown that the driving force for the formation and growth of $Zn(OH)_2$/ZnO particles in the initially homogeneous system (1) at 25 °C is the difference in the chemical potential of particles at the initial temperature (unsaturated system) and the synthesis temperature (supersaturated system). Using vibrational spectroscopy, X-ray phase and chemical analysis, diffuse light scattering and electrophoresis methods, it was found that the phase transformation of $Zn(OH)_2$ into ZnO takes place in the region of 85 – 90 °C. The colloid-chemical transformation of $Zn(NH_3)_4^{2+}$ ionic particles into colloidal polycrystals of $Zn(OH)_2$/ZnO composition was established for the first time to be a staged process. The first stage of the process in the solution volume is localized at the gas nanobubble-solution interface as a result of rapid formation, growth and removal of gas nanobubbles from the solution. The interaction of positively charged $Zn(OH)_2$ nanoparticles with the surface of larger negatively charged gas nanobubbles creates colloidal aggregates "bubble||surface film of hydroxide nanoparticles". Their adhesion forms an openwork foam-like structure of the colloid in the solution and in the film on the interfaces at the first stage of synthesis. After degassing of the electrolyte solution, the second stage develops, consisting of the nucleation and ionic-molecular growth of $Zn(OH)_2$/ZnO particles from the supersaturated solution, their distribution between the solution and the electrolyte – reactor wall – air interfaces. The film growth at this stage is regulated by the difference in surface charges of the double electric layer of the interface and polycrystalline colloidal particles. In the solution and on the interface, columnar $Zn(OH)_2$/ZnO structures grow as volumetric stars with conical hexagonal spikes.

KEYWORDS $Zn(OH)_2$, ZnO, layer, formation, glass, interface, mechanism, colloidal-chemical, NH_3 solution

ACKNOWLEDGEMENTS This study was performed in the framework of the state-financed topic AAAA-A19-119031890028-0 at ISSC UB RAS.

FOR CITATION Polyakov E.V., Maksimova M.A., Kuznetsova Yu.V., Buldakova L.Yu. Colloidal-chemical mechanism of $Zn(OH)_2$–ZnO layer formation at the glass – ammonia solution – Zn(II) interface. *Nanosystems: Phys. Chem. Math.*, 2023, **14** (2), 231–241.

1. Introduction

Colloidal-chemical synthesis of laminar systems (films, layers, coatings) from liquid phase, the systematic study of which began in the last century [1], has been developed in the last decade under the name of "chemical bath deposition" (CBD) methods [2–5]. Compared to physical methods, this is one of simple and relatively economical methods of creating films, layers, coatings on substrates, because it does not require expensive and special equipment, the use of high temperatures and high pressures, and is convenient for deposition on large-area substrates. This method can be used for producing thin films with controlled structure and morphology, such as nanocrystalline layers, nanowires and nanoribbons. CBD is used to make a variety of flat, spherical, porous films. The disadvantage of colloidal-chemical synthesis of films is its relatively low reproducibility compared to physical deposition methods. This limitation is eliminated by optimizing the growth parameters [6]. Among various chemical objects of film synthesis by CBD methods, the first place belongs to chalcogenide films [5, 7]. Along with them, of particular interest over the past decades was the production of 1D coatings, metallic nano-sized compounds, and semiconductors such as ZnO. Their synthesis makes it possible to create ultradisperse wires, wires and rods on inorganic and polymeric substrates for elements of solar converters, electronic circuits, radiation shields, and light concentrators [8–12].

In the general scheme of application of this method [2, 3] for obtaining Zn(II) oxide films, two groups can be distinguished. One of them is based on the spontaneous decomposition reactions of homogeneous alkaline solutions of zinc hydroxo-complexes [13, 14]. The other group assumes the use of alkaline ammonia solutions and additionally introduced

precursors based on organic ammonia derivatives (urea, hexamethylantetramine, mono-, di-, triethanolamine, dimethylamine, tetramethylammonium, etc.), the thermal decomposition of which at elevated temperatures and pressures leads to the release of ammonia into the solution and the formation of ammonia zinc complexes [15–17]. The use of organic ammonia derivatives and other organic components for the synthesis of oxide films associated with the release of ammonia gas into the air creates an additional load on the environment in the production of such functional materials [18].

The canonical method for the estimation of film synthesis parameters from an initially homogeneous solution at elevated temperatures is the thermodynamic analysis of the considered chemical system [4, 5]. The distribution diagrams of complex ions and calculation of solubility curves at different temperatures for predicting the region of ZnO film production in the system "$ZnCl_2$–NH_3–OH–H_2O – temperature" showed [19] that ZnO films can be obtained at solution pH above 7. The morphology of such films depends on the pH of the solution, the polycrystals of nanoparticles in the form of flowers or columnar structures growing in the area where $Zn(NH_3)_4^{2+}$ complexes predominate. In the region of pH>12, where $Zn(OH)_n^{2-n}$ ions dominate, nano-sized oxide flakes are formed. Solution temperature plays an important role in the morphology and equilibrium composition of oxide films. ZnO films deposited at high temperature (90 °C) have an oriented hexagonal structure (zincite) and [Zn]/[O] $\approx$ 1 stoichiometry, while at lower temperatures (70 °C) flaky amorphous films are formed. The main reaction that accompanies film growth is heterogeneous decomposition of ammonia or zinc hydroxo-complex in alkaline medium [19–21]. The cited papers note the thermodynamic probability of formation of ammonia molecules during decomposition of ammonia zinc complexes in an initially homogeneous solution, but the role of the gas phase in the growth mechanism of colloidal particles in solution and in the film is not considered. The presence of sulfide ions in the reaction bath does not exclude the formation of zinc oxide nanoparticles of a more complex composition [22]. According to X-ray photoelectron spectroscopy data, the oxide films grown in the region dominated by the ammonia complex are enriched with Zn(II) ions. The oxide growing in the region dominated by hydroxocomplexes contains Zn(II) vacancies in the metal sublattice [19]. The synthesis temperature also affects the ratio of the $Zn(OH)_2$/ZnO phases in the films and the optical bandgap of the solid phase. Luminescence intensity decreases when passing from $Zn(OH)_2$ to ZnO [23].

The application of thermodynamic modeling methods allows one to reveal the equilibrium characteristics and probable conditions of zinc oxide phase formation, but they do not establish the reasons for predominant phase release in the solution volume or in the interface region, the stages and mechanisms of colloidal-chemical transformations accompanying the processes of zinc complexes thermochemical decay in solution and the influence of system temperature on these processes.

Since numerous descriptions of conditions for producing chalcogenide and oxide films by the CBD method contain ammonia and ammonia zinc complexes as obligatory components, it was of interest to determine the general elements of the colloidal-chemical mechanism of formation and growth of nano-, microparticles of $Zn(OH)_2$/ZnO phases in the solution volume and on the "solution/reactor wall" interface during thermal action on the simplest in chemical respect model system

$$Zn^{2+} - NH_{3,aq} - NH_{3,gas} - H^+ - OH^- - H_2O - N_{2,gas} \quad (1)$$

as well as to find out the role of dissolved gas nano/micro-bubbles liberated in the solution volume in the mechanism of zinc oxide and zinc hydroxide formation depending on the temperature during the thermal action on (1).

2. Experimental

In order to establish the effect of chemical composition and temperature on the phase composition of products in a closed multiphase system (1), we used in this work the technique of thermodynamic analysis to quantify the chemical composition taking into account the following basic chemical components: NH_3(g), NH_3(a), O_2(g), N_2(g), H_2O(g), H_2O(a), H_2O(g), Zn(0), Zn(+2a), OH(–a), H(+a), $Zn(OH)_2$(ia), $ZnNH_3$(+2a), $Zn(NH_3)_2$(+2a), $Zn(NH_3)_3$(+2a), $Zn(NH_3)_4$(+2a), ZnOH(+a), $Zn(OH)_2$(0a), $Zn(OH)_3$(–a), $Zn(OH)_4$(–2a), ZnO, $Zn(OH)_2$. The dependences of the phase composition of system (1) were analyzed in pH–Eh, composition-temperature and composition-pressure coordinates using the HSC Chemistry 8 program. The "g" sign in the formulas refers to the gas phase, "a" – to the hydrated ions in solution, and the rest – to the liquid and solid phases.

Elemental analysis by inductively coupled plasma mass spectrometry (Elan 9000, [24]) was used to experimentally determine the kinetics of Zn(II) mass transfer during the transformation of a homogeneous zinc ammine solution into a colloidal $Zn(OH)_2$/ZnO solution in the aqueous phase and on the solution-glass substrate interface. The zinc salt solution for the kinetic experiment was prepared by dissolving 4.39 g of chemically pure zinc acetate $Zn(CH_3COO)_2 \cdot 2H_2O$ in 60 – 70 ml of deionized water (Millipore Simplicity system, solution resistance 18 MΩ·cm). Then 10 ml of concentrated ammonia was added to the solution and the pH of this solution was adjusted up to pH = 10.2 – 10.3 using a NaOH solution with a concentration of 0.05 M. After that the volume of the solution was brought up to 100 ml. In the kinetics experiments, 5 ml aliquots of the prepared solution were transferred sequentially with a glass pipette into glass test tubes. The test tubes were preliminarily chemically cleaned of traces of impurities by washing with concentrated hydrochloric acid and deionized water and then they were dried.

The experiments on the kinetics of spontaneous decomposition of a homogeneous ammonium solution of zinc ammine with isolation of $Zn(OH)_2$/ZnO established the regularities of changing of the concentration of Zn(II) in the form of colloid, filtrate and oxide/hydroxide film on a substrate depending on the isothermal heating time of the examined system (1) at a given temperature.

The colloidal part was separated by ultrafiltration through a double cellulose filter with a pore size of less than 100 nm under vacuum. The precipitate on the filter was dried at room temperature and dissolved in 2 mol/l hydrochloric acid (chemically pure grade) of a specified volume. Then we determined the mass of Zn in the volume and recalculated it in the mass (mol) of the metal in the form of colloid in (1) at a given time of synthesis. We also determined the mass of Zn in the filtrate after it was acidified to a concentration of 1.8 – 2.0 mol/l with hydrochloric acid directly in the test tube. The content of zinc, which formed a film on the walls of the quartz glass reactor, was determined after dissolving a layer with 2 mol/l hydrochloric acid with a volume equal to the volume of the studied solution, 5 ml. Along with chemical elemental analysis of $Zn(OH)_2$/ZnO formation in (1), layer formation was studied by Dynamic Light Scattering (DLS) and Laser Doppler Electrophoresis measurements carried out on a Zetasizer Nano ZS particle analyzer (Malvern Panalytical Ltd.) [24, 25].

The Raman spectral analysis of the samples was performed at room temperature using a Via Reflex Renishaw spectrometer ($\lambda = 532$ nm, $P = 25$ mW). The phase analysis of the products was fulfilled on a STADI-P X-ray powder automatic diffractometer (STOE) with CuKα1 radiation using the library of X-ray diffraction data PDF-2 (ICDD Release 2009). The morphology of the layers on the substrate was studied using the scanning electron microscopy (SEM) and EDX elemental analysis on a JSM JEOL 6390LA facility. The UV-visible absorption spectroscopy was performed using a Shimadzu UV-3101PC UV/Vis/Near-IR Spectrophotometer. The diffuse reflectance spectra of the layers were recorded in the interval of 220 – 800 nm by means of a Shimadzu UV-3600 UV-vis-NIR spectrophotometer using $BaSO_4$ crystals as a reference.

The measurement of the size and electrophoretic mobility of colloidal particles in dynamic light scattering and laser Doppler electrophoresis experiments had some special features. Since the transfer of the studied solution from the thermostat to the device cell did not make it possible to perform measurements in real time and temperature, the particle size was determined by heating and holding the examined system (1) directly in the Zetasizer Nano ZS cuvette. The result of the analysis of fluctuations of the Brownian motion velocity of particles was presented as the size of solvated particles (D, nm) by the Stokes–Einstein formula. The radiation source was a helium-neon laser with a wavelength of 633 nm. Measurements were taken in a glass cuvette at temperatures in the range of 25 – 60 °C at a scattering angle of 173 ° (backscattering), Fig. 1. In addition to the diffusion parameters, the device measured the electrical conductivity of the solution (Q) and the intensity of the backscattered photon flux. This made it possible to obtain D values taking into account the attenuation of the light flux as it passes through the cuvette wall and the constantly changing colloidal solution. The changes in the relative concentration of Zn(II) in the form of colloid (precipitate), filtrate (solute) and film of oxide/hydroxide on the substrate, as well as in the average hydrodynamic diameter of colloid particles D, their zeta potential and solution conductivity Q with the time of synthesis are shown as an example in Fig. 2.

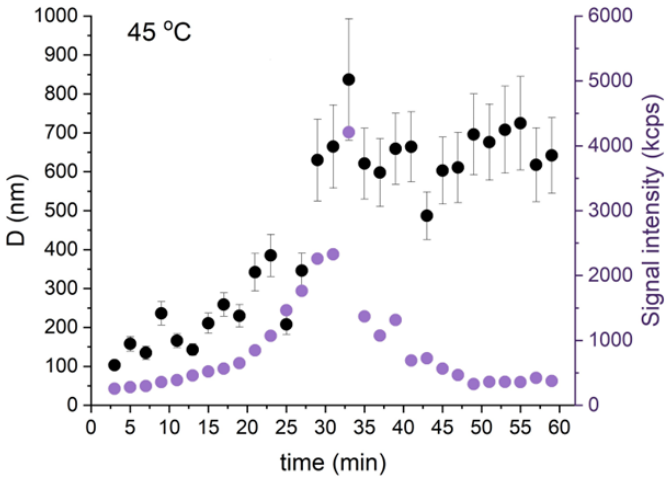

FIG. 1. Signal intensity (violet points) and mean hydrodynamic diameter (D, black points) of $Zn(OH)_2$/ZnO particles formed at 45 °C according to direct measurements. Confidence intervals characterize the scattering in the size distribution of the hydrodynamic diameter of growing particles at each time point

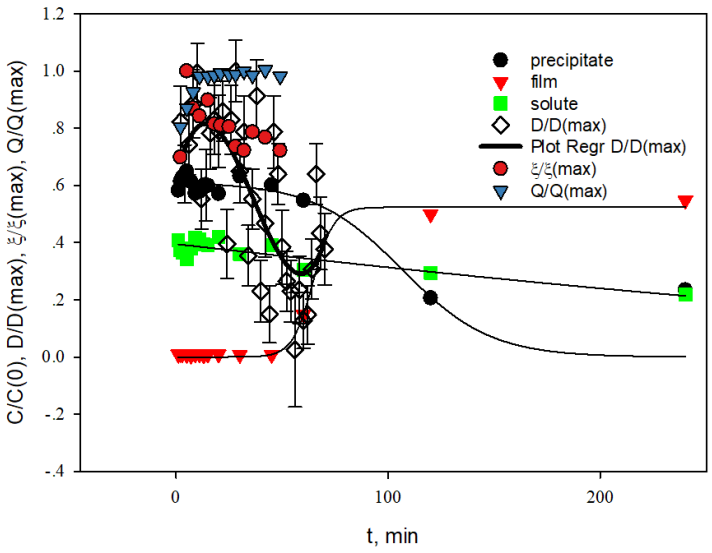

FIG. 2. Example of changes in the relative concentration of Zn(II), $C/C(0)$ in the form of colloid, film and ions, in NH_3–Zn(II) solution; changes in colloid particle size, $D/D_{\max}$, according to light scattering data ($D_{\max} = 400$ nm); changes in the relative conductivity $Q/Q_{\max}$ and the particle zeta potential $\xi/\xi_{\max}$ with the synthesis time t. C, $C(0)$ are the current and initial concentration of Zn(II) in the phase. The maximal zeta potential, $\xi_{\max} = +21.6$ mV; Q is the electrical conductivity; $Q_{\max} = 27.1$ mS/sm; temperature 55 °C, pH = 10.3

3. Experiment results

The thermodynamic study of the elements of the growth mechanism of $Zn(OH)_2$ – ZnO layers on the glass surface was performed in the model system Zn^{2+} – $NH_{3,aq}$ – NH_3(g) – OH^- – H_2O – N(g) (1). Here, hydrated ammonia molecules $NH_{3,aq}$ in the selected pH range simultaneously acted as a ligand and a film-forming agent. The fields of predominance of ionic particles and $Zn(OH)_2$ – ZnO – Zn(0) phases in Eh–pH coordinates, where Eh(B) is the electrochemical potential (1) relative to the hydrogen electrode for temperatures 25 and 85 °C, are shown in Fig. 3. From the data of thermodynamic calculation it is evident that the appearance of the solid phase in (1) when the temperature changes from 25 to 85 °C in the pH range 8.6 – 10.8 is caused by the formation of oversaturated solution relative to zinc hydroxide (< 35 °C) or oxide (> 40 °C) due to the system exit from the $Zn(NH_3)_4^{+2}$ complex stability field in this pH region. The simultaneous effect of pH and temperature of system (1) on the chemical and phase composition of zinc compounds according to the calculation data is illustrated in Fig. 4. It is seen that at 25 – 35 °C and pH < 10.3 the ammonia solution of Zn(II) is not saturated relative to the oxide or hydroxide. The main chemical form of ions in the solution is the $Zn(NH_3)_4^{+2}$ complex. Note that $Zn(NH_3)_4^{+2}$ is a cationic component of the complex whose stability is determined in the HSC Chemistry 8 database. It is obvious that in the examined pH region, ammonia complexes can exist in the form of ionic pairs with hydroxyl ions or mixed ligand hydroxo-complexes. There is no information in the thermodynamic literature on the existence and stability of mixed hydroxo-ammonium zinc complexes. It is known that for mixed ligand metal complexes MX, MY, the logarithm of the stability constant is $\log(\beta_{MXY}) \approx \frac{1}{2}(\log(\beta_{MX}) + \log(\beta_{MY}))$ [26]. For $Zn(NH_3)_4(OH)^+$, this estimation gives one $\log(\beta_{MXY}) \approx 6.9$, which is 2 log units less than $\log(\beta MY)$ of $Zn(NH_3)_4^{2+}$ complex [27]. This estimate shows that ammonia complexes are most likely to exist in alkaline solution mainly in the form of ionic pairs with OH-ions. From Figs. 4 and 5, it follows that the temperature increase in the equilibrium model system (1) at the zinc concentration 0.06 mol/l keeps it homogeneous in the pH interval 10.0 – 10.5 up to a temperature of 35 °C. With a further increase in pH in this temperature range, system (1) transits to a supersaturated solution state with a release of a mixture of ε-$Zn(OH)_2$ – ZnO phases. Simultaneously, the partial pressure of ammonia in the gas phase NH_3(g) increases, but the concentration of dissolved ammonia changes little if at all, Fig. 3. The transfer of NH_3(g) into the gas phase takes place from the electrolyte surface, as well as by the formation, growth in the electrolyte volume, and removal to the electrolyte surface of nano- and micro-bubbles of dissolved gases, primarily H_2O(g) and NH_3(g) [28].

According to the X-ray phase analysis of precipitates and films on the reactor surface, the observed picture of phase transformations in system (1) is different from the data of thermodynamic calculations in that the phase transition takes place in the region of higher temperatures, Figs. 6, 7(a).

The appearance of the ZnO phase (wurtzite) is observed at 95 – 99 °C. Independent results of Raman spectroscopy of films in the region of deformation vibration bands of hydroxide OH-groups (3190 and 3266 1/cm [29]) obtained at different temperatures of system (1) illustrate the gradual disappearance of the zinc hydroxide phase, Fig. 7(a). The

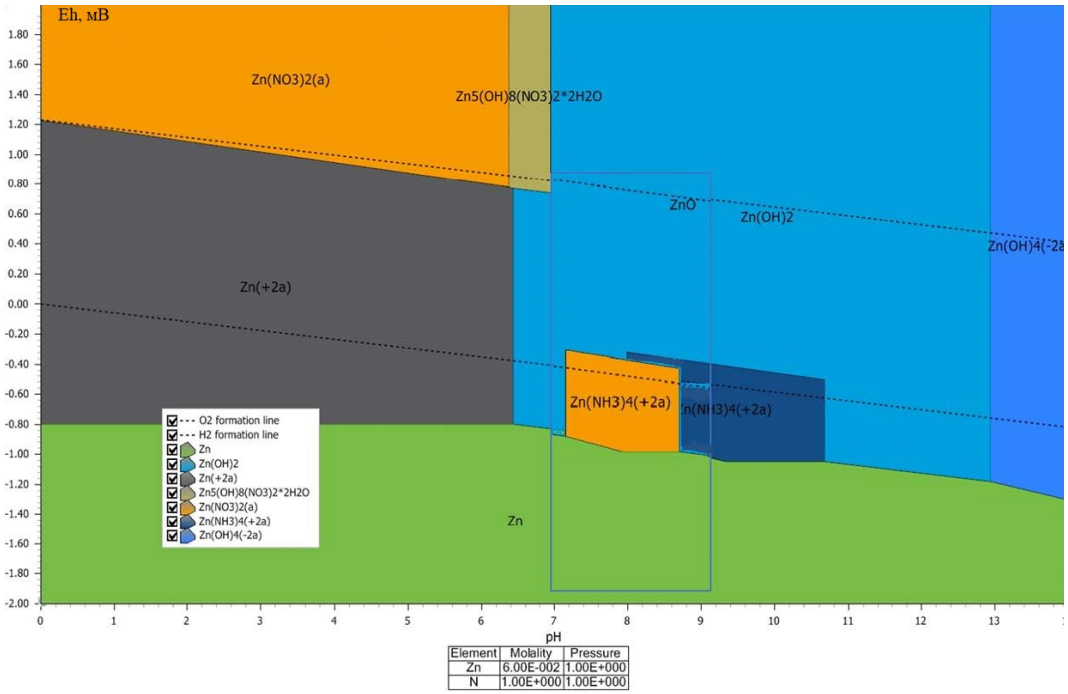

FIG. 3. Pourbaix diagram calculated for system (1) using the HSC Chemistry 8 program. The concentration of Zn(II) is 0.06 mol/l, the concentration of ammonia in solution is 1 mol/l, the total pressure of N_2–O_2–H_2O(g) gas mixture in the system is 1 atm, 22 °C. Eh is the electrochemical potential in the system relative to the hydrogen electrode, B. The dark blue area shows the field of predominance of the $Zn(NH_3)_4^{+2}$ complex. The inset in the blue frame shows the field of predominance (orange color) of the $Zn(NH_3)_4^{+2}$ complex at 85 °C in the same pH range.

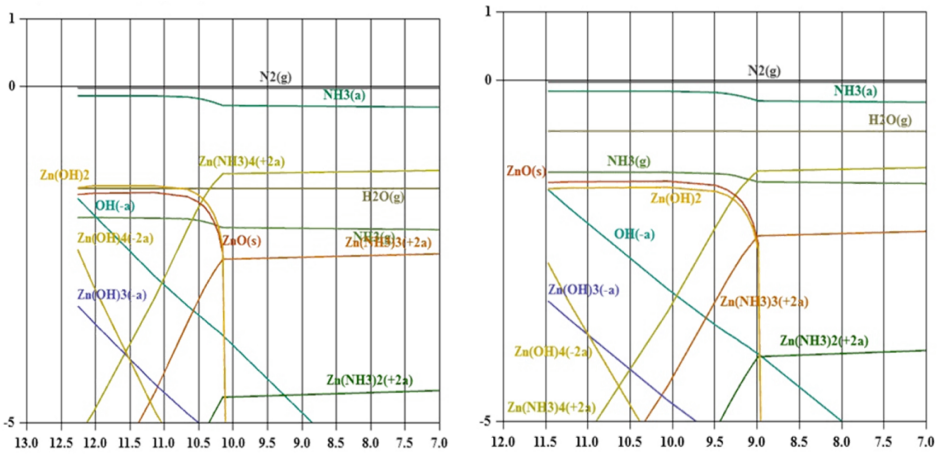

(a) (b)

FIG. 4. Changes in the chemical and phase composition in system (1) as a function of pH and temperature; the concentration of Zn(II) is 0.06 mol/l, the concentration of ammonia in solution is 1 mol/l, the total pressure of N_2–O_2–H_2O(g) gas mixture in the system is 1 atm.

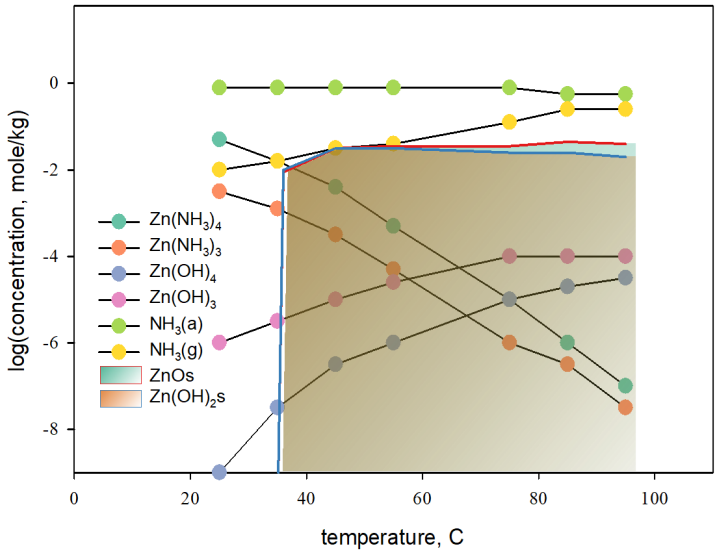

FIG. 5. The calculation results of the changes in the chemical and phase composition of the solution during synthesis as a function of temperature. The concentration of Zn = 0.06 mol/kg, NH_3 = 1 mol/kg, pH = 10.0 – 10.3. HSC Chemistry 8 program. (s) denotes the belonging to solid phase.

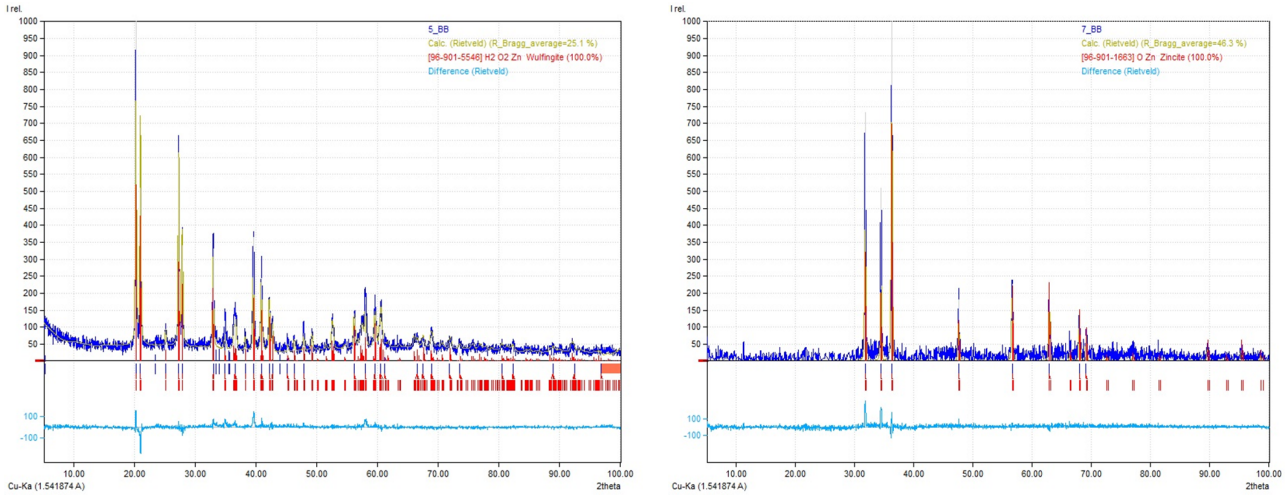

(a) (b)

FIG. 6. X-ray diffraction pattern of ε-$Zn(OH)_2$ (a) and ZnO (b) films deposited from the zinc ammonia solution on the glass surface. The film composition at (a) 80 °C – ε-$Zn(OH)_2$, (wulfingite) space group P 2_1 2_1 2_1, CSR (coherent scattering region) – 64 nm, at (b) 99 °C – ZnO, (wurtzite) space group P 6_3 m c, CSR – 71 nm. Dark blue line is the experimental data (1); yellow line is the result of description by the Rietveld method (2); red line is the tabulated values of phase intensities (3); light blue line is the difference between (1) and (2). Solution composition – Zn(II) = 0.12 mol/l, NH_3 = 1 mol/l, pH = 10.3.

change in the phase composition of the films, Figs. 6, 7, agrees with the literature data on the variation of the optical bandgap of the films obtained under the same conditions at different temperatures [20].

Measurements of the average hydrodynamic diameter of colloidal particles during synthesis at different temperatures showed that the precipitation of the solid phase in the form of a film on the electrolyte/reactor wall interface prevents the application of the dynamic light scattering method at temperatures above 55 °C. Typical dependence of the flux of detector-recorded photons backscattered on colloidal particles (Fig. 1) shows that the signal intensity passes through a maximum as the colloid forms, whereupon it decreases to background values due to their absorption by the $Zn(OH)_2$ film growing on the cuvette walls. At a temperature of 60 °C or higher, the film on the cuvette wall completely absorbs the photon flux already in the first minutes of the measurement. Therefore, we limited the temperature range of the study of colloidal properties of system (1) to 25 – 55 °C.

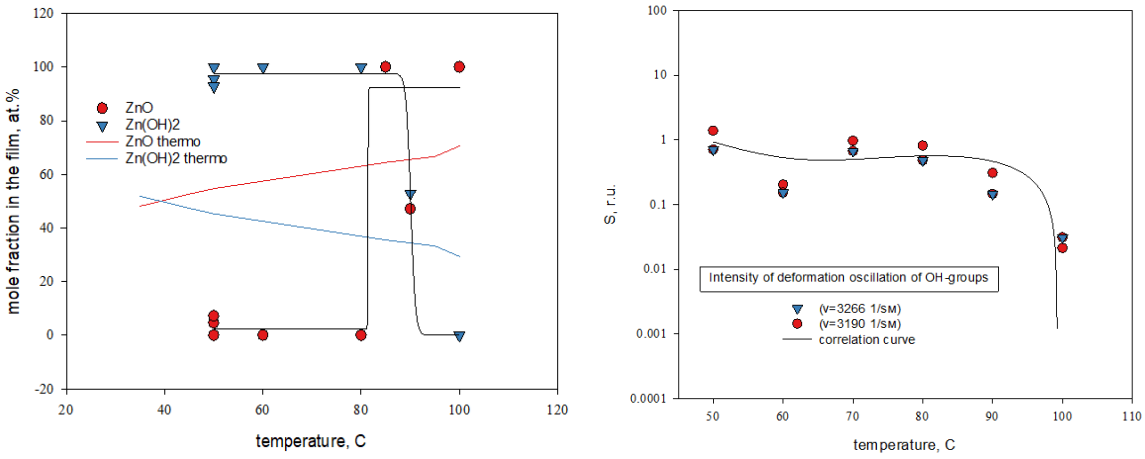

(a) (b)

FIG. 7. (a) Changes in the phase composition of the ZnO/$Zn(OH)_2$ film depending on the synthesis temperature. Dots – experiment, lines – thermodynamic calculation of the equilibrium composition. (b) Variation of the intensity (S) of deformation vibration bands of -OH groups in ε-$Zn(OH)_2$ (wulfingite) films on the glass surface with the synthesis temperature according to Raman spectroscopy data. S is the integrated intensity of signal in the absorption band (ν) region of the Raman spectrum. The line is the correlation curve "$\log(S)$–temperature".

According to the diffusion scattering measurements as a function of synthesis time, colloidal particles with an average size of 200 – 1000 nm, Fig. 8, and a positive value of ζ-potential, Fig. 9, are observed in system (1) at 25 °C and at elevated temperatures immediately after the preparation of the initial solution. At the same time, the solution looks optically transparent. The size of fixed particles (D) changes with synthesis time, regression line ($D/D_{\max}$), Fig. 2. Their ζ-potential first increases to the maximum value, then it decreases and further increases following the trend in the relative concentration $C/C(0)$ of zinc in the form of a film, Fig. 2.

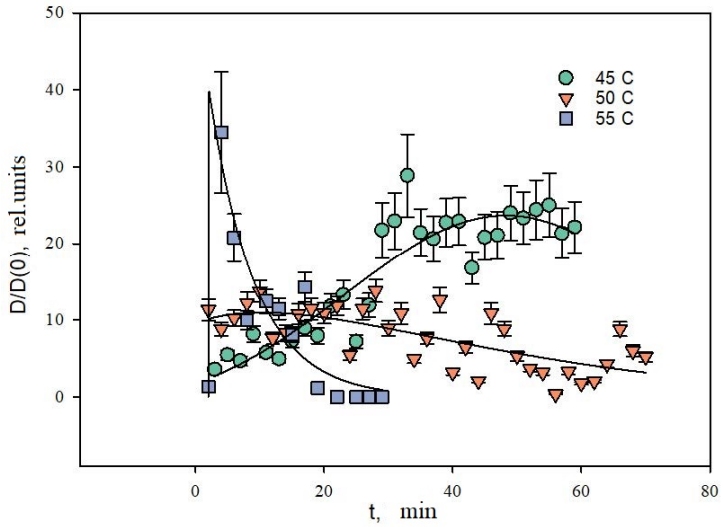

FIG. 8. Variation in the relative size $D/D(0)$ of ZnO/$Zn(OH)_2$ microcrystals in the film at synthesis temperatures 45, 50 and 55 °C with contact time. $D(0)$ is the value of the coherent scattering region of crystals calculated from phase analysis data (Debye–Scherrer equation). $D(0) = 29 \pm 5$ nm. The concentration of Zn(II) = 0.12 mol/l, NH_3 = 1 mol/l, pH = 10.3.

Two stages can be distinguished in the character of changes in the particle size D, Fig. 8, and ζ-potential, Fig. 9, with time at different synthesis temperatures. At the first stage, the main factor of the change (1) is the growth of conductivity (Q) of electrolyte solution, which is determined by thermal decay of $Zn(NH_3)_4^{2+}$ complex and hydrolysis of

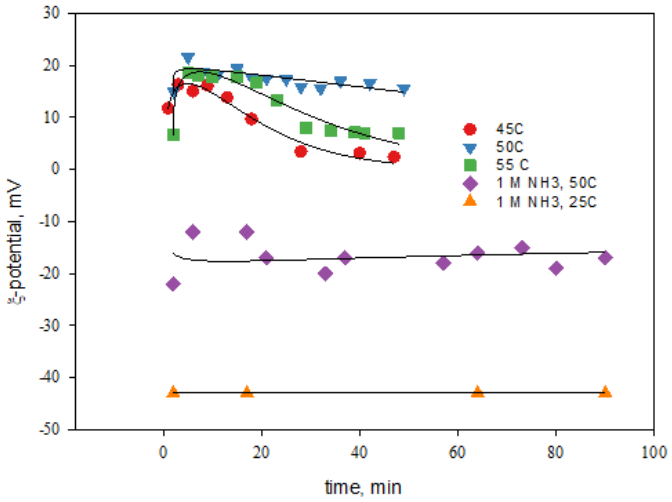

FIG. 9. Changes of ζ-potential of $Zn(OH)_2$/ZnO microcrystals with synthesis time during their growth from ammonia solution at different temperatures. The graph of behavior of ζ-potential of gas nanobubbles in ammonia solution without Zn(II) at 25 and 50 °C is given for comparison. Solution composition: Zn(II) = 0.12 mol/l, NH_3 = 1 mol/l, pH = 10.3.

ammonia molecules in solution according to the following reactions

$$\begin{aligned} Zn(NH_3)_4(OH)_2 &\rightarrow Zn^{2+}_{aq} + 4NH_{3,aq} + 2OH^-, \\ Zn^{2+}_{aq} + 2OH^- &\rightarrow Zn(OH)_{2,colloid}, \\ NH_{3,aq} + OH^- &\rightarrow NH_4OH \rightarrow NH^+_4 + OH^-. \end{aligned} \tag{2}$$

Destruction of $Zn(NH_3)_4(OH)_2$ ion pair leads to supersaturation with isolation of Zn(II) in the form of $Zn(OH)_2$ colloid and increases the concentration of ammonium ions in solution by reaction (2) and conductivity $Q(t)$, Fig. 10(a). The empirical relationship $Q(t) - t$ is described by the first order irreversible reaction equation throughout the temperature range 45 – 55 °C, Fig. 10(a):

$$Q(t) = a + b(1 - \exp(-ct)), \quad P(t) = (1 - (Q(t) - a)/b), \tag{3}$$

where a, b, c are equation parameters and $P(t)$ is an auxiliary function. Comparison of the conductivity in (1) with that of the ammonia solution at pH 10.3, Fig. 10(a), shows that ionic reactions (2) are completed by the accumulation of ammonium ions in solution during the first 10 to 15 minutes of synthesis. At the first stage, colloidal particles $Zn(OH)_2$ have a ζ-potential of approximately +(20 – 25) mV, which is typical of aqueous colloidal solutions of $Zn(OH)_2$, ZnO in the pH range 10 – 11 [6, 30]. The relatively large positive ζ-potential prevents the aggregation (increase in size) of particles and their attachment to interfaces, which explains the appearance of the induction period of film growth in $C/C(0) - t$ coordinates, Fig. 2. Even before the process of colloid formation in (1) begins, the appearance of nanoparticles identical to gas nanobubbles is noted in the homogeneous solution at 25 °C, Fig. 9 [28, 31, 32]. Their ζ-potential at pH 10.3 and 25 °C is negative, -40 mV, and increases to $-(15 – 20)$ mV when the temperature rises to 50 °C. This sign of the charge is characteristic of the gas nanobubbles in alkaline environment and is opposite to the sign of the ζ-potential of hydroxide colloid, Fig. 9. The presence of nano- (< 200 nm) and microbubbles (10 – 50 μm) of gas with negative zeta potential is typical for aqueous solutions of urea, ethanol, ammonia solutions, etc. Gas bubbles evolve over time, increasing in size and collapsing to form high-pressure microzones near the electrolyte-gas interface [32, 33].

The joint formation of colloidal particles and nanobubbles of gas in system (1) leads to their electrostatic attraction with a change in charge, size and morphology [34]. The interaction of gas nanobubbles and colloidal particles explains the stabilization and relatively large size of the observed colloidal particles due to adsorption of smaller positively charged $Zn(OH)_2$ nanoparticles on the surface of larger negatively charged gas nanobubbles and formation of colloidal aggregates "bubble||surface film of hydroxide nanoparticles" [34, 35]. Their further cohesion forms an openwork foamy colloid structure of solution and film on the solution/wall interface at the first stage of synthesis, Figs. 8, 11(a). The interaction of nanobubbles of gas and colloidal particles explains the large size of the observed colloidal particles, which is reflected in the morphology of films obtained under similar conditions, but annealed at 400 °C [36], Fig. 11(a).

At higher temperatures, the growth rate of the number and size of gas bubbles in (1) increases leading to their mass-transfer to the solute/gas interface and final removal from the solution [32, 33]. This allows us to suggest the following explanation for the change in the position of the maximum of the peak of the observed colloidal particle size distribution with temperature, Fig. 8. As the temperature increases, the time necessary to reach a maximum in the size distribution of the observed colloidal particles decreases, and at 55 °C the formation and then disappearance of large

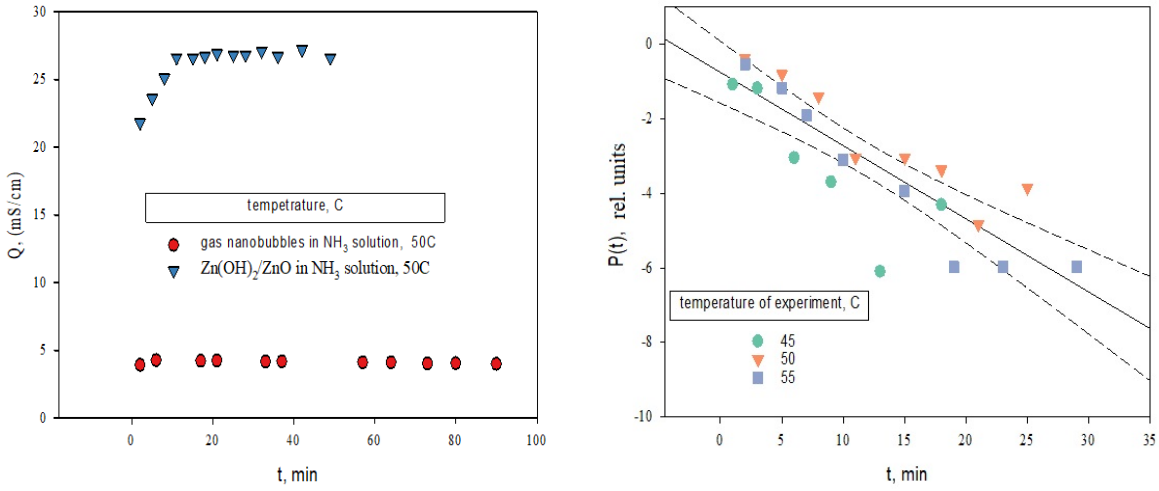

(a) (b)

FIG. 10. (a) Variation of the conductivity (Q) of colloidal solution $Zn(OH)_2$ (triangles) in system (1) and ammonia solution without addition of Zn(II) ions (circles) with time, 50 °C, pH 10.3. (b) Variation of the conductivity of solutions as a function of $Zn(OH)_2$ synthesis temperature, coordinates of eq. (3).

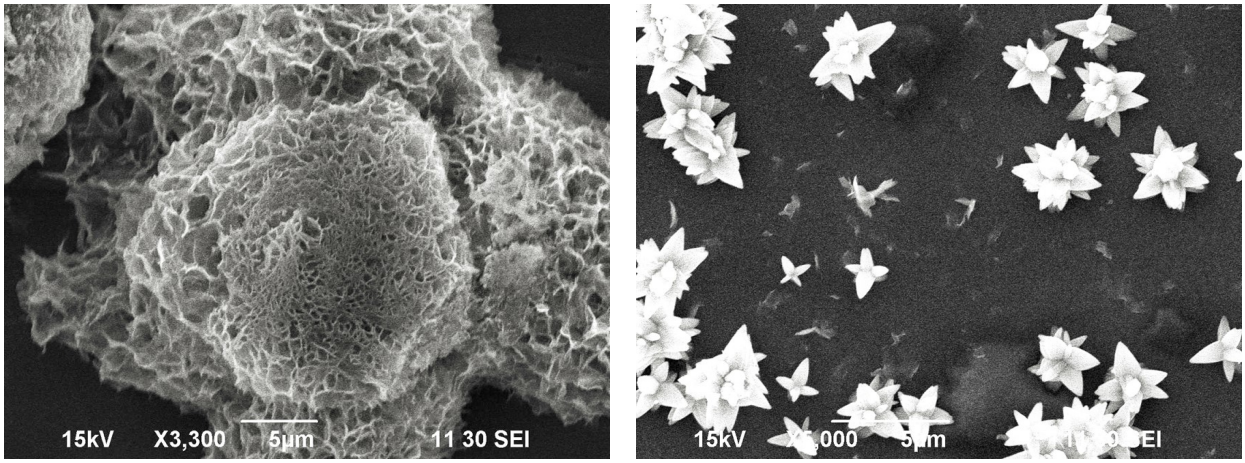

(a) (b)

FIG. 11. Microphotographs of films (a) – $Zn(OH)_2$, (b) – ZnO obtained after 5 minutes of synthesis at temperatures 50 °C (a), 90 °C (b)

colloidal particles and degassing of the solution occur in the first 1 – 2 minutes, Fig. 8. At the final stage of degassing of the solution, the colloidal aggregates of hydroxide nanoparticles on the surface of growing gas bubbles disintegrate, hydroxide nanoparticles that were formerly on their surface again pass to a state of bulk colloid, and the observed size of colloidal particles and their charge decrease, Fig. 9. Due to the removal of gas nanobubbles, the formation of openwork colloidal structures in the degassed solution (at elevated temperatures) becomes impossible. The same result should be achieved when the total pressure in the system increases, preventing the formation of gas bubbles in the electrolyte solution.

As the temperature rises, the second stage of the colloid formation process, which is a sequence of nucleation and ion-molecular growth reactions of $Zn(OH)_2$/ZnO nanoparticles in a degassed supersaturated solution volume and their heterogeneous distribution on the interfaces, becomes the main one, Fig. 2. The morphology of growing $Zn(OH)_2$ – ZnO crystallites at the second stage is determined by the conditions of their spontaneous crystallization and therefore differs greatly from the morphology of particles growing at the first stage on the surface of nanobubbles, Fig. 11(a,b). The driving force of the $Zn(OH)_2$/ZnO film growth on the reactor wall surfaces and the solution/air boundary is the difference in the electrochemical potentials of the double electric layer surface of the interfaces and nano-microcrystals. The morphology of crystallites at the second stage represents columnar structures and volumetric stars with spikes of hexagonal section

and conical shape, which is connected with their growth on lateral hexagonal faces of primary particles in conditions of gradual diminution of supersaturation [13–21].

4. Conclusion

The performed study of the equilibrium and dynamic conditions of $Zn(OH)_2$/ZnO nanoparticle formation in the model closed system Zn^{2+} – $NH_{3,aq}$ – NH_3(g) – OH^- – H_2O – N_2(g) (1) revealed that the driving force for the formation and growth of nanoparticles in the initially homogeneous system (1) at 25 °C is the difference in the chemical potential of particles at 25 °C (unsaturated system relative to $Zn(OH)_2$/ZnO formation) and a given synthesis temperature (supersaturated system). Using vibrational spectroscopy, X-ray phase and chemical analysis, diffuse light scattering and electrophoresis methods, it was found that the phase transformation of $Zn(OH)_2$ into ZnO occurs in the region of 85 – 90 °C, in contrast to the temperature of 35 – 40 °C according to thermodynamic simulation data. Changes in the relative concentration of Zn(II) in the form of colloid, the film and the ions in electrolyte solution and the electrical conductivity of the electrolyte solution with the time of synthesis corresponds to the first order reaction for ions Zn(II).

It has been shown for the first time that the colloidal-chemical transformation of $Zn(NH_3)_4^{2+}$ ionic particles into colloidal microcrystals of $Zn(OH)_2$ /ZnO composition is a staged process. The first stage of the process takes place in the solution volume mainly on the gas nanobubble-solution interfaces as a result of rapid formation, growth, and removal of gas nanobubbles from the solution. The driving force of the process at the first stage is the difference in the sign of the surface charges of nanobubbles and Zn(II) colloidal particles in the electrolyte volume. The interaction of small positively charged $Zn(OH)_2$ nanoparticles with the surface of larger negatively charged gas nanobubbles creates colloidal aggregates "surface film of hydroxide nanoparticles ||gas bubble". Their further cohesion leads to the formation of an openwork foamy structure of the colloid in solution and films on the interfaces at the first stage of synthesis. After degassing of the electrolyte solution, the second stage develops, which consists in nucleation and ionic-molecular growth of $Zn(OH)_2$/ZnO particles in the volume of the degassed supersaturated solution and in their distribution between the colloidal solution and "electrolyte – reactor wall – air" interfaces. In the absence of gas nanobubbles, columnar structures grow in the solution and at the interface in the form of volumetric stars with spikes of conical shape and hexagonal cross-section.

References

[1] Mokrushin S.G. Experimental study of laminar systems. *J. of Physical Chemistry*, 1934, **5** (8), P. 1082–1091.

[2] Fabian I.E., Chandrakant D.L., Rajan J. *Chemically Deposited Nanocrystalline Metal Oxide Thin Films: Synthesis, Characterizations, and Applications*. Springer Cham, 2021, 926 p.

[3] Guire M.R.D., Bauermann L.P., Parikh H., Bill J. Chemical Bath Deposition. In *Chemical Solution Deposition of Functional Oxide Thin Films*. Ed. Waser R., Kosec M., Payne D. Schneller T. Vienna, Springer, 2013.

[4] Markov V.F., Maskaeva L.N., Kitaev G.A. Peculiarites of microstructure and properties of lead sulfide films deposited from halide-containing solutions. *Inorganic materials*, 2000, **36** (7), P. 792–795.

[5] Kozhevnikova N.S., Markov V.F., Maskaeva L.N. Chemical deposition of metal sulfides from aqueous solutions: from thin films to colloidal particles. *J. of Physical Chemistry*, 2020, **94** (12), P. 1752–1766.

[6] Fatehah M.O., Hamidi A.A., Serge S. Stability of ZnO nanoparticles in solution. Influence of pH, dissolution, aggregation and disaggregation effects. *J. of Colloid Science and Biotechnology*, 2014, **3** (1), P. 75–84.

[7] Majid A., Bibi M. Cadmium based II-VI Semiconducting Nanomaterials Wet Chemical Synthesis Methods. *Topics in Mining, Metallurgy and Materials Engineering*, Springer, Cham, 2018, P. 43–101.

[8] Guillemin S., Rapenne L., Roussel H., Sarigiannidou E., Brémond G., Consonni V. Formation Mechanisms of ZnO Nanowires: The Crucial Role of Crystal Orientation and Polarity. *J. of Physical Chemistry C*, 2013, **117** (40), P. 20738–20745.

[9] He J.H., Lao C.S., Chen L.J., Davidovic D., Wang Z.L. Large-scale Ni-doped ZnO nanowire arrays and electrical and optical properties. *J. of the American Chemical Society*, 2005, **127** (47), P. 16376–16377.

[10] Comini E., Faglia G., Sberveglieri G., Pan Z.W., Wang Z.L. Stable and high-sensitive gas sensors based on semoconducting oxide nanobelts. *Applied Physics Letters*, 2002, **81** (10), P. 1869–1871.

[11] He J.H., Hsin C.L., Liu J., Chen L.J., Wang Z.L. Piezoelectric gated diode of a single ZnO nanowire. *Advanced Materials*, 2007, **19** (6), P. 781–784.

[12] Sun X., Li Q., Jiang J., Mao Y. Morphology-tunable synthesis of ZnO nanoforest and its photoelectrochemical performance. *Nanoscale*, 2014, **6** (15), P. 8769–8780.

[13] Pérez-Hernández R., Velázquez Salazar J.J., Yacaman M.J. Low-Temperature Synthesis and Growth Mechanism of ZnO Nanorods on Crystalline Si Substrate. *J. of Nano Research*, 2011, **14**, P. 69–82.

[14] Wang M., Jiang L., Jung Kim E., Hahn S.H. Electronic structure and optical properties of $Zn(OH)_2$: LDA+U calculations and intense yellow luminescence. *RSC Advances*, 2015, **5** (106), P. 87496–87503.

[15] Alnoor H., Chey Ch.O., Pozina G., Liu X., Khranovskyy V., Willander M., Nur O. Effect of precursor solutions stirring on deep level defects concentration and spatial distribution in low temperature aqueous chemical synthesis of zinc oxide nanorods. *AIP Advances*, 2015, **5**, 087180.

[16] Baviskar P.K., Nikam P.R., Gargote S.S., Ennaoui A., Sankapal B.R. Controlled synthesis of ZnO nanostructures with assorted morphologies via simple solution chemistry. *J. of Alloys and Compounds*, 2013, **551**, P. 233–242.

[17] Znaidi L. Sol-gel-deposited ZnO thin films: A review. *Materials Science and Engineering B*, 2010, **174**, P. 18–30.

[18] Le Pivert M., Martin N., Leprince-Wang Y. Hydrothermally grown ZnO nanostructures for water purification via photocatalysis. *Crystals*, 2022, **12** (3), 308.

[19] Gonzalez-Chan I.J., Moguel Z.P., Oliva A.I. Deposition of ZnO thin films by chemical bath technique: physicochemical conditions and characterization. *ECS J. of Solid State Science and Technology*, 2019, **8** (9), P. 536–544.

[20] Kahraman S., Çakmak H.M., Çetinkaya S., Çetinkara H.A., Güder H.S. CBD grown ZnO nanostructures: effects of solution temperature. *Int. J. of Materials Research*, 2013, **104** (8), P. 798–804.

[21] Trejo-Ramos A.I., Martín-Varguez P.E., Gonzalez-Chan I.J., Oliva A.I. Algorithm to obtain the species distribution diagrams and solubility curves for depositing ZnS, ZnO, and $Zn(OH)_2$ films in aqueous solution. *Computational and Theoretical Chemistry*, 2021, **1202**, 113325.
[22] Stefan M., Nistor S.V., Ghica D. ZnS and ZnO Semiconductor Nanoparticles Doped with Mn^{2+} Ions. Size Effects Investigated by EPR Spectroscopy. *Springer Series in Materials Science*, 2014, **205**, P. 3–27.
[23] Molefe F. V., Koao L. F., Dejene B. F., Swart H. C. Phase formation of hexagonal wurtzite ZnO through decomposition of $Zn(OH)_2$ at various growth temperatures using CBD method. *Optical Materials.* 2015, **46**, 292-298.
[24] Polyakov E.V., Tzukanov R.R., Volkov I.V., Buldakova L.Yu., Baklanova I.V., Lipina O.A., Zhukov V.P., Kuznetsova Yu.V., Tutyunnik A.P., Maximova M.A. Synthesis and comparative photocatalytic activity of CuO layers on SiO_2 substrates. *Nanosystems: Physics, Chemistry, Mathematics*, 2020, **11** (5), P. 601–607.
[25] Polyakov E.V., Tsukanov R.R., Buldakova L.Yu., Kuznetsova Yu.V., Volkov I.V., Zhukov V.P., Maksimova M.A., Dmitriev A.V., Baklanova I.V., Lipina O.A., Tyutyunnik A.P. Chemical Bath Precipitation and Properties of β-$Ni(OH)_2$ Films Prepared in Aqueous Ammoniac Solutions. *Russian J. of Inorganic Chemistry*, 2022, **67** (6), P. 912–920.
[26] Vasiliev V.P. *Thermodynamic properties of electrolyte solutions*. Vysshaya Shkola, 1982, 320 p.
[27] Kotrly S., Suka L. *Handbook on chemical equilibriq in analytical chemistry*. Ellis Horwood Limiòed, Chichester, 1985, 253 p.
[28] Margulis M.A. Sonoluminescence. *Uspekhi Fizicheskih Nauk*, 2000, **170** (3), P. 263–287.
[29] Lutz H.D, Jung C., Mörtel R., Jacobs H., Stahl R. Hydrogen bonding in solid hydroxides with strongly polarising metal ions, b-$Be(OH)_2$ and o-$Zn(OH)_2$. *Spectrochimica Acta Part A*, 1998, **54**, P. 893–901.
[30] Kim K.M., Kim T.H., Kim H.M., Kim H.J., Gwak G.H., Peak S.M., Oh J.M. Colloidal behaviors of ZnO nanoparticles in various aqueous media. *Toxicology and Environmental Health Sciences*, 2012, **4** (2), P. 121–131.
[31] Zhang X., Wang Q., Wu Zh., Tao D. An experimental study on size distribution and zeta potential of bulk cavitation nanobubbles. *Int. J. of Minerals, Metallurgy and Materials*, 2020, **27** (2), P. 152–161.
[32] Li M., Tonggu L., Zhan X., Mega T.L., Wang L. Cryo-EM Visualization of Nanobubbles in Aqueous Solutions. *Langmuir*, 2016, **32** (43), P. 11111–11115 .
[33] Agarwal A., Ng W.J., Liu Y. Principle and applications of microbubble and nanobubble technology for water treatment. *Chemosphere*, 2011, **84** (9), P. 1175–1180.
[34] Alheshibri M., Baroot A.A., Shui L., Zhang M. Nanobubbles and nanoparticles. *Current Opinion in Colloid & Interface Science*, 2021, **55** (43), 101470.
[35] Bui T.T., Nguyen D.C., Han M. Average size and zeta potential of nanobubbles in different reagent solutions. *J. of Nanoparticle Research*, 2019, **21** (8), P. 1–11.
[36] Pawar S.M., Gurav K.V., Shin S.W., Choi D.S., Kim I.K., Lokhande C.D., Rhee J.I., Kim J.H. Effect of bath temperature on the properties of nanocrystalline ZnO thin films. *J. of Nanoscience and Nanotechnology*, 2010, **10** (5), P. 3412–3415.

Submitted 16 December 2022; revised 6 March 2023; accepted 7 March 2023

Information about the authors:

Evgeny V. Polyakov – Institute of Solid State Chemistry of Ural Branch of Russian Academy of Sciences, 91, Pervomaiskaya str., 620108, Ekaterinburg, Russia; ORCID 0000-0001-7432-994X; polyakov@ihim.uran.ru

Maria A. Maksimova – Institute of Solid State Chemistry of Ural Branch of Russian Academy of Sciences, 91, Pervomaiskaya str., 620108, Ekaterinburg, Russia; ORCID 0009-0004-2807-2222; lab515@ihim.uran.ru

Julia V. Kuznetsova – Institute of Solid State Chemistry of Ural Branch of Russian Academy of Sciences, 91, Pervomaiskaya str., 620108, Ekaterinburg, Russia; ORCID 0000-0002-1253-8727; jukuznetsova@mail.ru

Larisa Yu. Buldakova – Institute of Solid State Chemistry of Ural Branch of Russian Academy of Sciences, 91, Pervomaiskaya str., 620108, Ekaterinburg, Russia; ORCID 0000-0003-3642-7121; buldakova@ihim.uran.ru

Conflict of interest: the authors declare no conflict of interest.

NANOSYSTEMS:
PHYSICS, CHEMISTRY, MATHEMATICS

Lomakin M.S., et al. *Nanosystems: Phys. Chem. Math.*, 2023, **14** (2), 242–253.
http://nanojournal.ifmo.ru

Original article

DOI 10.17586/2220-8054-2023-14-2-242-253

Pyrochlore phase in the Bi_2O_3–Fe_2O_3–WO_3–(H_2O) system: its formation by hydrothermal synthesis in the low-temperature region of the phase diagram

Makariy S. Lomakin[1,2,a], Olga V. Proskurina[1,3,b], Victor V. Gusarov[1,c]

[1]Ioffe Institute, St. Petersburg, Russia

[2]St. Petersburg Electrotechnical University "LETI", St. Petersburg, Russia

[3]St. Petersburg State Institute of Technology, St. Petersburg, Russia

[a]lomakinmakariy@gmail.com, [b]proskurinaov@mail.ru, [c]victor.v.gusarov@gmail.com

Corresponding author: Makariy S. Lomakin, lomakinmakariy@gmail.com

ABSTRACT The present paper investigates features of a (Bi, Fe, □)$_2$(Fe, W)$_2$O$_6$O$'_\delta$ cubic pyrochlore-structured phase (hereinafter BFWO) formation in the Bi_2O_3–Fe_2O_3–WO_3–(H_2O) system under the hydrothermal synthesis conditions at $T < 200$ °C and in the range of pH < 1. It was found that the BFWO phase is formed even when the amorphous precursor suspension is less than 100 °C. The BFWO phase particles have a conditionally spherical morphology and are polycrystalline. The dependency of the average particle size on the synthesis temperature correlates well with the dependency of the average crystallite size on this parameter: both values increase abruptly with an increase in the amorphous precursor suspension treatment temperature from 90 to 110 °C (from ∼140 and 70 nm to ∼180 and 90 nm, respectively), and with a further increase in the hydrothermal treatment temperature to 190 °C, they increase more smoothly (up to ∼210 and 110 nm, respectively). It was found that the average number of crystallites in a particle is ∼9 units regardless of the synthesis temperature, i.e. an increase in the BFWO phase particle size with the increasing temperature (in the considered temperature range) occurs mainly due to an increase in the size of their constituent crystallites.

KEYWORDS pyrochlore-structured phase, hydrothermal synthesis, phase formation, nanocrystals.

ACKNOWLEDGEMENTS The authors are grateful to D.P. Danilovich for assistance in performing the synthetic part of the work. XRD studies, SEM and EDXMA of samples were performed employing the equipment of the Engineering Center of the St. Petersburg State Institute of Technology (Technical University). The work was financially supported by the Russian Science Foundation (Project No. 20-63-47016).

FOR CITATION Lomakin M.S., Proskurina O.V., Gusarov V.V. Pyrochlore phase in the Bi_2O_3–Fe_2O_3–WO_3–(H_2O) system: its formation by hydrothermal synthesis in the low-temperature region of the phase diagram. *Nanosystems: Phys. Chem. Math.*, 2023, **14** (2), 242–253.

1. Introduction

The pyrochlore-structured complex oxide phases with variable composition are the objects of active researches in modern materials science [1–5]. Currently, there is an increased interest in ternary and more multicomponent pyrochlores containing d-elements, since this class of complex oxides has a set of promising physicochemical properties, among which are magnetic [6–8], electrophysical [9, 10], catalytic [11, 12] and optical [13–15] ones. In most of the presented works, the pyrochlore phase is obtained by the solid-state synthesis [6–11, 13], and only in some works, chemistry methods are used to obtain the pyrochlore phase, in particular, by the hydrothermal method [12, 14–16] or by co-precipitation followed by annealing [17, 18]. Important advantages of the hydrothermal method are the possibility of obtaining nanocrystalline materials and synthesizing oxide phases that are unstable at elevated temperatures [19, 20]. It should be noted that in most papers devoted to the hydrothermal synthesis of oxide nanomaterials, of hydrothermal treatment temperature is in the 100 to 250 °C range [21–24].

The hydrothermal treatment temperature and the pH value of the hydrothermal fluid are among the most important parameters of synthesis, since they affect the kinetics of the processes occurring under hydrothermal conditions, determining the crystalline phase precursor solubility and the reacting components diffusion rate. In this regard, the dimensional and morphological characteristics, as well as the chemical composition of the crystalline product, as a rule, strictly depend on these parameters [25–29].

In the Bi_2O_3–Fe_2O_3–WO_3–(H_2O) system, the cubic pyrochlore-structured phase (BFWO) was obtained by hydrothermal synthesis only at $T = 200$ °C [14, 16, 28] and 180 °C [15], while other isothermal regions of the phase diagram were not studied. In this work, the BFWO phase was obtained at lower temperatures of the amorphous precursor suspension treatment (90–190 °C).

The effect of the hydrothermal fluid pH on the chemical composition and size parameters of particles and crystallites of the BFWO phase was studied in [28]. It was shown that in the Bi_2O_3–Fe_2O_3–WO_3–(H_2O) system, the composition of the pyrochlore phase formed under hydrothermal conditions will coincide well with the nominal composition specified for the synthesis when the hydrothermal fluid pH is in the ∼2 to ∼5 range. The average particle and crystallite sizes in this pH range pass through an extremal value at pH ∼4–5, taking the smallest values at pH < 1. In other words, certain synthetic problems are inevitable when it is required to obtain the BFWO phase with the smallest possible particle and crystallite sizes and the composition specified for the synthesis at the same time. In this paper, a solution to this synthetic problem is proposed.

The aim of this work is to study features of the cubic pyrochlore-structured phase formation in the Bi_2O_3–Fe_2O_3–WO_3–(H_2O) system under the hydrothermal synthesis conditions at $T < 200$ °C and in the range of pH < 1.

2. Materials and Methods

2.1. Synthesis section

The synthesis procedure, which is the same for all samples, is described below, and Table 1 shows the values of the variable synthesis parameters (nominal composition specified for the synthesis and hydrothermal treatment temperature). To obtain one sample, **x** mmol of crystalline hydrate of bismuth (III) nitrate, $Bi(NO_3)_3{\cdot}5H_2O$ (puriss. spec.), and **y** mmol of crystalline hydrate of iron (III) nitrate, $Fe(NO_3)_3{\cdot}9H_2O$ (pur.), were dissolved in 8.3 ml of 6 M HNO_3 (puriss. spec.), after which 41.7 ml of distilled water was added to the resulting solution. Next, **z** mmol of sodium tungstate (VI) crystalline hydrate, $Na_2WO_4{\cdot}2H_2O$ (puriss. spec.), was dissolved in 50 ml of distilled water and the resulting solution was added dropwise into the acidic solution of bismuth and iron nitrates stirred with a magnetic stirrer at 800 rpm (∼30 mL of distilled water was then added there and used to rinse the beaker that had contained the sodium tungstate solution). After additional stirring at 1000 rpm for ∼1 h, the amorphous precursor suspension (pH < 1) obtained this way was transferred into Teflon chambers (∼80% filling) and placed in steel autoclaves, which were then put in a furnace heated up to **T**°C. After 24 h, the autoclaves were removed from the furnace and cooled in air. The resulting precipitates were separated from the mother liquor (it was poured out), rinsed with distilled water several times by decantation and dried at 70 °C for 24 h.

According to the synthesis procedure described above, four series of samples were obtained (series 1 is the main one, series 2, 3 and 4 are additional), the synthetic parameters of which are presented in Table. 1. When obtaining samples of series 1, the amorphous precursor suspension treatment temperature was varied, and the remaining series of samples were obtained in order to conduct additional studies. Series 2 was obtained in order to determine the effect of the amount of iron (III) in the nominal composition on the phase composition of the hydrothermal synthesis products; series 3 was produced for determining the phase composition of the precursor suspension dispersed phase before the hydrothermal treatment; while series 4 was produced for determining the phase composition of the hydrothermal synthesis products in the absence of some component in the nominal composition.

Samples of series 3 were obtained by the following procedure: when synthesizing samples of series 2: the suspensions remaining after autoclaves filling were centrifuged, the liquid phase poured out, and the resulting wet precipitate dried at 70 °C for 24 h. When obtaining samples of series 4, the volumes of mixed solutions remained constant, only the presence or absence of some component in the solutions varied. Rinsing of these samples after hydrothermal synthesis was carried out in isopropyl alcohol. The W+H^+ HTS 150 °C sample was synthesized by adding sodium tungstate (VI) solution to the nitric acid solution. The Bi+W HTS 150 °C sample was synthesized by adding sodium tungstate (VI) solution to the acidic bismuth (III) nitrate solution. The Fe+W HTS 150 °C sample was synthesized by adding sodium tungstate (VI) solution to the acidic iron (III) nitrate solution. The Bi+Fe HTS 150 °C sample was synthesized by adding 50 ml of distilled water to the acidic solution of bismuth (III) and iron (III) nitrates.

2.2. Characterization

The crystal structure of the obtained samples was analyzed by X-ray diffraction (XRD) using a Rigaku SmartLab 3 Powder X-ray Diffractometer (Rigaku Corporation, Japan). X-ray diffraction patterns (Co-K_α radiation (series 1 samples), Cu-K_α radiation (series 2, 3 and 4 samples), K_β filter) were recorded in the Bragg-Brentano geometry at room temperature. The observed peak parameters (the absolute intensity (I_{abs}), Bragg angle ($2\theta_{obs}$), full width at half maximum ($FWHM_{obs}$), and the integral width (β_{obs})) were determined using the Rigaku SmartLab Studio II software package. The same software package employed the method of fundamental parameters for plotting curves of the volume lognormal crystallite size distribution. The instrumental broadening ($FWHM_{instr}$) was corrected by using a standard recorded under similar conditions. The used standard was a single-crystal $SrTiO_3$ plate with a polished side perpendicular to the crystallographic direction [100]. According to the criterion that determines the type of peak profile [30], peaks in all samples were pseudo-Voigt, therefore, the calculation of the corrected value of the full width at half-height ($FWHM_{corr}$) was carried out taking into account the pseudo-Voigt peak shape (equation (1), [30]). The average crystallite size (D) and microstresses (ε_s) were calculated by the Williamson-Hall method for the case of pseudo-Voigt peaks observed in diffraction patterns (equation (8), [31]). The calculation was performed using the peaks with Miller indices of 311, 222,

TABLE 1. Obtained samples, nominal composition specified for the synthesis and synthesis temperature

Sample		Nominal composition	n(Bi) (**x**), mmol	n(Fe) (**y**), mmol	n(W) (**z**), mmol	**T**, °C
Series 1	$Fe_{1.5}$ HTS 90 °C	$Bi_{0.5}Fe_{1.5}WO_6$	3.5	10.5	7.0	90
	$Fe_{1.5}$ HTS 110 °C					110
	$Fe_{1.5}$ HTS 130 °C					130
	$Fe_{1.5}$ HTS 150 °C					150
	$Fe_{1.5}$ HTS 170 °C					170
	$Fe_{1.5}$ HTS 190 °C					190
Series 2	$Fe_{0.5}$ HTS 150 °C	$Bi_{0.5}Fe_{0.5}WO_{4.50}$	3.5	3.5	7.0	150
	$Fe_{1.5}$ HTS 150 °C	$Bi_{0.5}Fe_{1.5}WO_6$	3.5	10.5	7.0	
	$Fe_{3.0}$ HTS 150 °C	$Bi_{0.5}Fe_{3.0}WO_{8.25}$	3.5	21.0	7.0	
Series 3	$Fe_{0.5}$ no HTS_no rinsing	$Bi_{0.5}Fe_{0.5}WO_{4.50}$	3.5	3.5	7.0	–
	$Fe_{1.5}$ no HTS_no rinsing	$Bi_{0.5}Fe_{1.5}WO_6$	3.5	10.5	7.0	–
	$Fe_{3.0}$ no HTS_no rinsing	$Bi_{0.5}Fe_{3.0}WO_{8.25}$	3.5	21.0	7.0	–
Series 4	W+H^+ HTS 150 °C	WO_3	–	–	7.0	150
	Bi+W HTS 150 °C	$Bi_{0.5}WO_{3.75}$	3.5	–	7.0	
	Fe+W HTS 150 °C	$Fe_{1.5}WO_{5.25}$	–	10.5	7.0	
	Bi+Fe HTS 150 °C	$Bi_{0.5}Fe_{1.5}O_3$	3.5	10.5	–	

Note 1: Sample $Fe_{1.5}$ HTS 150 °C is included in both Series 1 and 2

400, 511, 440, 531, 622, 444, and 711, assuming $\lambda(\mathrm{Co}K_{\alpha 1})$ = 1.789001 Å, $K_{Scherrer} = 0.94$, and $K_{strain} = 4$. The use of the Williamson-Hall method for calculating the average crystallite size was justified by the presence of microstresses in all the samples, and the illegitimacy of using the traditional Scherrer's formula in this case.

Scanning electron microscopy (SEM) images and bulk elemental composition of the samples were obtained on a Tescan Vega 3 SBH scanning electron microscope (Tescan Orsay Holding, Czech Republic) with an Oxford Instruments Energy Dispersive X-ray Microanalysis (EDXMA) attachment. The relative number of elements was calculated using the AZtec software, and only such series of electronic transitions as Fe (K-series), Bi and W (L-series) were taken into account in the calculation. The characteristic emission spectra of each sample were accumulated from three sites with a total area of ∼9 mm^2, with a set of statistics for at least 2.5 million pulses at each site. The readings from each site were averaged, and the measurement error was determined at a confidence level of 0.95. The histograms of the volume particle size distribution were constructed on the basis of random 500-particle samples for each synthesized sample from series 1. The normal distribution curves describing the constructed histograms were plotted using the Origin 2018 software package.

3. Results and discussions

3.1. Chemical composition

The EDXMA data on the bulk chemical composition of the obtained samples are presented in Table 2. In all samples of series 1 and 2, the bismuth and tungsten atomic ratio generally corresponds to the nominal composition (except for the $Fe_{3.0}$ HTS 150 °C sample, in which there is a lack of tungsten), while the quantity of iron atoms in relation to these elements is much less, than in the nominal composition. The depletion of the bulk composition of these samples in iron (III) is apparently due to the fact that a significant part of this component remains in the cooled hydrothermal fluid, and therefore is removed during sediment rinsing. It should be noted that in the case of the $Fe_{1.5}$ HTS 190 °C sample, a certain excess of iron in its bulk composition relative to other samples of series 1 is due to the presence of another iron-containing phase in this sample (see 3.2. XRD analysis).

In addition, from the obtained data on the bulk composition of samples of series 3, it follows that, the distribution of components between the dispersed phase and the dispersion medium of the precursor suspension is very uneven: tungsten

TABLE 2. Bulk chemical composition of the obtained samples, in rel. at. units, according to the EDXMA data

Sample		Nominal composition	Bulk chemical composition		
			Bi/W±Δ	Fe/W±Δ	Bi/Fe±Δ
Series 1	$Fe_{1.5}$ HTS 90 °C	$Bi_{0.5}Fe_{1.5}WO_6$	0.50±0.02	0.40±0.01	1.26±0.06
	$Fe_{1.5}$ HTS 110 °C		0.54±0.04	0.35±0.02	1.57±0.03
	$Fe_{1.5}$ HTS 130 °C		0.56±0.03	0.36±0.01	1.53±0.12
	$Fe_{1.5}$ HTS 150 °C		0.53±0.05	0.37±0.03	1.41±0.06
	$Fe_{1.5}$ HTS 170 °C		0.54±0.02	0.39±0.01	1.38±0.05
	$Fe_{1.5}$ HTS 190 °C		0.54±0.02	0.57±0.06	0.96±0.08
Series 2	$Fe_{0.5}$ HTS 150 °C	$Bi_{0.5}Fe_{0.5}WO_{4.50}$	0.54±0.03	0.31±0.01	1.78±0.04
	$Fe_{1.5}$ HTS 150 °C	$Bi_{0.5}Fe_{1.5}WO_6$	0.53±0.05	0.37±0.03	1.41±0.06
	$Fe_{3.0}$ HTS 150 °C	$Bi_{0.5}Fe_{3.0}WO_{8.25}$	0.58±0.04	0.51±0.01	1.13±0.07
Series 3	$Fe_{0.5}$ no HTS_no rinsing	$Bi_{0.5}Fe_{0.5}W_{4.50}$	0.37±0.02	0.06±0.01	6.12±1.13
	$Fe_{1.5}$ no HTS_no rinsing	$Bi_{0.5}Fe_{1.5}WO_6$	0.32±0.02	0.15±0.01	2.08±0.12
	$Fe_{3.0}$ no HTS_no rinsing	$Bi_{0.5}Fe_{3.0}WO_{8.25}$	0.29±0.01	0.28±0.01	1.03±0.06
Series 4	W+H^+ HTS 150 °C	WO_3	–	–	–
	Bi+W HTS 150 °C	$Bi_{0.5}WO_{3.75}$	0.53±0.05	–	–
	Fe+W HTS 150 °C	$Fe_{1.5}WO_{5.25}$	–	0.54±0.01	–
	Bi+Fe HTS 150 °C	$Bi_{0.5}Fe_{1.5}O_3$	*no solid phase formed*		

(VI) is located predominantly in the solid phase, iron (III) – in the liquid phase, and bismuth (III) is distributed over these phases approximately equally. In the bulk composition of all samples of series 3, impurity amounts of sodium are also found, since the sediment was not rinsed during their preparation.

3.2. XRD analysis

Powder X-ray diffraction patterns of samples of series 1 are presented in Fig. 1. All the observed peaks refer to the cubic pyrochlore-structured BFWO phase (CSD 1961005, [16]), the only exception is the $Fe_{1.5}$ HTS 190 °C sample, the diffraction pattern of which demonstrates weak peaks from the α-Fe_2O_3 phase, in addition to peaks from the BFWO phase. The results of phase composition analysis of this sample indicate that the phase diagram of the Bi_2O_3–Fe_2O_3–WO_3–(H_2O) system has a two-phase region in which the BFWO phase coexists with the hematite phase in the region of compositions enriched in iron (III) oxide. The obtained experimental data can be useful for determining the boundary of the homogeneity region of the BFWO phase from the side iron oxide (III) – under hydrothermal conditions at low T (from 100 to $\sim$ 200°C). An increase in the hydrothermal fluid pH, according to the data on phase equilibria in the Fe_2O_3-H_2O system [32], will lead to an increase in the FeOOH$\rightarrow$ α-Fe_2O_3 transition temperature, which must be taken into account when studying the BFWO – α-Fe_2O_3 phase equilibrium region. It should be noted that the hematite phase may turn out to be nanocrystalline in the obtained samples, and a part of iron (III) may also be present in the amorphous phase located, for example, along the BFWO grain boundaries [33, 34]. In both described cases, X-ray diffraction does not make it possible to identify the iron-containing impurity phase in the presence of a complex oxide, in which the main scattering centers are “heavy” bismuth and tungsten atoms.

The unit cell parameter a of the BFWO phase is, within the error, the same for all samples of series 1 and is 10.33(1) Å, which indicates the absence of a noticeable change in the BFWO phase composition in these samples. It should be noted that the amorphous halo is not found on the presented diffraction patterns, from which it can be qualitatively concluded that the degree of the amorphous phase transformation into the crystalline BFWO phase is close to 1.

Fig. 2a shows the dependencies of the average crystallite size of the BFWO phase on the synthesis temperature, and Fig. 2b shows the curves of the volume lognormal crystallite size distribution based on peak 222 depending on the synthesis temperature (series 1 samples). The average crystallite size of the BFWO phase was estimated in two ways: (1) by the Williamson–Hall graphical method (Fig. 3), where the peaks corresponding to different crystallographic directions were included in the calculations, and (2) as a weighted average of the volume lognormal crystallite size

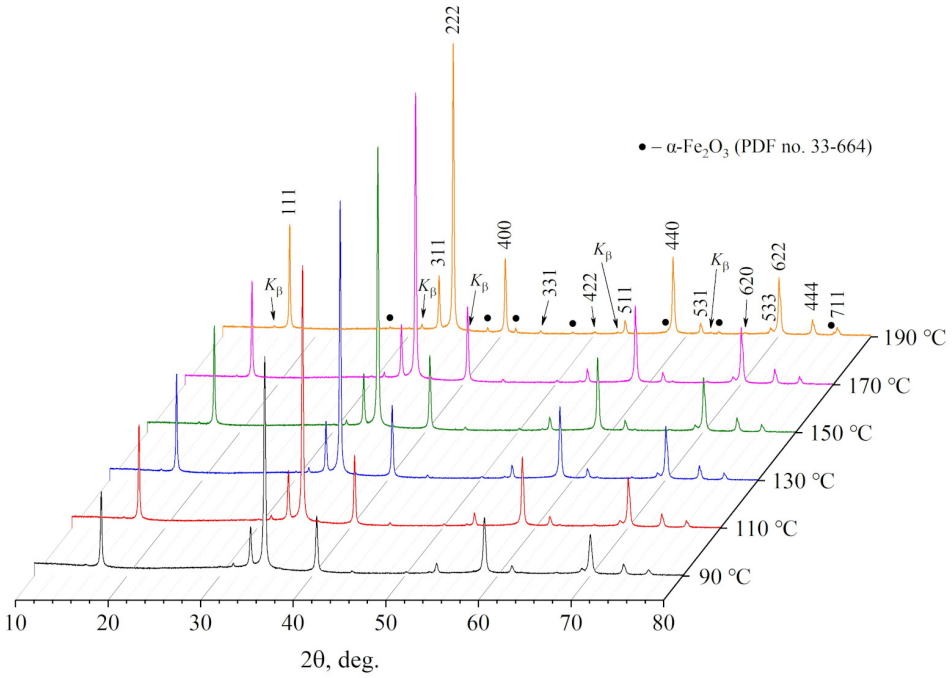

FIG. 1. XRD patterns (series 1 samples)

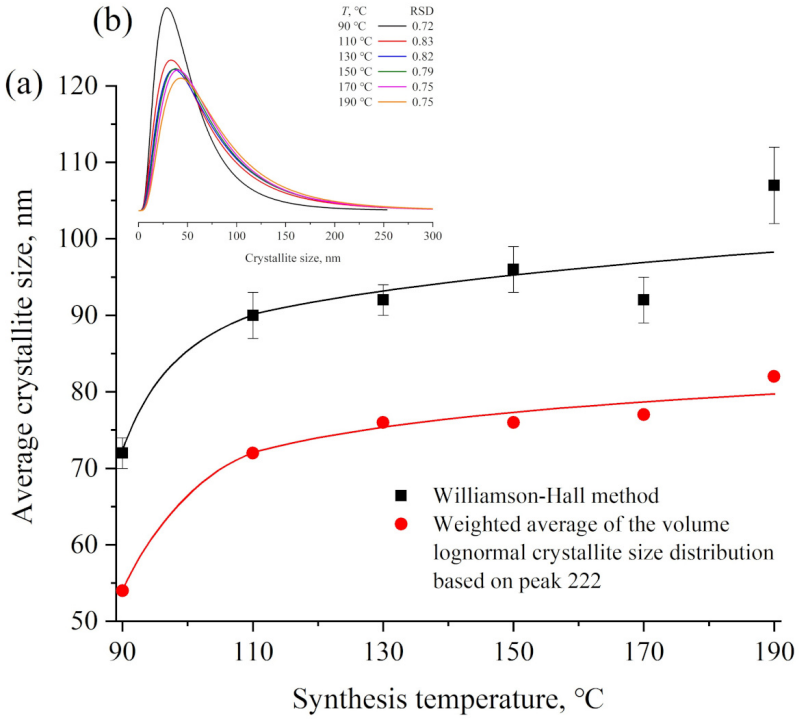

FIG. 2. (a) dependencies of the average crystallite size of the BFWO phase on the synthesis temperature and (b) curves of the volume lognormal crystallite size distribution based on peak 222 depending on the synthesis temperature (RSD – relative standard deviation) (series 1 samples)

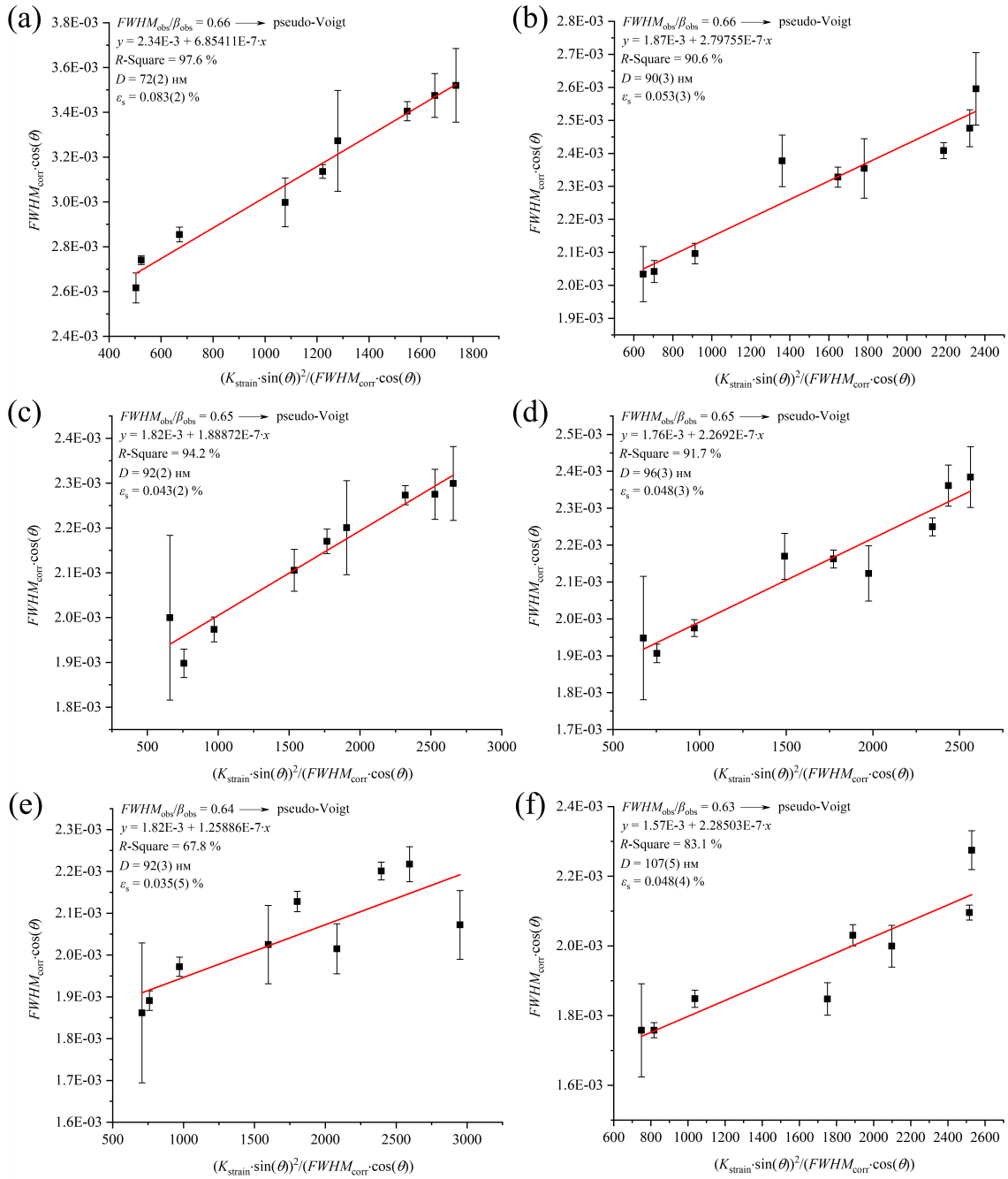

FIG. 3. Williamson-Hall plots for samples obtained at different synthesis temperatures (a (90 °C), b (110 °C), c (130 °C), d (150 °C), e (170 °C), f (190 °C)) (series 1 samples)

distribution based on peak 222. The average crystallite size calculated by method (1) turns out to be larger for each temperature taken than that calculated by method (2), however, both presented correlate well with each other. With an increase in the precursor suspension treatment temperature from 90 to 110 °C, the average in all crystallographic directions crystallite size increases abruptly from ∼70 to 90 nm, and the average in the [111] direction crystallite size from ∼55 to 70 nm; with a further increase in the hydrothermal treatment temperature to 190 °C, the average crystallite size increases more smoothly to ∼110 nm in the first case and to ∼80 nm in the second. It can be assumed that the differences in the average crystallite sizes calculated by the two methods are due either to some anisotropy of the crystallites or to the fact that the instrumental broadening of the device is taken into account in the first case using an external standard, while in the second case it is calculated based on the optical configuration of the device.

Powder X-ray diffraction patterns of samples of series 2, 3, and 4 are shown in Figs. 4,5,6, respectively. In the $Fe_{0.5}$ HTS 150 °C sample, in addition to peaks belonging to the BFWO phase (a = 10.33(1) Å), broad peaks are observed at 2θ angles (Cu-K_α radiation): 22.6, 28.1 (possibly Bi_2WO_6 (PDF no. 73-1126)), 36.4 and 55.3°, which indicate the presence of impurity amounts of an unidentifiable phase. The appearance of an impurity crystalline phase indicates that

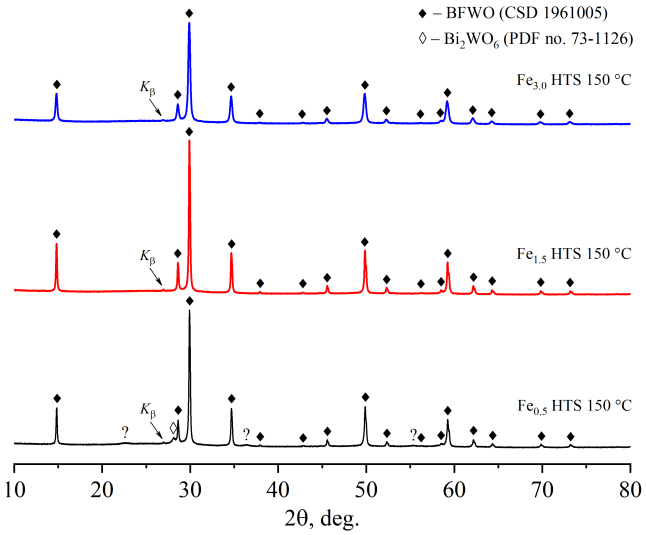

FIG. 4. XRD patterns (series 2 samples)

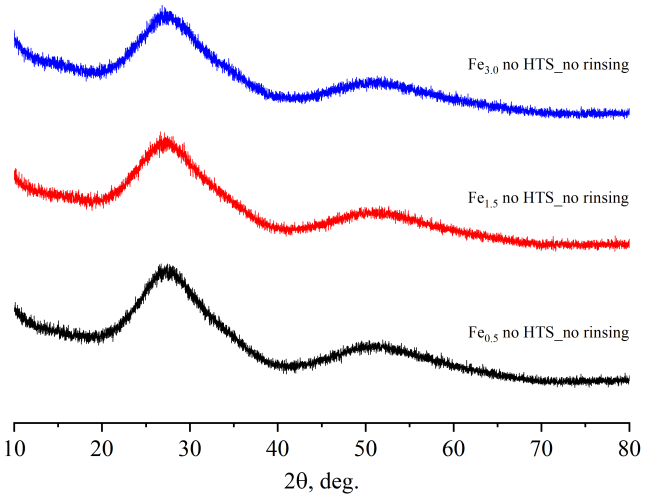

FIG. 5. XRD patterns (series 3 samples)

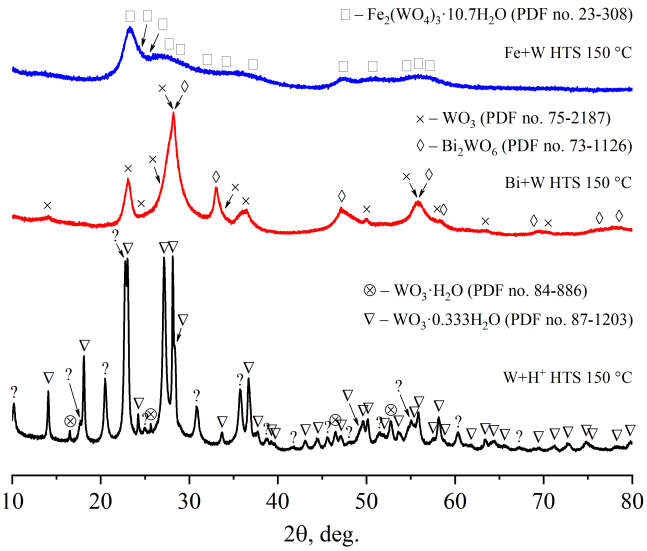

FIG. 6. XRD patterns (series 4 samples)

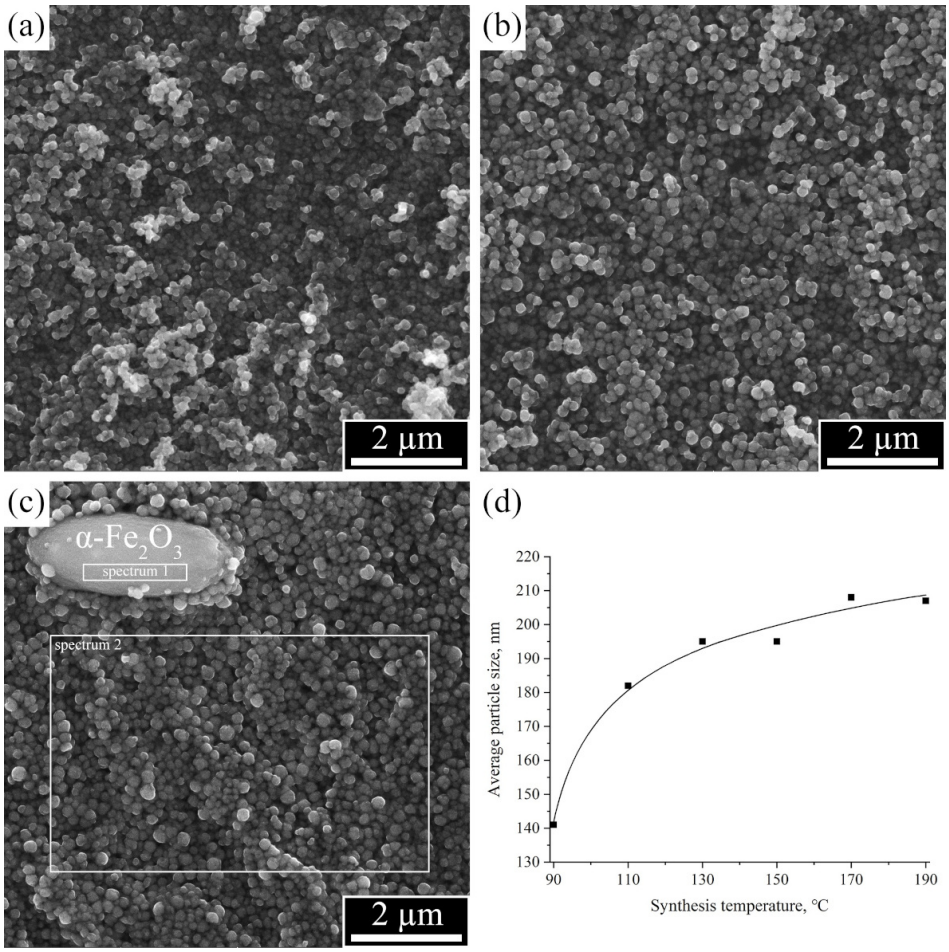

FIG. 7. (a (90 °C), b (110 °C), c (190 °C)) SEM data and (d) dependency of the BFWO phase average particle size on the synthesis temperature (series 1 samples)

the bulk composition of this sample, apparently is in the region of the phase diagram, which is more depleted in iron oxide, in comparison with the boundaries of the BFWO phase homogeneity region. In the $Fe_{1.5}$ HTS 150 °C and $Fe_{3.0}$ HTS 150 °C samples, the only crystalline phase is the BFWO phase (a = 10.33(1) Å and 10.35(1) Å, respectively), whose peaks in the second case turn out to be more broadened. The presented values of the BFWO phase unit cell parameter a indicate that the composition of this phase in the $Fe_{3.0}$ HTS 150 °C sample is more enriched in bismuth (III) than in other samples.

Thus, based on the data on the chemical and phase composition of the samples of series 1 and 2, it can be concluded that when the nominal composition of a sample contains a 2–4 times excess of iron (III) (relative to the stoichiometry of the BFWO phase homogeneity region) and the temperature of the precursor suspension hydrothermal treatment does not exceed ∼170 °C, there occurs the formation of the BFWO phase without impurities of other crystalline phases and with the Bi/W atomic ratio specified for the synthesis. In the case when the excess of iron (III) is ∼8 times, the composition of the forming BFWO phase turns out to be somewhat depleted in tungsten (VI) relative to the nominal composition specified for the synthesis. Otherwise, in the absence of an excess of iron (III), the bulk composition of the crystalline product formed as a result of hydrothermal synthesis (at pH < 1) is beyond the BFWO phase homogeneity region.

Powder X-ray diffraction patterns of samples of series 3 (Fig. 5) do not show any peaks from crystalline phases, which suggests that the dispersed phase of the precursor suspension is X-ray amorphous.

According to phase composition data (Fig. 6), no peaks characteristic of the pyrochlore-structured phase are observed in the samples of series 4. In the W+H^+ HTS 150 °C sample, most of the reflections belong to the $WO_3 \cdot 0.333H_2O$ (PDF no. 87-1203) and $WO_3 \cdot H_2O$ (PDF no. 84-886) phases, and the rest are not identified; in the Bi+W HTS 150 °C sample the Bi_2WO_6 (PDF no. 73-1126) and WO_3 (PDF no. 75-2187) phases are detected; in the Fe+W HTS 150 °C sample the $Fe_2(WO_4)_3 \cdot 10.7H_2O$ (PDF no. 23-308) phase is found while in the Bi+Fe HTS 150 °C sample the solid phase is absent.

3.3. SEM

The SEM data of samples of series 1 are presented in Fig. 7. In all single-phase samples of this series, only one morphological motif is observed, i.e. conditionally spherical particles, the size of which depends on the precursor suspension

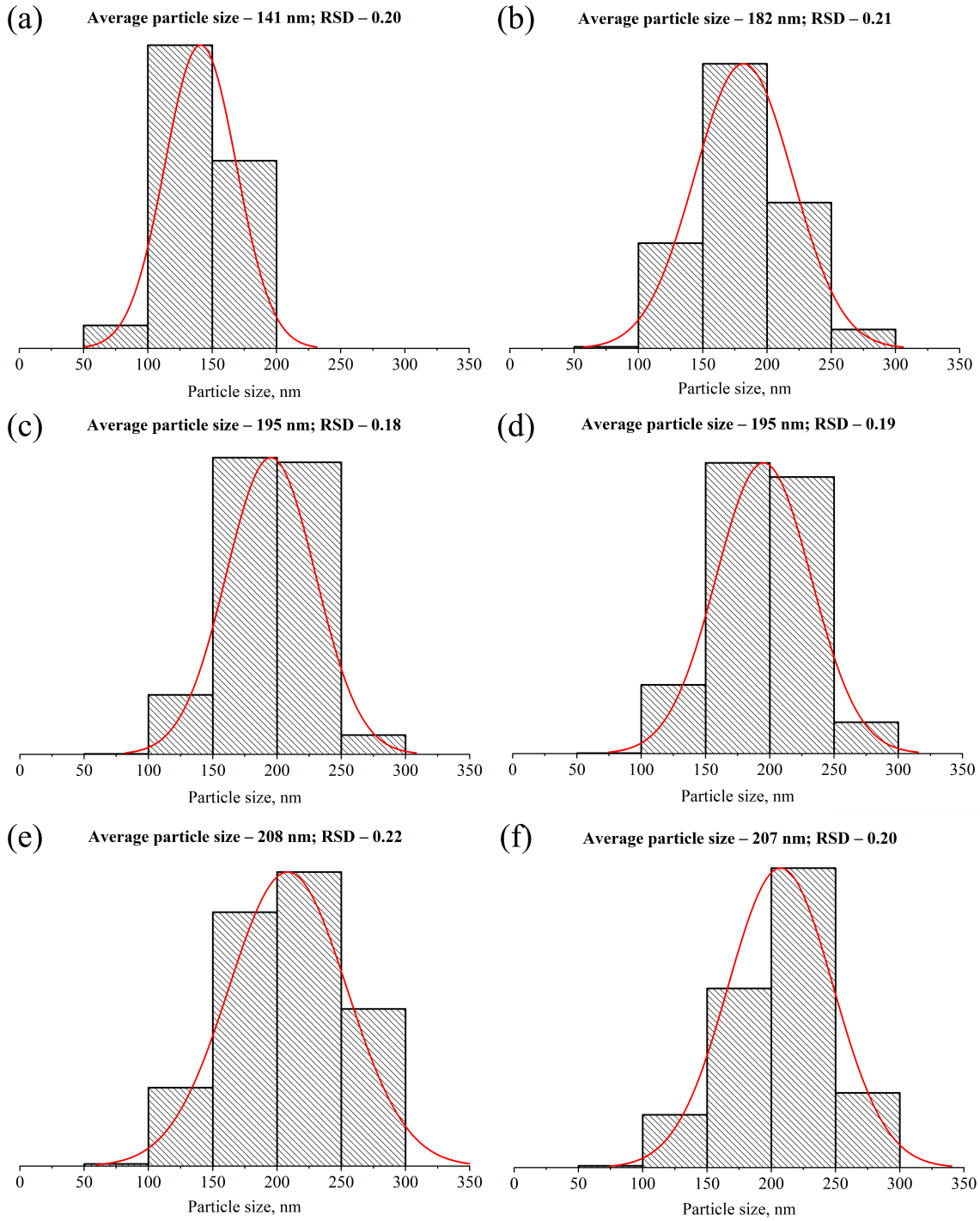

FIG. 8. Histograms and corresponding curves of the volume normal particle size distribution and normal distribution parameters, i.e. average size and RSD (relative standard deviation), for samples obtained at different synthesis temperatures (a (90 °C), b (110 °C), c (130 °C), d (150 °C), e (170 °C), f (190 °C)) (series 1 samples)

treatment temperature. In the $Fe_{1.5}$ HTS 190 °C sample, in addition to the BFWO phase particles, rare large particles resembling an elongated spheroid can be observed. According to the local EDXMA data, these large particles are the α-Fe_2O_3 phase (spectrum 1: $Bi_{0.73}Fe_{20.0}WO_{34.10}$), which peaks were detected in the diffraction pattern of the sample. It is interesting to note that the composition of the BFWO phase (spectrum 2: $Bi_{0.59}Fe_{0.38}WO_{4.46}$), obtained from a certain limited area that does not contain hematite particles, generally coincides with the bulk composition of single-phase samples of this series.

The constructed histograms of the volume particle size distribution are well described by the normal distribution function (Fig. 8), from which average particle sizes of the BFWO phase were determined. The dependency of the average particle size (Fig. 7d) on the synthesis temperature correlates well with the dependency of the average crystallite size on this parameter (Fig. 2): with an increase in the precursor suspension treatment temperature from 90 to 110 °C, the average particle size increases abruptly from ∼140 to 180 nm, and with a further increase in the hydrothermal treatment temperature to 190 °C, it increases more smoothly to ∼210 nm.

It should be noted that the BFWO phase particles observed in the micrographs are predominantly polycrystalline, which follows from a comparison of the average particle and crystallite sizes. Assuming that all particles and crystallites are conditionally spherical, and their diameters are equal to the average particle (Fig. 7d) and crystallite sizes (Fig. 2, Williamson-Hall method), respectively, the average number of crystallites in a particle will be ∼9 units regardless of the synthesis temperature. This fact may indicate that the increase in the BFWO phase particle size with temperature (in the considered temperature range) occurs mainly due to an increase in the size of their constituent crystallites. A jump-like increase in the average crystallite and, as a result, particle size following an increase in the precursor suspension treatment temperature from 90 to 110 °C may apparently, indicate a sharp increase in the amorphous precursor components solubility upon transition to the hydrothermal synthesis mode ($T > 100$ °C).

4. Conclusion

The characterized cubic pyrochlore-structured phase (BFWO) in the Bi_2O_3–Fe_2O_3–WO_3–(H_2O) system was obtained by hydrothermal synthesis at $T < 200$ °C and in the range of pH < 1. It was found that the BFWO phase is formed even when the precursor suspension treatment temperature is less than 100 °C, i.e. is beyond the lower limit of the hydrothermal synthesis. It was shown that when a sample nominal composition contains a 2–4 times excess of iron (III) (relative to the stoichiometry of the BFWO phase homogeneity region) and the precursor suspension hydrothermal treatment temperature does not exceeds ∼170 °C, then the formation of the BFWO phase without impurities of other crystalline phases and with the Bi/W atomic ratio specified for the synthesis is observed. In this case, the excess of iron (III) remains in the liquid phase and is removed from the system by rinsing the crystalline precipitate. With an increase in the hydrothermal treatment temperature to ∼190 °C, along with the pyrochlore phase, a hematite phase (α-Fe_2O_3) is formed. In the case of as much as the 8-time excess of iron (III), the composition of the forming BFWO phase turns out to be somewhat depleted in tungsten (VI) relative to the nominal composition specified for the synthesis. Otherwise, when there is no sufficient excess of iron (III) in the nominal composition of the sample, as a result of hydrothermal synthesis, multiphase mixtures containing the BFWO phase are formed, the bulk composition of which is in the region of the phase diagram that is more depleted in iron oxide, compared to the BFWO phase homogeneity region boundaries. It is shown that in the absence of any component in the nominal composition, a pyrochlore-structured phase is not formed as a result of hydrothermal synthesis.

It was established that the precursor suspension is dispersed phase X-ray amorphous, and the isothermal exposure for 24 h at all studied synthesis temperatures is sufficient to achieve complete transformation of the amorphous phase into the crystalline BFWO. The BFWO phase unit cell parameter a is 10.33(1) Å regardless of the synthesis temperature (the nominal composition being $Bi_{0.5}Fe_{1.5}WO_6$), which indicates that there is no noticeable change in the formed BFWO phase composition with temperature variation in the studied range.

The dependency of the average particle size on the synthesis temperature correlates well with the dependency of the average crystallite size on this parameter: both values increase abruptly with an increase in the amorphous precursor suspension treatment temperature from 90 to 110 °C while with a further increase in the hydrothermal treatment temperature to 190 °C, they increase more smoothly. Apparently, such a nature of the dependencies of these values on temperature may indicate a sharp increase in the solubility of the amorphous precursor components upon transition to the hydrothermal synthesis mode (T > 100 °C).

It was found that the average number of crystallites in a particle is ∼9 units regardless of the synthesis temperature. This fact may indicate that the increase in the BFWO phase particle size with increasing temperature (in the considered temperature range) occurs mainly due to an increase in the size of their constituent crystallites.

References

[1] Greedan J.E. Frustrated rare earth magnetism: spin glasses, spin liquids and spin ices in pyrochlore oxides. *Journal of Alloys and Compounds*, 2006, **408–412**, P. 444–455.

[2] Gardner J.S., Gingras M.J.P., Greedan J.E. Magnetic pyrochlore oxides. *Reviews of Modern Physics*, 2010, **82**(1), P. 53–107.

[3] Jitta R.R., Gundeboina R., Veldurthi N.K., Guje R., Muga V. Defect pyrochlore oxides: as photocatalyst materials for environmental and energy applications – a review. *Journal of Chemical Technology & Biotechnology*, 2015, **90**(11), P. 1937–1948.
[4] Anantharaman A.P., Dasari H.P. Potential of pyrochlore structure materials in solid oxide fuel cell applications. *Ceramics International*, 2021, **47**(4), P. 4367–4388.
[5] Wiebe C.R., Hallas A.M. Frustration under pressure: Exotic magnetism in new pyrochlore oxides. *APL Materials*, 2015, **3**(4), P. 041519.
[6] Ellert O.G., Egorysheva A.V., Gajtko O.M., Kirdyankin D.I., Svetogorov R.D. Highly frustrated Bi-Cr-Sb-O pyrochlore with spin-glass transition. *Journal of Magnetism and Magnetic Materials*, 2018, **463**, P. 13–18.
[7] Egorysheva A.V., Ellert O.G., Gaitko O.M., Brekhovskikh M.N., Zhidkova I.A., Maksimov Yu.V. Fluorination of Bi1.8Fe1.2SbO7 pyrochlore solid solutions. *Inorganic Materials*, 2017, **53**(9), P. 962–968.
[8] Babu G.S., Bedanta S., Valant M. Evidence of the spin glass state in $(Bi_{1.88}Fe_{0.12})(Fe_{1.42}Te_{0.58})O_{6.87}$ pyrochlore. *Solid State Communication*, 2013, **158**, P. 51–53.
[9] Jusoh F.A., Tan K.B., Zainal Z., Chen S.K., Khaw C.C., Lee O.J. Novel pyrochlores in the Bi_2O_3–Fe_2O_3–Ta_2O_5 (BFT) ternary system: synthesis, structural and electrical properties. *Journal of Materials Research and Technology*, 2020, **9**(5), P. 11022–11034.
[10] Zhuk N.A., Krzhizhanovskaya M.G., Sekushin N.A., Sivkov D.V., Muravyov V.A. Nb-doping effect on microstructure, thermal and dielectric properties of bismuth nickel tantalate pyrochlore. *Ceramics International*, 2023, **49**(2), P. 2934–2940.
[11] Valant M., Babu G.S., Vrcon M., Kolodiazhnyi T., Axelsson A.-K. Pyrochlore range from Bi_2O_3–Fe_2O_3–TeO_3 system for LTCC and photocatalysis and the crystal structure of new $Bi_3(Fe_{0.56}Te_{0.44})_3O_{11}$. *Journal of the American Ceramic Society*, 2012, **95**(2), P. 644–650.
[12] Playford H.Y., Modeshia D.R., Barney E.R., Hannon A.C., Wright C.S., Fisher J.M., Amieiro-Fonseca A., Thompsett D., O'Dell L.A., Rees G.J., Smith M.E., Hanna J.V., Walton R.I. Structural Characterization and Redox Catalytic Properties of Cerium(IV) Pyrochlore Oxides. *Chemistry of Materials*, 2011, **23**(24), P. 5464–5473.
[13] Zhuk N.A., Krzhizhanovskaya M.G., Koroleva A.V., Semenov V.G., Selyutin A.A., Lebedev A.M., Nekipelov S.V., Sivkov D.V., Kharton V.V., Lutoev V.P., Makeev B.A. Fe,Mg-Codoped Bismuth Tantalate Pyrochlores: Crystal Structure, Thermal Stability, Optical and Electrical Properties, XPS, NEXAFS, ESR, and ^{57}Fe Mössbauer Spectroscopy Study. *Inorganics*, 2023, **11**(1), P. 8.
[14] Lomakin M.S., Proskurina O.V., Sergeev A.A., Buryanenko I.V., Semenov V.G., Voznesenskiy S.S., Gusarov V.V. Crystal structure and optical properties of the Bi–Fe–W–O pyrochlore phase synthesized via a hydrothermal method. *Journal of Alloys and Compounds*, 2021, **889**, P. 161598.
[15] Lomakin M.S., Proskurina O.V., Levin A.A., Sergeev A.A., Leonov A.A., Nevedomsky V.N., Voznesenskiy S.S. Pyrochlore Phase in the Bi_2O_3–Fe_2O_3–WO_3–(H_2O) System: its Formation by Hydrothermal-Microwave Synthesis and Optical Properties. *Russian Journal of Inorganic Chemistry*, 2022, **67**(6), P. 820–829.
[16] Lomakin M.S., Proskurina O.V., Danilovich D.P., Panchuk V.V., Semenov V.G., Gusarov V.V. Hydrothermal Synthesis, Phase Formation and Crystal Chemistry of the pyrochlore/Bi_2WO_6 and pyrochlore/α-Fe_2O_3 Composites in the Bi_2O_3–Fe_2O_3–WO_3 System. *Journal of Solid State Chemistry*, 2020, **282**, P. 121064.
[17] Annamalai K., Radha R., Vijayakumari S., Kichanov S.E., Balakumar S. Insight into the investigation on nanostructured defect pyrochlore $Bi_{2-x}Fe_xWO_6$ and its photocatalytic degradation of mixed cationic dyes. *Materials Science in Semiconductor Processing*, 2022, **150**(2), P. 106961.
[18] Annamalai K., Radha R., Vijayakumari S., Balakumar S. High-temperature stabilized defect pyrochlore $Bi_{2-x}Fe_xWO_6$ nanostructures and their effects on photocatalytic water remediation and photo-electrochemical oxygen evolution kinetics. *Catalysis Science & Technology*, 2023, **13**(5), P. 1409–1424.
[19] Shandilya M., Rai R., Singh J. Review: hydrothermal technology for smart materials. *Advances in Applied Ceramics*, 2016, **115**(6), P. 354–376.
[20] Modeshia D.R., Walton R.I. Solvothermal synthesis of perovskites and pyrochlores: crystallisation of functional oxides under mild conditions. *Chemical Society Reviews*, 2010, **39**(11), P. 4303–4325.
[21] Ejsmont A., Goscianska J. Hydrothermal Synthesis of ZnO Superstructures with Controlled Morphology via Temperature and pH Optimization. *Materials*, 2023, **16**(4), P. 1641.
[22] Xiong D., Qi Y., Li X., Liu X., Tao H., Chen W., Zhao X. Hydrothermal synthesis of delafossite $CuFeO_2$ crystals at 100 C. *RSC Advances*, 2015, **5**, P. 49280–49286.
[23] Grendal O., Blichfeld A., Skjærvø S., van Beek W., Selbach S., Grande T., Einarsrud M.-A. Facile Low Temperature Hydrothermal Synthesis of $BaTiO_3$ Nanoparticles Studied by In Situ X-ray Diffraction. *Crystals*, 2018, **8**(6), P. 253.
[24] Zhang X., Liu X., Lu P., Wang L., Zhang Z., Wang X., Wang Z. Hydrothermal Synthesis of Lanthanide Stannates Pyrochlore Nanocrystals for Catalytic Combustion of Soot Particulates. *The Scientific World Journal*, 2015, **2015**, P. 254165.
[25] Almjasheva O.V., Popkov V.I., Proskurina O.V., Gusarov V.V. Phase formation under conditions of self-organization of particle growth restrictions in the reaction system. *Nanosystems: Physics Chemistry Mathematics*, 2022, **13**(2), P. 164–180.
[26] Almjasheva O.V., Lomanova N.A., Popkov V.I., Proskurina O.V., Tugova E.A., Gusarov V.V. The minimum size of oxide nanocrystals: phenomenological thermodynamic vs crystal-chemical approaches. *Nanosystems: Physics Chemistry Mathematics*, 2019, **10**(4), P. 428–437.
[27] Wang Y., Zhang S., Zhong Q., Zeng Y., Ou M., Cai W. Hydrothermal Synthesis of Novel Uniform Nanooctahedral $Bi_3(FeO_4)(WO_4)_2$ Solid Oxide and Visible-Light Photocatalytic Performance. *Industrial & Engineering Chemistry Research*, 2016, **55**(49), P. 12539–12546.
[28] Lomakin M.S., Proskurina O.V., Gusarov V.V. Influence of hydrothermal synthesis conditions on the composition of the pyrochlore phase in the Bi_2O_3–Fe_2O_3–WO_3 system, *Nanosystems: Physics Chemistry Mathematics*, 2020, **11**(2), P. 246–251.
[29] Proskurina O.V., Tomkovich M.V., Bachina A.K., Sokolov V.V., Danilovich D.P., Panchuk V.V., Semenov V.G., Gusarov V.V. Formation of Nanocrystalline $BiFeO_3$ under Hydrothermal Conditions. *Russian Journal of General Chemistry*, 2017, **87**(11), P. 2507–2515.
[30] Terlan B., Levin A.A., Börrnert F., Zeisner J., Kataev V., Schmidt M., Eychmüller A., A Size-Dependent Analysis of the Structural, Surface, Colloidal, and Thermal Properties of $Ti_{1-x}B_2$ (x =0.03–0.08) Nanoparticles. *European Journal of Inorganic Chemistry*, 2016, **21**, P. 3460–3468.
[31] Terlan B., Levin A.A., Börrnert F., Simon F., Oschatz M., Schmidt M., Cardoso-Gil R., Lorenz T., Baburin I.A., Joswig J.-O., Eychmüller A. Effect of Surface Properties on the Microstructure, Thermal, and Colloidal Stability of VB2 Nanoparticles. *Chemistry of Materials*, 2015, **27**(14), P. 5106–5115.
[32] Smith F.G., Kidd D.J. Hematite-goethite relation in neutral and alkaline solution under pressure. *American Mineralogist*, 1949, **34**(5), P. 403–412.
[33] Gusarov V.V., Egorov F.K., Ekimov S.P., Suvorov S.A. A Mossbauer study of the E kinetics of the film states formation at the interaction of magnesium and iron oxides. *The Journal of Physical Chemistry*, 1987, **61**(6), P. 1652–1654. (in Russian)
[34] Kirillova S.A., Almjasheva O.V., Panchuk V.V., Semenov V.G. Solid-phase interaction in ZrO_2–Fe_2O_3 nanocrystalline system. *Nanosystems: Physics Chemistry Mathematics*, 2018, **9**(6), P. 763–769.

Submitted 15 October 2022; revised 6 December 2022; accepted 10 December 2022

Information about the authors:

Makariy S. Lomakin – Ioffe Institute, 26, Politekhnicheskaya St., 194021, St. Petersburg, Russia; St. Petersburg Electrotechnical University "LETI", 5, Professor Popov St., 197376, St. Petersburg, Russia; ORCID0000-0001-5455-4541; lomakinmakariy@gmail.com

Olga V. Proskurina – Ioffe Institute, 26, Politekhnicheskaya St., 194021, St. Petersburg, Russia; St. Petersburg State Institute of Technology, 26, Moskovsky Ave., 190013, St. Petersburg, Russia; ORCID 0000-0002-2807-375X; proskurinaov@mail.ru

Victor V. Gusarov – Ioffe Institute, 26, Politekhnicheskaya St., 194021, St. Petersburg, Russia; ORCID 0000-0003-4375-6388; victor.v.gusarov@gmail.com

Conflict of interest: the authors declare no conflict of interest.

NANOSYSTEMS:
PHYSICS, CHEMISTRY, MATHEMATICS

Original article

Jamdade S.G., et al. *Nanosystems: Phys. Chem. Math.*, 2023, **14** (2), 254–263.
http://nanojournal.ifmo.ru
DOI 10.17586/2220-8054-2023-14-2-254-263

Structural and magnetic study of Tb^{3+} doped zinc ferrite by sol-gel auto-combustion technique

Shrinivas G. Jamdade[1], Popat S. Tambade[2], Sopan M. Rathod[3]

[1]Department of Physics, Nowrosjee Wadia College, Pune, India
[2]Department of Physics, Prof. Ramkrishna More Arts, Commerce and Science College, Akurdi, Pune, India
[3]Department of Physics, Abasaheb Garware College, Pune, India

Corresponding author: Shrinivas G. Jamdade, hv_jamdade@yahoo.com

ABSTRACT In this study, the influence of Tb^{3+} substitution in zinc ferrite is reported. $ZnTb_xFe_{(2-x)}O_4$ ($x = 0$, 0.025, 0.05, 0.075, 0.1, 0.125, and 0.15) were prepared using sol-gel auto-combustion technique. All the samples were sintered at 400 °C for 4 hours. The structure has been studied using XRD, FTIR, UV-visible, and VSM. X-ray diffraction evaluation demonstrates formation of spinel ferrite with nano size distribution. Vibrating sample magnetometer was used to study the magnetic properties of the samples. It was found that as terbium content increases, the coercive field decreases while the saturation magnetization increases. The Tb^{3+} doped nano-crystalline zinc ferrites show ferrimagnetic behavior. FTIR analysis show the presence of two expected bands attributed to tetrahedral and octahedral metal oxygen vibrations at 320 and 450 cm^{-1}.

KEYWORDS sol-gel auto-combustion technique, zinc ferrite, terbium additive, cubic spinel structure, nano structure

FOR CITATION Jamdade S.G., Tambade P.S., Rathod S.M. Structural and magnetic study of Tb^{3+} doped zinc ferrite by sol-gel auto-combustion technique. *Nanosystems: Phys. Chem. Math.*, 2023, **14** (2), 254–263.

1. Introduction

Nano crystalline spinel ferrites were studied by many researchers in recent years. The most common formula for the spinel ferrite is given as AB_2O_4 where A^{2+} ions occupy tetrahedral with B^{3+} ions at the octahedral sites. Cation distribution in the tetrahedral and octahedral sites changes the properties of spinel ferrites. It has been studied that the properties of ferrites were changed with the help of the doping and substitution of a foreign ion, and introduction of a metal cation with higher electronegativity. Rare-earth elements (RE) are commonly used additives for improving the spinel ferrite properties [1, 2]. In case of spinel ferrites, the conduction mechanism and magnetic properties are mostly due to the spin coupling of 3d electrons which arises from the Fe–Fe interaction. But, when spinel ferrite Fe^{3+} ions are partially replaced by rare-earth ions of 4f elements, the RE–FE interaction appears and results in 3d–4f coupling. This 3d–4f coupling in ferrites results in variation in the electric and magnetic properties due to the orbital nature of the unpaired 4f electrons of RE ions [3, 4].

Among various spinel ferrites, zinc ferrite has a wide range of applications such as photoconductive materials, information storage, sensors, electronic devices, and in high frequency applications. $ZnFe_2O_4$ magnetization studies show the presence of a paramagnetic phase at room temperature and a weak anti-ferromagnetic property below its Neel temperature [5–7]. Recent studies on nano-crystalline $ZnFe_2O_4$ ferrite also mentioned the presence of ferrimagnetic ordering at room temperature. These changes in magnetic ordering are owing to the cation's redistribution between tetrahedral and octahedral sites. Thus, the properties shown by $ZnFe_2O_4$ ferrites are changed with the crystallite size and inversion of cations on the sites [8–10].

Various methods were developed to have different nano-crystalline $ZnFe_2O_4$ spinel ferrites like microwave based hydrothermal, decomposition of double layered hydroxide precursor, hydrothermal synthesis, urea combustion, reverse micelle method, dip-coating, solvo-thermal analysis, and co-precipitation [11–14]. The sol-gel auto combustion method is preferred because of its high degree of compositional homogeneity, low processing temperature, and low cost [15–21]. In the present study, the aim is to see the influence of rare-earth ion Tb^{3+} on structural and magnetic properties of Zn ferrites. $ZnTb_xFe_{(2-x)}O_4$ nano ferrite is synthesized by sol-gel auto combustion method followed by its heat treatment and then its characterization is done by XRD, UV-visible, FTIR, and VSM tools. One can find several papers concerning to different properties of doped nano-crystalline zinc ferrites [23–25].

2. Synthesis details

Terbium substituted zinc nano crystalline ferrite ($ZnTb_xFe_{(2-x)}O_4$) ($x = 0$, 0.025, 0.05, 0.075, 0.1, 0.125, and 0.15 represented by JX1, JX2, JX3, JX4, JX5, JX6, and JX7, respectively, in all figures) were prepared by sol-gel auto-combustion method. The high purity AR grade ferrite nitrate ($(Fe(NO_3)_2)\cdot 9H_2O$), zinc nitrate ($(Zn(NO_3)_2)\cdot 6H_2O$), terbium nitrate ($(Tb(NO_3)_2)\cdot 5H_2O$), ammonium hydroxide solution (NH_4OH) were used. The citric acid ($C_6H_8O_7$, H_2O) was used as a fuel. The nitrates and citric acid in stochiometric proportion are dissolved in 100 ml distilled water, which is stirred till homogenous solution is obtained. Drop by drop ammonium hydroxide solution is added to maintain pH = 7 during the stirring process. Then the mixed solution was kept on hot plate at 80 °C for 2 to 3 hours to obtain the sol of it. After half an hour this sol becomes a viscous gel. Then, we get fine powder of ferrite nanoparticles after auto-combustion happens. The powder was sintered at 400 °C for 4 hours in the muffle furnace.

3. Results and discussion

3.1. X-ray diffraction (XRD) analysis

XRD analysis of prepared $ZnTb_xFe_{(2-x)}O_4$, where JX1 is $x = 0$, JX2 is $x = 0.025$, JX3 is $x = 0.05$, JX4 is $x = 0.075$, JX5 is $x = 0.1$, JX6 is $x = 0.125$, and JX7 is $x = 0.15$ nano-particles sintered at 400 °C for 4 hours, were performed using X-ray diffractometer with CuKα radiation of wavelength 1.5405 Å. XRD Fig. 1 for pure and terbium doped zinc ferrite powder sample shows six major diffractions peaks in the range of 2θ equal to 29 – 30, 35 – 36, 42 – 43, 53 – 54, 56 – 57, and 62 – 63 corresponding to planes (220), (311), (400), (422), (511), and (440), respectively. These peaks are found to be associated with cubic spinel structure (JCPDS card number 22-1012). The robust reflection comes from the (311) plane denoting the spinel structure. The moderate peak intensity indicates low degree of crystallinity of prepared ferrite samples while the broadening of peaks indicates the nanometer size of the crystallite. Many researchers have mentioned orthorhombic phase ($TbFeO_3$) formation in the rare-earth doped ferrites even at a low doping concentration. In our case, we observed the secondary phase as a small reflection peak at $2\theta = 31.78°$ as $TbFeO_3$ phase while Fe_2O_3 phase is seen at $2\theta = 36.66°$ for the reflection plane (121) and (110), respectively [2].

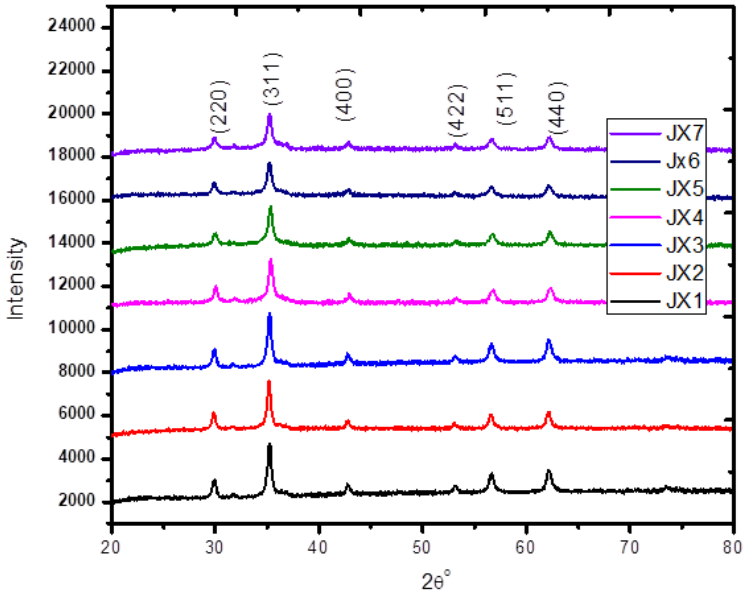

FIG. 1. XRD pattern of $ZnTb_xFe_{(2-x)}O_4$ powder

Using XRD data, lattice constant values of ferrite samples were calculated by Bragg's equation

$$a = d \cdot \sqrt{h^2 + k^2 + l^2}, \tag{1}$$

where d is interplanar distance and h, k, l are the miller indices. Normally the lattice constant value increases with addition of rare-earth doping owing to the difference in radii of rare-earth ions and Fe^{3+} ions. However, a slight decrease is observed for the sample JX4 with $x = 0.075$. This suggests the possibility of some Tb^{3+} ions occupying the tetrahedral sites up to this terbium concentration, which results in the contraction of the unit cell. For $x > 0.075$, lattice constant is increasing owing to the expansion of the unit cell caused by the Tb^{3+} substitution. As the Tb^{3+} ions, having large ionic radii (0.923 Å), enters into the octahedral (B) site in place of Fe^{3+} ions having smaller radii (0.67 Å) results into internal stress to make the lattice distorted and unit cell expansion. Similar results have been reported by many researchers, this is attributed to the nonlinear variation of lattice constant owing to the distribution of cations at A and B sites [3].

The crystallite size was calculated using Debye–Scherrer formula,

$$D = 0.89 \cdot \frac{\lambda}{\beta \cos\theta}. \tag{2}$$

The crystallite size was calculated for all the compositions using the high intensity (311) peak. The obtained crystallite size of the samples is within the nano region. The crystal size varies from 5 to 7 nm. The preparation condition followed here probably gives rise to different rates of ferrite formation for different concentrations of Tb^{3+} favouring the variation in crystallite size. The crystallite size was observed to increase up to $x = 0.05$ by increasing Tb^{3+} concentration. Thereafter crystallite size is found to decrease with terbium content. Excess of Tb^{3+} ions on or near the grain boundaries which impedes the grain boundary mobility may be the reason for this decrease. The average crystallite size (D) and lattice strain (ε) also was calculated using Williamson–Hall (W-H) equation which is given as

$$\frac{\beta \cos\theta}{\lambda} = \frac{1}{D} + \frac{\varepsilon \sin\theta}{\lambda}. \tag{3}$$

Here ε is the lattice strain, D is the crystallite size, λ is the wavelength of X-ray used, β is the Full Width at Half Maximum and θ is Bragg's angle. From above equation (3) the plot of $\beta \cos\theta$ versus $\sin\theta$ will be in the form of a straight-line equation giving the slope as lattice strain and from the intercept we can calculate the crystallite size. Non-zero slopes of the W-H plot are indicative of inhomogeneous (strained) growth of the unit cells. These values are in good agreement with the value obtained from the Debye–Scherrer formula. The crystallite size obtained from Debye–Scherrer's formula and W-H plot are tabulated in Table 1. The uncertainties in all values mentioned in Table 1 are ± 0.5 %.

In the present case, the lattice strain was seen to decrease with Tb^{3+} doping up to $x = 0.05$ and then increases for $x \geq 0.05$. The variation in lattice strain parameter also may be due to presence of impurity phases and incomplete replacement of Fe^{3+} cations by Tb^{3+} cations. The dislocation density is given as $\rho_d = 1/D^2$, where D is the crystallite size of the sample. In the present case, the dislocation density increases up to $x = 0.1$ except $x = 0.05$ and then reduces with Tb^{3+} ion concentration as the crystallite size of all the samples is small [3, 4]. Thus, the size of nano crystals (D) and the lattice parameter (a) non monotonically increases while the lattice strain and the dislocation density non-linearly decrease with doping of Tb^{3+} in the Zinc ferrite sample.

X-ray density were calculated using the equation

$$\delta_s = \frac{8M}{Na^3}. \tag{4}$$

Here 8 represents the number of atoms in the unit cell of the spinel lattice, M is the molecular weight of TbZn ferrite samples, N is Avogadro number, and a is lattice constant. The values of X-ray density of the synthesized sample vary from 5.3189 to 5.688 g/cm^3 (Fig. 2). The increase in X-ray density of samples is due to increase in the molar mass of the doped Tb^{3+} ions (158.92 g/mole) as compared to Fe^{3+} (55.84 g/mole), and Zn^{2+} (65.41 g/mole) ion. Fig. 2 depicts the change in the value of X-ray density with terbium substitution.

The distance between magnetic ions (hopping length) in site A (tetrahedral) and B site (octahedral) where calculated by using the following relations

$$L_A = M_A - M_A = \left(\frac{\sqrt{3}}{4}\right) a, \tag{5}$$

$$L_B = M_B - M_B = \left(\frac{\sqrt{2}}{4}\right) a, \tag{6}$$

$$L_{AB} = M_A - M_B = \left(\frac{\sqrt{\pi}}{4}\right) a, \tag{7}$$

where a is the lattice constant.

The determination of the inter-atomic distance is an amenable method to give one a description of the crystallographic structure and the magnetic properties, where M_A and M_B refer to the cations at the center of the tetrahedral (A) and octahedral (B) sites, respectively [5]. The variations in the hopping length for tetrahedral site (L_A) and octahedral site (L_B) were shown in Fig. 2. It is clear that the distance between the magnetic ions increases as the Tb^{3+} content increases except for JX3, $x = 0.1$ sample.

3.2. UV-visible spectroscopy analysis

Figure 3 illustrates the DRS (absorption mode) optical absorption spectra for $ZnTb_xFe_{(2-x)}O_4$ ($x = 0$, 0.025, 0.05, 0.075, 0.1, 0.125, and 0.15) nanoparticles in the UV-visible range for the prepared samples at room temperature sintered at 400 °C. There are three bands of absorption found at 280, 350 and 420 nm in correlation with the XRD conclusion. This absorption builds upon the constitution and measure of heat content of the test samples as given in the Figs. 3 and 4.

Three kinds of electronic shifts take place in the optical absorption of Fe^{3+} samples. As is disclosed from Fig. 3 that for $x = 0.1$ composition sample, the electronic transition for charge carries over lies in the wavelength range of 450

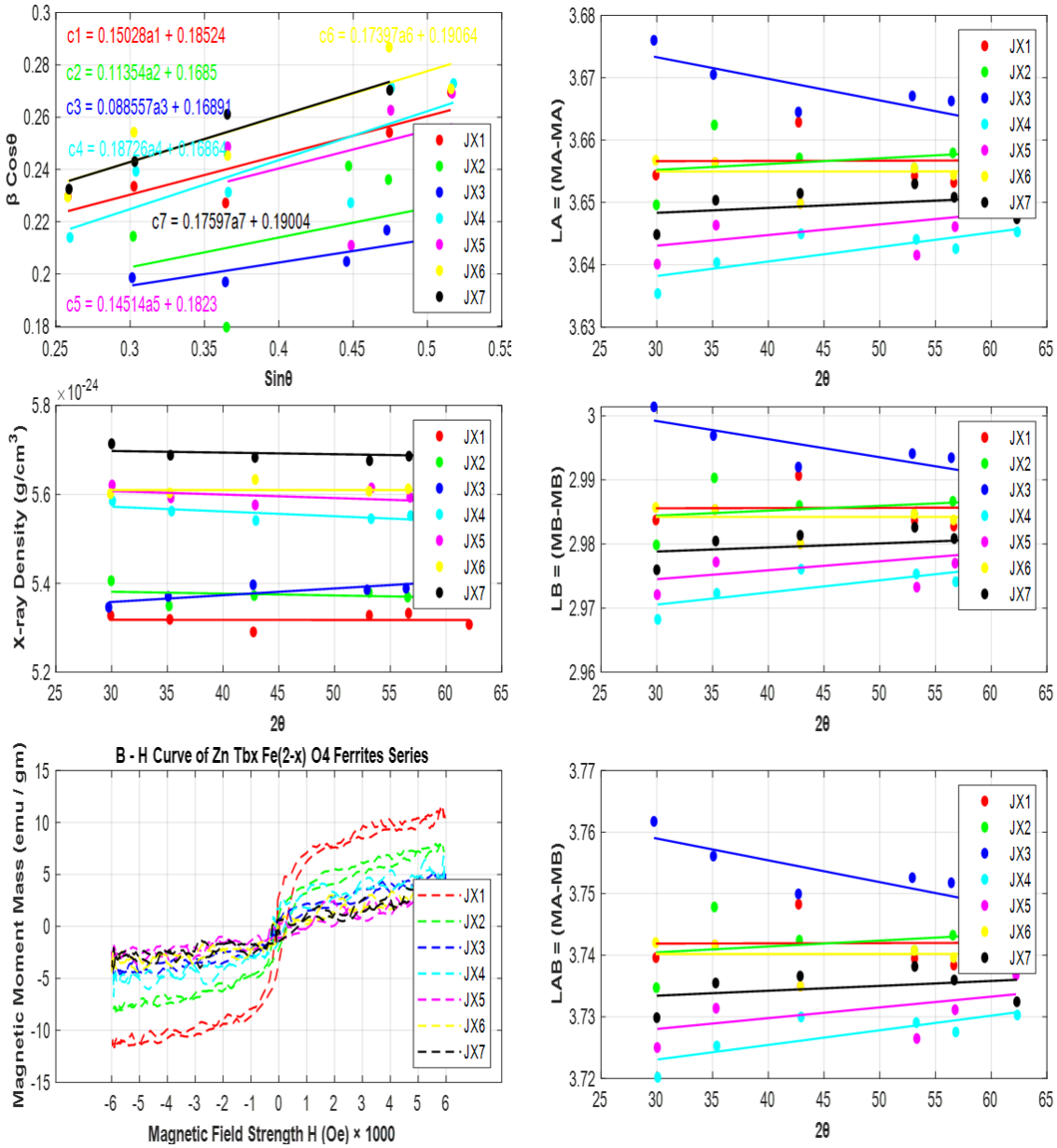

FIG. 2. W-H Plots, X-ray Density verses 2θ, M–H loops, LA verses 2θ, LB verses 2θ, and LAB verses 2θ for $ZnTb_xFe_{(2-x)}O_4$ powder

to 500 nm which is in the optical region while the ligand field change over occurs in the interval of wavelength 750 to 780 nm also in the optical region.

The band gap energy is calculated using the formula

$$E = h\gamma = \frac{hc}{\lambda}. \tag{8}$$

The band gap energy decreases from 2.579 to 2.103 eV for the samples which are sintered at 400 °C. The outcome shows that composition and annealing measure of the heat contained in the samples put a major impact on the optical characteristics [6–8].

3.3. FTIR analysis

The FTIR spectra of the investigated $ZnTb_xFe_{(2-x)}O_4$ samples are shown in Fig. 5. In the wave number range of 1600 to 200 cm^{-1} two main metal oxygen bands are seen in the infrared spectra of spinel ferrites The higher band γ_1, generally observed in the range of 520 to 530 cm^{-1}, is caused by the stretching vibrations of the tetrahedral metal oxygen bond and the lowest band γ_2, usually observed in the range 400 to 420 cm^{-1}, is caused by metal oxygen vibration in the octahedral sites. IR absorption bands mainly appear owing to the oxygen ions vibrations with cations at different

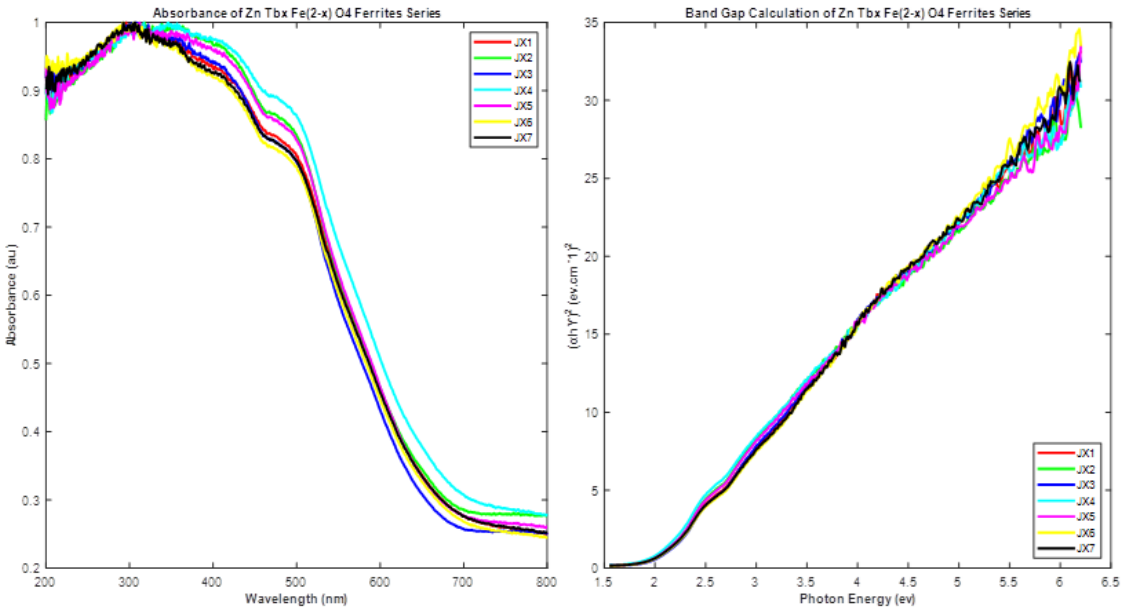

FIG. 3. Absorbance spectra, and $(\alpha h\gamma)^2$ versus photon energy $(h\gamma)$ for $ZnTb_xFe_{(2-x)}O_4$ powder

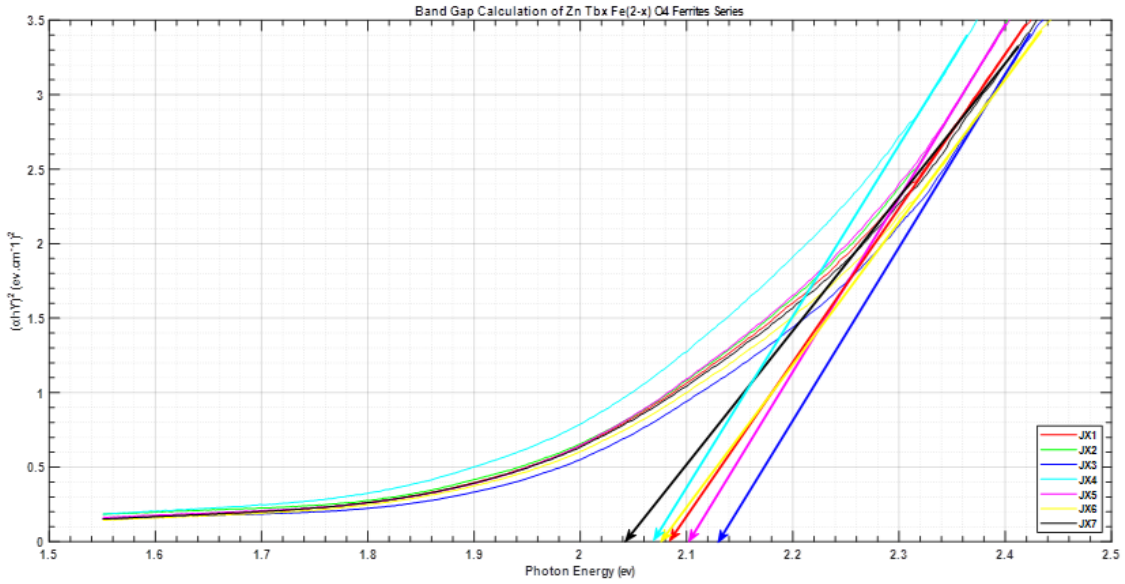

FIG. 4. $(\alpha h\gamma)^2$ versus photon energy $(h\gamma)$ for $ZnTb_xFe_{(2-x)}O_4$ powder

frequencies. But the spinel structure exhibits two IR vibrational bands at $\gamma_1 = 546.86$ cm^{-1} and at $\gamma_2 = 449.42$ cm^{-1} corresponding to familiar intrinsic vibrations of tetrahedral site and octahedral site.

The vibrational frequencies of the IR bands γ_1 and γ_2 are such that the values of γ_1 slightly increase but γ_2 shifts to the lower frequency side with the increase of terbium content. It is known that increase in the site radius reduces the fundamental frequency and therefore the centered frequency should shift towards the lower frequency side. The shift in γ_1 may be due to the perturbation occurring in the Fe^{3+}–O^{2-} bonds by the substitution of Tb^{3+} ions. Increase in site radius may be expected due to the replacement of smaller Fe^{3+} ions by larger Tb^{3+} ions in the octahedral sites. Decrease in γ_2 and increase in γ_1 observed for the sample with $x = 0.1$ may be due to the formation of $TbFeO_3$ phase [9–11].

3.4. VSM analysis

Figure 2 shows magnetic hysteresis loop of samples at room temperature. The saturation magnetization (M_S), coercivity (H_c), and magnetic remanence (M_r) of all the samples are given in Table 2. It is clear from the value that MS is decreasing with increase in Tb^{3+} concentration owing to large Tb^{3+} ion radii (0.93 Å) than ionic radii of Fe^{3+} ions (0.695 Å) preferably occupying octahedral (B sites). The magnetic moments of rare-earth ions generally originate from

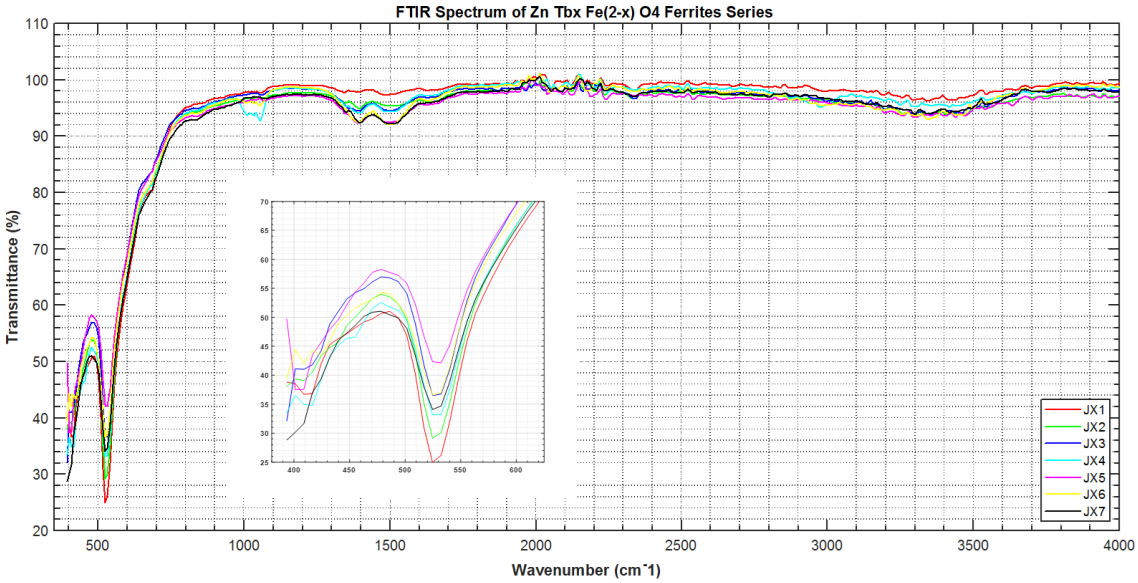

FIG. 5. FTIR spectra for $ZnTb_xFe_{(2-x)}O_4$ powder

localized 4f electrons and these are characterized by lower magnetic ordering temperatures. Therefore, their magnetic dipolar orientations exhibit disordered form at room temperature and hence are paramagnetic and contribute very little to the magnetization of doped ferrites at room temperature. As the terbium concentration increases, B sub-lattice magnetization decreases. Further substitution of Fe^{3+} magnetic ions by paramagnetic Tb^{3+} ions in B site deteriorates AB super-exchange interaction. Thus, the ferrimagnetic ordering of Zn ferrite is disturbed by the addition of Tb^{3+} ions and hence M_S decreases.

The high magnetization at low doping is attributed to the ratio of Fe^{3+} to Fe^{2+} being maximum at $x = 0$ composition. The saturation magnetization monotonically decreases with increasing Tb^{3+} concentration. Value of saturation magnetization depends on grain size and preparation temperature. The decrease in saturation magnetization is owing to the magnetic disorder on B sites caused by the presence of paramagnetic terbium ion on B site. It has been observed that the spin canting is caused by the doping of rare earth ions. Since Tb is a rare earth metal ion, and it causes the transformation of co-linear ferrimagnetic order into non-colinear arrangement of spins on B sites, hence saturation magnetization is reduced. Also, no more Fe^{3+} ions are transferred to the octahedral sites which lead to the decrease of saturation magnetization. The decrease of saturation magnetization for higher concentration of Tb^{3+} ions may also be attributed to the secondary $TbFeO_3$ phase which has a low value of magnetization.

The coercivity value slowly increases with increase of Tb^{3+} content till it reaches maximum value at $x = 0.1$ composition and then decreases. The increase in coercivity at $x = 0.1$ may be attributed to an enhancement of the magneto crystalline anisotropy and reduction in the grain size. The coercivity is enhanced due to reduction of particle size until single domain particles are reached and then decreases as the super paramagnetic limit is approached. For $x \geq 0.1$, the coercivity decreases which may be due to the decrease in the magnetic anisotropy. The large and small grains would reduce the coercivity due to the emergence of super para-magnetism. The magnetic anisotropy is the accumulative contribution of cations in A site and B site. Therefore, magnetic LS coupling at lattice sites is directly related to the magnetic property such as super para-magnetism. The increase in coercivity may also be related to the appearance of secondary phases $TbFeO_3$ on or near the grain boundaries which impede the motion of domain walls.

The reduction in M_r may be explained on the basis of magnetic dilution. The Zn ion is a divalent cation while terbium is trivalent, when a divalent ion replaced by a trivalent ion then some of the Fe^{3+} ions are converted to Fe^{2+} ions to maintain the electro-neutrality which results in the reduction of magnetic moment as Fe^{3+} has magnetic moment of $5\mu_B$ while that of Fe^{2+} has $4\mu_B$. The super exchange interaction decreases as Fe^{2+}–O^{2-}–Fe^{3+} exchange interaction is weaker than Fe^{2+}–O^{2-}–Fe^{3+} which is responsible for the reduction in M_r.

The saturation magnetization (M_S), coercivity (H_c), remanence (M_r) and Statured Magnetic Field (H_M) values are found to be in the range of 10.53 – 3.39 emu/g, 0.20 – 1.09 Oe, 2.95 – 0.30 emu/g, and 5.985 – 5.90 Oe, respectively. These values demonstrate the ultra-soft ferrimagnetic nature of different $ZnTb_xFe_{(2-x)}O_4$ ferrites at room temperature. The values of the magnetic parameters are given in Table 2. The uncertainties in all values mentioned in Table 2 are ± 0.05 %.

TABLE 1. Diffraction Angle (2θ), d Interplaner Spacing (d), Full Width at Half Maxima (β), Lattice Constants (a), Volume of Cell (V_{cell}), X-ray Density (DX), Crystallite Size (D), and Bandgap (eV) with substitution for $ZnTbxFe_{(2-x)}O_4$

x	2θ	d	FWHM (β)	Lattice Parameter (a) Å	V_{cell} (Å^3)	X-ray Density (DX) in gmcm^{-3}	D (nm) (DS Method)	D (nm) (WH Method)	Strain (ε) D-S Method	Strain (ε) W-H Method	Dislocation Density (δ)	Bandgap (eV)
0	35.22	2.5460	0.2450	8.4440	602.0727	5.319	5.871	5.3984	0.1587	0.15028	0.03010	2.08
0.025	35.16	2.5502	0.2249	8.4580	605.0623	5.349	6.395	5.9347	0.1503	0.11354	0.03010	2.1
0.05	35.08	2.5558	0.2082	8.4767	609.0801	5.370	6.905	5.9203	0.1391	0.08855	0.02265	2.103
0.075	35.38	2.5348	0.2511	8.4071	594.1984	5.562	5.731	5.92979	0.1603	0.18726	0.03158	2.065
0.1	35.32	2.5390	0.2714	8.4209	597.1347	5.592	5.302	5.48546	0.1673	0.14514	0.03315	2.1
0.125	35.22	2.5460	0.2667	8.4440	602.0727	5.603	5.393	5.24548	0.1655	0.17397	0.03298	2.08
0.15	35.28	2.5418	0.2550	8.4301	599.1032	5.688	5.642	5.2620	0.1577	0.17597	0.02984	2.04

TABLE 2. Summary of Coercivity (H_C), Saturation Magnetization (M_S), Retentivity (M_r), Squareness Ratio (S_R), Statured Magnetic Field (H_M), μ peak (Peak Relative Permeability), Molecular Weight of Composition, Magneton Number n_B (Calculated), Magneton Number n_B (Observed), and Anisotropic Constant (K) with substitution for $ZnTb_xFe_{(2-x)}O_4$.

x	H_C (Oe)	M_S (emu/g)	M_r (emu/g)	S_R (M_r/M_S)	H_M	μ peak (Peak Relative Permeability)	Molecular Weight of Composition	Magneton Number n_B (Calculated)	Magneton Number n_B (Observed)	Anisotropic Constant
0	0.25	10.533	2.95	0.280072	5.967	1404.70847	241.066	0.454637	0.671039	2.7429688
0.025	0.3	7.1799	1.1	0.153205	5.925	964.31783	243.646	0.313223	0.671055	2.2437188
0.05	0.3	5.1389	0.65	0.126486	5.985	683.27600	246.223	0.226556	0.673039	1.6059063
0.075	0.2	6.032	1.7	0.281830	5.93	809.46261	248.8008	0.268713	0.668366	1.2566667
0.1	1.09	3.392	0.4	0.117924	5.9	457.50304	251.3778	0.152672	0.669066	3.8513333
0.125	0.41	3.76	0.3	0.079787	5.96	502.03239	253.9558	0.170971	0.670724	1.6058333
0.15	0.69	3.44	0.6	0.174418	5.976	458.07649	256.5315	0.158006	0.669748	2.4725

The experimental magnetic moment (n_B) (observed) was calculated using the relation

$$n_B = \frac{MM_S}{5585}. \tag{9}$$

Table 2 shows n_B values. The squareness ratio, $R = M_r/M_S$, for all the samples were calculated from M_S and M_r data which indicates ferrimagnetic behavior of synthesized samples. Usually, the nanoparticles are considered to be in the multi-magnetic domain for $R \geq 0.5$ and in single magnetic domain when $R < 0.5$. Thus, all nanoparticles are within a single magnetic domain. It is worth noting that squareness ratio values are below than 0.5 signify the presence of strong surface spin disordering.

3.5. SEM analysis

Scanning electron microscopy was done to reveal the microstructure of ferrite and the morphology of the nanoparticles. The SEM images (Fig. 6) show a non-uniform particle distribution. All the samples show agglomeration of particles with nearly spherical kind of morphology. The agglomeration of the particles leads to the present structure. It is due to the effect of reaction time and sintering temperature.

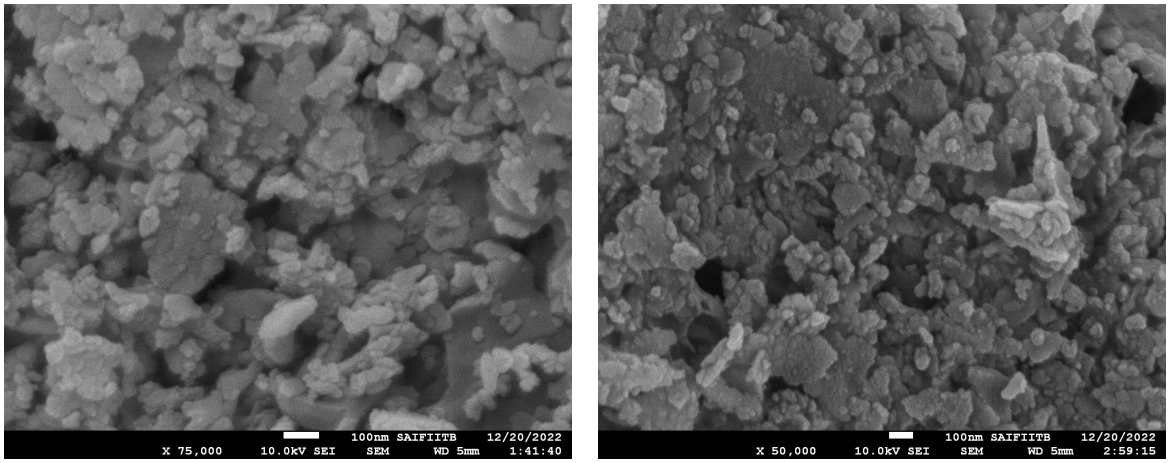

(a) (b)

FIG. 6. SEM images of $ZnTb_xFe_{(2-x)}O_4$ powder for $x = 0.025$ (a) and 0.075 (b)

3.6. EDX analysis

EDX has been performed in order to study the composition of the samples. EDX study exhibits the elemental percentage of each element expected to be present in the ferrite sample. The height of the peaks in the EDX graphs (Fig. 7) represents the proportion of each element in the finally sintered ferrite sample. With the increase of Tb concentration, the graph exhibits an increase in height of the Tb peaks. The atomic ratio of Zn:Tb:Fe is about 1:1:4 indicating that the chemical formula of the prepared specimen is consistent with the experimental stoichiometry. Also, all the elements are seen to be present in their respective compositions (Table 3). Terbium concentration was found to be in the grain boundary rather than that in grains. This indicates low solubility of terbium in the spinel structures. This indicates that only a small amount of terbium may be actually getting substituted inside the spinel lattice.

TABLE 3. Elementwise weight % and atomic % of different composition of $ZnTb_xFe_{2-x}O_4$ ferrite

Element	Weight %	Weight %	Weight %	Atomic %	Atomic %	Atomic %
x	0.0	0.05	0.125	0.0	0.05	0.125
Fe K	65.29	52.23	51.85	69	57.52	58.98
Zn L	34.05	43.32	38.05	30.75	40.76	36.98
Tb L	0.66	4.45	10.11	0.24	1.72	4.04

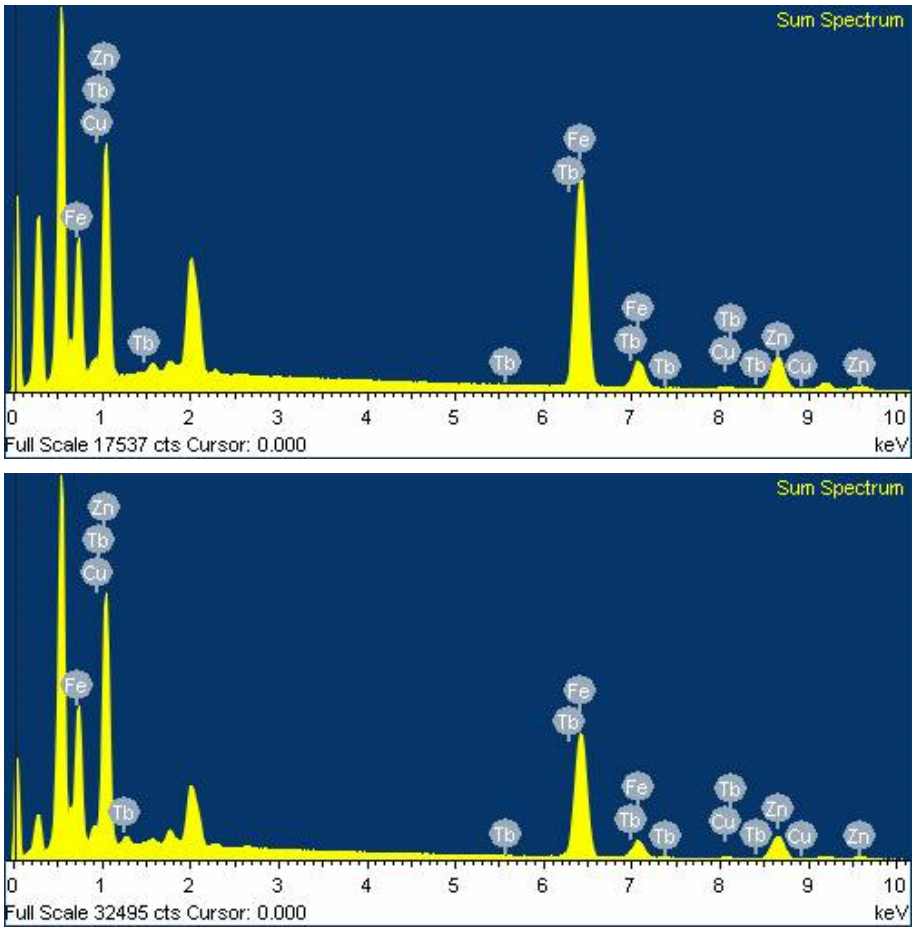

FIG. 7. EDX images of $ZnTb_xFe_{(2-x)}O_4$ powder for $x = 0.025$ (a) and 0.075 (b)

4. Conclusion

Fine particles of $ZnTb_xFe_{(2-x)}O_4$ were prepared by sol-gel auto-combustion technique. The particle size steadily increases with increase in terbium content. The crystallite size lies in the range of 5 to 7 nm. XRD shows partial immersion of Tb^{3+} ions in the spinel lattice and other ions are reversed into secondary phases on grain boundaries. Structural distortions are seen in the lattice. It is revealed that with an increase in terbium amount, the coercive field decreases significantly after maximum value while the saturation magnetization and permanent magnetization also decreases. This may be due to particle size effect, magnetic dilution, spin canting phenomena, and hence reduction of super exchange interaction. The results revealed that terbium cation could reduce magneto crystalline anisotropy of zinc ferrite and consequently altered the magnetic phase to a soft one.

References

[1] Hu J.Y., Liu X.S., Kan X.C., Feng S.J., Liu C.C., Wang W., Rehman K.M.U., Shazed M., Zhou S.Q., Wu Q.Y. Characterization of texture and magnetic properties of $Ni_{0.5}Zn_{0.5}Ti_xFe_{2-x}O_4$ spinel ferrites. *J. Magn. Magn. Mater.*, 2019, **489**, 165411.

[2] Li L.Z., Zhong X.X., Wang R., Tu X.Q., Peng L. Structural and magnetic properties of Co-substituted NiCu ferrite nanopowders. *J. Magn. Magn. Mater.*, 2017, **433**, P. 98–103.

[3] Kokare M.K., Jadhav N.A., Kumar Y., Jadhav K.M., Rathod S.M. Effect of Nd^{3+} doping on structural and magnetic properties of $Ni_{0.5}Co_{0.5}Fe_2O_4$ nanocrystalline ferrites synthesized by sol-gel auto combustion method. *J. of Alloys and Compounds*, 2018, **748**, P. 1053–1061.

[4] Kokare M.K., Jadhav N.A., Singh V., Rathod S.M. Effect of Sm^{3+} substitution on the structural and magnetic properties of NiCo nanoferrites. *Optics and Laser Technology*, 2019, **112**, P. 107–116.

[5] Gao Y., Wang Z., Pei J.J., Zhang H.M. Structure and magnetic properties correlated with cation distribution of $Ni_{0.5-x}Mo_xZn_{0.5}Fe_2O_4$ ferrites prepared by sol-gel auto-combustion method. *Ceram. Int.*, 2018, **44**, P. 20148–20153.

[6] Rekorajska A., Cichowicz G., Cyranski M.K., Grden M., Pekala M., Blanchard G.J., Krysinski P. Synthesis and Characterization of Tb-Doped Nanoferrites. *Chem. Nano Mat.*, 2018, **4**, P. 231–242.

[7] Rehman A.U., Morley N.A., Amin N., Arshad M.I., Nabi M.A., Mahmood K., Iqbal F. Controllable synthesis of La^{3+} doped $Zn_{0.5}Co_{0.25}Cu_{0.25}Fe_{2-x}La_xO_4$ ($x = 0.0$, 0.0125, 0.025, 0.0375, 0.05) nano-ferrites by sol-gel auto-combustion route. *Ceram. Int.*, 2020, **46** (18A), P. 29297–29308.

[8] Awati V., Badave K., Bobade D. Effect of Tb^{3+} substitution on structural, optical and magnetic properties of $NiCuZnFe_2O_4$ prepared by sol-gel route. *Indian J. of Physics*, 2022, **96** (1), P. 89–101.

[9] Bulai G., Diamandescu L., Dumitru I., Gurlui S., Feder M., Caltun O.F. Effect of rare earth substitution in cobalt ferrite bulk materials. *J. Magn. Magn. Mater.*, 2015, **390**, P. 123–131.
[10] Hussain K., Amin N., Arshad M.I. Evaluation of structural, optical, dielectric, electrical, and magnetic properties of Ce^{3+} doped $Cu_{0.5}Cd_{0.25}Co_{0.25}Fe_{2-x}O_4$ spinel nano-ferrites. *Ceram. Int.*, 2021, **47**, P. 3401–3410.
[11] Kumar K.V. Tunable optical bandgap of gadolinium substituted nickel-zinc ferrite nanoparticles-effect of calcination temperature on its optical parameters. *Advances in Materials Physics and Chemistry*, 2022, **12**, P. 33–45.
[12] Rathod S.M., Deonikar V.G., Mirage P.P. Synthesis of Nano-Sized Cerium Doped Copper Ferrite, Their Magnetic and Optical Studies. *Adv. Sci. Lett.*, 2016, **22**, P. 964–966.
[13] Ghodake J.S., Kambale R.C., Shinde T.J., Maskar P.K., Suryavanshi S.S. Magnetic and microwave absorbing properties of Co^{2+} substituted nickel–zinc ferrites with the emphasis on initial permeability studies. *J. Magn. Magn. Mater.*, 2016, **401**, P. 938–942.
[14] Kumar R., Kumar H., Singh R.R., Barman P.B. Variation in magnetic and structural properties of Co-doped Ni–Zn ferrite nanoparticles: a different aspect. *J. Sol-Gel Sci. Technol.*, 2016, **78**, P. 566–575.
[15] Bhame S.D., Joy P. Magnetoelastic properties of terbium substituted cobalt ferrite. *Chemical Physics Letters*, 2017, **685**, P. 465–469.
[16] Liu Z., Peng Z., Lv C., Fu X. Doping effect of Sm^{3+} on magnetic and dielectric properties of Ni–Zn ferrites. *Ceram. Int.*, 2017, **43**, P. 1449–1454.
[17] Li L.Z., Zhong X.X., Wang R., Tu X.Q. Structural, magnetic and electrical properties of Zr-substitued NiZnCo ferrite nanopowders. *J. Magn. Magn. Mater.*, 2017, **435**, P. 58–63.
[18] Kabbur S.M., Waghmare S.D., Nadargi D.Y., Sartale S.D., Kambale R.C., Ghodake U.R., et al. Magnetic interactions and electrical properties of Tb^{3+} substituted NiCuZn ferrites. *J. Magn. Magn. Mater.*, 2019, **473**, P. 99–108.
[19] Slimani Y., Almessiere M.A., Güner S., Tashkandi N.A., Baykal A., Sarac M.F., Nawaz M.U., Ercan I. Calcination effect on the magneto-optical properties of vanadium substituted NiFe2O4 nanoferrites. *J. Mater. Sci.: Mater. Electron*, 2019, **30** (10), P. 9143–9154.
[20] Slimani Y., Almessiere M.A., Güner S., Kurtan U., Shirsath S.E., Baykal A., Ercan I. Magnetic and microstructural features of Dy^{3+} substituted $NiFe_2O_4$ nanoparticles derived by sol-gel approach. *J. Sol-Gel Sci. Technol.*, 2020, **95** (1), P. 202–210.
[21] Hua J., Maa Y., Kana X., Liua C., Zhanga X., Rao R., Wanga M., Zheng G. Investigations of Co substitution on the structural and magnetic properties of Ni–Zn spinel ferrite. *J. Magn. Magn. Mater.*, 2020, **513**, 167200.
[22] Devi H.F., Thoithoi Devi K., Singh T.D. Synthesis, characterization, optical and electrical properties of citrate mediated terbium doped ZnO nanoparticles for multifunctional applications. *Integrated Ferroelectrics*, 2020, **204**, P. 81–89.
[23] Deonikar V.G., Kulkarni V.D., Rathod S.M., Kima H. Fabrication and characterizations of structurally engineered lanthanum substituted nickel-cobalt ferrites for the analysis of electric and dielectric properties. *Inorganic Chemistry Communications*, 2020, **119**, 108074.
[24] Skoog D.A., Holler E.J.F., Crouch S.R. *Principles of Instrumental Analysis*. Thomson Books Company Limited, 2007.
[25] Smit J. *Magnetic Properties of Materials*. McGrawHill Book Company, New York, 1971.

Submitted 1 December 2022; revised 29 January 2023; accepted 25 February 2023

Information about the authors:

Shrinivas G. Jamdade – Department of Physics, Nowrosjee Wadia College, Pune, India; ORCID 0000-0002-9393-5619; hv_jamdade@yahoo.com

Popat S. Tambade – Department of Physics, Prof. Ramkrishna More Arts, Commerce and Science College, Akurdi, Pune, India; ORCID 0000-0002-2108-7067; pstam3@rediffmail.com

Sopan M. Rathod – Department of Physics, Abasaheb Garware College, Pune, India; ORCID 0000-0003-2357-9791; smragc@rediffmail.com

Conflict of interest: the authors declare no conflict of interest.

NANOSYSTEMS:
PHYSICS, CHEMISTRY, MATHEMATICS

Original article

Leonov N.A., Kozlov D.A., et al. *Nanosystems: Phys. Chem. Math.*, 2023, **14** (2), 264–271.
http://nanojournal.ifmo.ru
DOI 10.17586/2220-8054-2023-14-2-264-271

Formation of a 10 Å phase with halloysite structure under hydrothermal conditions with varying initial chemical composition

Nikita A. Leonov[1,a], Daniil A. Kozlov[2,3,b], Demid A. Kirilenko[1,c], Nikolay A. Bert[1,d], Anna O. Pelageikina[1,e], Andrey A. Nechitailov[1,f], Mikhail B. Alikin[4,g], Andrei A. Krasilin[1,h]

[1]Ioffe Institute, St. Petersburg, Russia

[2]Lomonosov Moscow State University, Moscow, Russia

[3]Kurnakov Institute of General and Inorganic Chemistry, Russian Academy of Sciences, Moscow, Russia

[4]St. Petersburg State Technological University (Technical University), St. Petersburg, Russia

[a]nikita_leonov_1998@mail.ru, [b]danilko_zlov@mail.ru, [c]zumsisai@gmail.com, [d]ikolay.bert@mail.ioffe.ru, [e]Pelaanna@yandex.ru, [f]aan.shuv@mail.ioffe.ru, [g]alikinmix@gmail.com, [h]ikrasilin@mail.ioffe.ru

Corresponding author: N. A. Leonov, nikita_leonov_1998@mail.ru

ABSTRACT We studied the process of obtaining nanostructured halloysite by varying the parameters for creating the initial composition. The initial composition was synthesized by co-hydrolysis of $(C_3H_7O)_3Al$ and $(C_2H_5O)_4Si$ in the C_6H_{14}–$NH_3{\cdot}H_2O$ system. Aluminum hydrosilicate with the composition $Al_2Si_2O_5(OH)_4$ was synthesized under hydrothermal conditions (220 °C, 2 MPa, 96 h). Particles of plate-like morphology with average length 100 – 200 nm and 60 nm thickness were obtained. The PXRD patterns revealed the presence of two phases. Plate-like kaolinites are found. Also we observed the formation of a halloysite-like phase. Studies of synthesized samples by IR spectroscopy and thermal analysis revealed the presence of organic-modified hydrosilicate with phase transition around 412 °C. The resulting phase is promising for studying the processes of adsorption and further exfoliation.

KEYWORDS aluminum, hydrosilicates, hydrothermal synthesis, kaolinite, halloysite

ACKNOWLEDGEMENTS The research was supported by the President of the Russian Federation grant MK-1962.2021.1.3. STEM studies were carried out using the equipment of the JRC PMR IGIC RAS. TEM studies were partially performed in the Joint Research Center 'Materials science and characterization in advanced technology'. The XRPD and IR studies were performed using the equipment of the Engineering Centre of St. Petersburg State Technological Institute (Technical University).

FOR CITATION Leonov N.A., Kozlov D.A., Kirilenko D.A., Bert N.A., Pelageikina A.O., Nechitailov A.A., Alikin M.B., Krasilin A.A. Formation of a 10 Å phase with halloysite structure under hydrothermal conditions with varying initial chemical composition. *Nanosystems: Phys. Chem. Math.*, 2023, **14** (2), 264–271.

1. Introduction

Recently, many works have been devoted to the use of layered hydrosilicates in various fields, including adsorption [1], catalysis [2] and the encapsulation of functional substances [3]. Hydrosilicates with the structure of imogolite [4], chrysotile [5,6] and halloysite [7] provided even more opportunities for such use due to their high specific surface area [8] and nanotubular morphology [9]. The latter originated from a number of structural peculiarities of the hydrosilicate layer, specifically, the size mismatch between metal-oxygen and silicon-oxygen sheets, as well as the difference in composition on the opposite sides of the layer [10]. Depending on structure type and chemical composition, scrolling can occur in various directions up to the formation of single-walled nanotubes [11] and sphere-like particles [12].

The functional properties of hydrosilicates may be enhanced by various methods of modification. Namely, metal-silicate composite materials were obtained from transition metal hydrosilicates by processing in hydrogen [13, 14], or in a solution containing a strong reducing agent under hydrothermal conditions [15], to produce magnetically controlled adsorbents and catalysts with a broad spectrum of activity. New metallic or oxide phases can also be imposed externally [16]. Some papers were devoted to the modification of the surface of hydrosilicates with acids [17, 18] and organic ligands [19–21].

Despite the wide range of applications for aluminum hydrosilicate nanoscrolls with halloysite structure, most researchers have been constrained to the use of the halloysite mineral. Attempts to synthesize nanoscrolls with halloysite structure by a hydrothermal process similar to one used to obtain chrysotile have not met with any significant success. According to the energy model of scrolling of hydrosilicate layers [22], these challenges arised due to the competition for scrolling direction fostered by the layer's tendency to minimize elastic and surface energies. It is noteworthy that this competition likely prevented the formation of not only aluminum hydrosilicate nanoscrolls with halloysite structure, but

also a whole range of structural analogs such as hydrogermanates of various metals [23]. To overcome these challenges, the following approaches are usually proposed:

(A) increasing size mismatch between the sheets by changing their chemical composition;
(B) changing the initial chemical composition structure;
(C) exfoliation of hydrosilicate layers with platy morphology.

In [24], the scrolling of aluminum hydrosilicate layers was observed only after a significant number of Si^{4+} ions were substituted for Ge^{4+}, which led to an increase in size mismatch between the sheets. At the same time, it is worth noting the results of [25], where the substitution of Si^{4+} for Ge^{4+} in nickel hydrosilicates with chrysotile structure resulted in the opposite effect, that is, the stabilization of plate-like morphology (see also [22]).

As far as we know, few papers have dealt with the application of approach B to the synthesis of nanotubular hydrosilicates with halloysite structure. In particular, work [26], which is available only in Russian, reported on the production of nanoscrolls with halloysite structure by hydrothermal treatment of a thermally pre-treated Al–Si-containing xerogel. A similar approach of using thermal annealing prior to hydrothermal treatment was used in [27]. These results, however, do not allow one to draw unequivocal conclusions in favor of the formation of nanoscrolls with halloysite structure. Finally, within the framework of approach C, hydrosilicate nanoscrolls can be obtained from plates using one [28] or several [29] stages of exfoliation, which indicates the key role of the interlayer interaction in stabilizing the plate-like morphology.

In this work, a further improvement of approach B to varying the initial chemical composition was proposed. It was shown in [22] that the main condition for the stabilization of plate-like morphology is a decrease in the specific surface energy on the edge surfaces of the hydrosilicate layer, which facilitates the thickening of model plates. The chemical reason for this phenomenon lies in the processes of surface hydroxylation, which is why attempts have been made to synthesize the initial compositions using anhydrous media.

2. Experimental

In total, 3 modes of synthesis of the initial composition were studied (Fig. 1): 1 – reverse precipitation of AlOOH from $AlCl_3 \cdot 6H_2O$ (“puriss.”) with an aqueous solution of $NH_3 \cdot H_2O$ (“puriss. spec.”) with amorphous SiO_2 (aerosil A-300, (“puriss.”)); 2 – joint hydrolysis of $(C_3H_7O)_3Al$ (“X”) and $(C_2H_5O)_4Si$ (“puriss.”) in the C_6H_{14}–$NH_3 \cdot H_2O$ system; 3 – joint hydrolysis of the same compounds in the C_8H_{18}–$NH_3 \cdot H_2O$ system.

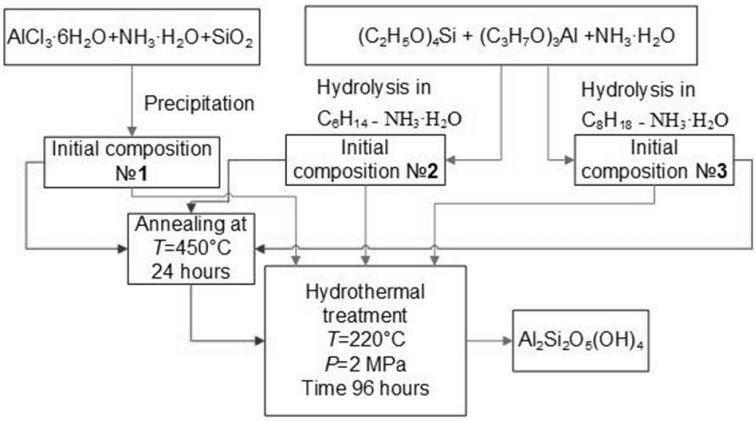

FIG. 1. Synthesis scheme

Synthesis mode 1 involved dispersing 3 g sample of SiO_2 in 27 ml of 2 M aqueous solution of $NH_3 \cdot H_2O$ with constant stirring for 1 hour. Next, 0.05 M aqueous solution of $AlCl_3$ was added drop by drop until the molar ratio of Al/Si = 1 was achieved. The resulting precipitate was washed with distilled water by centrifugation to a neutral reaction of the solution. Subsequently, the precipitate was dried in air at the temperature of 105 °C and ground in an agate mortar.

Synthesis mode 2 involved mixing 1.9 g sample of $(C_3H_7O)_3Al$ and 3.72 ml of $(C_2H_5O)_4Si$ in 90 ml of C_6H_{14} for 24 h. Next, 2 ml of 2 M aqueous solution of $NH_3 \cdot H_2O$ was added to the mixture and stirred for another 24 h. The resulting precipitate was washed with distilled water by centrifugation to a neutral reaction. After that, the precipitate was dried in air at the temperature of 80 °C and ground in an agate mortar. The molar excess $(C_2H_5O)_4Si$ was pre-established experimentally by energy-dispersive X-ray spectroscopy (EDS) of the Al/Si ratio in the initial composition (Fig. 2). Analogical procedures were followed for synthesis mode 3, which used the C_8H_{18} homologue with a longer chain to synthesize the initial composition.

Prior to hydrothermal treatment, parts of the dried and ground sediments of the initial compositions with masses of 2 g were pre-annealed in air at 450 °C at a heating rate of 5 °/min. The isothermal holding time was 24 h with cooling in the furnace (Fig. 1). The samples of the initial compositions and annealing products weighting 0.2 g underwent

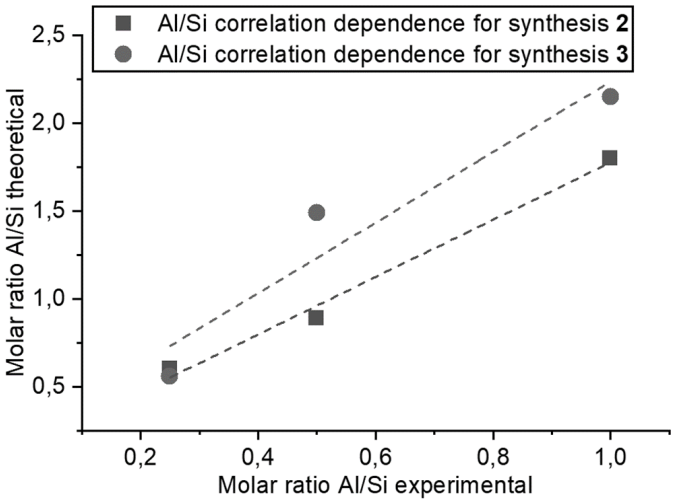

FIG. 2. Correlation dependence of Al/Si for hydrolysis in mixtures C_6H_{14}–$NH_3{\cdot}H_2O$ and C_8H_{18}–$NH_3{\cdot}H_2O$

hydrothermal treatment in PTFE-lined autoclaves with a capacity of 25 ml at a temperature of 220 °C and pressure of 2 MPa for 96 h. Distilled water was used as a hydrothermal medium. The products of hydrothermal treatment were dried in air at a temperature of 80 °C.

The phase composition of the products of hydrothermal treatment and thermal annealing was studied by powder X-ray diffraction (PXRD) using a Rigaku SmartLab 3 diffractometer (CuKα-radiation). The analysis of the obtained X-ray diffractograms was carried out using the ICDD PDF-2 database. The morphology of the products of hydrothermal treatment and thermal annealing, as well as elemental analysis, were studied on a FEI Quanta 200 scanning electron microscope (SEM) with an integrated EDAX X-ray Si(Li) spectrometer. In addition, the morphology of hydrothermal treatment and thermal annealing was studied using a transmission electron microscope (TEM) JEM-2100F and Tescan Amber GMH in scanning transmission electron microscopy (STEM) mode. Synchronous thermal analysis was performed on a Mettler Toledo TGA/DSC 1-Star system in the 35 – 992 °C temperature range. IR spectra were taken with a Shimadzu IRTracer-100 Fourier transform-infrared spectrometer at room temperature (Shimadzu, Kyoto, Japan). The spectra were recorded by averaging of 64 scans in the range from 4000 to 350 cm^{-1} with a resolution of 4 cm^{-1} in KBr tablets.

3. Results and discussion

The PXRD patterns of the hydrothermal treatment (HTT) products of synthesis variants 1, 2 and 3 before and after annealing at 450 °C are shown in Fig. 3. The main phase formed during HTT is plate-like kaolinite $Al_2Si_2O_5(OH)_4$. The only exception is the sample obtained during the HTT of the initial composition synthesized in mode 2 (without pre-annealing). In this case, the formation of a phase with extended period (up to 10 Å) was observed, which was similar to the 10 Å phase of halloysite $Al_2Si_2O_5(OH)_4 \cdot 2H_2O$. Preliminary thermal annealing of the initial compositions at 450 °C and HTT resulted in either a decrease in the intensity of the main kaolinite reflexes (in the case of synthesis variants 1 and 3) and the formation of an amorphous phase, or the disappearance of the 10 Å phase from the products of HTT (in the case of synthesis 2).

The electron microscopy study of the HTT products showed (Figs. 4 and 5) that the particles had plate-like morphology regardless of whether the initial compositions were pre-annealed or not. The length of the plates was 50 – 200 nm, while the thickness varied from 10 up to 60 nm.

The analysis of the elemental composition (Table 1) showed that the content of possible impurities was below the detection limit in all samples, and the molar Al/Si ratio was either close to stoichiometric for the halloysite formula of $Al_2Si_2O_5(OH)_4$.

Figures 6 and 7 show the IR spectra of the studied samples. According to [30, 31], the absorption bands in the region of 1640 – 1650 cm^{-1} were caused by the deformation vibrations of H–O–H water molecules in the interlayer space and the physically sorbed water. The absorption band at 916 cm^{-1} is related to the Al–OH. The bands at 796 and 755 cm^{-1} corresponded to Si–O–Al bond vibrations. In the same region, Si–O valence vibrations were also manifested. Intense bands of 1000 – 1050 cm^{-1} and 696 with complex contouring were caused by in-plane stretching vibrations and sharp stretching vibration. The bands at 544 and 467 cm^{-1} correspond to the in-plane stretching vibrations of the Si–O–Al and Si–O–Si groups.

Let us consider in more details the part of the IR spectrum in the region of valence vibrations of hydroxyl groups (3300 – 3800 cm^{-1}). The complex character of the bands in the region of O–H valence vibrations was due to the different environments in which these groups are located, as well as the presence of impurity phases, for example, gibbsite (see

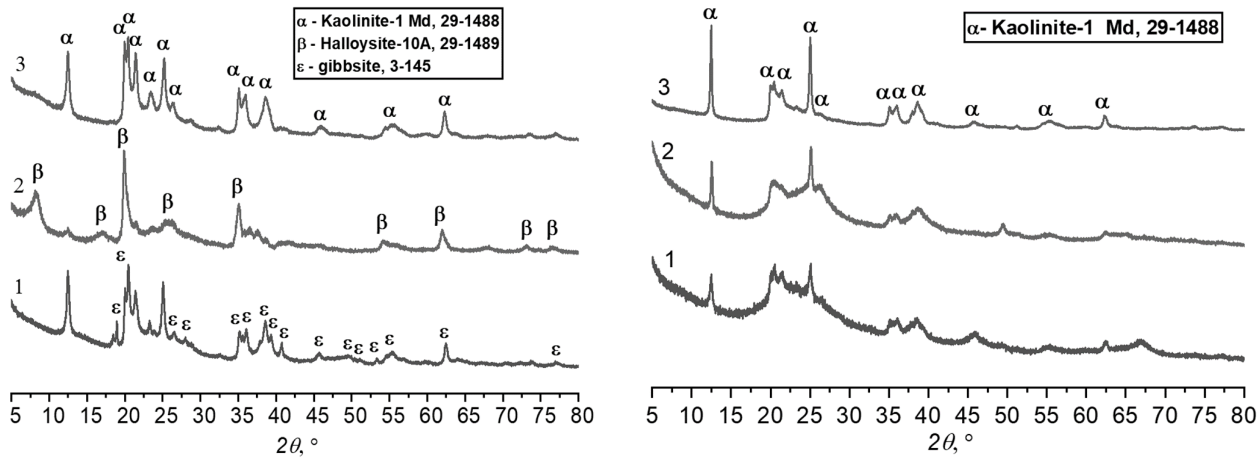

(a) (b)

FIG. 3. X-ray diffraction patterns of the products of hydrothermal treatment of 1, 2 and 3 modes of synthesis before thermal annealing of the initial composition (a) and after annealing of the initial composition at 450 °C (b)

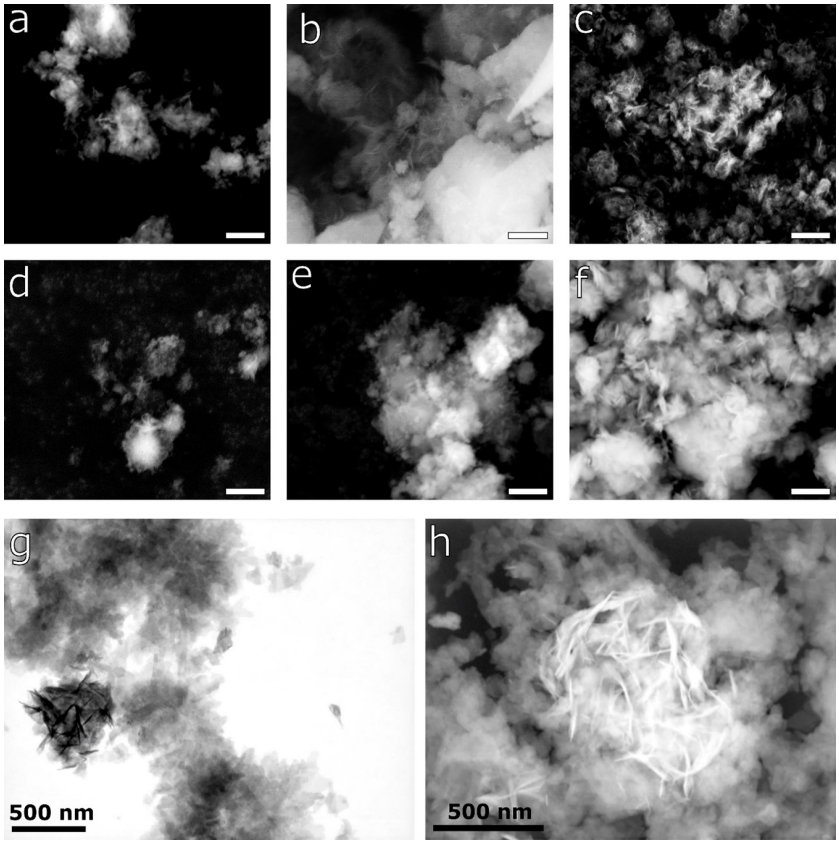

FIG. 4. SEM (a–f) and STEM (g–h) micrographs of hydrothermal treatment products: a, b, c – 1, 2 and 3 modes of synthesis; d, e, f – 1, 2 and 3 modes of synthesis after annealing of the initial composition at 450 °C (scale bar 2 μm); g,h – hydrothermal treatment product of mode 2

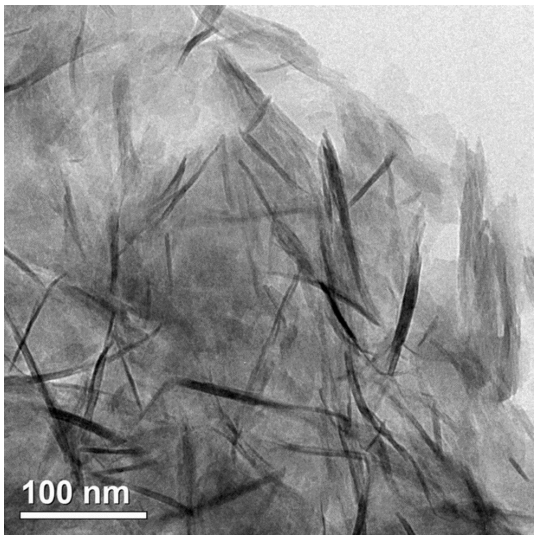

FIG. 5. TEM micrograph of the hydrothermal treatment product of synthesis mode 2

TABLE 1. Elemental composition of the HTT products of the initial compositions before and after pre-annealing at 450 °C (according to EDS)

Initial composition	Elemental composition, at. %			Al/Si
	O	Al	Si	
1	63.4±0.7	18.2±0.2	18.4±0.5	0.99±0.01
2	62.9±6.1	16.5±2.6	20.6±3.6	0.80±0.04
3	63.9±1.3	17.4±0.7	18.7±0.9	0.93±0.05
1 (450 °C)	63.2±3.1	17.4±7.8	19.4±4.8	0.9±0.6
2 (450 °C)	65.2±1.8	17.4±1.6	17.3±0.4	1.02±0.08
3 (450 °C)	61.5±0.8	17.9±0.2	20.6±0.7	0.87±0.02

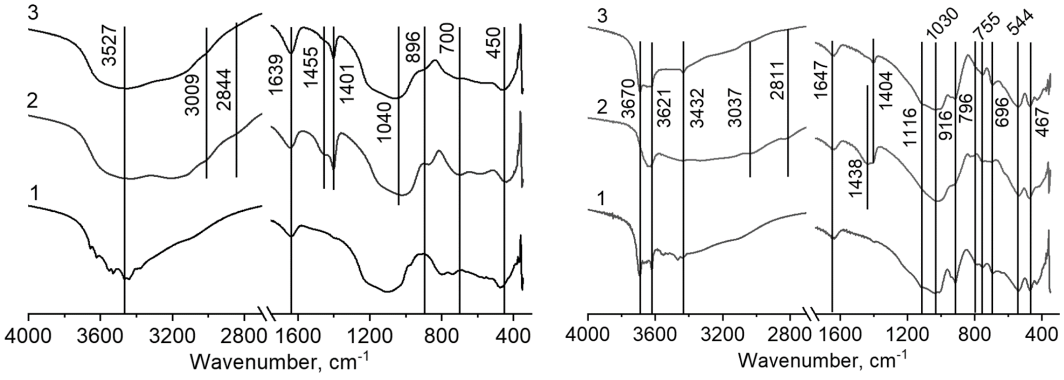

(a) (b)

FIG. 6. IR transmission spectra of initial compositions (a) and products of hydrothermal treatment (b) of 1, 2 and 3 modes of synthesis

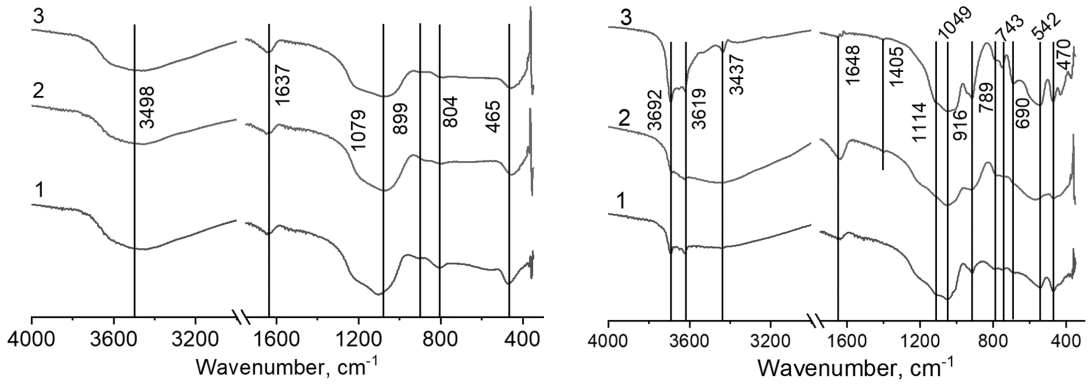

FIG. 7. IR transmission spectra of the initial compositions after annealing at 450 °C (a), as well as the products of their hydrothermal treatment (b) of 1, 2 and 3 modes of synthesis

Fig. 3). In accordance with the structure of halloysite and kaolinite [32], hydroxyl groups were divided into "inner surface" O–H and "inner" O–H. The interlayer (inner O–H) groups are located between silicon oxide tetrahedra and aluminum oxide octahedra. The inner surface O–H groups are located in the interlayer space and are connected only to aluminum oxide octahedra [32]. The band at 3670 cm^{-1} corresponded to the valence vibrations of OH groups on the surface of the inner layer of the nanotube, whereas the band at 3621 cm^{-1} corresponded to the valence vibrations of the interlayer OH groups. Additionally, the adsorbed water manifested itself in the form of a wide band in the region of 3500 cm^{-1}.

The bands at 3037, 2811 and 1405 cm^{-1} correspond to symmetric, asymmetric and scissor-like valence vibrations of stretching and deformation of CH_2 [33], which indicate the presence of an organic component in the system. There is also a band at 1438 cm^{-1} in the spectrum presumably corresponding to the vibration of C–O–Al bonds. HTT leaded to a significant decrease in the intensity of these bands but did not completely remove them. In contrast, preliminary thermal annealing at 450 °C leaded to the disappearance of all bands associated with organic groups (Fig. 7).

Figure 8 illustrates the results of synchronous thermal analysis of the initial composition synthesized in mode 2 and the product of its HTT. The initial composition was characterized by a continuous loss of mass throughout the studied temperature range. According to IR spectroscopy data (Fig. 6), mass losses at the initial stage were associated with the removal of adsorbed water [34], as well as the removal of organic compounds. In a higher temperature region, the differential curve showed an effect associated with volumetric dehydroxylation of the hydrosilicate phase [35–37] in the initial composition. Following the hydrothermal treatment, the mass loss of the sample was significantly reduced (and practically absent in the range of 120 – 300 °C), which indicated a likely decrease in the specific surface area as a result of recrystallization and fewer opportunities for adsorption of water or organic solvent. The first thermal effect and the associated mass loss following HTT were observed at a relatively low temperature (below 100 °C), which correlated with the temperature of removal of interlayer water molecules from the structure of 10 Å halloysite [38]. With an increase in temperature, a series of effects were distinctly observed on the DTG curve that are also associated with volumetric dehydroxylation of hydrosilicates. However, unlike in the case of the original composition, there are several stages of mass loss. The highest high-temperature peak (528 °C) corresponds to the transformation of the 7 Å impurity phase (Fig. 3(a)), while the average peak in the series (480 °C) correlates to the greatest extent with the literature data on 10 Å halloysite [38]. The origin of the first peak of the series (412 °C) may be associated with the transition of the organically modified part of the hydrosilicate.

4. Conclusion

Layered aluminum hydrosilicates were obtained by hydrothermal treatment of initial compositions with various chemical prehistory. The formation of a 10 Å phase with a 10 Å halloysite structure was observed when using $Al(OC_3H_7)_3$ and $Si(OC_2H_5)_4$ as the initial reagents of the product of the alkaline co-hydrolysis in the C_6H_{14}–$NH_3 \cdot H_2O$ system. The increased distance between the hydrosilicate layers was created by organic ligands as evidenced by IR spectroscopy data. The use of traditional precipitation, annealing of initial compositions before the hydrothermal treatment, as well as varying the length of the organic solvent molecule led to the formation of a 7 Å phase with kaolinite structure. Although the increase in the interlayer distance was not enough to overcome the trend of the interlayer interaction and the formation of nanoscrolls, the resulting phase is promising for studying the processes of adsorption and further exfoliation.

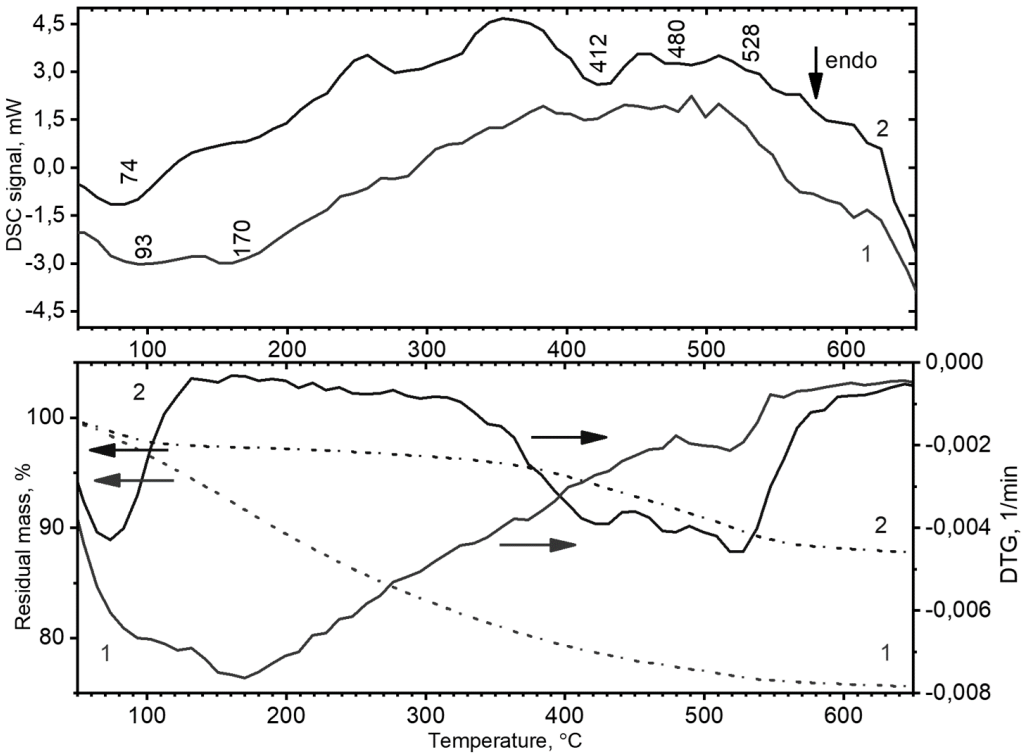

FIG. 8. DSC curves of thermal effects, thermogravimetry curves obtained in a dynamic air atmosphere for the initial composition (1) and the product of hydrothermal treatment of synthesis mode 2 (2)

References

[1] Pimneva L.A. Study of the adsorption of manganese ions (II) in natural kaolinite. *Modern high technologies*, 2017, **7**, P. 61–65.

[2] Minyukova T.P., Shtertser N.V., Khassin A.A., Plyasova L.M., Kustova G.N., Zaikovskii V.I., Baronskaya N.A., Kuznetsova A.V., Davydova L.P., Yur'eva T.M., Shvedenkov Yu.G., Van Den Heuvel J.C. Evolution of Cu–Zn–Si oxide catalysts in the course of reduction and reoxidation as studied by in situ x-ray diffraction analysis, transmission electron microscopy, and magnetic susceptibility methods. *Kinetics and Catalysis*, 2008, **49** (6), P. 821–830.

[3] Bikbau M.Ya. Nano cement morphological peculiarities, structure properties and concrete on their base. *Concrete technology*, 2014, **4**, P. 38–44.

[4] Koji Wada, Naganori Yoshinaga. The structure of "imogolite". *American Mineralogist*, 1969, **52** (1–2), P. 50–71.

[5] Levin A., Khrapova E., Kozlov D., Krasilin A., Gusarov V. Structure refinement, microstrains and crystallite sizes of Mg–Ni-phyllosilicate nanoscroll powders. *J. Appl. Cryst.*, 2022, **55**, P. 484–502.

[6] Bates T.F., Sand L.B., Mink J.F. Tubular Crystals of Chrysotile Asbestos. *Science*, 1950, **111**, P. 512–513.

[7] Bates T.F., Hildebrand F.A., Swineford A. Morphology and structure of endellite and halloysite. *American Mineralogist*, 1950, **35** (7–8), P. 463–484.

[8] Lukuttsova N.P., Golovin S.N. Aggregative stability of aqueous suspensions of halloysite nanotubes. *Construction materials*, 2018, **1** (2), P. 4–10.

[9] Arsent'ev M.Y., Golubeva O.Y. Comparative Study of Internal Mechanical Stresses in the Structures of Montmorillonite and Halloysite. *Glass Phys. Chem.*, 2020, **46**, P. 598–604.

[10] Szczepanik B., Slomkiewicz P., Garnuszek M., Czech K., Banas D., Kubala-Kukus A., Stabrawa I. The effect of chemical modification on the physico-chemical characteristics of halloysite: FTIR, XRF, and XRD studies. *J. of Molecular Structure*, 2015, **1084**, P. 16–22.

[11] Krasilin A.A., Khrapova E.K., Maslennikova T.P. Cation Doping Approach for Nanotubular Hydrosilicates Curvature Control and Related Applications. *Crystals*, 2020, **10**, 654.

[12] Parfitt R.L., Furkert R. J., Henmi T. Identification and Structure of Two Types of Allophane from Volcanic Ash Soils and Tephra. *Clays and Clay Minerals*, 1980, **28**, P. 328–334.

[13] Krasilin A.A., Khrapova E.K., Nominé A., Ghanbaja J., Belmonte T., Gusarov V.V. Cation Redistribution along the Spiral of Ni-Doped Phyllosilicate Nanoscrolls: Energy Modelling and STEM/EDS Study. *Chem. Phys. Chem.*, 2019, **20**, P. 1–9.

[14] Kirichenko O.A., Shuvalova E.V., Redina, E.A. Low-temperature copper hydrosilicates: catalysts for reduction of aromatic nitro compounds with molecular hydrogen. *Russ. Chem. Bull.*, 2019, **68**, P. 2048–2052.

[15] Hara T., Mascotto S., Weidmann C., Smarsly B.M. The effect of hydrothermal treatment on column performance for monolithic silica capillary columns. *J. of Chromatography A*, 2011, **1218**, P. 3624–3635.

[16] Krasilin A.A., Bodalyov I.S., Malkov A.A., Khrapova E.K., Maslennikova T.P., Malygin A.A. On an adsorption/photocatalytic performance of nanotubular $Mg_3Si_2O_5(OH)_4/TiO_2$ composite. *Nanosystems: Phys. Chem. Math.*, 2018, **9** (3), P. 410–416.

[17] Krasilin A.A., Straumal E.A., Yurkova L.L., Khrapova E.K., Tomkovich M.V., Shunina I.G., Vasil'eva L.P., Lermontov S.A., Ivanov V.K. Sulfated Halloysite Nanoscrolls as Superacid Catalysts for Oligomerization of Hexene-1. *Russ. J. Appl. Chem.*, 2019, **92**, P. 1251–1257.

[18] Sidorenko A.Yu., Kravtsova A.V., Aho A., Heinmaa I., Wärna J., Pazniak H., Volcho K.P., Salakhutdinov N.F., Murzin D.Yu., Agabekov V.E. Highly selective Prins reaction over acid-modified halloysite nanotubes for synthesis of isopulegol-derived 2H-chromene compounds. *J. of Catalysis*, 2019, **374**, P. 360–377.

[19] Thill A., Picot P., Bellon L. A mechanism for the sphere/tube shape transition of nanoparticles with an imogolite local structure (imogolite and allophane). *Applied Clay Science*, 2017, **141**, P. 308–315.

[20] Pigniè M.-C., Shcherbakov V., Charpentier T., Moskura M., Carteret C., Denisov S., Mostafavi M., Thill A., Caër S. Confined water radiolysis in aluminosilicate nanotubes: the importance of charge separation effects. *Nanoscale*, 2021, **13**, P. 3092–3105.
[21] Cavallaro G., Lazzara G., Milioto S., Parisi F., Sanzillo V. Modified Halloysite Nanotubes: Nanoarchitectures for Enhancing the Capture of Oils from Vapor and Liquid Phases. *ACS Appl. Mater. Interfaces*, 2014, **6**, P. 606–612.
[22] Krasilin A.A. Energy modeling of competition between tubular and platy morphologies of chrysotile and halloysite layers. *Clays and Clay Minerals*, 2020, **1**, P. 1–12.
[23] Krasilin A.A., Khrapova E.K. Effect of hydrothermal treatment conditions on formation of nickel hydrogermanate with platy morphology. *Russ. J. Appl. Chem.*, 2017, **90**, P. 22–27.
[24] White R.D., Bavykin D.V., Walsh F.C. Spontaneous Scrolling of Kaolinite Nanosheets into Halloysite Nanotubes in an Aqueous Suspension in the Presence of GeO_2. *J. of Physical Chemistry*, 2012, **116**, P. 8824–8833.
[25] Perbost R., Amouric M., Olives J. Influence of Cation Size on the Curvature of Serpentine Minerals: HRTEM-AEM Study and Elastic Theory. *Clays Clay Miner.*, 2003, **51**, P. 430–438.
[26] Maslennikova T.P., Korytkova E.N., Pivovarova L.N. Hydrothermal synthesis of nanotube composition $Al_2Si_2O_5(OH)_4 \cdot 2H_2O$ with halloysite structure. *Physics and Chemistry of Glass*, 2012, **S6**, P. 890–893.
[27] Golubeva O.Yu, Alikina Y.A., Kalashnikova T.A. Influence of hydrothermal synthesis conditions on the morphology and sorption properties of porous aluminosilicates with kaolinite and halloysite structures. *Applied Clay Science*, 2020, **199**, P. 1–12.
[28] Makóa É., Kovács A., Antal V., Kristóf T. Thin-walled nanoscrolls by multi-step intercalation from tubular halloysite-10 Å and its rearrangement upon peroxide treatment. *Applied Clay Science*, 2017, **146**, P. 131–139.
[29] Xiaoguang Li, Qinfu Liu, Hongfei Cheng, Sridhar Komarneni. High-yield production of mesoporous nanoscrolls from kaolinite by ultrasonic assisted exfoliation. *Microporous and Mesoporous Materials*, 2017, **241**, P. 66–71.
[30] Kloprogge J.T. Characterisation of Halloysite by Spectroscopy. *Developm. Clay Sci.*, 2016, **7**, P. 115–136.
[31] Jiangyan Yuan, Jing Yang, Hongwen Ma, Shuangqing Su, Qianqian Chang, Sridhar Komarneni. Hydrothermal synthesis of nano-kaolinite from K-feldspar. *Ceramics International*, 2018, **44** (13), P. 15611–15617.
[32] Tan D., Yuan P., Liu D., Du P. Chapter 8 - Surface Modifications of Halloysite. *Developm. Clay Sci.*, 2016, **7**, P. 167–201.
[33] Weng On Yah, Atsushi Takahara, Yuri M. Lvov. Selective Modification of Halloysite Lumen with Octadecylphosphonic Acid: New Inorganic Tubular Micelle. *J. of the American Chemical Society*, 2012, **134** (3), P. 1853–1859.
[34] Li Y., Zhang Y., Zhang Y., Liu M., Zhang F., Wang L. Thermal behavior analysis of halloysite selected from Inner Mongolia Autonomous Region in China. *J. Therm. Anal. Calorim.*, 2017, **129**, P. 1333–1339.
[35] Erzsébet Horváth, Ray L. Frost, Éva Makó, János Kristóf, Tamás Cseh. Thermal treatment of mechanochemically activated kaolinite. *Thermochimica Acta*, 2003, **404** (1–2), P. 227–234.
[36] Gábor M., Tóth M., Kristóf J., Komáromi-Hiller G. Thermal Behavior and Decomposition of Intercalated Kaolinite. *Clays Clay Miner.*, 1995, **43**, P. 223–228.
[37] Krasilin A.A., Danilovich D.P., Yudina E.B., Bruyere S., Ghanbaja J., Ivanov V.K. Crystal violet adsorption by oppositely twisted heat-treated halloysite and pecoraite nanoscrolls. *Applied Clay Science*, 2019, **173**, P. 1–11.
[38] Joussein E., Petit S., Churchman J., Theng B., Righi D., Delvaux B. Halloysite clay minerals – a review. *Clay Minerals*, 2005, **40**, P. 383–426.

Submitted 18 December 2022; revised 19 December 2022; accepted 10 February 2023

Information about the authors:

Nikita A. Leonov – Ioffe Institute, 26 Politekhnicheskaya, 194021, St. Petersburg, Russia; ORCID 0000-0001-8886-0731; nikita_leonov_1998@mail.ru

Daniil A. Kozlov – Lomonosov Moscow State University, Leninsky gory, 1, 119991, Moscow, Russia; Kurnakov Institute of General and Inorganic Chemistry, Russian Academy of Sciences, Leninsky pr., 31, 119991, Moscow, Russia; ORCID 0000-0003-0620-8016; kozlov@inorg.chem.msu.ru

Demid A. Kirilenko – Ioffe Institute, 26 Politekhnicheskaya, 194021, St. Petersburg, Russia; ORCID 0000-0002-1571-209X; zumsisai@gmail.com

Nikolay A. Bert – Ioffe Institute, 26 Politekhnicheskaya, 194021, St. Petersburg, Russia; ORCID 0000-0001-6136-4877; nikolay.bert@mail.ioffe.ru

Anna O. Pelageikina – Ioffe Institute, 26 Politekhnicheskaya, 194021, St. Petersburg, Russia; ORCID 0009-0000-6320-2011; Pelaanna@yandex.ru

Andrey A. Nechitailov – Ioffe Institute, 26 Politekhnicheskaya, 194021, St. Petersburg, Russia; ORCID 0000-0002-9895-6822; aan.shuv@mail.ioffe.ru

Mikhail B. Alikin – St. Petersburg State Technological University (Technical University), 190013, St. Petersburg, Russia; ORCID 0000-0002-0770-9675; alikinmix@gmail.com

Andrei A. Krasilin – Ioffe Institute, 26 Politekhnicheskaya, 194021, St. Petersburg, Russia; ORCID 0000-0002-3938-3024; ikrasilin@mail.ioffe.ru

Conflict of interest: the authors declare no conflict of interest.

NANOSYSTEMS:
PHYSICS, CHEMISTRY, MATHEMATICS

Chernova E.A., Gurianov K.E., et al. *Nanosystems: Phys. Chem. Math.*, 2023, **14** (2), 272–278.
http://nanojournal.ifmo.ru
DOI 10.17586/2220-8054-2023-14-2-272-278

Original article

Comparative study of transport properties of membranes based on graphene oxide prepared by Brodie and improved Hummers' methods

Ekaterina A. Chernova[1,4,a], Konstantin E. Gurianov[1,b], Victor A. Brotsman[2,c], Rishat G. Valeev[3,d], Olesya O. Kapitanova[2,e], Mikhail V. Berekchiian[1,f], Alexei V. Lukashin[1,g]

[1]Lomonosov Moscow State University, Faculty of Materials Science, Moscow, Russia

[2]Lomonosov Moscow State University, Faculty of Chemistry, Moscow, Russia

[3]Udmurt Federal Research Center of the Ural Brunch of Russian Academy of Sciences, Izhevsk, Russia

[4]Tula State University, Tula, Russia

[a]chernova.msu@gmail.com, [b]gurianovke@yandex.ru, [c]brotsman_va@mail.ru, [d]rishatvaleev@mail.ru, [e]olesya.kapitanova@gmail.com, [f]mikhail.berekchiyan@yandex.ru, [g]alexey.lukashin@gmail.com

Corresponding author: Ekaterina A. Chernova, chernova.msu@gmail.com

PACS 81.05.Rm, 47.56.+r

ABSTRACT A comparative study of transport characteristics of composite membranes based on graphene oxide prepared by Hummers' (H-GO) and Brodie (B-GO) methods is presented. By using Raman and XPS spectroscopy combined with gas and vapor measurements at non-zero pressure drop, it is shown that the difference in preparation methods results not only in different composition and microstructure of the membranes, but also in different water vapor permeability and resistance towards pressure drops during membrane performance. The H-GO samples are found to be more defective and stronger oxidized with C/O ratio of 1.8, whereas B-GO revealed a total C/O ratio of 2.6 with more perfect microstructure. The higher oxidation degree of H-GO membranes allows one to achieve higher water vapor permeability (up to ∼170 Barrer at 100 % humidity) but dramatically lower stability towards pressure revealing the irreversible loss in permeability up to 46 % during the application of pressure drop of 1 bar. In contrast, B-GO membranes show slightly lower permeability (∼140 Barrer at 100 % humidity) but enhanced pressure stability revealing the irreversible permeability loss of only 4 % at pressure drop of 1 bar which is about 10-fold smaller compared to H-GO stability. This could be explained by the difference in microstructural features of the H-GO and B-GO. Graphene oxide prepared by Hummer's method has more flexible and defective nanosheets, whereas Brodie's method gives rise to more rigid nanosheets with more perfect microstructure. The obtained results suggest that it is possible to prepare graphene oxide membranes with high resistance towards pressure using only the composition-microstructure interplay without additional modification with pressure-stabilizing agents.

KEYWORDS graphene oxide membranes, Hummers' method, Brodie method, oxidation degree, pressure stability, water vapor permeability

ACKNOWLEDGEMENTS The work is supported by the state program of world-class scientific and educational centers (assignment number FEWG-2021-0014) for the youth laboratory on the research direction "Studying gas permeability and physicochemical properties of sealing composite and carbon materials". The authors are grateful to Dr. Andrei Eliseev and his laboratory (Lomonosov Moscow State University) for help with experimental studies. The authors acknowledge shared services center "Surface and novel materials" of UdmFRC of UB RAS for XPS data acquisition.

FOR CITATION Chernova E.A., Gurianov K.E., Brotsman V.A., Valeev R.G., Kapitanova O.O., Berekchiian M.V., Lukashin A.V. Comparative study of transport properties of membranes based on graphene oxide prepared by Brodie and improved Hummers' methods. *Nanosystems: Phys. Chem. Math.*, 2023, **14** (2), 272–278.

1. Introduction

At present time, the dehydration of natural and technological gas mixtures has become one of the most important tasks in the conditioning of natural gas for pipeline transport, preparation of pure gases for electronics, chemical industry and medicine enterprises. To solve this problem, membrane technologies are developed, since the use of compact membrane modules can significantly reduce capital investments, and the energy intensity of the entire process. The key factors determining the effectiveness of membrane technology are the permeability and selectivity of the membrane material as well as its long-term stability and resistance towards external conditions including pressure drops. Currently, polymeric materials dominate in the membrane technological processes, however, they are prone to physical aging and plasticization

which significantly reduces both the performance and long-term stability of the membranes introducing challenges in design of membrane materials [1].

A reasonable alternative to polymers are carbon membranes, which are considered as advanced materials among with the graphene oxide (GO) and its modified derivatives [2]. Graphene oxide is a two-dimensional material which could be considered as a modification of graphene richly decorated with oxygen-containing groups, including hydroxyl, epoxy, carbonyl and carboxyl groups making GO a suitable candidate for dehumidification technologies. Graphene oxide is obtained by intercalation and oxidation steps of carbon precursors (commonly, graphite and carbon nanotubes) [2–4]. For industrial applications, the pressure stability of graphene oxide still remains an important issue. Generally, the permeability of GO-based membranes decreases with increasing operating pressure which is attributed to compaction of GO nanosheets and shrinking of interlayer spacing [5]. To enhance GO pressure stability, various pressure-resistant agents are introduced into interlayer galleries of GO. For instance, the layered carbon nitride (C_3N_4) nanoparticles [6], single-walled carbon nanotubes [7], functionalized fullerenes [8], zeolitic imidazolate framework particles [9] were reported to stabilize GO towards pressure drops. Moreover, the intercalation of positively charged copper hydroxide nanostrands [10] or K^+ ions [11] in GO were claimed even to increase water permeance with pressure. These results are promising, however, it is more desirable to manage the pressure stability using only intrinsic interplay of composition and microstructure in GO, because additional modification steps could strongly increase the complexity and costs of the graphene oxide membranes; moreover, the integration of foreign substances into GO matrix could inevitably induce the formation of additional structural defects. The stability of GO towards elevated pressures and pressure drops could be obviously based on the method of GO preparation. The understanding of this interrelation could give an opportunity to design the pressure-stable GO microstructure originally at the stage of its synthesis.

Four different classical methods are employed to obtain GO: the method of Brodie [12], Staudenmaier [13], Hoffman [14], and Hummers'/Offeman (or, simply, Hummers' method) [15]. The methods have a variety of modifications, for instance, at least, classical [15], modified [16] and improved Hummers' [3] methods have been reported. Each method of preparation endows the resulting GO with different chemistries making a strong impact on the microstructure and functional characteristics of GO membranes [17–19]. For instance, it was shown that Brodie-GO membranes reveal higher selectivity towards H_2 molecules due to a narrower interlayer spacing between GO nanosheets compared to Hummers' GO [18]. In other work, it was reported that, due to different chemistry, Brodie-GO is considered as a better photocatalytic platform than Hummers' GO [19]. It could be assumed that the difference in microstructure and chemistries of GO prepared by different methods could be employed for the enhancement of GO-based membranes for gas dehumidification without the need to modify GO with various pressure-resistant reagents.

In this work, a comparative analysis of the compositional and transport characteristics of membranes based on graphene oxide obtained by the improved Hummers' method (H-GO) [4] and Brodie method (B-GO) [5] is performed. The microstructure and chemical composition of the membranes is examined by scanning electron microscopy, Raman and X-ray photoelectron spectroscopy. The permeability of the membranes towards water vapors is studied under various humidity and pressure drops of the feed stream focusing on the possibility of pressure stability enhancement using only the interplay of microstructure and chemical composition of neat GO membranes. Our results present the general concept for improving functional properties of graphene oxide by careful choice of preparation method rather than post-modification with foreign substances.

2. Experimental part

Graphene oxide samples were obtained by improved Hummers' method and modified Brodie method. To prepare H-GO samples, graphite was oxidized by potassium permanganate with the graphite: $KMnO_4$ ratio of 1:6 [12]. The detailed description of the synthesis is presented in [6]. For the preparation of B-GO, potassium chlorate was used as an oxidant taking graphite/$KClO_3$ ratio of 1:16. In a 100 ml flat-bottomed flask, 0.7 g of thermally expanded graphite and 9.6 g of potassium chlorate were added with constant stirring and cooling in an ice bath. To the resulting mixture, a fuming nitric acid was added dropwise (24.5 ml, one drop per second). The flask was left under constant stirring and room temperature for 12 hours, and then the reaction mixture was heated to 60 °C and left for 8 hours at this temperature to further oxidize the graphite. As a result, the first batch of graphene oxide (B-GO1) was obtained. The resulting suspension was diluted with water in a ratio of 1:1 by volume, then the precipitate was separated by vacuum filtration and repeatedly washed with deionized water until the pH = 6. The precipitate was dried by sublimation and then subjected to re-oxidation as described above. The resulting mixture was stirred at 60 °C for 20 hours. The obtained graphene oxide was repeatedly washed with deionized water until the pH = 6. For the purification from residual inorganic ions, the resulting H-GO and B-GO suspensions were subjected to dialysis for 30 days under constant stirring. The suspensions were further used for the formation of selective layers of composite membranes.

For composite membranes preparation, porous anodic aluminum oxide (AAO) membranes (pore diameter of ∼80 nm, thickness ∼100 μm) were used as reliable supports for GO thin selective layers. The AAO films preparation is described in [13, 14]: briefly, a standard anodic oxidation of aluminum foils with high purity (99.999 %) in 0.3 M $H_2C_2O_4$ at 120 V was employed followed by selective removal of aluminum and etching of a barrier layer to get highly-permeable porous AAO supports with the N_2 permeance of 90 – 100 $m^3 \cdot m^{-2} \cdot bar^{-1} \cdot h^{-1}$ [15].

To obtain composite membranes, water-methanol suspensions with the concentration of 1 mg/ml were prepared by diluting the original H-GO and B-GO suspensions with methanol. The suspensions were carefully deposited on the surface of AAO supports by spin-coating at the rate of 1500 rpm. To achieve dense packing of the GO nanoflakes, vacuum suction was used upon the spin-coating and the several aliquots (30 – 50 mkl) of GO suspensions were deposited successively. To make sure that the obtained composite membranes have no large parasitic defects, the membranes were examined using optical microscope Carl Zeiss and tested for N_2 permeability.

To study the thickness and microstructure of the membranes, scanning electron microscopy (SEM) of membrane cross-sections was performed using Nvision 40 (Carl Zeiss) microscope. To get the average thickness of the selective layers, the SEM micrographs were statistically processed with ImageJ software.

To estimate the defectiveness of the H-GO and B-GO samples, the Raman spectroscopy was employed using a Renishaw InVia instrument with Leica DMLM optics ($50\times$ objective) and 20 mW 633 nm He–Ne laser. The obtained spectra were processed with Wire 3.4 Renishaw software, using Pseudo-Voigt functions positioned at 1340 ± 20 and $\sim 1590 \pm 10$ cm^{-1} for D- and G-peaks, respectively. Because graphene oxide is far more defective compared to graphene, the $I(D)/I(G)$ ratio for H-GO and B-GO was calculated using integrated areas of D and G peaks divided by their FWHM to get more reliable estimates of defectiveness.

To check the chemical composition of the membranes, X-ray photoelectron (XPS) spectra were registered on SPECS instrument by employing MgK-α excitation (excitation energy, $E_{ex} = 1254$ eV). Pure graphite C1s energy (284.6 eV) was used to calibrate the resulting spectra. The spectra were quantitatively processed with CasaXPS software using Shirley type background and mixed Gauss (70 %) – Lorentz (30 %) functions for spectra deconvolution. During the processing, the FWHM of spectral peaks was kept constant for all the spectral components. The subdivision of the C–C band into sp^2–C, sp^3–C-hybridized components was neglected due to an insufficient spectral resolution [16].

To study the transport characteristics of the membranes, a set of individual permanent gases (H_2, N_2, O_2, CO_2, CH_4, C_4H_{10} and SF_6) was used. For the analysis, the membranes were tightened between a feed chamber and calibrated permeate chamber of a two-compartment measurement cell. Then, the permeate chamber was evacuated using a vacuum pump until the residual pressure of less than 0.1 mbar was achieved. After this, the stream of the measured gas was introduced into the feed chamber and a pressure-time curve was registered during the gas inflowing across the membrane into the permeate chamber. The fluxes of the permanent gases were calculated using a slope of the linear part of the pressure-time curve.

To study the water vapor permeability under a steady mode, a feed stream containing a mixture of dry N_2 and N_2 flux with controlled humidity was used. To obtain wet N_2 flux, the N_2 stream was bubbled through the vessel with liquid water. The control of the entire feed stream humidity was performed by setting the ratio of dry N_2 and wet N_2 fluxes. The feed stream was introduced to the feed side of the membrane, while the permeate side was blown with He flux (pressure = 1 bar). The permeability was measured under varied relative humidity of the feed stream (inlet relative humidity RH_{in}). For each humidity value, the membrane was blown with feed stream for at least 30 minutes to achieve an equilibrium steady flux across the membrane. During the experiment, the dependence of outlet relative humidity (RH_{out}) of the He flux was measured with time. The humidity and temperature of both gas fluxes were controlled using HIH-4000 sensors (Honeywell, USA). The experiments were performed at the temperatures of 23 – 25 °C.

3. Results and discussion

The results of SEM have shown that the selective layers based on B-GO and H-GO are represented by thin and uniform layered films covering the entire surface of AAO supports. The average thickness of HGO- and BGO selective layers stands in the range 18 – 20 nm (Fig. 1(a,b)).

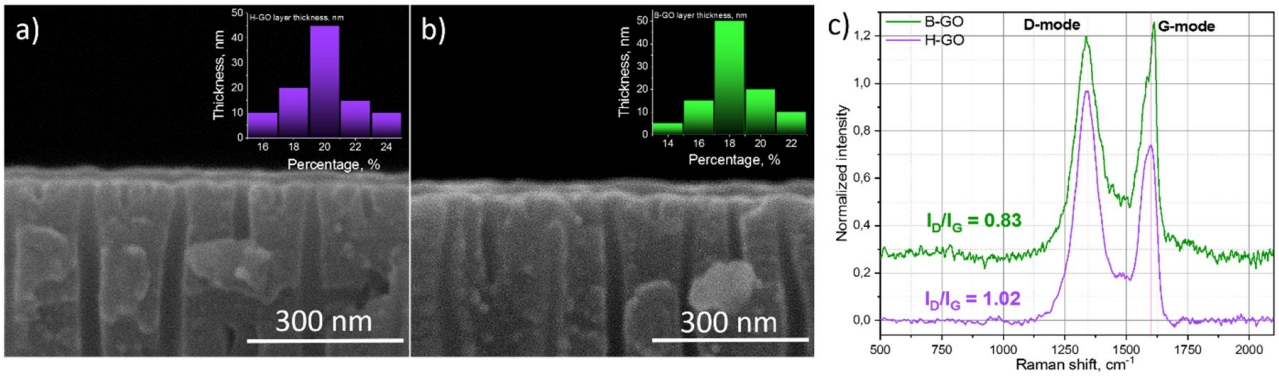

FIG. 1. SEM micrographs of cross-sections of the composite membranes with selective layers based on: a) H-GO; b) B-GO; c) Raman spectra for H-GO and B-GO membranes

Raman spectra of H-GO and B-GO show the typical D-mode (defect-activated peak coming from transverse optical phonons (TO phonons) with A_{1g} symmetry in graphene lattice) and G-mode (coming from optical phonon with E_{2g}-symmetry) (Fig. 1(c)). Generally, the D-peak is responsible for various types of defects in GO including sp^3-carbons, edges, nanoflakes tilting, etc., whereas G-peak shows the vibrations of sp^2-carbons in GO skeleton. It should be noted that graphene oxide is intrinsically sp^3-rich and defective phase, and its Raman spectra are more complex containing D'', D', and D^* modes overlapping with apparently visible D and G peaks and making impact into peak areas [20, 21]. At the same time, the ratio of intensities of D and G modes ($I(D)/I(G)$ ratio) are commonly used to estimate the defectiveness of carbon materials. In the present study, the $I(D)/I(G)$ ratio was calculated using heights of D and G peaks (see Experimental part) which gives one more reliable estimates for GO [20] rather than simple dividing of integrated areas of peaks commonly practiced in most of the works on graphene oxide. According to the results, it was revealed that B-GO sample has smaller $I(D)/I(G)$ ratio which could be estimated as lower level of defects in its structure compared to H-GO.

According to the XPS results (Fig. 2(a–d)), the GO sample obtained by improved Hummers' method is stronger oxidized achieving the C/O ratio of 1.8, whereas the C/O ratio of B-GO reaches 2.6, which is more close to mildly thermally-reduced GO [22]. Moreover, the ratio of single- to double- oxygen bonded carbon (C–O/C=O) reaches 4.0 for B-GO and only 2.8 for H-GO showing the strong and dominating contribution of C–O bonded groups (hydroxyls and epoxy groups) over C=O component (carbonyl, carboxyl groups) for graphene oxide obtained by the Brodie method (Fig. 2(e,f)). According to model structure of GO, the hydroxyl and epoxide groups are commonly located on the basal surface of GO nanoflakes [23]. Thus, B-GO membrane has less oxidized nanosheets with dominating presence of basal oxygen groups and is expected to be more rigid with smaller number of defects compared to H-GO-based membrane.

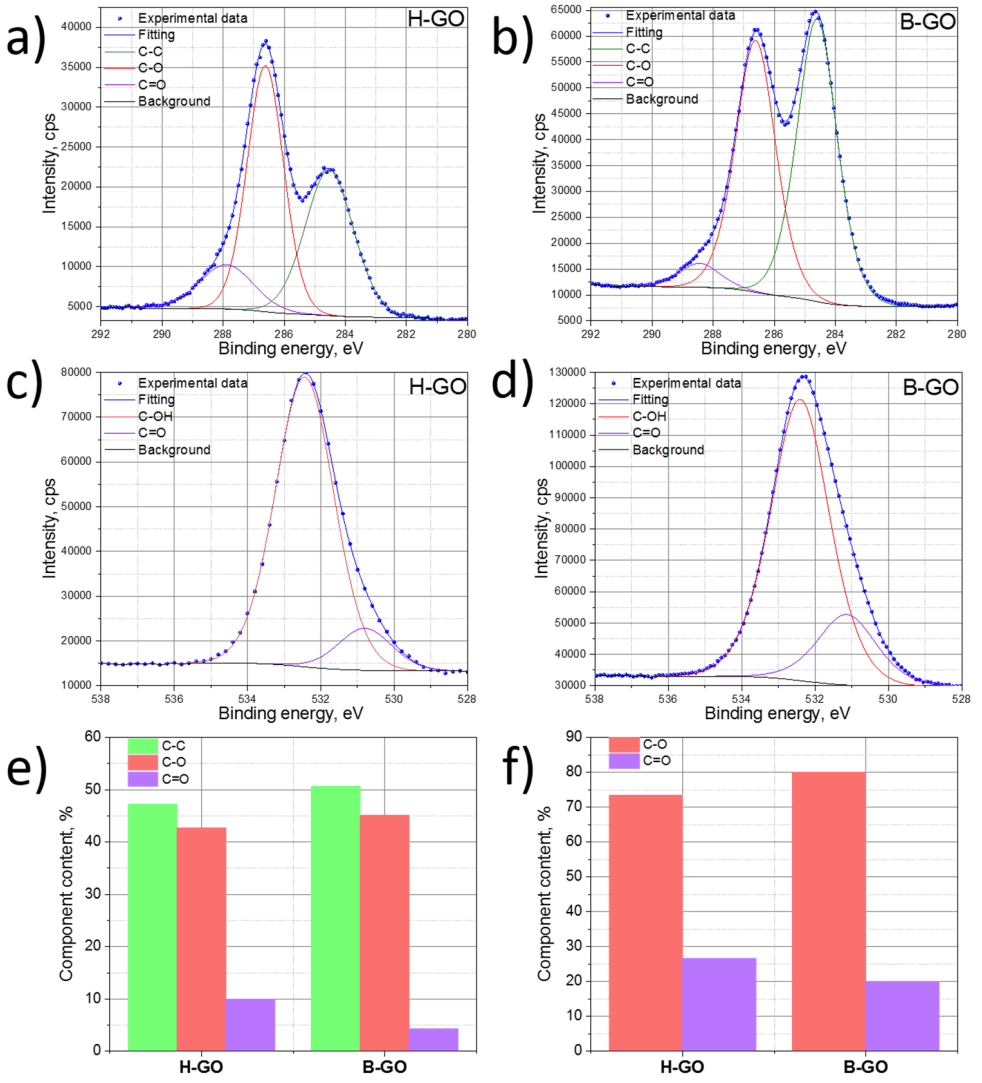

FIG. 2. XPS spectra of the composite membranes: a), c), and b), d), represent C1s spectra and O1s spectra for H-GO and B-GO samples, respectively; e),f) spectral components content calculated from C1s spectra (e), and O1s spectra (f) for H-GO and B-GO-based membranes

Both composite membranes based on H-GO and B-GO reveal low permeability towards permanent gases achieving the values not exceeding 0.002 – 0.003 Barrer for H_2 gas. Generally, there is a linear dependence of gas permeance on the inverse square root from molecular mass of gases obeying the Knudsen diffusion equation [24, 25].

Such a small permeability is achieved by dense packing of GO nanosheets upon spin-coating under vacuum suction, and favors a high potential for application of both H-GO and B-GO films in membrane technologies for selective gas dehumidification (Fig. 3(a)). It should be noted that B-GO membrane has smaller gas permeability compared to H-GO which could be attributed to more perfect structure of B-GO with smaller number of defects which stays in line with the Raman spectroscopy data. The results on gas permeability stay in good agreement with literature data suggesting nearly barrier gas permeability which is typical for dense thin graphene oxide films [26].

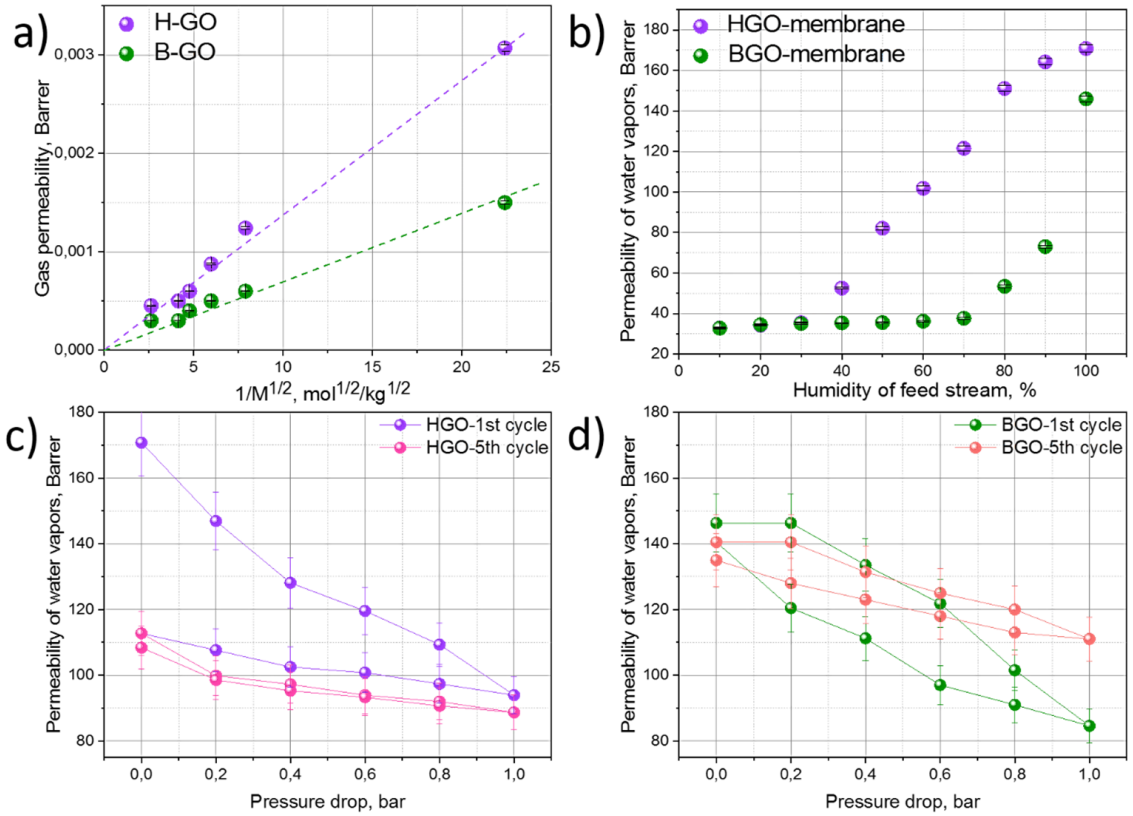

FIG. 3. Transport characteristics of composite membranes based on two types of graphene oxide: H-GO (Hummer' method) and B-GO (Brodie method): a) permeability of permanent gases: SF_6, C_4H_{10}, CO_2, N_2, CH_4, H_2; b) permeability of water vapors in the relative humidity range (RH) from 10 to 100 %; c), d) pressure stability of: c) H-GO and b) B-GO composite membranes in the range of pressure drop from 0 to 1 bar. The first and the fifth pressure cycle are shown

The H-GO and B-GO membranes exhibit relatively high water vapors permeability staying in the range of 30 – 170 Barrer depending on the humidity of the feed stream (Fig. 3(b)). It should be noted that in the low humidity range (up to 30 – 40 %), both H-GO and B-GO films have very close values of permeability, whereas, starting from humidity of 40 %, the permeability of H-GO begins to increase rapidly while the water vapor transport across B-GO remains small enough until the humidity of 80 % at which the B-GO permeability begins to increase sharply. The different shapes of water vapor permeability curves for H-GO and B-GO are evident and could arise from the difference in microstructure and chemical composition of the films. The high oxidation degree of H-GO and deep extent of oxidation (the high presence of C=O groups) favors the sorption and capillary condensation of water molecules in H-GO microstructure [22], thus, resulting in higher water vapor permeability in the humidity range of gas stream from 40 up to 100 %. In contrast, graphene oxide prepared by the Brodie method has greater C/O ratio with smaller amount of oxygen functional groups resulting in more rigid microstructure and lower water vapor permeability.

The prominent difference in the H-GO and B-GO membranes performance could be seen when the membranes are subjected to stepwise pressure cycling with pressure drops in the range from 0 to 1 bar (step of 0.2 bar) during water vapor permeability testing at 100 % humidity (Fig. 3(c,d)). During the first pressure cycle, the H-GO membrane loses up to 46 % of its original permeability, and, after pressure release, the membrane reveals an irreversible permeability decrease of ∼30 %. The observed strong decrease in membrane permeability could be attributed to highly-oxidized and soft nature of nanoflakes in H-GO membrane which tend to compaction under pressure elevation resulting in shrinking the pathways

for water molecules transport. Nearly the same trend is observed for the B-GO membrane, however, it has higher stability: after the pressure release, the membrane restores its permeability with the irreversible loss of only ∼4 % revealing more rigid and stable microstructure of the B-GO compared to H-GO membrane. During further pressure cycling, the H-GO and B-GO membranes reveal stabilization of water vapor permeability. Under the 5-th pressure cycle, both H-GO and B-GO membranes exhibit the dynamical pressure decrease of ∼20 % with irreversible pressure loss of ∼4 % showing some kind of a limit in structural compaction of GO (Fig. 3(c,d)). The same trend for gradual compaction and stabilization of microstructure was shown for the permeation of H-GO membranes towards liquid water in nanofiltration experiments [27]. It could be assumed, that the observed difference in pressure stability in H-GO and B-GO is encoded in their synthesis method which pre-determines the extent of graphite oxidizing and the resulting defect content and rigidity of GO nanoflakes. To achieve enhanced pressure stability of graphene oxide, its microstructure should be close to that of B-GO membranes but with higher content of basal hydroxyl and epoxy groups to provide higher water vapor permeability. Thus, for the design of pressure-stable and highly-permeable membranes, the protocol of GO synthesis should be reconsidered carefully to avoid strong over-oxidation and defects formation in GO samples. The obtained results show that it could be possible to achieve pressure-stable GO using only microstructure-composition interplay as is shown for the B-GO membrane. This route could be considered as an alternative to modification of GO with various pressure-resistant agents such as, for instance, carbon nitride layers [6] or single-walled carbon nanotubes [7] to avoid complication of GO preparation for industry.

It should be noted that the performance of GO membranes under pressure requires further in-depth experimental studying including in-situ and operando X-ray diffraction analysis of d-spacing changing during pressure cycling which requires more sophisticated equipment. At present, most of the studies report the liquid (or vapor) water permeability under the average feed stream pressures in the range of 1 [28] to 6 bar [29] and even up to 50 bar [30], whereas the size of d-spacing for GO membranes is commonly measured and presented for the pressure of 1 bar. As a result, it is hard to correlate the membrane performance with dynamical pathways for water molecules transport in GO microstructure.

4. Conclusions

Gas and vapor transport characteristics as well as the resistance towards pressure drops is studied comparatively for membranes based on graphene oxide synthesized by Hummers' (H-GO) and Brodie's (B-GO) methods. It is revealed that B-GO membrane exhibits stronger resistance towards elevated pressure owing to higher uniformness of its microstructure provided by more rigid, less defective and lower oxidized planar nanoflakes. To enhance the pressure stability of graphene oxide, a careful control of synthesis conditions is required to provide the balance between GO oxidation degree and the rigidity of its nanoflakes. Thus, it is possible to control the pressure resistance of GO by adjusting its composition-microstructure interplay which could be considered as an alternative approach rather than introducing additional pressure-stabilizing agents.

References

[1] Kim J.H. Grand Challenges in Membrane Applications—Gas and Vapor. *Frontiers in Membrane Science and Technology*, 2022, **1**.

[2] Alen S.K., Nam S., Dastgheib S.A. Recent Advances in Graphene Oxide Membranes for Gas Separation Applications. *Int. J. of Molecular Sciences*, 2019, **20** (22), 5609.

[3] Marcano D.C., Kosynkin D.V., Berlin J.M., Sinitskii A., Sun Z., Slesarev A., Alemany L.B., Lu W., Tour J.M. Improved Synthesis of Graphene Oxide. *ACS Nano*, 2010, **4** (8), P. 4806–4814.

[4] Dreyer D.R., Park S., Bielawski C.W., Ruoff R.S. The chemistry of graphene oxide. *Chem. Soc. Rev.*, 2010, **39** (1), P. 228–240.

[5] Wei N., Peng X. Xu Z. Understanding Water Permeation in Graphene Oxide Membranes. *ACS Applied Materials & Interfaces*, 2014, **6** (8), P. 5877–5883.

[6] Liu L., Zhou Y., Xue J., Wang H. Enhanced antipressure ability through graphene oxide membrane by intercalating g-C_3N_4 nanosheets for water purification. *AIChE J.*, 2019, **65**, (10), e16699.

[7] Han Y., Jiang Y., Gao C. High-Flux Graphene Oxide Nanofiltration Membrane Intercalated by Carbon Nanotubes. *ACS Applied Materials & Interfaces*, 2015, **7** (15), P. 8147–8155.

[8] Tang X., Qu Y., Deng S.-L., Tan Y.-Z., Zhang Q., Liu Q. Fullerene-regulated graphene oxide nanosheet membranes with well-defined laminar nanochannels for precise molecule sieving. *J. Mater. Chem. A*, 2018, **6** (45), P. 22590–22598.

[9] Li W., Zhang Y., Su P., Xu Z., Zhang G., Shen C., Meng Q. Metal–organic framework channelled graphene composite membranes for H_2/CO_2 separation. *J. Mater. Chem. A*, 2016, **4** (48), P. 18747–18752.

[10] Huang H., Song Z., Wei N., Shi L., Mao Y., Ying Y., Sun L., Xu Z., Peng X. Ultrafast viscous water flow through nanostrand-channelled graphene oxide membranes. *Nature Communications*, 2013, **4**, 2979.

[11] Yang R., Fan Y., Yu R., Dai F., Lan J., Wang Z., Chen J., Chen L. Robust reduced graphene oxide membranes with high water permeance enhanced by K+ modification. *J. of Membrane Science*, 2021, **635**, 119437.

[12] Brodie B.C. XIII. On the atomic weight of graphite. *Philosophical Transactions of the Royal Society of London*, 1859, **149**, P. 249–259.

[13] Staudenmaier L. Verfahren zur Darstellung der Graphitsäure. *Berichte der deutschen chemischen Gesellschaft*, 1898, **31** (2), P. 1481–1487.

[14] Hofmann U., König E. Untersuchungen über Graphitoxyd. *Zeitschrift für anorganische und allgemeine Chemie*, 1937, **234** (4), P. 311–336.

[15] Hummers W.S., Offeman R.E. Preparation of Graphitic Oxide. *J. of the American Chemical Society*, 1958, **80** (6), 1339.

[16] Yoo M.J., Park H.B. Effect of hydrogen peroxide on properties of graphene oxide in Hummers method. *Carbon*, 2019, **141**, P. 515–522.

[17] Talyzin A., Mercier G., Klechikov A., Hedenström M., Johnels D., Wei D., Cotton D., Opitz A., Moons E. Brodie vs Hummers graphite oxides for preparation of multi-layered materials. *Carbon*, 2017, **115**, P. 430–440.

[18] Ibrahim A.F.M., Banihashemi F., Lin Y.S. Graphene oxide membranes with narrow inter-sheet galleries for enhanced hydrogen separation. *Chemical Communications*, 2019, **55** (21), P. 3077–3080.
[19] Pedrosa M., Da Silva E.S., Pastrana-Martínez L.M., Drazic G., Falaras P., Faria J.L., Figueiredo J.L., Silva A.M.T. Hummers' and Brodie's graphene oxides as photocatalysts for phenol degradation. *J. of Colloid and Interface Science*, 2020, **567**, P. 243–255.
[20] Eckmann A., Felten A., Mishchenko A., Britnell L., Krupke R., Novoselov K.S., Casiraghi C. Probing the Nature of Defects in Graphene by Raman Spectroscopy. *Nano Letters*, 2012, **12** (8), P. 3925–3930.
[21] King A.A.K., Davies B.R., Noorbehesht N., Newman P., Church T.L., Harris A.T., Razal J.M., Minett A.I. A New Raman Metric for the Characterisation of Graphene oxide and its Derivatives. *Scientific Reports*, 2016, **6**, 19491.
[22] Chernova E.A., Petukhov D.I., Chumakov A.P., Kirianova A.V., Sadilov I.S., Kapitanova O.O., Boytsova O.V., Valeev R.G., Roth S.V., Eliseev Ar., Eliseev An. The role of oxidation level in mass-transport properties and dehumidification performance of graphene oxide membranes. *Carbon*, 2021, **183**, P. 404–414.
[23] Zhu Y., Murali S., Cai W., Li X., Suk J.W., Potts J.R., Ruoff R.S. Graphene and Graphene Oxide: Synthesis, Properties, and Applications. *Advanced Materials*, 2010, **22** (35), P. 3906–3924.
[24] Reinecke S.A., Sleep B.E. Knudsen diffusion, gas permeability, and water content in an unconsolidated porous medium. *Water Resources Research*, 2002, **38** (12), P. 15–16.
[25] Do D.D. Adsorption Analysis: Equilibria and Kinetics. In: *Series on Chemical Engineering*. Imperial College Press 1998, P. 892.
[26] Nair R.R., Wu H.A., Jayaram P.N., Grigorieva I.V., Geim A.K. Unimpeded Permeation of Water Through Helium-Leak–Tight Graphene-Based Membranes. *Science*, 2012, **335** (6067), P. 442–444.
[27] Chong J.Y., Wang B., Li K. Water transport through graphene oxide membranes: the roles of driving forces. *Chemical Communications*, 2018, **54** (20), P. 2554–2557.
[28] Zhang Z., Xiao X., Zhou Y., Huang L., Wang Y., Rong Q., Han Z., Qu H., Zhu Z., Xu S., Tang J., Chen J. Bioinspired Graphene Oxide Membranes with pH-Responsive Nanochannels for High-Performance Nanofiltration. *ACS Nano*, 2021, **15** (8), P. 13178–13187.
[29] Li Y., Zhao W., Weyland M., Yuan S., Xia Y., Liu H., Jian M., Yang J., Easton C.D., Selomulya C., Zhang X. Thermally Reduced Nanoporous Graphene Oxide Membrane for Desalination. *Environmental Science & Technology*, 2019, **53** (14), P. 8314–8323.
[30] Wang Z., Ma C., Xu C., Sinquefield S.A., Shofner M.L., Nair S. Graphene oxide nanofiltration membranes for desalination under realistic conditions. *Nature Sustainability*, 2021, **4** (5), P. 402–408.

Submitted 24 November 2022; revised 9 February 2023; accepted 1 April 2023

Information about the authors:

Ekaterina A. Chernova – Lomonosov Moscow State University, Faculty of Materials Science, 119991, Moscow, GSP-1, 1-73 Leninskiye Gory, Russia; Tula State University, 300012, Tula, Lenina avenue 92, Russia; ORCID 0000-0002-5812-9515; chernova.msu@gmail.com

Konstantin E. Gurianov – Lomonosov Moscow State University, Faculty of Materials Science, 119991, Moscow, GSP-1, 1-73 Leninskiye Gory, Russia; gurianovke@yandex.ru

Victor A. Brotsman – Lomonosov Moscow State University, Faculty of Chemistry, 119991, Moscow, GSP-1, 1-3 Leninskiye Gory, Russia; ORCID 0000-0002-8374-9265; brotsman_va@mail.ru

Rishat G. Valeev – Udmurt Federal Research Center of the Ural Brunch of Russian Academy of Sciences (UdmFRC of UB RAS), Izhevsk, st. them. Tatiana Baramzina 34, 426067, Russia; ORCID 0000-0001-8981-8527; rishatvaleev@mail.ru

Olesya O. Kapitanova – Lomonosov Moscow State University, Faculty of Chemistry, 119991, Moscow, GSP-1, 1-3 Leninskiye Gory, Russia; ORCID 0000-0002-7384-3426; olesya.kapitanova@gmail.com

Mikhail V. Berekchiian – Lomonosov Moscow State University, Faculty of Materials Science, 119991, Moscow, GSP-1, 1-73 Leninskiye Gory, Russia; mikhail.berekchiyan@yandex.ru

Alexei V. Lukashin – Lomonosov Moscow State University, Faculty of Materials Science, 119991, Moscow, GSP-1, 1-73 Leninskiye Gory, Russia; alexey.lukashin@gmail.com

Conflict of interest: all authors declare that they have no potential conflict of interests.

NANOSYSTEMS:
PHYSICS, CHEMISTRY, MATHEMATICS

Original article

Alexandrov A.A., et al. *Nanosystems: Phys. Chem. Math.*, 2023, **14** (2), 279–285.
http://nanojournal.ifmo.ru
DOI 10.17586/2220-8054-2023-14-2-279-285

Features of $Ca_{1-x}Y_xF_{2+x}$ solid solution heat capacity behavior: diffuse phase transition

Alexander A. Alexandrov[1,2,a], Anna D. Rezaeva[1,b], Vasilii A. Konyushkin[1,c], Andrey N. Nakladov[1,d], Sergey V. Kuznetsov[1,e], Pavel P. Fedorov[1,f]

[1]Prokhorov General Physics Institute of the Russian Academy of Sciences, Moscow Russia

[2]Kurnakov Institute of General and Inorganic Chemistry of the Russian Academy of Sciences, Moscow, Russia

[a]alexandrov1996@yandex.ru, [b]1032192969@rudn.ru, [c]vasil@lst.gpi.ru,
[d]andy-nak@yandex.ru, [e]kouznetzovsv@gmail.com, [f]ppfedorov@yandex.ru

Corresponding author: Pavel P. Fedorov, ppfedorov@yandex.ru

ABSTRACT A series of single crystals of a $Ca_{1-x}Y_xF_{2+x}$ solid solution with a fluorite structure containing 1–19 mol.% YF_3 (x =0.01–0.19) has been grown. Thermal analyzer STA 449 F3 Jupiter in DSC mode recorded the temperature dependences of the heat capacity C_p(T) in the temperature range from the room temperature to 1300 °C. A diffuse phase transition in the solid state for concentrations x =0.01–0.03 is fixed as an anomaly on the C_p(T) curves with a maximum at 1150 ± 50 °C. With an increase in the content of YF_3 (x =0.05–0.19), a very wide structured peak is recorded in the range of 650–1100 °C. The heat capacity anomaly is associated with the reversible rearrangement of defect nanoclusters, which affects the change in the anion sublattice.

KEYWORDS CaF_2–YF_3 phase diagram, inorganic fluorides, fluorite, diffuse phase transition, solid solution, heterovalent isomorphism, defect clusters.

ACKNOWLEDGEMENTS Authors express their sincere gratitude to E. V. Chernova for her most kind assistance in the preparation of the present manuscript. The study was funded by grant of Russian Science Foundation No. 22-13-00167, https://rscf.ru/project/22-13-00167.

FOR CITATION Alexandrov A.A., Rezaeva A.D., Konyushkin V.A., Nakladov A.N., Kuznetsov S.V., Fedorov P.P. Features of $Ca_{1-x}Y_xF_{2+x}$ solid solution heat capacity behavior: diffuse phase transition. *Nanosystems: Phys. Chem. Math.*, 2023, **14** (2), 279–285.

1. Introduction

Compounds with the fluorite-type crystal structure ($Fm\bar{3}m$ space symmetry group) include MF_2 difluorides (M = Ca, Sr, Ba, Cd, higher temperature polymorph of PbF_2) as well as $SrCl_2$, UO_2 and CeO_2. At T∼(0.7–0.8)*$T_{melting}$, all these substances exhibit the very specific anomaly in their physical properties that has been named as diffuse phase transition [1–14]. The term "Faraday transition" has been also suggested for such a phenomenon because it has been described for PbF_2 by Michael Faraday in 1834 [9]. Experimental data for the heat capacity, thermal expansion, ionic conductivity, elastic constants and other physical properties, including neutron scattering and Brillouin scattering patterns of the aforementioned substances, confirm the said anomaly. The mechanism of the diffuse phase transition is well-known, and it is described in terms of the interaction between point anti-Frenkel anionic defects [5, 10] and soft phonon modes [12]. The concentration of the latter defects increases with the temperature increase, resulting in cooperative interaction between the individual defects and disordering of the anionic sublattice ("sublattice melting"). The high-temperature form of fluorite MX_2 compounds is characterized by formation of complex short-living defect clusters containing an excess of interstitial anions, anionic vacancies and relaxed lattice anions [7, 11]. The diffuse phase transition is accompanied by an increase in the anionic conductivity and transition of MF_2 to the superionic state [6].

Thoroughly conducted thermochemical experiments [1, 4] and simulations [5, 12–14] indicate that, for all diffuse phase transitions, one have only observed an anomaly in the heat capacities as relatively wide (half-width about 200 K) maxima in the curves describing the temperature dependences of the C_p(T) values, while there were no thermal analysis data confirming the existence of the first- or second order phase transitions, or effects indicating non-zero enthalpies of the said first order phase transitions [10]. Thorough measurements of the thermal expansion coefficients for the specimens in the fluorite-type compounds [8] also have revealed the similar anomalies for the temperature dependences of the said coefficients.

The above said CaF_2 heat capacity maximum [1] indicates only that the thermodynamic stability of the corresponding system goes through its minimum. This situation can be characterized as the "flag of catastrophe" from the catastrophe theory [15] point of view, and the said diffuse phase transition is not a real first or second order phase transition from the thermodynamic point of view: the same phase of the same space symmetry group just maintains its existence.

In binary systems involving components undergoing a diffuse phase transition, there are anomalies on the curve of the maximum concentration of solid solution (solvus). In many systems, solvus curves have an abnormal S-type shape. Such curve shape is caused by the factor that the higher temperature disordered form of fluorites is more prone to the heterovalent isomorphism than the lower temperature forms [16]. For example, a clearly expressed S-type solvus curve exists in the CaF_2-LaF_3 [17] and SrF_2-LaF_3 [18] systems. A very complex profile of the solidus curve for the CaF_2-based solid solution has been observed in the NaF-CaF_2 system [19].

The division of the fluorite-type region of solid solutions in binary systems into high-temperature and low-temperature regions suggests that the temperature band of the diffuse phase transition should go to the low-temperature region when the matrix is doped with an isomorphic component. This assumption, put forward in [16], was confirmed both in thermodynamic modeling and in separate measurements of some physical properties, including ionic conductivity [10, 20–22]. However, this hypothesis has not been systematically tested before.

The purpose of this work is to test the behavior of the diffuse phase transition in calcium fluoride when the CaF_2 matrix is doped with yttrium fluoride. The CaF_2-YF_3 system is a classical system, which is used as an example for illustration of the mechanism of heterovalent isomorphism, in particular, the formation of the mineral yttrofluorite [23,24]. This is a model system describing the behavior of other rare-earth fluorides of the yttrium subgroup. The phase diagram of CaF_2–YF_3 systems has been carefully studied [25–29], see Fig. 1 [30, 31]. A fluorite solid solution $Ca_{1-x}Y_xF_{2+x}$ (phase F), a series of ordered low-temperature fluorite-like phases, and a high-temperature non-stoichiometric phase with a tysonite structure (phase T) are formed in the system. The maximum on the melting curve of the $Ca_{1-x}Y_xF_{2+x}$ fluorite solid solution at $x = 0.11$ (11 mol.% YF_3) is the source of functional optical single-crystal materials [32, 33].

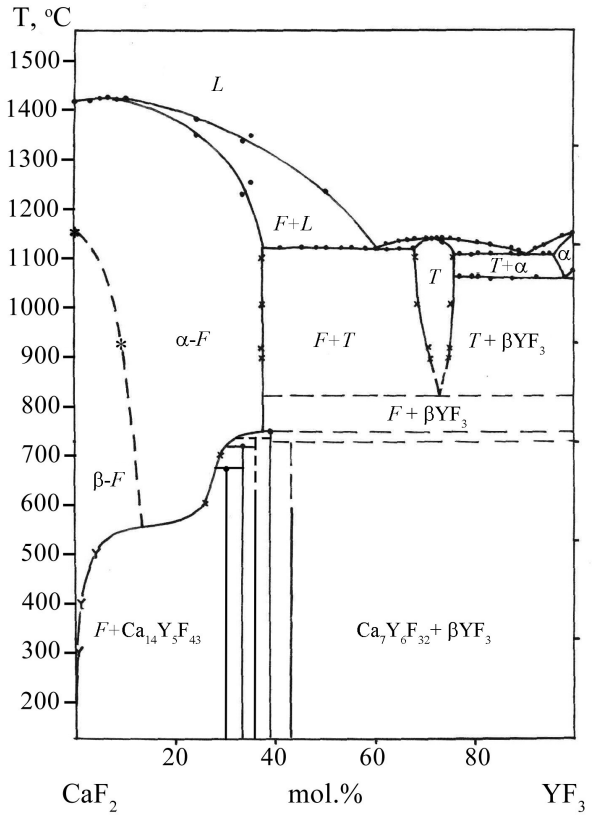

FIG. 1. Phase diagrams of the CaF_2-YF_3 systems [30,31]

The dotted line dividing the $Ca_{1-x}Y_xF_{2+x}$ solid solution field (phase F) into two parts (α and β) in Fig. 1 reflects the ideas concerning to the behavior of the diffuse phase transition with the change of concentration that took place before our work began.

2. Experimental

CaF_2 (optical crystals shards, State Optical Institute, St.-Petersburg) and YF_3 (99.99 wt%, LANHIT, Moscow) were used as the starting reagents.

$Ca_{1-x}Y_xF_{2+x}$ single crystals, where $x = 0$, 0.01, 0.03, 0.05, 0.07, 0.10, 0.12, 0.15 (nominal compositions), 10 mm in diameter, 45 mm long, were grown by the Bridgman-Stockbarger technique (Fig. 2). A portion of the initial mixture was loaded into a seven-channel graphite crucible and placed in a growth setup. The growth chamber was preliminarily

TABLE 1. Characteristics of the studied samples of the $Ca_{1-x}Y_xF_{2+x}$ single crystals

Number	Nominal composition, mol% YF_3	Lattice parameter a, Å	EDX data, mol% YF_3
1	1.0	5.4664	1.2
2	3.0	5.4686	2.9
3	5.0	5.4732	5.6
4	7.0	5.4786	7.6
5	10.0	5.4834	12.4
6	12.0	5.4893	14.0
7	15.0	5.4976	19.2

evacuated to 10^{-2} Torr. The crucible was heated to the charge melting temperature of 1440 °C. The melt was fluorinated by CF_4 and then crucible pulled into the cold zone at a rate of 5 mm/h. After growth, the crystals were removed from the crucible and purified of graphite by mechanical treatment and ethanol. A plate with a diameter of 10 mm and a thickness of l mm was cut from the crystal, which was then ground in a jasper mortar. The grown $Ca_{1-x}Y_xF_{2+x}$ crystals did not have a characteristic optical heterogeneity – a cellular substructure [34].

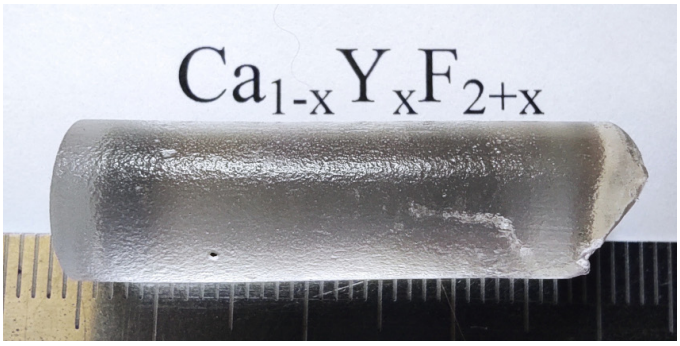

FIG. 2. $Ca_{1-x}Y_xF_{2+x}$ single crystal (sample number 6, $x = 0.14$)

X-ray phase analysis was performed on a Bruker D8 Advance diffractometer (Germany) with CuKα radiation in the angle range from 15 to 80 ° 2Θ with a step of 0.02 ° and a signal accumulation time of 0.4 s per point. Elemental analysis was performed on a Carl Zeiss NVision 40 microscope with an Oxford Instruments X-MAX 80 mm^2 attachment on powder samples with the accumulation of several spectra for statistical significance.

The samples were measured on a STA 449 F3 Jupiter synchronous thermal analysis instrument using a Type S DSC sensor and platinum-rhodium crucibles. The heating rate was 20 °C/min. The weighed portions of the powders (20–50 mg) were placed in Pt–Rh crucibles and covered with a lid. The reference crucible remained empty in all dimensions. The argon flow into the furnace chamber was 70 ml/min. The maximum temperature was 1330 °C. A sapphire standard 5.2 mm in diameter and 0.25 mm thick was used as a reference.

The heat capacity was calculated using formula (1):

$$C_p = \frac{m_{Standart}}{m_{Sample}} \cdot \frac{DSC_{Sample} - DSC_{Baseline}}{DSC_{Standart} - DSC_{Baseline}} \cdot C_{p,Standart}, \quad (1)$$

by software Netzsch Proteus Thermal Analysis with using ASTM E 1257, ISO 11357-4, DIN 51007 standards.

3. Results and discussion

The lattice parameters and compositions evaluated by EDX for samples are summarized in Table 1. The temperature dependences of the specific heat capacity are shown in Fig. 3.

When evaluating the measurement results (Fig. 3), it should be noted that the absolute values of the heat capacity cannot be trusted, except for the low-temperature (up to 800 °C) range for pure CaF_2 (Fig. 3a). In all other cases, the measurements obtained during the second and third heatings differ sharply in magnitude. The reasons for this are not entirely clear. They can be associated both with a change in the degree of compactness of the powder (sintering) and with the partial preservation of the high-temperature defective structure of the sample after heat treatment. However, some characteristic features of the observed anomaly on the C_p(T) curves remain, which will be the subject of analysis.

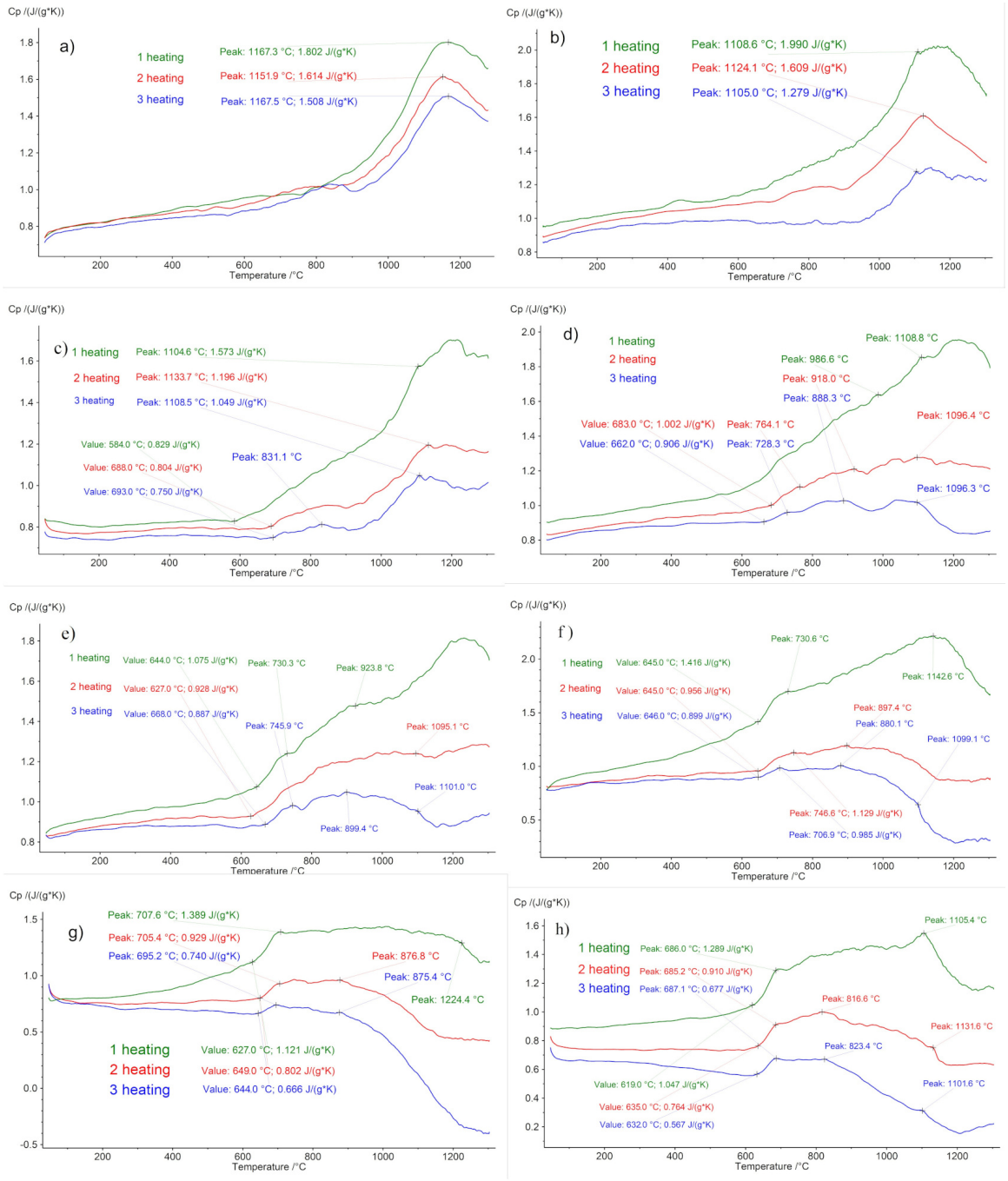

FIG. 3. Temperature dependences of the specific heat capacity. Nominal composition: a – CaF_2, b – sample number 1, c – sample number 2, d – sample number 3, e – sample number 4, f – sample number 5, g – sample number 6, h – sample number 7

For pure calcium fluoride (Fig. 3a), the maximum temperature of the C_p(T) curve corresponds to the results of Naylor [1]. At a low impurity content (∼1 mol % YF_3), the character of the dependence changes slightly, although the specific heat capacity peak is somewhat broadened (Fig. 3b). In this case, the beginning of the effects cannot be distinguished.

With an increase in the content of yttrium fluoride, the nature of the temperature dependencies of the specific heat capacity changes significantly. A low temperature component appears, a pronounced onset of the effects is formed, the specific heat capacity anomaly is structured, and starting from 10 mol.% YF_3, three extrema can be clearly distinguished on it (Fig. 3(f–h)). With a change in the concentration of yttrium fluoride, the temperatures of these effects change slightly, staying within 600–1150 °C (Fig. 4). This behavior differs sharply from the initial expectation of a monotonic decrease in the maximum at the specific heat capacity anomaly with increasing temperature.

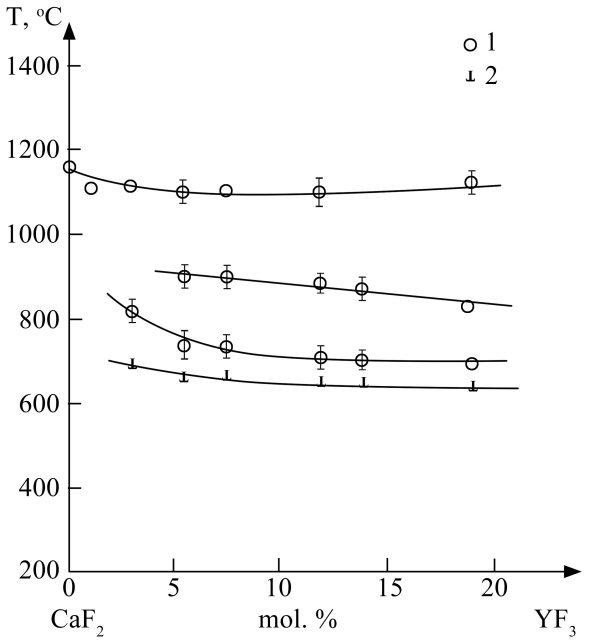

FIG. 4. Temperatures of heat capacity anomalies in $Ca_{1-x}Y_xF_{2+x}$ single crystals. 1 – peak position, 2 – onset. Lines are guides to the eyes

Apparently, the observed effects can be associated with the rearrangement of defect clusters. Since these effects are at least partially reversible upon heating-cooling, it can be concluded that the rearrangement is mainly associated with changes in the anionic sublattice.

Usually, when discussing the cluster structure of defects in heterovalent solid solutions, rearrangements with increasing concentration are considered, leaving aside the effect of temperature [35]. One of few exceptions is the work of Osiko [36].

Structural investigations of $Ca_{1-x}Y_xF_{2+x}$ solid solution and analogues systems were objects of numerous works. The complexity of the cluster structures has been revealed by X-ray diffraction, spin resonance, spectroscopic, extended X-ray-absorption fine structure (EXAFS), MNR ^{19}F and computer simulation techniques [37–44]. Dipoles Y^{3+}–F^-_{int}, formed at a low content of YF_3 in the solid solution, rapidly undergo further association with increasing concentration. Dimers $(Y^{3+}–F^-_{int})_2$ [36] transform into so-called 2:2:2 clusters due to the relaxation of the anionic sublattice [39]. To describe the structure formed at a high concentration of yttrium fluoride, very exotic models were initially proposed [38], which were replaced by the Y_6F_{37} cubooctahedral cluster [41, 45–47]. The size of such clusters with their defective periphery is about 1.5 nm. It is these clusters that form the basis of ordered fluorite-like phases in the CaF_2-YF_3 system.

The presence of a dominant type of clusters does not exclude the existence of a wide range of clusters in crystals. The set of coordination polyhedra of rare-earth elements in solid solutions leads to a broadening of the luminescence spectra with transition to the disordered structure, see, for example, [48].

Clustering causes an increase in electrical conductivity with concentration [49, 50]. The composition containing $\sim$3 mol.% YF_3 approximately corresponds to the so-called percolation threshold, i.e. association of clusters (their defective periphery) into a single network in the bulk of the crystal [49].

As for high-temperature studies, the study of Catlow e.a [42] of a similar system $Ca_{0.9}Er_{0.1}F_{2.1}$ by the EXAFS method in the range of 298–1070 K did not record noticeable changes. In the context of this work, the investigation by Hoffmann et al. [43] devoted to the study of the crystal structure of $Ca_{0.94}Y_{0.06}F_{2.06}$ at different temperatures up to 1400 K is of particular importance. Hoffmann et.al., using the neutron diffraction technique, recorded the destruction of cubooctahedral Y_6F_{37} cluster starting from $\sim$630 °C and their complete disappearance at $\sim$900 °C.

4. Conclusions

In this paper, new and unexpected data were obtained concerning the manifestations of a diffuse phase transition in a heterovalent $Ca_{1-x}Y_xF_{2+x}$ solid solution with a fluorite structure. The obtained data indicate the rearrangement of defect nanoclusters not only with concentration, but also with temperature. The relevant instructions open up a new way to control the functional properties of materials based on the corresponding solid solutions. Of paramount interest are both studies of this phenomenon by a complex of structural and physicochemical methods, and a detailed study of similar systems. An interesting and promising problem is the possible implementation of diffuse phase transitions in high-temperature cubic polymorphs of ZrO_2 and HfO_2 and solid solutions based on them.

References

[1] Naylor B.F. Heat contents at high temperatures of magnesium and calcium fluorides. *J. Amer. Chem. Soc.*, 1945, **67**, P. 150–152.

[2] Bredig M.A. The order-disorder (l) transition in UO_2 and other solids of the fluorite type of structure. *Colloq. Inter. CNRS*, 1972, **205**, P. 183–197.

[3] Catlow C.R.A., Comings J.D., Germano F.A., Harley R.T. Hayes W. Brillouin scattering and theoretical studies of high-temperature disorder in fluorite crystals. *J. Phys. C: Solid State Phys.*, 1978, **11**, P. 3197–3212.

[4] Schröter W., Nölting J. Specific heats of crystals with the fluorite structure. *J. Phys. Coll. (Paris)*, 1980, **41**, P. 6–20.

[5] Oberschmidt J. Simple thermodynamic model for the specific-heat anomaly and several other properties of crystals with the fluorite structure. *Phys. Rev. B*, 1981, **23**, P. 5038–5047.

[6] Chadwick A.V. High-temperature transport in fluorites. *Solis State Ionics*, 1983, **8**, P. 209–220.

[7] Hutchings M.T., Clausen K., Dickens M.H., Hayes W., Kjems J.K., Schnabel P.G., Smith C. Investigation of thermally induced anion disorder in fluorites using neutron scattering techniques. *J. Phys.* C, 1984, **17**, P. 3903–3940.

[8] Roberts R.B., White G.K. Thermal expansion of fluorites at high temperatures. *J. Phys. C*, 1986, **19**, P. 7167–7172.

[9] Hull S. Superionics: crystal structures and conduction processes. *Rep. Prog. Phys.* 2004, **67**, P. 1233–1314.

[10] Vlieg E., den Hartog H.W. The superionic phase transition of fluorite-type crystals. *J. Phys. Chem. Solids*, 1986, **47**(5), P. 521–528.

[11] Allnatt A.R., Chadwick A.V., Jacobs P.W.M. A model for the onset of fast-ion conduction in fluorites. *Proc. R. Soc. London A*, 1987, **410**, P. 385–408.

[12] Schmalzl K., Strauch D., Schober H. Lattice-dynamical and groud-state properties of CaF_2 studied by inelastic neutron scattering and density-functional methods. *Phys. Rev. B*, 2003, **68**, P. 144301–144313.

[13] Eapen J., Annamareddy A. Entropic crossovers in superionic fluorites from specific heat. *Ionics*, 2017, **23**, P. 1043–1047.

[14] Fossati P.C.M., Chartier A., Boulle A. Structural aspects of the superionic transition in AX_2 compounds with the fluorite structure. *Frontiers in Chemistry*, 2021, **9**, # 723507 (19 pp.)

[15] Gilmore R. *Catastrophe Theory for Scientists and Engineers*. New York, Dover, 1993.

[16] Fedorov P.P., Sobolev B.P. Phase diagrams of the CaF_2-(Y,Ln) F_3 systems. II. A discussion. *J. Less-Common Metals*, 1979, **63**, P. 31–44.

[17] Svantner M., Mariani E., Fedorov P.P., Sobolev B.P. Solid solution with fluorite structure in the CaF_2–LaF_3 system. *Kristall und Technik-Crystal Research and Technology*, 1979, **14**(3), P. 365–369.

[18] Fedorov P.P., Alexandrov A.A., Voronov V.V., Mayakova M.N., Baranchikov A.E., Ivanov V.K. Low-temperature phase formation in the SrF_2–LaF_3 system. *J. Amer. Ceram. Soc.*, 2021, **104**(6), P. 2836–2848.

[19] Fedorov P.P., Maykova M.N., Kuznetsov S.V., Maslov V.A., Sorokin N.I., Baranchikov A.E., Ivanov V.K., Pynenkov A.A., Uslamina M.A., Nishchev K.N. Phase Diagram of the NaF–CaF_2 System and the Electrical Conductivity of a CaF_2-Based Solid Solution. *Russ. J. Inorg. Chem.*, 2016, **61**(11), P. 1472–1478.

[20] Catlow C.R.A., Comins J.D., Germano F.A., Harley R.T. Hayes W., Owen I.B. Studies of effects of trivalent impurity ions on the transition to the superionic state of fluorites. *J. Phys. C: Solid State Phys.*, 1981, **14**, P. 329–335.

[21] Andersen N.H., Clausen K., Kjems J.K. Heavily doped $M_{1-x}U_xF_{2+2x}$ fluorites studied by quasielastic neutron scattering (M = Ba) and specific heat measurements (M = Pb). *Solid State Ionics*, 1983, **9–10**, P. 543–548.

[22] Ouwerkerk M., Kelder E.M., Schoonman J. Conductivity and specific heat of fluorites $M_{1-x}U_xF_{2+2x}$ (M = Ca, Sr, Ba and Pb). *Solid State Ionics*, 1983, **9–10**, P. 531–536.

[23] Bokii G.B. *Kristallokhimiya (Crystal Chemistry)*. M.: Nauka, 1971. (in Russian)

[24] Filatov S.K., Krivovichev S.V., Bubnova R.S. *Obschaya kristallokhimiya (General Crystal Chemistry)*. S.-Peterburg: Izd. SPbGU, 2018. (in Russian)

[25] Seiranian K.B., Fedorov P.P., Garashina L.S., Molev G.V., Karelin V.V., Sobolev B.P. Phase diagram of the system CaF_2–YF_3. *J. Crystal Growth*, 1974, **26**(1), P. 61–64.

[26] Fedorov P.P., Izotova O.E., Alexandrov V.B., Sobolev B.P. New phases with fluorite-derived structure in CaF_2–(Y, Ln)F_3 systems. *J. Solid State Chem.*, 1974, **9**(4), P. 368–374.

[27] Gettmann W., Greis O. Uber fluorit- und tysonitverwandte ordnungsphasen im system CaF_2–YF_3. *J. Solid State Chem.*, 1978, **26**(3), P. 255–263.

[28] Greis O., Haschke J.M. *Rare Earth Fluorides. Handbook on the Physics and Chemistry of Rare Earth*. Ed. K.A. Gscheidner & L. Eyring. Amsterdam, New York, Oxford. 1982, **5**, Ch. 45, P. 387–460.

[29] Sobolev B.P., Fedorov P.P. Phase diagramms of the CaF_2–(Y,Ln)F_3 systems. I. Experimental. *J. Less-Common Metals*, 1978, **60**, P. 33–46.

[30] Fedorov P.P. Third law of thermodynamics as applied to phase diagrams. *Rus. J. Inorg. Chem.*, 2010, **55**(11), P. 1722–1739.

[31] Fedorov P.P., Chernova E.V. Interactions of Yttrium and Lanthanum Fluorides with Other Fluorides. *J. Fluorine Chem.*, 2022, **263**, #110031 (9 pp.).

[32] Fedorov P.P. *Investigation of phase diagrams of the CaF_2-(Y,Ln)F_3 systems and polymorphism of rare earth trifluorides*. Thesis. M.: 1977. (in Russian)

[33] Sobolev B.P. *The Rare Earth Trifluorides. P.2. Introduction to Materials Science of Multicomponent Metal Fluoride Crystals*. Barcelona, Institut d'Estudis Catalans, 2001.

[34] Kuznetsov S.V., Fedorov P.P. Morphological Stability of Solid-Liquid Interface during Melt Crystallization of Solid Solutions $M_{1-x}R_xF_{2+x}$. *Inorg. Mater.*, 2008, **44**(13), P. 1434–1458. (Supplement).

[35] Fedorov P.P. Association of point defects in non stoichiometric $M_{1-x}R_xF_{2+x}$ fluorite-type solid solutions. *Butll. Soc. Cat. Cien.*, 1991, **12**(2), P. 349–381.

[36] Osiko V.V., Prokhorov A.M. *Investigation of the structure of crystals with an admixture of rare earth elements by spectroscopic methods. In: Problems of modern crystallography*. M.: Nauka, 1975, P. 280–301.

[37] Cheetham A.K., Fender B.E.F., Steele D., Taylor R.I., Willis B.T.M. Defect structure of fluorite compounds containing excess anions. *Solid State Comm.*, 1970, **8**, P. 171–173.

[38] Cheetham A.K., Fender B.E.F., Cooper M.J. Defect structure of calcium fluoride containing excess anions: Bragg scattering. *J. Phys. C.: Solid State Phys.*, 1971, **4**, P. 3107–3121.

[39] Allnatt A.R., Yuen P.S. Defect interactions in ionic fluorite structures: Pair clusters in CaF_2 doped by YF_3. *J. Phys. C.: Solid State Phys.*, 1975, **8**, P. 2199–2212.

[40] Jacobs P.W.M., Ong S.H. Studies of defect clustering in CaF_2:Y^{3+} by ionic conductivity and thermal depolarization. *J. Phys. Chem. Sol.*, 1980, **41**, P. 431–436.

[41] Laval J.P., Frit B. Defect structure of anion-excess fluorite-related $Ca_{1-x}Y_xF_{2+x}$ solid solutions *J. Solid State Chem.*, 1983, **49**, P. 237–246.

[42] Catlow C.R.A., Chadwick A.V., Corish J., Moroney L.M., O'Reilly A.N. Defect structure of doped CaF_2 at high temperatures. *Phys. Rev. B*, 1989, **39**(3), P. 1897–1906.

[43] Hofmann M., Hull S., Mclntyre G.J., Wilson C.C. A neutron diffraction study of the superionic transition in $(Ca_{1-x}Y_x)F_{2+x}$. *J. Phys.: Condens. Matter.*, 1997, **9**, P. 845–857.

[44] Wang F., Grey C.P. Probing the defect structure of anion-excess $Ca_{1-x}Y_xF_{2+x}$ (x =0.03–0.32) with high-resolution 19F magic-angle spinning nuclear magnetic resonance spectroscopy. *Chem. Mater.*, 1998, **10**, P. 3081–3091.

[45] Bevan D.J.M., Greis O., Strahle J. A new structural principle in anion-excess fluorite-related superlattices. *Acta Cryst.*, 1980, **36**(6), P. 889–890.

[46] Bendall P.J., Catlow C.R.A., Corish J., Jacobs P.W.M. Jacobs. Defect aggregation in anion-excess fluorites. II. Clusters containing more than two impurity atoms. *J. Solid State Chem.*, 1984, **51**, P. 159–169.

[47] Kazanskii S.A., Ryskin A.I., Nikiforov A.E., Zaharov A.Yu., Ougrumov M.Yu., Shakurov G.S. EPR spectra and crystal field of hexamer rare-earth clusters in fluorites. *Phys. Rev. B*, 2005, **72**, #014127 (11 pp).

[48] Bagdasarov Kh. S., Voronko Yu.K., Kaminskii A.A., Krotova L.V., Osiko V.V. Modification of the optical properties of $CaF_2^-TR^{3+}$ crystals by yttrium impurities. *Phys. stat. sol.*, 1965, **12**, P. 905–912.

[49] Ivanov-Shits A.K., Sorokin N.I., Fedorov P.P., Sobolev B.P. Specific features of ionic transport in nonstoichiometric fluorite-type $Ca_{1-x}R_xF_{2+x}$ (R = La-Lu, Y, Sc) phases. *Solid State Ionics*, 1990, **37**, P. 125–137.

[50] Sobolev B.P., Sorokin N.I., Bolotina N.B. Nonstoichiometric single crystals $M_{1-x}R_xF_{2+x}$ and $R_{1-y}M_yF_{3-y}$ (M = Ca, Sr, Ba, R – rare earth elements) as fluorine-ionic conductive solid electrolytes. *In: Photonic and electronic properties of fluoride materials*. Ed. A. Tressaud, K. Poeppelmeier. Amsterdam: Elsevier, 2016, P. 465–491.

Submitted 27 January 2023; revised 20 February 2023; accepted 27 March 2023

Information about the authors:

Alexander A. Alexandrov – Prokhorov General Physics Institute of the Russian Academy of Sciences, Vavilova str., 38, Moscow 119991, Russia; Kurnakov Institute of General and Inorganic Chemistry of the Russian Academy of Sciences, Leninskii pr. 31, Moscow, 119991, Russia; ORCID 0000-0001-7874-7284; alexandrov1996@yandex.ru

Anna D. Rezaeva – Prokhorov General Physics Institute of the Russian Academy of Sciences, Vavilova str., 38, Moscow 119991, Russia; ORCID 0000-0009-0005-9050-0184; 1032192969@rudn.ru

Vasilii A. Konyushkin – Prokhorov General Physics Institute of the Russian Academy of Sciences, Vavilova str., 38, Moscow 119991, Russia; ORCID 0000-0002-6028-8937; vasil@lst.gpi.ru

Andrey N. Nakladov – Prokhorov General Physics Institute of the Russian Academy of Sciences, Vavilova str., 38, Moscow 119991, Russia; ORCID 0000-0002-4060-8091; andy-nak@yandex.ru

Sergey V. Kuznetsov – Prokhorov General Physics Institute of the Russian Academy of Sciences, Vavilova str., 38, Moscow 119991, Russia; ORCID 0000-0002-7669-1106; kouznetzovsv@gmail.com

Pavel P. Fedorov – Prokhorov General Physics Institute of the Russian Academy of Sciences, Vavilova str., 38, Moscow 119991, Russia; ORCID 0000-0002-2918-3926; ppfedorov@yandex.ru

Conflict of interest: the authors declare no conflict of interest.

NANOSYSTEMS:
PHYSICS, CHEMISTRY, MATHEMATICS

Vasil'ev B.V., et al. *Nanosystems: Phys. Chem. Math.*, 2023, **14** (2), 286–287.
http://nanojournal.ifmo.ru
DOI 10.17586/2220-8054-2023-14-2-286-287

Corrigendum

Correction to the paper "Synthesis and magnetic properties of cobalt ferrite nanoparticles formed under hydro and solvothermal condition"

Boris V. Vasil'ev[1,2,a], Ruslan Yu. Smyslov[1,b], Demid A. Kirilenko[3,4,c], Ilya S. Kritchenkov[5,d], Alexander N. Bugrov[1,2,e],

[1]Institute of Macromolecular Compounds RAS, St. Petersburg, Russia
[2]St. Petersburg Electrotechnical University "LETI", St. Petersburg, Russia
[3]Ioffe Institute RAS, St. Petersburg, Russia
[4]ITMO University, St. Petersburg, Russia
[5]St. Petersburg State University, St. Petersburg, Russia

[a]boris8152@gmail.com, [b]urs@macro.ru, [c]demid.kirilenko@mail.ioffe.ru, [d]i.s.kritchenkov@spbu.ru, [e]alexander.n.bugrov@gmail.com

Corresponding author: Alexander N. Bugrov, alexander.n.bugrov@gmail.com

PACS 75.20.-g; 75.75.+a

ABSTRACT This paper is a corrigendum related to the article Vasil'ev B.V., Smyslov R.Yu., Kirilenko D.A., Bugrov A.N. Synthesis and magnetic properties of cobalt ferrite nanoparticles formed under hydro and solvothermal condition. *Nanosystems: Phys. Chem. Math.*, 2021, **12** (4), P. 492–504, http://nanojournal.ifmo.ru/en/articles-2/volume12/12-4/chemistry/paper11/

KEYWORDS single-domain cobalt ferrite, ferrimagnetic nanocrystals, size-controlled synthesis, stoichiometry, Rietveld refinement, coercive field, saturation magnetization, squareness

FOR CITATION Vasil'ev B.V., Smyslov R.Yu., Kirilenko D.A., Kritchenkov I.S., Bugrov A.N. Correction to the paper "Synthesis and magnetic properties of cobalt ferrite nanoparticles formed under hydro and solvothermal condition". *Nanosystems: Phys. Chem. Math.*, 2023, **14** (2), 286–287.

In the paper [1], Fig. 3 contains a graphic misprint. The correct part (b) in this figure is given below.

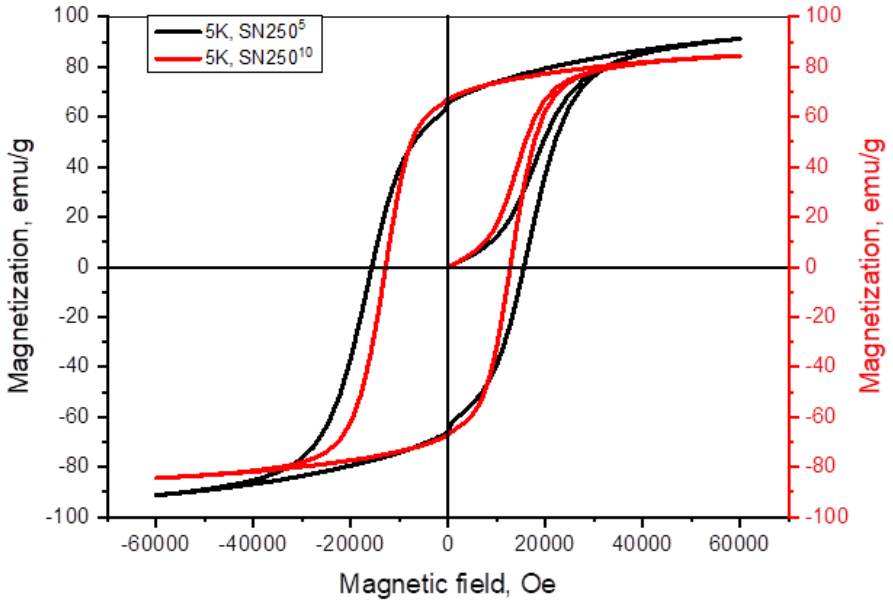

FIG. 1. The low-temperature magnetic hysteresis (M–H) loops for $Co_xFe_{3-x}O_4$ nanoparticles synthesized under solvo- (a,b) and hydrothermal conditions (c)

In connection with the correction of Fig. 3(b) [1], it is necessary to correct a paragraph on p. 497. Now it should read like this:

Studies of the synthesized cobalt ferrite nanoparticles using SQUID magnetometry showed that their magnetization curves have hysteresis loops regardless of the type of precursor used, as well as the chosen conditions of hydrolysis and dehydration (Fig. 3, Table 3). It should also be noted that "constricted" hysteresis loops were recorded for cobalt ferrite nanoparticles obtained under hydrothermal conditions or in an organic solvent at temperatures of 150 and 200 °C (Fig. 3), which are typical for a mixture of soft and hard magnetic materials [1, 29, 30]. In this case, such a "necking" in the central part of the M–H loop can be explained by a small amount of superparamagnetic single-domain particles in ferrimagnetic $Co_xFe_{3-x}O_4$ nanocrystals.

In Table 3 on Page 502 [1], the row titled "SN250^5" should be now written as:

SN250^5	0.72	65.7	91	15700	0.09	7	77	245	0	0	65	0

In ACKNOWLEDGMENTS, some information was omitted by the authors. Therefore, the correct version of the acknowledgments is given below.

Acknowledgments

X-ray diffraction experiments were performed on the Engineering Center equipment of the St. Petersburg State Technological Institute (Technical University). TEM studies were carried out in the Federal Joint Research Center "Material science and characterization in advanced technology" funded by the Ministry of Education and Science of the Russian Federation. We appreciate Evgeniy V. Shevchenko from the Centre for Diagnostics of Functional Materials for Medicine, Pharmacology and Nanoelectronics (SPbU Research Park) for finding the discrepancy in the data obtained by measuring the magnetic characteristics of the ferrites by SQUID magnetometry. We give special thanks to Alexandr S. Sakhatskiy from the latter Research Park for measuring our systems using a SQUID magnetometer.

References

[1] Vasil'ev B.V., Smyslov R.Yu., Kirilenko D.A., Bugrov A.N. Synthesis and magnetic properties of cobalt ferrite nanoparticles formed under hydro and solvothermal condition. *Nanosystems: Phys. Chem. Math.*, 2021, **12** (4), P. 492–504.

Submitted 6 March 2023; accepted 6 March 2023

Information about the authors:

Boris V. Vasil'ev – Institute of Macromolecular Compounds RAS, Bolshoy pr. 31, 199004 Saint Petersburg, Russia; Saint Petersburg Electrotechnical University "LETI", ul. Professora Popova 5, 197022 Saint Petersburg, Russia; ORCID 0000-0002-9315-7087; boris8152@gmail.com

Ruslan Yu. Smyslov – Institute of Macromolecular Compounds RAS, Bolshoy pr. 31, 199004 Saint Petersburg, Russia; ORCID 0000-0003-3633-4347; urs@macro.ru

Demid A. Kirilenko – Ioffe Institute RAS, Politekhnicheskaya ul. 26, 194021 Saint Petersburg, Russia; ITMO University, Kronverskii avenue 49, 197101 Saint Petersburg, Russia; ORCID 0000-0002-1571-209X; demid.kirilenko@mail.ioffe.ru

Ilya S. Kritchenkov – Saint Petersburg State University, University emb., 7–9, Saint Petersburg, 191034, Russia; ORCID 0000-0003-0108-0690; i.s.kritchenkov@spbu.ru

Alexander N. Bugrov – Institute of Macromolecular Compounds RAS, Bolshoy pr. 31, 199004 Saint Petersburg, Russia; Saint Petersburg Electrotechnical University "LETI", ul. Professora Popova 5, 197022 Saint Petersburg, Russia; ORCID 0000-0003-1052-4919; alexander.n.bugrov@gmail.com

Conflict of interest: the authors declare no conflict of interest.

NANO ФИХМ

NANOSYSTEMS:

PHYSICS, CHEMISTRY, MATHEMATICS

INFORMATION FOR AUTHORS

The journal publishes research articles and reviews, and also short scientific papers (letters) which are unpublished and have not been accepted for publication in other magazines. Articles should be submitted in English. All articles are reviewed, then if necessary come back to the author to completion.

The journal is indexed in Web of Science Core Collection (Emerging Sources Citation Index), Chemical Abstract Service of the American Chemical Society, Zentralblatt MATH and in Russian Scientific Citation Index.

Author should submit the following materials:

1. Article file in English, containing article title, the initials and the surname of the authors, Institute (University), postal address, the electronic address, the summary, keywords, MSC or PACS index, article text, the list of references.
2. Files with illustrations, files with tables.
3. The covering letter in English containing the article information (article name, MSC or PACS index, keywords, the summary, the literature) and about all authors (the surname, names, the full name of places of work, the mailing address with the postal code, contact phone number with a city code, the electronic address).
4. The expert judgement on possibility of publication of the article in open press (for authors from Russia).

Authors can submit a paper and the corresponding files to the following addresses: nanojournal.ifmo@gmail.com, popov1955@gmail.com.

Text requirements

Articles should be prepared with using of text editors MS Word or LaTex (preferable). It is necessary to submit source file (LaTex) and a pdf copy. In the name of files the English alphabet is used. The recommended size of short communications (letters) is 4-6 pages, research articles– 6-15 pages, reviews – 30 pages.

Recommendations for text in MS Word:

Formulas should be written using Math Type. Figures and tables with captions should be inserted in the text. Additionally, authors present separate files for all figures and Word files of tables.

Recommendations for text in LaTex:

Please, use standard LaTex without macros and additional style files. The list of references should be included in the main LaTex file. Source LaTex file of the paper with the corresponding pdf file and files of figures should be submitted.

References in the article text are given in square brackets. The list of references should be prepared in accordance with the following samples:

[1] Surname N. *Book Title*. Nauka Publishing House, Saint Petersburg, 2000, 281 pp.
[2] Surname N., Surname N. Paper title. *Journal Name*, 2010, **1** (5), P. 17-23.
[3] Surname N., Surname N. Lecture title. In: Abstracts/Proceedings of the Conference, Place and Date, 2000, P. 17-23.
[4] Surname N., Surname N. Paper title, 2000, URL: http://books.ifmo.ru/ntv.
[5] Surname N., Surname N. Patent Name. Patent No. 11111, 2010, Bul. No. 33, 5 pp.
[6] Surname N., Surname N. Thesis Title. Thesis for full doctor degree in math. and physics, Saint Petersburg, 2000, 105 pp.

Requirements to illustrations

Illustrations should be submitted as separate black-and-white files. Formats of files – jpeg, eps, tiff.

NANOSYSTEMS:

PHYSICS, CHEMISTRY, MATHEMATICS

Журнал зарегистрирован
Федеральной службой по надзору в сфере связи, информационных технологий и массовых коммуникаций
(свидетельство ПИ № ФС 77 - 49048 от 22.03.2012 г.)
ISSN 2220-8054

Учредитель: федеральное государственное автономное образовательное учреждение высшего образования
«Национальный исследовательский университет ИТМО»

Издатель: федеральное государственное автономное образовательное учреждение высшего образования
«Национальный исследовательский университет ИТМО»

Отпечатано в Учреждении «Университетские телекоммуникации»
Адрес: 197101, Санкт-Петербург, Кронверкский пр., 49

Подписка на журнал НФХМ
На второе полугодие 2023 года подписка осуществляется через
ОАО «АРЗИ», подписной индекс Э57385